




12-2013

Adsorption and Diffusion of Gases in Nano-Porous Materials

Nethika Sahani Suraweera

University of Tennessee - Knoxville, nsurawee@vols.utk.edu

Follow this and additional works at: https://trace.tennessee.edu/utk_graddiss

 Part of the [Chemical Engineering Commons](#), [Computational Engineering Commons](#), and the [Nanoscience and Nanotechnology Commons](#)

Recommended Citation

Suraweera, Nethika Sahani, "Adsorption and Diffusion of Gases in Nano-Porous Materials. " PhD diss., University of Tennessee, 2013.
https://trace.tennessee.edu/utk_graddiss/2618

This Dissertation is brought to you for free and open access by the Graduate School at TRACE: Tennessee Research and Creative Exchange. It has been accepted for inclusion in Doctoral Dissertations by an authorized administrator of TRACE: Tennessee Research and Creative Exchange. For more information, please contact trace@utk.edu.

To the Graduate Council:

I am submitting herewith a dissertation written by Nethika Sahani Suraweera entitled "Adsorption and Diffusion of Gases in Nano-Porous Materials." I have examined the final electronic copy of this dissertation for form and content and recommend that it be accepted in partial fulfillment of the requirements for the degree of Doctor of Philosophy, with a major in Chemical Engineering.

David J. Keffer, Major Professor

We have read this dissertation and recommend its acceptance:

Craig E. Barnes, Claudia J. Rawn, Robert M. Counce, Paul M. Dalhaimer

Accepted for the Council:

Carolyn R. Hodges

Vice Provost and Dean of the Graduate School

(Original signatures are on file with official student records.)

Adsorption and Diffusion of Gases in Nano- Porous Materials

A Dissertation Presented for the

Doctor of Philosophy

Degree

The University of Tennessee, Knoxville

Nethika Sahani Suraweera

December 2013

DEDICATION

To Dinesh, Ahas and Rue

ACKNOWLEDGEMENTS

I wish to thank my advisor, Prof. David Keffer for his great guidance, continual support and advice. His enthusiasm and encouragement played an important role in helping me meet the requirements of my Doctor of Philosophy degree. I express special thanks to Prof. Craig Barnes for his active participation, support, and insightful feedback at various stages of this research. I am grateful to the current and past students of Computational Materials Research group and Prof. Craig Barnes's research group. I sincerely thank all the above persons for providing a wonderful learning experience and opportunity to work with them. I express my gratitude to Dr. Claudia Rawn, Dr. Paul Dalhaimer and Dr. Robert Counce for serving on my committee. I also wish to express my gratitude to STAIR administrative assistant, Jane Breder for her sincerely kind help in dealing with any official matter. Finally, I greatly appreciate the support and encouragement from my family and friends.

ABSTRACT

In this work, a systematic computational study directed toward developing a molecular-level understanding of gas adsorption and diffusion characteristics in nano-porous materials is presented. Two different types of porous adsorbents were studied, one crystalline and the other amorphous. Physisorption and diffusion of hydrogen in ten iso-reticular metal-organic frameworks (IRMOFs) were investigated. A set of nine adsorbents taken from a class of novel, amorphous nano-porous materials composed of spherosilicate building blocks and isolated metal sites was also studied, with attention paid to the adsorptive and diffusive behavior of hydrogen, methane, carbon dioxide and their binary mixtures. Both classes of materials were modeled to correspond to experimentally synthesized materials. While much research has targeted adsorption in IRMOFs, very little has appeared for these amorphous silicates, which contain cubic silicate building blocks: Si_8O_{20} [spherosilicate units], cross-linked by SiCl_2O_2 [silicon chloride] bridges and decorated with either $-\text{OTiCl}_3$ [titanium chloride] or $-\text{OSiMe}_3$ [trimethylsilyl] groups. Based only on physisorption, the amorphous silicates show competitive adsorptive capacities and selectivities with other commercial gas adsorbents.

The tools employed in this dissertation were computational in nature. Adsorptive properties, such as adsorption isotherms, binding energies and selectivities, were generated from Grand Canonical Monte Carlo molecular (GCMC) simulations. Self-diffusivities and activation energies for diffusion were generated using Molecular Dynamics simulations. Adsorption isotherms are reported at temperatures of 77 K [Kelvin] and 300 K for pressures ranging up to 100 bar. The most favorable adsorption sites for all gases studied in the amorphous silicates are located in front of the faces of the spherosilicate cubes. Regardless of material, the hydrogen adsorption process is governed by entropic considerations at 300 K. At 77 K energetic considerations control hydrogen adsorption at low pressures and entropic effects dominate at high pressure. For methane and carbon dioxide at 300 K, the adsorption process is governed by energetic considerations at low pressure and by entropic (packing) constraints at high pressure. The amorphous silicates showed very high selectivity for carbon dioxide over hydrogen. The presence of titanium sites did not enhance physisorptive capacity or selectivity.

TABLE OF CONTENTS

Chapter 1: Introduction.....	1
References.....	9
Chapter 2: On the Relationship between the Structure of Metal-Organic Frameworks and the Adsorption and Diffusion of Hydrogen	15
Abstract.....	17
2.1 Introduction.....	18
2.2 Simulation Methods.....	21
2.2.1 Crystal Structures.....	21
2.2.2 PI-GCMC Simulation	21
2.2.3 Molecular Dynamics Simulations.....	23
2.2.4 Force Fields.....	24
2.2.5 Accessible volume and surface area Calculation.....	25
2.3 Results and Discussion	26
2.3.1 Adsorption Isotherms.....	26
2.3.2 Density Distributions	27
2.3.3 Energies of adsorption	28
2.3.4 Surface area and accessible volume.....	29
2.3.5 Correlation plots.....	29
2.3.6 Self-Diffusivity	35
2.4 Conclusions.....	37
Acknowledgements.....	38
References.....	39
Appendix A: Tables and Figures	45

Chapter 3: Hydrogen Adsorption and Diffusion in Amorphous, Metal-Decorated Nano-Porous

Silica	58
Abstract	60
3.1 Introduction	61
3.2 Simulation Methods	63
3.2.1 Model for Spherosilicate Structures.....	63
3.2.2 Grand Canonical Monte Carlo Simulation	64
3.2.3 Quantum Mechanical Calculations	65
3.2.4 Molecular Dynamics Simulations.....	66
3.3 Results and Discussion	66
3.3.1 Adsorption Isotherms.....	66
3.3.2 Energies of adsorption	69
3.3.3 Hydrogen adsorption sites.....	70
3.3.4 Self-Diffusivity	72
3.3.5 Comparison with Experiments.....	73
3.4 Conclusions.....	74
Acknowledgements.....	75
References.....	75
Appendix B: Tables and Figures.....	81
Appendix C: Supplementary Document	97

Chapter 4: Methane and Carbon Dioxide Adsorption and Diffusion in Amorphous, Metal-

Decorated Nano-Porous Silica.....	106
Abstract	108
4.1 Introduction.....	109
4.2 Simulation Methods	112

4.2.1 Model for Spherosilicate Structures.....	112
4.2.2 Grand Canonical Monte Carlo Simulation	114
4.2.3 Quantum Mechanical Calculations	116
4.2.4 Molecular Dynamics Simulations.....	117
4.3 Results and Discussion	118
4.3.1 CH ₄ Adsorption.....	118
4.3.2 CO ₂ Adsorption.....	122
4.4 Conclusions.....	127
Acknowledgements.....	127
References.....	128
Appendix D: Tables and Figures	132
Appendix E: Supplementary Document	149
Chapter 5: The Adsorption Properties of Amorphous, Metal-Decorated Nanoporous Silica for Mixtures of Carbon Dioxide, Methane and Hydrogen	161
Abstract.....	163
5.1 Introduction.....	164
5.2 Simulation Methods	166
5.3 Results and Discussion	169
5.3.1 CH ₄ /H ₂ Binary Mixtures	171
5.3.2 CO ₂ /H ₂ Binary Mixtures	173
5.3.3 CO ₂ /CH ₄ Binary Mixtures	174
5.4. Conclusions.....	176
Acknowledgements.....	176
References.....	177

Appendix F: Tables and Figures	180
Appendix G: Supplementary Document	191
Chapter 6: Conclusions	200
6.1 Chapter summary	201
6.2 Significance.....	203
6.3 Future work.....	204
References.....	205
Vita.....	206

LIST OF TABLES

Chapter 2

Table 2.1	The Lennard-Jones parameters for the atoms in the frameworks of the IRMOFs	45
Table 2.2	Unit cell length, unit cell masses, accessible surface areas and accessible volumes for the IRMOFs studied.....	46
Table 2.3	Self-Diffusivity and Activation Energy for IRMOFs	47
Table 2.4	Correlation factors for the relationship of self-diffusivity (at 300 K) and activation energy with surface area, accessible volume and adsorbate-framework energy (at 300 K and 1 bar).....	48

Chapter 3

Table 3.1	Structural details for selected spherosilicate structures.....	82
Table 3.2	The Lennard-Jones parameters for the atoms in the frameworks of the spherosilicate structures.....	83
Table 3.3	Self-Diffusivity and Activation Energies	84
Table 3.4	Correlation factors for the relationship of self-diffusivity (at 300 K) and activation energy with surface area, accessible volume and adsorbate-framework energy (at 300 K and 1 bar).....	85

Chapter 4

Table 4.1	Structural details for selected spherosilicate structures	133
Table 4.2	The Lennard-Jones parameters and partial atomic charges for adsorbent and adsorbate atoms	134
Table 4.3	Self-Diffusivity and Activation Energies for CH ₄ and CO ₂	135
Table 4.4	Correlation factors for the relationship of self-diffusivity (at 300 K) and activation energy with surface area, accessible volume and adsorbate-framework energy (at 300 K and 1 bar) for CH ₄ and CO ₂	136

Chapter 5

Table 5.1	Structural details for selected spherosilicate structures	181
Table 5.2	The Lennard-Jones parameters and partial atomic charges for adsorbent and adsorbate atoms.....	182
Table 5.S1	Isotherm and energy data for CO ₂ /H ₂ equimolar mixture adsorption.....	191
Table 5.S2	Isotherm and energy data for CH ₄ /H ₂ equimolar mixture adsorption.....	192
Table 5.S3	Isotherm and energy data for CO ₂ /CH ₄ equimolar mixture adsorption.....	193
Table 5.S4	Isotherm and energy data for pure component adsorption.....	194

LIST OF FIGURES

Chapter 2

Figure 2.1	Structures of the 10 IRMOFs investigated in this work. The six structures on the left have been experimentally synthesized. The four structures on the right have not, to our knowledge, been synthesized, but the likelihood of synthesis is high based on the existence of functional analogs for the single ring connector. (legend: Zn-purple, O-red, C-green, H-yellow, Br-brown, N-blue).....	49
Figure 2.2	Hydrogen adsorption isotherms at 300 K on a weight percent basis (top) and on a molecules per cage basis (bottom).....	50
Figure 2.3	Hydrogen adsorption isotherms at 77 K on a weight percent basis (top) and on a molecules per cage basis (bottom).....	51
Figure 2.4	Density distributions at 300 K and 1 bar. The surface is drawn at a contour value of $0.0001 \text{ molecules}/\text{\AA}^3$. For each IRMOF, two views are shown, including (I) a view of the unit cell with a small cage in the center and (II) a vertex. IRMOF Legend: (a) IRMOF-1, (b) IRMOF-2, (c) IRMOF-3, (d) IRMOF-7, (e) IRMOF-8, (f) IRMOF-10, (g) IRMOF-10Br ² , (h) IRMOF-10Br ³ , (i) IRMOF-10NH ₂ ² , (j) IRMOF-10NH ₂ ³ . Color legend: violet-Zn, red-O, green-C, white-H, brown-Br, blue-N.....	52
Figure 2.5	Density distributions at 77 K and 1 bar. The surface is drawn at a contour value of $0.015 \text{ molecules}/\text{\AA}^3$. For each IRMOF, two views are shown, including (I) a view of the unit cell with a small cage in the center and (II) a vertex. IRMOF Legend: (a) IRMOF-1, (b) IRMOF-2, (c) IRMOF-3, (d) IRMOF-7, (e) IRMOF-8, (f) IRMOF-10, (g) IRMOF-10Br ² , (h) IRMOF-10Br ³ , (i) IRMOF-10NH ₂ ² , (j) IRMOF-10NH ₂ ³ . Color legend: violet-Zn, red-O, green-C, white-H, brown-Br, blue-N.....	53

Figure 2.6	Adsorbate framework energy as a function of bulk pressure for 300 K (top) and 77 K (bottom).....	54
Figure 2.7	Relationship between surface area and accessible volume on a mass basis (top) and cage basis (bottom).....	55
Figure 2.8	Correlation coefficients relating accessible volume (top) and surface area (bottom) to adsorbate-framework energy as a function of temperature and pressure.....	56
Figure 2.9	Correlation coefficients relating hydrogen adsorption to IRMOF properties as a function of temperature and pressure. (top) Correlation between hydrogen adsorption and free volume. (middle) Correlation between hydrogen adsorption and adsorbate-framework energy. (bottom) Correlation between hydrogen adsorption and surface area.....	57

Chapter 3

Figure 3.1	(a) spherosilicate cube, (b) O_2SiCl_2 bridge, (c) $-OSiMe_3$ end group and (d) $-OTiCl_3$ end group. (e) Course grain structure (Cubes: grey, bridges: red, $-OTiCl_3$:green, $-OSiMe_3$: blue) (f) Atomic structure. (Cl-green, Ti-dark grey, Si-yellow/orange, O-red, C-light gray, H- white).....	86
Figure 3.2	Gravimetric H_2 adsorption isotherms at 300 K (a) low density structure.(b) middle density structure.(c)high density structure.....	87
Figure 3.3	Gravimetric H_2 adsorption isotherms at 77 K (a) low density structure.(b) middle density structure.(c)high density structure.....	88
Figure 3.4	H_2 adsorption isotherms for 0 % $-OTiCl_3$ structure (a) Gravimetric H_2 adsorption isotherms at 300 K.(b) Gravimetric H_2 adsorption isotherms at 77 K. (c) Volumetric H_2 adsorption isotherms at 77 K.....	89
Figure 3.5	Energy between H_2 and framework at 300 K (a) low density structure (b)	90

	for 0 % -OTiCl ₃ structure	
Figure 3.6	Energy between H ₂ and framework at 77 K (a) low density structure (b) for 0 % -OTiCl ₃ structure	91
Figure 3.7	Energy between adsorbed H ₂ (a) low density structures (b) for 0 % -OTiCl ₃ structure.....	92
Figure 3.8	Pair correlation function between H ₂ -H ₂ . (a) at 77 K and 1 bar, (b) at 77 K and 100 bar, (c) at 300 K and 100 bar.....	93
Figure 3.9	Pair correlation function between H ₂ -Si. (a) at 77 K and 1 bar, (b) at 77 K and 100 bar, (c) at 300 K and 100 bar.....	94
Figure 3.10	Pair correlation function between H ₂ -Ti for low density 100% -OTiCl ₃ structure.....	95
Figure 3.11	Experimental and Simulation Isotherms comparison.(a) Simulation isotherms (b) Experimental isotherms	96
Figure 3.S1	Volumetric H ₂ adsorption isotherms at 77 K (a) low density structure.(b) middle density structure.(c) high density structure	99
Figure 3.S2	Volumetric H ₂ adsorption isotherms at 300 K (a) low density structure.(b) middle density structure.(c) high density structure	100
Figure 3.S3	Volumetric H ₂ adsorption isotherms at 77 K (a) for 0 % TiCl ₃ structure (b) for 50 % TiCl ₃ structure (c) for 100 % TiCl ₃ structure	101
Figure 3.S4	Volumetric H ₂ adsorption isotherms at 300 K for 0 % TiCl ₃ structure (b) for 50 % TiCl ₃ structure (c) for 100 % TiCl ₃ structure	102
Figure 3.S5	Pair correlation function between H ₂ -O. (a) at 77 K and 1 bar, (b) at 77 K and 100 bar, (c) at 300 K and 100 bar.....	103
Figure 3.S6	Pair correlation function between H ₂ -Cl. (a) at 77 K and 1 bar, (b) at 77 K	104

	and 100 bar, (c) at 300 K and 100 bar.....	
Figure 3.S7	Pair correlation function between Ti-Ti for low density 100% -OTiCl ₃ structure	105
Chapter 4		
Figure 4.1	(a) Silicate cube matrix after initial cross linking with SiCl ₄ . Golden termini are residual SnMe ₃ groups in the matrix that are exchanged in final functionalization of the matrix (b).	137
Figure 4.2	Coarse grain beads. (a) spherosilicate cube, (b) O ₂ SiCl ₂ bridge, (c) -OSiMe ₃ end group and (d) -OTiCl ₃ end group. (Cl-green, Ti-dark grey, Si-yellow/orange, O-red, C-light gray, H- white).....	138
Figure 4.3	(a) Course grain structure (Cubes: grey, bridges: red, -OTiCl ₃ :green, -OSiMe ₃ : blue) (b) Atomic structure. Atomic color legend as in Figure 4.2.....	139
Figure 4.4	Gravimetric CH ₄ adsorption isotherms at 300 K. (a) low density structure.(b) middle density structure.(c) high density structure	140
Figure 4.5	Energy between CH ₄ and framework at 300 K. (a) low density structure with varying TiCl ₃ content. (b) for 0 % -OTiCl ₃ structure with varying density	141
Figure 4.6	Energy between adsorbed CH ₄ (a) low density structure with varying -OTiCl ₃ content. (b) for 0 % -OTiCl ₃ structure with varying density	142
Figure 4.7	Pair correlation functions at 300 K and 100 bar. (a) between CH ₄ - CH ₄ (b) between CH ₄ -Si (c) between CH ₄ -Ti for low density 100 % -OTiCl ₃ structure	143

Figure 4.8	Comparison of experimental CO ₂ adsorption isotherm at 273.15 K with simulated CO ₂ adsorption isotherms at 300 K with and without framework charges for high density 0% -OTiCl ₃ structure.....	144
Figure 4.9	Gravimetric CO ₂ adsorption isotherms at 300 K. (a) low density structure.(b) middle density structure.(c) high density structure	145
Figure 4.10	Energy between CO ₂ and framework at 300 K. (a) low density structure with varying -OTiCl ₃ content. (b) for 0 % -OTiCl ₃ structure with varying density	146
Figure 4.11	Energy between adsorbed CO ₂ . (a) low density structure with varying -OTiCl ₃ content. (b) for 0 % -OTiCl ₃ structure with varying density.....	147
Figure 4.12	Pair correlation functions at 300 K and 20 bars. (a) between CO ₂ - CO ₂ (b) between CO ₂ -Si (c) between CO ₂ -Ti for low density 100 % -OTiCl ₃ structure	148
Figure 4.S1	Gravimetric CH ₄ adsorption isotherms at 300 K. (a) 0 % -OTiCl ₃ structure (b) 50 % -OTiCl ₃ structure.(c) 100 % -OTiCl ₃ structure	151
Figure 4.S2	Volumetric CH ₄ adsorption isotherms at 300 K (a) low density structure.(b) middle density structure.(c) high density structure	152
Figure 4.S3	Volumetric CH ₄ adsorption isotherms at 300 K for 0 % -OTiCl ₃ structure (b) for 50 % -OTiCl ₃ structure (c) for 100 % -OTiCl ₃ structure..	153
Figure 4.S4	Pair correlation functions at 300 K and 100 bars. (a) between CH ₄ -O (b) between CH ₄ -Cl.....	154
Figure 4.S5	Pair correlation function between Ti-Ti for the low density 100% -OTiCl ₃ structure.....	155
Figure 4.S6	Gravimetric CO ₂ adsorption isotherms at 300 K. with framework charges	156

	for low density structure.....	
Figure 4.S7	Gravimetric CO ₂ adsorption isotherms at 300 K. (a) 0 % -OTiCl ₃ structure (b) 50 % -OTiCl ₃ structure.(c) 100 % -OTiCl ₃ structure.....	157
Figure 4.S8	Volumetric CO ₂ adsorption isotherms at 300 K (a) low density structure.(b) middle density structure.(c) high density structure.....	158
Figure 4.S9	Volumetric CO ₂ adsorption isotherms at 300 K for 0 % -OTiCl ₃ structure (b) for 50 % -OTiCl ₃ structure (c) for 100 % -OTiCl ₃ structure..	159
Figure 4.S10	Pair correlation functions at 300 K and 100 bars. (a) between CO ₂ -O (b) between CO ₂ -Cl.....	160
Chapter 5		
Figure 5.1	(a) spherosilicate cube, (b) O ₂ SiCl ₂ bridge, (c) -OSiMe ₃ end group and (d) -OTiCl ₃ end group. (e) Course grain structure (Cubes: grey, bridges: red, -OTiCl ₃ :green, -OSiMe ₃ : blue) (f) Atomic structure. (Cl-green, Ti-dark grey, Si-yellow/orange, O-red, C-light gray, H- white).....	183
Figure 5.2	Selectivity comparison for CO ₂ /H ₂ mixture adsorption in 0% -OTiCl ₃ low density structure	184
Figure 5.3	CO ₂ /H ₂ mixture adsorption in 0% -OTiCl ₃ low density structure (a) Isotherms, (b) Energy for CO ₂ , (c) Energy for H ₂	185
Figure 5.4	Snap shots for gas mixture adsorption (a) CH ₄ /H ₂ , (b) CO ₂ /H ₂ , (c) CO ₂ /CH ₄ (adsorbed CH ₄ molecules-maroon, adsorbed H ₂ molecules-blue, Cl-green, Ti-dark grey, Si-yellow/orange, O-red, C-light gray, H-white).....	186
Figure 5.5	Selectivity comparison based on effect of density for 0% Ti structure (a) CH ₄ /H ₂ , (b) CO ₂ /H ₂ , (c) CO ₂ /CH ₄	187

Figure 5.6	Selectivity comparison based on effect of Ti content for low density structure (a) CH ₄ /H ₂ , (b) CO ₂ /H ₂ , (c) CO ₂ /CH ₄	188
Figure 5.7	Gravimetric isotherms comparison based on effect of density for 0% Ti structure (a) CH ₄ /H ₂ , (b) CO ₂ /H ₂ , (c) CO ₂ /CH ₄	189
Figure 5.8	Gravimetric isotherms comparison based on effect of Ti content for low density structure (a) CH ₄ /H ₂ , (b) CO ₂ /H ₂ , (c) CO ₂ /CH ₄	190
Figure 5.S1	Selectivity comparison between GCMC and IAST for equimolar binary mixture of CH ₄ /H ₂ (a) low density 0 % -OTiCl ₃ structure. (b) low density 50 % -OTiCl ₃ structure. (c) low density 100 % -OTiCl ₃ structure (d) middle density 0 % -OTiCl ₃ structure. (e) middle density 50 % -OTiCl ₃ structure. (f) middle density 100 % -OTiCl ₃ structure. (g) high density 0 % -OTiCl ₃ structure. (h) high density 0 % -OTiCl ₃ structure. (i) high density 0 % -OTiCl ₃ structure.....	195
Figure 5.S2	Selectivity comparison between GCMC and IAST for equimolar binary mixture of CO ₂ /H ₂ (a) low density 0 % -OTiCl ₃ structure. (b) low density 50 % -OTiCl ₃ structure. (c) low density 100 % -OTiCl ₃ structure (d) middle density 0 % -OTiCl ₃ structure. (e) middle density 50 % -OTiCl ₃ structure. (f) middle density 100 % -OTiCl ₃ structure. (g) high density 0 % -OTiCl ₃ structure. (h) high density 0 % -OTiCl ₃ structure. (i) high density 0 % -OTiCl ₃ structure.....	196
Figure 5.S3	Selectivity comparison between GCMC and IAST for equimolar binary mixture of CO ₂ /CH ₄ (a) low density 0 % -OTiCl ₃ structure. (b) low density 50 % -OTiCl ₃ structure. (c) low density 100 % -OTiCl ₃ structure (d) middle density 0 % -OTiCl ₃ structure. (e) middle density 50 % -OTiCl ₃ structure. (f) middle density 100 % -OTiCl ₃ structure. (g) high density 0 % -OTiCl ₃ structure. (h) high density 0 % -OTiCl ₃ structure. (i) high density 0 % -OTiCl ₃ structure.....	197

Figure 5.S4 Volumetric isotherms comparison based on effect of density for 0% Ti structure (a) CH₄/H₂, (b) CO₂/H₂, (c) CO₂/CH₄..... 198

Figure 5.S5 Volumetric isotherms comparison based on effect of Ti content for low density structure (a) CH₄/H₂, (b) CO₂/H₂, (c) CO₂/CH₄..... 199

CHAPTER 1

Introduction

As the depletion of fossil fuels and the pollution caused by their combustion presents challenges to our energy future, alternative energy sources are being investigated. Utilizing hydrogen [1-3] and natural gas (NG) [4, 5] as sustainable energy carriers and efficient fuels are popular topics of current research and development projects. Hydrogen is mainly produced by steam reforming of natural gas. At the same time other methods such as water splitting (biological/photoelectrochemical/solar thermal) and reforming of biomass and wastes are being investigated [6-9].

Finding a safe and economical storage media for hydrogen remains an important issue. Particularly for on-board vehicular use, hydrogen is usually stored in high pressure tanks, which greatly add to the weight of a storage system and pose an explosion hazard. Some of the new storage methods suggested include liquefaction and adsorption in metal hydrides, activated carbon and metal organic frameworks (MOFs). Each alternative has strengths and weaknesses as a storage medium [8, 10]. In 2011 the Department of Energy (DOE) set the targets for onboard hydrogen storage systems for light-duty vehicles for gravimetric capacity of 5.5 wt.% hydrogen (1.8 kWh/kg system) and volumetric capacity of 0.04 kg hydrogen/L (1.3 kWh/L system) to be achieved by 2017 [11]. These targets will allow some hydrogen-fueled vehicle platforms to meet customer performance expectations, while the “ultimate full fleet” targets of 2.5 kWh/kg system (7.5 wt%), 2.3 kWh/L system (0.070 kg hydrogen/L), and \$8/kWh (\$266/kg H₂) are intended to facilitate the introduction of hydrogen-fueled propulsion systems across the majority of vehicle classes and models.

Adsorption materials used for hydrogen may rely on either chemisorption or physisorption. Materials based on chemisorption, such as metal hydrides, possess large binding energies and consequently display high adsorptive capacities but have slow discharge rates[12]. Adsorption materials based on physisorption, such as single-walled carbon nanotubes (SWNTs) or metal organic frameworks (MOFs), have smaller binding energies and consequently display lower adsorptive capacities, but do not suffer from the significant transport limitations[12]. As neither class of materials currently meets all of the of DOE targets for volumetric capacity, gravimetric capacity and discharge rates, developing efficient adsorbents for hydrogen storage remains of great importance.

At the same time, utilization of natural gas (NG) [4, 5] as a cleaner fuel is a currently active research area. Generating energy from NG produces CO₂, but it is comparatively less than that from other fossil fuels. Commercialization of these fuels in automobiles is a matter of finding efficient methods to separate, capture and store these energy carriers. Storage of energy-related gases in porous materials has been researched in a variety of materials [13, 14]. Currently existing compressed natural gas (CNG) vehicles store gas in high-pressure tanks (greater than 200 atm), which again pose an explosive hazard and add extra weight to vehicles. To address the need for better methane-storage technologies, the US DOE has set the target for methane storage systems at 180 v(STP)/v (STP equivalent of methane per volume of adsorbent material storage system) under 35 bar and near ambient temperature [15]. Current research has been able to develop porous materials that can absorb CH₄ even beyond these targets [16].

The burning of non-renewable fossil fuels produces a steady increase of carbon dioxide in the atmosphere with uncertain but potentially significant impacts on global ecosystems [17]. Solutions for mitigating the impact of CO₂ such as capture and storage of CO₂ [18-20] are being investigated. Development of new, cost-effective, advanced technologies for CO₂ sequestration is continually pursued. Porous materials are being tested and optimized as efficient adsorbents and storage media for CO₂ [21-23].

Separation of gas mixtures containing CH₄, CO₂ and H₂ is currently an interesting topic of study due to interest in clean energy production and concern over environmental issues, including greenhouse gas emissions. Technologies for utilization of methane [4, 5, 24] and hydrogen [1-3] as cleaner fuels are currently being employed and improved. CH₄ is obtained mainly from natural gas (NG). Industrial and municipal landfill gas is also a good source of CH₄ [24]. In both cases CH₄ should be separated from CO₂ and other impurities in order to increase the energy density and to protect methane transportation pipelines and tanks from corrosion caused by CO₂, while in the presence of water forms small amounts of H₂CO₃.

To use hydrogen as a clean fuel in fuel cells, hydrogen is mainly produced by steam reforming of natural gas [25]. The synthetic gas produced by this process contains impurities like CO₂ and CH₄ and need to be removed before hydrogen can be used effectively. Adsorption

separation, using porous materials is a process that generally consumes low energy, therefore an attractive technology to use in gas separation applications.

Due to rising levels of greenhouse gas emissions, separation of CO₂ from mixtures of gases such as the gas emitted from the burning of fossil fuels is of great importance [17]. Flue gas which is the exhaust of fossil-fuel-based power plants accounts for roughly 33–40% of global CO₂ emissions [26]. Therefore industrial carbon capture technologies are vital in environmental safety. New, cost-effective, advanced technologies for CO₂ sequestration are continually being investigated, designed and developed. A variety of nano-porous materials, such as carbonaceous materials, zeolites and metal-organic frameworks (MOFs) have been investigated experimentally and computationally for the adsorptive separation of binary gas mixtures of CH₄-CO₂, H₂-CH₄ and CO₂-CH₄. [18, 26-29]

There remains interest in developing low-cost but high-performance adsorbents for carbon sequestration, gas separation and energy storage applications. In this work, two kinds of nano-porous materials have been studied with respect to adsorption and diffusion of H₂, CH₄ and CO₂: Isoreticular Metal Organic Frameworks (IRMOFs) and amorphous metal-decorated nano-porous silica adsorbents. Hydrogen adsorption and diffusion were studied in IRMOFs. Adsorption and diffusion of the pure gases of H₂, CO₂ and CH₄ and the adsorption of their binary mixtures were studied in metal-decorated nano-porous silica materials.

Isoreticular Metal Organic Frameworks (IRMOFs)[30-32] are nano-porous materials which are commonly synthesized in a building block approach from oxide-centered Zn₄O tetrahedral vertices interconnected by dicarboxylate linkers, resulting in 3-dimensional cubic framework. Linker molecules can be modified in different ways to create a set of different IRMOFs of the same family having different pore sizes and different functionalities. (Details of these structures are included in Chapter 2.)

Investigating hydrogen adsorption in MOFs is a popular research topic. Numerous experimental and simulation research groups have performed investigations to measure and understand hydrogen storage in MOF structures. Experimental results [30, 33, 34] show that none of the currently synthesized MOFs have been able to achieve sufficient hydrogen adsorption quantities at room temperature and atmospheric pressure. They perform as good

hydrogen storage media only at cryogenic temperatures and high pressures. For example, experimental results for IRMOF-1 by Saha et al.[35] show that even at 77 K the pressure should be more than 20 bar to achieve 5.5 wt% DOE target. Modeling and simulation studies have also been performed to analyze various aspects of hydrogen adsorption in MOFs [36-39]. Classical simulations, primarily using Grand Canonical Monte Carlo, have been used to generate adsorption isotherms in MOFs [40]. Quantum mechanical studies identify adsorption sites and binding energies [39, 41]. There remains a need for the systematic analysis of the relationship between the structural characteristics of the IRMOF and the resulting adsorptive properties. The correlation between surface area, free volume, binding energy with the amount of H₂ adsorbed and its diffusivity is required to identify directions for further functionalization to develop materials that may perform as better hydrogen absorbers.

The study of amorphous metal-decorated nano-porous silica adsorbents was motivated by quantum mechanical studies done by Bushnell et al. [42] showing that there exist favorable binding energies for adsorption and desorption of gases in the structures with isolated Ti centers. Binding energies calculated by Bushnell et al. fell between those associated with physisorption and chemisorptions, implying strong but reversible adsorption. In order to test this effect a synthetic strategy was developed to make porous spherosilicate matrices that contain isolated titanium metal centers [43, 44]. These spherosilicate materials have an inorganic cross-linked polymer-like structure and atomically dispersed -OTiCl₃ groups that approximate isolated metal centers. When reduced, the Ti metal centers are predicted to bind hydrogen, as described by Bushnell et al. [42]. In an oxidized state, the Ti metal centers appear as -OTiCl₃, which may still impact the adsorption of gases. The amorphous spherosilicate matrix provides a nano-porous, high-surface-area support to the structure.

The framework of these adsorbents is composed of spherosilicate or silsesquioxane units, cage-like structures in the shape of cubes, hexagonal prisms, octagonal prisms, and decagonal or dodecagonal prisms [45, 46]. In this study we considered cubic polyhedral oligomeric silsesquioxanes (POSS), comprised of 8 Si atoms, with formula (RSiO_{1.5})₈ where R is either a functional ending group or a cross linker which is connected to another spherosilicate unit. They belong to the family of polycyclic compounds consisting of silicon–oxygen bonds. Their ability to incorporate numerous elements throughout the periodic table has been experimentally reported

[43, 44]. Applications are being developed for the metal–POSS compounds as metal catalyst supports [47]. Theoretical modeling studies have been previously done by McCabe et al. for POSS systems [48].

Metal-containing POSS compounds have been studied as heterogeneous metal catalyst supports [49]. Applications are being developed for the metal–POSS compounds themselves as highly active homogeneous catalysts [50, 51], among which POSS-ligated titanium(IV) complexes (Ti-POSS) have proven to be highly active for epoxidation of alkenes [49, 52, 53]. Recently there has been considerable research on heterogenization of homogeneous catalysts due to the ease of separation and purification of the products and the recovery of the catalysts.

POSS structures have also been previously studied for their adsorption capability. An organic–inorganic hybrid porous polymer namely polyaspartimide (PAI) was tested as a solid CO₂ adsorbent by Shanmugam et al.[54]. Adsorption of copper and nickel ions in aqueous solution using nano-cellulose hybrids containing R-POSS, as a novel biosorbent was studied by Xie et al. [55]. Hongbo et al. observed strong adsorption energies between N₂ molecules, resulting in high adsorptive capacities in the study of adsorption and desorption properties of hybrid aerogels derived from methacryloxypropyltrimethoxysilane based silsesquioxane [56]. Maiti et al. investigated hydrogen catalysis and sequestration in Pd-POSS systems [57].

In Chapter 2, the relationship between the structure of metal-organic frameworks and the adsorption and diffusion of hydrogen is studied. Even though there has been a tremendous amount of work on the subject of hydrogen adsorption in MOFs, there is still a need for establishing clear correlations between structural characteristics and adsorptive properties across a broad swath of temperatures and pressures. The objective of this study is to provide such a systematic analysis. Ten different IRMOFs have been analyzed in this work: IRMOF-1, IRMOF-2, IRMOF-3, IRMOF-7, IRMOF-8, IRMOF-10, IRMOF-10NH₂2 (IRMOF-10 with amine groups at position two), IRMOF-10NH₂3 (IRMOF-10 with amine groups at position three), IRMOF-10Br2 (IRMOF-10 with a bromine atom at position two) and IRMOF-10Br3 (IRMOF-10 with a bromine atom at position three). The first six structures have been synthesized and the last four structures have not been synthesized, but should be possible based on the fact that analogously functionalized connectors with a single carbon ring exist. These ten IRMOFs were

chosen because they capture changes in cage size, functionalization with a halide and a polar group, as well as placement of functional groups. In order to understand the temperature dependence, simulations were performed for hydrogen adsorption at both 77 K and 300 K. In order to understand the pressure dependence, simulations were performed from 0.1 bar to 10 bar. Isotherms, diffusivities, binding energies, site locations and geometries, SAs and AVs are calculated and statistically correlated to each other across all absorbent materials, temperatures and pressures.

In Chapter 3, hydrogen adsorption and diffusion in amorphous, metal-decorated nano-porous silica is investigated. The class of adsorbents studied in this work have been synthesized in a manner in which the surface area and free volume of the silica matrix and amount of titanium present (as $-\text{OTiCl}_3$) in the material can be controlled [43, 44, 47]. The results of molecular-level simulations to study physisorption and diffusion in these materials is reported, fundamental structure/property relationships were developed. Adsorption isotherms and energies at 77 K and 300 K for pressures up to 100 bar were generated via molecular simulation describing physisorption. Particularly, the impact of surface area, accessible volume energy of adsorption and Ti content on the adsorptive and diffusive behavior of H_2 were investigated. Adsorption sites were identified using pair correlation functions.

In Chapter 4, studies of pure component methane and carbon dioxide adsorption and diffusion in amorphous, metal-decorated nano-porous silica are presented. The adsorbent contains cubic silicate building blocks (silsesquioxane units: Si_8O_{20}), which are cross-linked by SiCl_2O_2 bridges and decorated with either OTiCl_3 or $\text{Si}(\text{CH}_3)_3$ groups. The model structures were generated to correspond to experimentally synthesized materials, matching physical properties including density, surface area, and accessible volume. This study reports and analyses the results of molecular-level simulations to study physisorption and diffusion of CO_2 and CH_4 in these materials. Adsorption isotherms and energies at 300 K for pressures up to 100 bar for CH_4 and up to 52 bar for CO_2 were generated via molecular simulation. Based on the pair correlation functions most favorable adsorption sites for adsorbates were identified.

In Chapter 5, studies on the adsorption of three binary gas mixtures, composed of combinations of H_2 , CH_4 and CO_2 , in amorphous, metal-decorated nano-porous silica are

presented. Adsorption of equimolecular binary gas mixers were simulated in each structure. H₂-CH₄ mixtures were simulated at 300 K and up to 100 bars. CH₄-CO₂ and H₂-CO₂ mixtures were simulated at 300 K and up to 50 bars. In every case the materials were selective for CO₂ over CH₄ and H₂ and were selective for CH₄ over H₂.

References

- [1] I.P. Jain, *Hydrogen the fuel for 21st century*, Int. J. Hydrog. Energy. 34 (2009), pp. 7368-7378.
- [2] T.K. Mandal and D.H. Gregory, *Hydrogen: a future energy vector for sustainable development*, Proc. Inst. Mech. Eng. Part C-J. Eng. Mech. Eng. Sci. 224 (2010), pp. 539-558.
- [3] N.A. Kelly, T.L. Gibson, M. Cai, J.A. Spearot and D.B. Ouwerkerk, *Development of a renewable hydrogen economy: optimization of existing technologies*, Int. J. Hydrog. Energy. 35 (2010), pp. 892-899.
- [4] W.M. Frota, J.A.S. Sa, S.S.B. Moraes, B.R.P. Rocha and K.A.R. Ismail, *Natural gas: The option for a sustainable development and energy in the state of Amazonas*, Energy Policy. 38 (2010), pp. 3830-3836.
- [5] M. Taniowski, *Sustainable chemical technologies in production of clean fuels from fossil fuels*, Clean-Soil Air Water. 36 (2008), pp. 393-398.
- [6] S. Elnashaie, Z.X. Chen and P. Prasad, *Efficient production and economics of clean-fuel hydrogen*, Int. J. Green Energy. 4 (2007), pp. 249-282.
- [7] K.B. Lee, M.G. Beaver, H.S. Caram and S. Sircar, *Reversible chemisorption of carbon dioxide: simultaneous production of fuel-cell grade H₂ and compressed CO₂ from synthesis gas*, Adsorpt.-J. Int. Adsorpt. Soc. 13 (2007), pp. 385-397.
- [8] K. Nath and D. Das, *Production and storage of hydrogen: Present scenario and future perspective*, J. Sci. Ind. Res. 66 (2007), pp. 701-709.
- [9] E. Pasculete, F. Condrea and C. Radulescu, *Hydrogen and sustainable energy. Research for hydrogen production*, Environ. Eng. Manag. J. 6 (2007), pp. 45-49.
- [10] K.L. Lim, H. Kazemian, Z. Yaakob and W.R.W. Daud, *Solid-state Materials and Methods for Hydrogen Storage: A Critical Review*, Chem. Eng. Technol. 33 (2010), pp. 213-226.
- [11] *Fuel Cell Technologies Office Multi-Year Research, Development and Demonstration Plan*, US Dept. of Energy- Energy Efficiency and Renewable Energy-Fuel Cell Technologies Office, 2011.

- [12] J. Yang, A. Sudik, C. Wolverton and D.J. Siegel, High capacity hydrogen storage materials: attributes for automotive applications and techniques for materials discovery, *Chem. Soc. Rev.* 39 (2010), pp. 656-675.
- [13] Q.F. Zhang, E. Uchaker, S.L. Candelaria and G.Z. Cao, *Nanomaterials for energy conversion and storage*, *Chem. Soc. Rev.* 42 (2013), pp. 3127-3171.
- [14] S.Q. Ma and L. Meng, *Energy-related applications of functional porous metal-organic frameworks*, *Pure and Applied Chemistry.* 83 (2011), pp. 167-188.
- [15] M.R. Tim Burchell, *Low pressure storage of natural gas for vehicular applications*, SAE, Washington, D.C., 2000.
- [16] S. Ma, D. Sun, J.M. Simmons, C.D. Collier, D. Yuan and H.-C. Zhou, *Metal-organic framework from an anthracene derivative containing nanoscopic cages exhibiting high methane uptake*, *J Am Chem Soc.* 130 (2008), pp. 1012-1016.
- [17] T.A. Boden, G. Marland, and R.J. Andres, *Global, Regional, and National Fossil-Fuel CO₂ Emissions.*, Carbon Dioxide Information Analysis Center, Oak Ridge National Laboratory, U.S. Department of Energy, Oak Ridge, Tenn., (USA).
- [18] P.F. N Florin, *Carbon capture technology: future fossil fuel use and mitigating climate change*, Grantham Institute for Climate Change, London (UK), 2010.
- [19] C. Ehlig-Economides and M.J. Economides, *Sequestering carbon dioxide in a closed underground volume*, *Journal of Petroleum Science and Engineering.* 70 (2010), pp. 118-125.
- [20] J.D. Figueroa, T. Fout, S. Plasynski, H. McIlvried and R.D. Srivastava, *Advances in CO₂ capture technology - The US Department of Energy's Carbon Sequestration Program*, *International Journal of Greenhouse Gas Control.* 2 (2008), pp. 9-20.
- [21] K.S. Walton, A.R. Millward, D. Dubbeldam, H. Frost, J.J. Low, O.M. Yaghi and R.Q. Snurr, *Understanding inflections and steps in carbon dioxide adsorption isotherms in metal-organic frameworks*, *J. Am. Chem. Soc.* 130 (2008), pp. 406-+.
- [22] A.R. Millward and O.M. Yaghi, *Metal-organic frameworks with exceptionally high capacity for storage of carbon dioxide at room temperature*, *J. Am. Chem. Soc.* 127 (2005), pp. 17998-17999.

- [23] M. Sevilla and A.B. Fuertes, *Sustainable porous carbons with a superior performance for CO₂ capture*, Energy & Environmental Science. 4 (2011), pp. 1765-1771.
- [24] H.R. Amini and D.R. Reinhart, *Regional prediction of long-term landfill gas to energy potential*, Waste Manage. 31 (2011), pp. 2020-2026.
- [25] J.R. Hufton, S. Mayorga and S. Sircar, *Sorption-enhanced reaction process for hydrogen production*, Aiche Journal. 45 (1999), pp. 248-256.
- [26] H.Q. Yang, Z.H. Xu, M.H. Fan, R. Gupta, R.B. Slimane, A.E. Bland and I. Wright, *Progress in carbon dioxide separation and capture: A review*, J. Environ. Sci. 20 (2008), pp. 14-27.
- [27] C.E. Wilmer, O.K. Farha, Y.S. Bae, J.T. Hupp and R.Q. Snurr, *Structure-property relationships of porous materials for carbon dioxide separation and capture*, Energy & Environmental Science. 5 (2012), pp. 9849-9856.
- [28] Q.Y. Yang and C.L. Zhong, *Molecular simulation of carbon dioxide/methane/hydrogen mixture adsorption in metal-organic frameworks*, J. Phys. Chem. B. 110 (2006), pp. 17776-17783.
- [29] D. Wu, C.C. Wang, B. Liu, D.H. Liu, Q.Y. Yang and C.L. Zhong, *Large-scale computational screening of metal-organic frameworks for CH₄/H₂ separation*, Aiche Journal. 58 (2012), pp. 2078-2084.
- [30] J.L.C. Rowsell, A.R. Millward, K.S. Park and O.M. Yaghi, *Hydrogen sorption in functionalized metal-organic frameworks*, J. Am. Chem. Soc. 126 (2004), pp. 5666-5667.
- [31] H. Li, M. Eddaoudi, M. O'Keeffe and O.M. Yaghi, *Design and synthesis of an exceptionally stable and highly porous metal-organic framework*, Nature. 402 (1999), pp. 276-279.
- [32] M. Eddaoudi, J. Kim, N. Rosi, D. Vodak, J. Wachter, M. O'Keeffe and O.M. Yaghi, *Systematic design of pore size and functionality in isorecticular MOFs and their application in methane storage*, Science. 295 (2002), pp. 469-472.

- [33] N.L. Rosi, J. Eckert, M. Eddaoudi, D.T. Vodak, J. Kim, M. O'Keeffe and O.M. Yaghi, *Hydrogen storage in microporous metal-organic frameworks*, Science. 300 (2003), pp. 1127-1129.
- [34] F.M. Mulder, T.J. Dingemans, H.G. Schimmel, A.J. Ramirez-Cuesta and G.J. Kearley, *Hydrogen adsorption strength and sites in the metal organic framework MOF5: Comparing experiment and model calculations*, Chem. Phys. 351 (2008), pp. 72-76.
- [35] D.P. Saha, Z.J. Wei and S.G. Deng, *Hydrogen adsorption equilibrium and kinetics in metal-organic framework (MOF-5) synthesized with DEF approach*, Sep. Purif. Technol. 64 (2009), pp. 280-287.
- [36] P. Ryan, L.J. Broadbelt and R.Q. Snurr, *Is catenation beneficial for hydrogen storage in metal-organic frameworks?*, Chem. Commun. (2008), pp. 4132-4134.
- [37] H. Frost, T. Duren and R.Q. Snurr, *Effects of surface area, free volume, and heat of adsorption on hydrogen uptake in metal-organic frameworks*, J. Phys. Chem. B. 110 (2006), pp. 9565-9570.
- [38] H. Frost and R.Q. Snurr, *Design requirements for metal-organic frameworks as hydrogen storage materials*, J. Phys. Chem. C. 111 (2007), pp. 18794-18803.
- [39] M. Fischer, F. Hoffmann and M. Froba, *Molecular simulation of hydrogen adsorption in metal-organic frameworks*, Colloid Surf. A-Physicochem. Eng. Asp. 357 (2010), pp. 35-42.
- [40] G. Garberoglio, A.I. Skoulidas and J.K. Johnson, *Adsorption of gases in metal organic materials: Comparison of simulations and experiments*, J. Phys. Chem. B. 109 (2005), pp. 13094-13103.
- [41] K. Sillar, A. Hofmann and J. Sauer, *Ab Initio Study of Hydrogen Adsorption in MOF-5*, J. Am. Chem. Soc. 131 (2009), pp. 4143-4150.
- [42] J.E. Bushnell, P. Maitre, P.R. Kemper and M.T. Bowers, *Binding energies of Ti+(H₂)(1-6) clusters: Theory and experiment*, J Chem Phys. 106 (1997), pp. 10153-10167.
- [43] J.C. Clark, S. Saengkerdsud, G.T. Eldridge, C. Campana and C.E. Barnes, *Synthesis and structure of functional spherosilicate building block molecules for materials synthesis*, Journal of Organometallic Chemistry. 691 (2006), pp. 3213-3222.

- [44] J.C. Clark and C.E. Barnes, Reaction of the $\text{Si}_8\text{O}_{20}(\text{SnMe}_3)_8$ building block with silyl chlorides: A new synthetic methodology for preparing nanostructured building block solids, *Chemistry of Materials*. 19 (2007), pp. 3212-3218.
- [45] D.B. Cordes, P.D. Lickiss and F. Rataboul, *Recent developments in the chemistry of cubic polyhedral oligosilsesquioxanes*, *Chemical Reviews*. 110 (2010), pp. 2081-2173.
- [46] T. Jaroentomeechai, P.K. Yingsukkamol, C. Phurat, E. Somsook, T. Osotchan and V. Ervithayasuporn, *Synthesis and reactivity of nitrogen nucleophiles-induced cage-rearrangement silsesquioxanes*, *Inorganic Chemistry*. 51 (2012), pp. 12266-12272.
- [47] N.N. Ghosh, J.C. Clark, G.T. Eldridge and C.E. Barnes, *Building block syntheses of site-isolated vanadyl groups in silicate oxides*, *Chem. Commun.* (2004), pp. 856-857.
- [48] C. McCabe, S.C. Glotzer, J. Kieffer, M. Neurock and P.T. Cummings, *Multiscale simulation of the synthesis, assembly and properties of nanostructured organic/inorganic hybrid materials*, *J. Comput. Theor. Nanosci.* 1 (2004), pp. 265-279.
- [49] H.C.L. Abbenhuis, S. Krijnen and R.A. van Santen, Modelling the active sites of heterogeneous titanium epoxidation catalysts using titanium silasequioxanes: Insight into specific factors that determine leaching in liquid-phase processes, *Chemical Communications*. (1997), pp. 331-332.
- [50] R. Duchateau, Incompletely condensed silsesquioxanes: Versatile tools in developing silica-supported olefin polymerization catalysts, *Chemical Reviews*. 102 (2002), pp. 3525-3542.
- [51] R. Hanssen, R.A. van Santen and H.C.L. Abbenhuis, *The dynamic status quo of polyhedral silsesquioxane coordination chemistry*, *Eur. J. Inorg. Chem.* (2004), pp. 675-683.
- [52] S. Krijnen, H.C.L. Abbenhuis, R. Hanssen, J.H.C. van Hooff and R.A. van Santen, *Solid-phase immobilization of a new epoxidation catalyst*, *Angewandte Chemie-International Edition*. 37 (1998), pp. 356-358.
- [53] S. Krijnen, B.L. Mojet, H.C.L. Abbenhuis, J.H.C. Van Hooff and R.A. Van Santen, MCM-41 heterogenised titanium silsesquioxane epoxidation catalysts: a spectroscopic investigation of the adsorption characteristics, *Physical Chemistry Chemical Physics*. 1 (1999), pp. 361-365.

- [54] N. Shanmugam, K.T. Lee, W.Y. Cheng and S.Y. Lu, Organic-inorganic hybrid polyaspartimide involving polyhedral oligomeric silsesquioxane via Michael addition for CO₂ capture, *J. Polym. Sci. Pol. Chem.* 50 (2012), pp. 2521-2526.
- [55] K.L. Xie, L.X. Jing, W.G. Zhao and Y.L. Zhang, Adsorption removal of Cu₂₊ and Ni₂₊ from waste water using nano-cellulose hybrids containing reactive polyhedral oligomeric silsesquioxanes, *J. Appl. Polym. Sci.* 122 (2011), pp. 2864-2868.
- [56] H.B. Ren, Y.C. Qin, C.W. Shang, Y.T. Bi and L. Zhang, *Adsorption and desorption properties of hybrid aerogels derived from MPMS-SSO at 77 K*, *Rare Metal Materials and Engineering.* 39 (2010), pp. 475-478.
- [57] A. Maiti, R.H. Gee, R. Maxwell and A.P. Saab, *Hydrogen catalysis and scavenging action of Pd-POSS nanoparticles*, *Chem. Phys. Lett.* 440 (2007), pp. 244-248.

CHAPTER 2

On the Relationship between the Structure of Metal-Organic Frameworks and the Adsorption and Diffusion of Hydrogen

This chapter is a slightly revised version of a paper by the same title published in the *Journal of Molecular Simulation* in 2011 by **Nethika S. Suraweera**, R. Xiong, J.P. Luna, D.M. Nicholson, and D.J. Keffer:

Suraweera, N.S., Xiong, R., Luna, J.P., Nicholson, D.M., Keffer, D.J., “On the Relationship between the Structure of Metal-Organic Frameworks and the Adsorption and Diffusion of Hydrogen”, *Molec. Simul.*, 37(7) 2011 pp. 621-639.

The use of “we” in this part refers to the co-authors and the author of this dissertation. My primary contributions to this paper include (1) all of the simulation work (2) analysis of data, and (3) most of the writing

Reproduced with permission from *Molec. Simul.* 2011. Copyright © Taylor and Francis, 2011

Abstract

In this work, the adsorptive and diffusive behavior of molecular hydrogen in ten different Iso-Reticular Metal-Organic Frameworks (IRMOFs) is studied using molecular-level simulation. Hydrogen adsorption isotherms and heats of adsorption at 77 K and 300 K were generated for ten MOFs at low pressure conditions (up to 10 bar) using Path Integral Grand Canonical Monte Carlo simulations. Self-diffusivities and activation energies for diffusion were generated using Molecular Dynamics simulation. Density distributions showing the location and shape of the adsorption sites are also provided. Statistical correlations for all of the properties as a function of surface area (SA), accessible volume (AV), and binding energy are provided. Based on this work, we observe that at pressures up to 10 bar at 300 K, the adsorption process is virtually completely governed by entropic considerations, resulting in a strong correlation between the amount of hydrogen adsorbed and the AV of the adsorbent. At 77 K, we observe more than one adsorption regimes. At low pressures, the adsorption process is governed by energetic considerations, resulting in a strong correlation between the amount of hydrogen adsorbed and the energy of adsorption. At the high end of the pressure range, the adsorption becomes a process dominated by entropic considerations, again resulting in a strong correlation between the amount of hydrogen adsorbed and the AV. Only in the intermediate regime, does one observe that an increase in SA results in an increase in the amount of hydrogen adsorbed. Self-diffusivity of hydrogen at infinite dilution is highly correlated with both the energy of adsorption and AV. The diffusion in larger IRMOFs is faster because of an entropic advantage and specifically not because of a lower activation energy for diffusion.

Keywords: hydrogen adsorption, GCMC simulation, statistical mechanics, adsorption isotherm, self-diffusivity, activation energy, MOF, IRMOF

2.1 Introduction

Using hydrogen as a sustainable energy source is frequently addressed as an alternative to fossil fuels. Research and development are being carried out throughout the world for utilizing hydrogen as an efficient fuel [1-3]. Steam reforming of natural gas is a prevalent means of hydrogen production and other methods such as water splitting (biological/photoelectrochemical/solar thermal) and reforming of biomass and wastes are being investigated [4-7]. Meanwhile finding a safe and economical way to store hydrogen gas, particularly for on-board vehicular use, remains a challenge. Hydrogen is difficult to store in sufficient quantities without placing it under high pressure, something that greatly adds to the weight of a storage system and increases the explosion hazard. Compressed gas, liquefaction, metal hydrides, physisorption and adsorption in activated carbon are some of the methods used for hydrogen storage. Each of them has strengths and weaknesses as a storage medium[6, 8]. In 2009 the Department of Energy (DOE) set the targets for onboard hydrogen storage systems for light-duty vehicles as weight efficiency of 5.5 wt.% hydrogen and volumetric density of 0.04 kg hydrogen/L to be achieved in 2015.[9]

Adsorption materials based on chemisorptions of hydrogen, such as metal hydrides, possess large binding energies and consequently display high adsorptive capacities but may have slow discharge rates[10]. Adsorption materials based on physisorption, such as single-walled carbon nanotubes (SWNTs) or metal organic frameworks (MOFs), have smaller binding energies and consequently display lower adsorptive capacities, but do not suffer from the significant transport limitations[10]. Neither class of materials currently meets all of the of DOE targets for volumetric capacity, gravimetric capacity and discharge rates. Therefore, developing efficient adsorbents for hydrogen storage remains of great importance.

Isorecticular Metal Organic Frameworks (IRMOFs) are a class of metal organic frameworks discovered by Yaghi and co-workers [11-13]. They are microporous materials which synthesized in a building block approach from oxide-centered Zn_4O tetrahedral vertices interconnected by dicarboxylate linkers, resulting in 3-dimensional cubic framework. Different linker molecules can be used to create a set of different IRMOFs of the same family having different pore sizes and different functionalities. Structures of the IRMOFs investigated in this manuscript are provided in Figure 2.1.

IRMOFs have been widely analyzed for their ability to store hydrogen both experimentally and via simulation. Currently synthesized IRMOFs have not been able to fulfill the DOE requirements for hydrogen storage. A systematic analysis of the relationship between the structural characteristics of the IRMOF and the resulting adsorptive properties can help to identify directions for further functionalization to develop materials that satisfy all of the DOE requirements.

The study of hydrogen adsorption in MOFs has received great attention. Many groups have done investigations to measure and understand hydrogen storage in MOF structures. Experimental adsorption isotherms of hydrogen in MOFs are numerous [11, 14, 15]. The experimental results show that none of the MOFs have been able to achieve sufficient hydrogen adsorption quantities at room temperature and atmospheric pressure. At cryogenic temperatures and high pressures they can act as good hydrogen storage media. The experimental results for IRMOF-1 by Saha *et al.*[16] show that even at 77 K the pressure should be more than 20 bar to achieve 5.5 wt% DOE target.

Numerous modeling efforts have also been performed to analyze various aspects of hydrogen adsorption in MOFs [17-20]. Quantum mechanical studies identify adsorption sites and binding energies [20, 21]. Numerous classical simulations, primarily using Grand Canonical Monte Carlo, have also been used to generate adsorption isotherms in MOFs [22].

A study by Frost *et al.* [18] identifies three regimes of adsorption. At low pressure, the amount of hydrogen adsorbed corresponds to the heat of adsorption. At intermediate pressures, the amount of hydrogen adsorbed corresponds to the available surface area (SA). At high loadings, the amount of hydrogen adsorbed corresponds to the available accessible volume (AV). Based on these types of calculations, one can estimate the required heat of adsorption to meet the current targets at a given temperature and pressure[19].

Modifications can be done to structures to improve the hydrogen uptake such as catenation [17, 23-26], impregnating nonvolatile guest molecules into the framework [23], incorporating unsaturated metal sites within the framework [27, 28], and adding charges to the system [29]. All of these methods have potential advantages and disadvantages.

While clearly there has been a tremendous amount of work on the subject of hydrogen adsorption in MOFs, there is still a need for establishing clear correlations between structural

characteristics and adsorptive properties across a broad swath of temperatures and pressures. The objective of this study is to provide such a systematic analysis. To this end, ten different IRMOFs have been analyzed in this work, as shown in Figure 2.1. The first six structures on the left, IRMOF-1, IRMOF-2, IRMOF-3, IRMOF-7, IRMOF-8, and IRMOF-10 have been synthesized. The last four IRMOF-10NH₂² (IRMOF-10 with amine groups at position two), IRMOF-10NH₂³ (IRMOF-10 with amine groups at position three), IRMOF-10Br² (IRMOF-10 with a bromine atom at position two) and IRMOF-10Br³ (IRMOF-10 with a bromine atom at position three) have not been synthesized, but should be possible based on the fact that analogously functionalized connectors with a single carbon ring exist, e.g. IRMOF-2 for bromine and IRMOF-3 for the amine group. These ten IRMOFs were chosen because they capture changes in cage size, functionalization with a halide and a polar group, as well as placement of functional groups. In order to understand the temperature dependence, simulations were performed at both 77 K and 300 K. In order to understand the pressure dependence, simulations were performed from 0.1 bar to 10 bar. Isotherms, diffusivities, binding energies, site locations and geometries, SAs and AVs are calculated and statistically correlated to each other across all absorbent materials, temperatures and pressures.

2.2 Simulation Methods

2.2.1 Crystal Structures

The crystal structures of the six IRMOFs studied in this work that have been experimentally synthesized were obtained from crystallographic data provided by Eddaoudi *et al.* [13]. The Zn_4O tetrahedra are located at the vertices and they are connected via different organic linkers (in IRMOF-1: 1,4-benzenedicarboxylate (BDC)) to form three-dimensional nano-porous cubic frameworks with different unit cell dimensions. Only for IRMOF-1 are the positions of hydrogen atoms experimentally resolved. For all other IRMOFs, the hydrogen positions bound to benzene rings were determined by maintaining the same CH bond lengths, CCH bond angles and CCCH dihedral angles as present in IRMOF-1. For several of the structures, there were multiple equivalent positions for some atoms. For example, in IRMOF-3, there are four equivalent positions for the amine group on each benzene ring. In this case, we generated crystals containing 6x6x6 cages and randomly placed the amine on each linker. This larger block of 216 cages was used as the repeat unit in the simulations. Other structures, such as IRMOF-7 and IRMOF-8, have multiple orientations for each organic linker. In IRMOF-8, the orientation of each linkers was selected randomly from those reported in the crystallographic data. In IRMOF-7, such random orientation results in overlap of nearby linkers; therefore the linkers were not oriented randomly but rather were arranged to avoid overlap. The four IRMOFs that have not been experimentally synthesized are variations on IRMOF-10. Therefore, we used the IRMOF-10 structure and added either a bromine atom or an amine group in such a way as to maintain the bond distances, bond angles and dihedral angles present in IRMOF-2 (bromine) and IRMOF-3 (amine). This turned out to yield acceptable structures except for the bromine at position 3, which overlapped with an adjacent hydrogen. We therefore, optimized the position of the bromine (CCBr angle is 110°) using the UFF potential [30]. All structures are available in an archived site online [31].

2.2.2 PI-GCMC Simulation

The Path Integral Grand Canonical Monte Carlo (PI-GCMC) simulation technique [32, 33] was employed to calculate hydrogen adsorption in the IRMOFs. It is well known when the molecular mass is small and when temperature is low, quantum effects become non-negligible in

the trajectory of molecules. Even at 300 K, quantum effects could lead to an overestimation of adsorption by several percent [34]. Therefore we have adopted the path integral (PI) formalism in the standard Grand Canonical Monte Carlo (GCMC) simulation. The formalism creates an isomorphism between a quantum particle and a classical closed-ring polymer molecule to account for quantum effects. The details for the formalism can be found in the Feynman's theory [35]. Details of the path integral technique can be found in several references [36-38].

As in the standard GCMC method, the chemical potential (μ), volume (V) and temperature (T) of the system are fixed and the simulation delivers, among other properties, the number of particles in the system and the potential energy corresponding to a particular choice of μ , V and T . The path integral formalism approximates the quantum partition function with the partition function of a classical system. [32, 33, 37]

$$Q(\mu, V, T) \approx Q_{PI} = \frac{1}{N!} \left(\frac{2\pi m P k T}{h^2} \right)^{3NP/2} \int d\vec{q}_1 \dots d\vec{q}_N \times \exp[-\beta(U^{ext} + U^{int})] \quad (1)$$

The path integral partition function, Q_{PI} in Eq. (1), describes a system of ring polymers, each containing P beads of mass m . N is number of particles. The vectors \vec{q}_i stand for the center of mass positions, orientations, and configurations of each of the ring polymers. The polymers experience both an external potential U^{ext} , and an internal potential U^{int} .

The residual chemical potential μ^{res} , is the difference between the chemical potential of the real fluid and that of the ideal gas at the same density and temperature. $\mu = \mu^{res} + \mu^{vib} + \mu^{rot,nucl}$, μ^{vib} and $\mu^{rot,nucl}$ are the vibrational and coupled rotational and nuclear contributions to the chemical potential of the ideal gas, respectively. From SM modeling, we know vibrational and coupled rotational and nuclear partition function, we can calculate the chemical potentials. Therefore as long as we defined the total chemical potential, the residual chemical potential was determined. There are four types of moves involved in the PI-GCMC method: (i) center-of-mass translation, (ii) center-of-mass rotation, (iii) molecule insertion and (iv) molecule deletion, which were randomly attempted in a ratio of 3:3:2:2. We have used $P = 30$ beads per molecule in our simulation considering computation efficiency and statistics accuracy. This number was proved to be sufficient to ensure the convergence of the total energy[22]. A pool of configurations of ring polymers used in the insertion step is generated using molecular dynamics (MD) simulation in the ideal gas state. [37, 39]

For a given choice of chemical potential and temperature, we performed two simulations: one in the bulk phase and one in the adsorbed phase. We generated adsorption isotherms by plotting the fractional loading obtained from the adsorbed phase as a function of the pressure obtained from the bulk phase. We chose the volume of the bulk and adsorbed phases such that the average number of hydrogen molecules in the system turned out to be bound by 100 and 2500.

A spherical cut-off was used in the simulation. The cut-off distance was set to 15 Å. Beyond this cut-off distance, a long-range correction was used to compensate for the cut-off error. Standard periodic boundary conditions and the minimum image convention were employed in all three directions. For each state point in this simulation, 10 million configurations were used to guarantee equilibrium and another 10 million configurations were performed to get the desired average ensemble properties.

2.2.3 Molecular Dynamics Simulations

Classical equilibrium MD simulations were performed to obtain diffusivities of hydrogen adsorbed in each IRMOF. The equations of motion were integrated using the two-time step r-RESPA algorithm of Tuckerman and co-workers[40]. Intramolecular degrees of freedom were accounted for in the short time loop, with a step size of 0.2 fs. 10 short steps were performed per long time step. The temperature was controlled using the Nosé-Hoover thermostat[41, 42]. The system was equilibrated for 2 ns. Following equilibration, an additional 8 ns was simulated for data production. During data production, positions of the center-of-mass of the hydrogen molecules were saved every 5 ps and were used to calculate the self-diffusivity via the Einstein relation. Uncertainties in the self-diffusivity are reported as the standard deviation of the x, y, and z components of the diffusivity.

For the diffusivity calculations, we adopted Feynman-Hibbs (FH) effective Buch potential method [43, 44] in molecular dynamics simulations to account the quantum effects. This is much more computationally efficient than the PIMC method. As has been shown by others, the FH effective Buch potential is capable of accurately reproducing properties from Path Integral Monte Carlo. We also validated that points on the isotherm could be reproduced using either the FH effective Buch potential or the PI method to within 0.06 %. Therefore, the MD

simulations employed the FH effective Buch potential. Specifically, FH effective Buch potential truncated at the quadratic term was used [43].

$$U_{FH}(r) = U_{LJ}(r) + \left(\frac{\hbar^2}{24\mu kT} \right) \nabla^2 U_{LJ}(r) \quad (2)$$

where $U_{LJ}(r)$ is the Lennard-Jones (LJ) interaction potential, r is the separation, \hbar is Planck's constant over 2π , μ is the reduced mass (For the H₂-H₂ interactions, $\mu=m/2$ and for H₂-sorberent interaction, $\mu=m$, where m is the mass of H₂ molecule.), k is Boltzmann's constant, and T is the absolute temperature. The Laplacian of the potential is

$$\nabla^2 U_{LJ}(r) = U''_{LJ}(r) + \frac{2}{r} U'_{LJ}(r) = 4\epsilon \left(\frac{132\sigma^{12}}{r^{14}} - \frac{30\sigma^6}{r^8} \right) \quad (3)$$

2.2.4 Force Fields

In determining an appropriate interaction potential, we use the LJ potential to model hydrogen in the GCMC simulations. Hydrogen is treated as a classical closed-ring polymer molecule. Each bead on the molecule has the same mass as classical single hydrogen molecule and LJ potential with parameters $\sigma_{H_2} = 2.96 \text{ \AA}$ and $\epsilon_{H_2}/k_B = 34.2 \text{ K}$. The potential with these parameters has been shown to be able to reproduce results obtained from the Silvera-Goldman (SG) [45] potential within 5% [46], Garberoglio *et al.* [22] also used this LJ potential parameter to obtain good results at low temperature and pressure by comparing with experimental data.

In these simulations, we assume that the framework atoms of the IRMOFs are rigid. Therefore, we require only non-bonded interactions between the molecular hydrogen and the atoms of the adsorbent. The LJ parameters for the atoms in the framework are taken from the literature [30], from which we can compute all parameters for the interaction between molecular hydrogen and that framework atoms. All the LJ cross-interaction parameters were determined by the Lorentz-Berthelot mixing rules.

2.2.5 Accessible volume and surface area Calculation

In a bulk system, 100% of the volume is accessible, but in an adsorbent, some volume is occupied by the adsorbent framework. To obtain the AV in the adsorbed phase, we used a purely geometrical method [18]. The space within the framework is divided into a 3-D grid which each box in the grid has a very small volume and a probe size of 0 Å was inserted into each box and tested for overlap with the atoms of the MOF. Probing the material in this manner enables us to determine the volume of the simulation cell that is not occupied by framework atoms. The volumes of the boxes that did not overlap with other framework atoms were used to calculate the available AV.

The SA of the framework was calculated by a similar geometrical method. A 2-D grid was created on the spherical surface of each framework atom and a point probe was inserted onto each small surface block and tested for overlap with other framework atoms. The sum of all elements in which no overlap was present was used as an estimate of the SA. This probe has zero-volume, making the calculation purely geometric and consistent with the AV calculation. It has been used before to estimate interfacial SAs in hydrated proton exchange membranes [47].

2.3 Results and Discussion

2.3.1 Adsorption Isotherms

In Figures 2.2 and 2.3, we report adsorption isotherms at 300 K and 77 K respectively. Each figure presents the isotherms as a weight percentage (Figures 2.2(a) and 2.3(a)) and on a molecule per cage basis (Figures 2.2(b) and 2.3(b)). The weight percentage is of practical relevance. The molecule per cage basis provides a better understanding of the molecular mechanism underlying adsorption.

At 300 K, the highest weight percentage of hydrogen is less than 0.3 wt% for all IRMOFs studied here. Adsorption up to 10 bar occurs within the linear regime for all IRMOFs. While the relationship between the structure of the framework and the amount of hydrogen adsorbed is not clear in the isotherm based on weight percent, a much simpler picture emerged when plotted on a molecule per cage basis in Figure 2.2(b). In Figure 2.2(b), all isotherms collapse onto one of three curves. These three curves correspond to the size of the cage. Those IRMOFs with linkers that separate connectors by a single phenyl ring (IRMOFs 1, 2, 3 and 7) fall on the same curve. Those IRMOFs with linkers that contain a biphenyl ring (IRMOFs 10, 10NH₂², 10NH₂³, 10Br², 10Br³) fall on the same curve. The IRMOF with a linker that contains a naphthalene arranged lengthwise (IRMOF-8) is on an intermediate curve. Clearly, the size of the linker is determining how much hydrogen can adsorb. These 300 K adsorption isotherms hint at an adsorption mechanism that is almost completely dominated by the AV of the cage and is virtually independent of adsorption energy or SA. We shall confirm this observation shortly.

The gravimetric plots of the adsorption isotherms indicate that IRMOF-10 adsorbs the most hydrogen on a wt% basis. There are two reasons for this. For these IRMOFs, adsorption is already dominated by entropic factors (AV) at 300 K. IRMOF-10 has the highest AV. The addition of amine groups or bromine atoms to the IRMOF-10 structure does not result in substantially greater adsorption, but increases the molecular weight of the framework. Therefore the largest cage without any functionalization adsorbs the most material in this temperature regime, for all pressures up to 10 bar.

In Figure 2.3, the hydrogen adsorption isotherms at 77 K are plotted on both a gravimetric and per cage basis. We first note that the maximum adsorption observed for any of

these materials is less than 6 wt% for pressures up to 10 bar. When the isotherms are presented on per cage basis, three families of curves are apparent, with one exception. Those IRMOFs with linkers that contain a single phenyl ring (IRMOFs 1, 2, 3) yield quantitatively similar adsorption isotherms. Those IRMOFs with linkers that contain a biphenyl ring (IRMOFs 10, 10NH₂², 10NH₂³, 10Br², 10Br³) yield quantitatively similar adsorption isotherms. The IRMOF with a linker that contains a naphthalene arranged lengthwise (IRMOF-8) is on an intermediate curve. All of this behavior was observed in the high temperature case as well. The larger cages adsorb more hydrogen than do the smaller cages. The addition of functionalized groups impacts adsorption only nominally. The only exception is IRMOF-7, which has a significantly higher SA than to all the other small cage IRMOFs. IRMOF-7 shows enhanced adsorption at all loadings relative to the other IRMOFs with small cages. The mechanisms behind this behavior shall be discussed shortly.

Adsorption isotherms for five of these IRMOFs (IRMOF-1, 3, 10, 10NH₂², 10NH₂³) have also been reported for RDX, an explosive with three polar nitro groups [48]. In that work, the addition of a polar functional group like the amine makes a very significant impact on the adsorption isotherms of RDX. The presence of the amine groups formed stabilizing bonds with the nitro groups that are not involved in binding with the zinc-carboxylate complex. Thus the absence of any impact of functionalization group on the adsorption isotherms of hydrogen can be attributed to the fact that hydrogen is not a polar molecule.

2.3.2 Density Distributions

One of the advantages of molecular simulation is that one can track trajectories of all molecules in the simulation. By sampling the positions of the molecules, one can determine the distribution of the adsorbates within the pore space. In Figure 2.4, we illustrate these density distributions at 300 K for each of the 10 IRMOFs. For each IRMOF, two views of the distribution are presented. The first shows the distribution within the cage as a whole, where a “small” cage is located in the center of the images. The second view shows the distribution around a single vertex. Each vertex is surrounded by four small and four big cages. In these images, the face of the vertex visible to the reader is opening onto a big cage. In these distributions, a white surface is drawn at a given density level. All volume contained within that surface corresponds to a higher adsorbate density. All volume contained outside that surface

corresponds to a lower adsorbate density. The value of the surface in the 300 K density distributions is $0.0001 \text{ molecules}/\text{\AA}^3$. But choice of this value is somewhat arbitrary, but it is important that it is held constant for all IRMOFs in Figure 2.4.

From the density distributions around the vertex, one can observe two points. First, the deepest energy wells (corresponding to most favorable adsorption sites) are in the big cages for all IRMOFs. Second, the shape of the adsorption site is the same in nine of the ten IRMOFs. There is a three fold symmetry, owing to the fact that for a given cage, three phenyl rings are linked to the zinc-carboxylate complex. The exception to the common shape of the adsorption site is again IRMOF-7, which shows that the decomposition of a larger site into four smaller sites, one directly in front of the Zn atom and the other three situated near the metal complex but between the phenyl rings.

From the density distributions of the cage, one can observe how the adsorption sites centered around each vertex are arranged in a three-dimensional array to form a lattice of adsorption sites within the pore space. Diffusion through the IRMOF can be visualized as an activated hop from one site to the next. This model allows for both intracage and intercage hops. Activated diffusion of adsorbed species in MOF has been previously observed for hydrogen [49], benzene[50] and RDX [48, 51]. The only exception to this model is IRMOF-7 in which there are heavily occupied sites not only in the vertex but also along the naphthalene surfaces and even through the windows of the cages.

In Figure 2.5, we present the analogous density distributions at 77 K. The value of the surface in the 77 K density distributions is $0.015 \text{ molecules}/\text{\AA}^3$, 150 times higher than that used in the density distribution at 300 K in Figure 2.5. Once we account for the fact that much more material is adsorbed at the lower temperature, the density distributions are remarkably similar. The distributions around the vertices show the same preference for big cages and the same three-fold symmetry in their shape. IRMOF-7 continues to prove an exception to the rule in terms of the shape of the adsorption site.

2.3.3 Energies of adsorption

In Figure 2.6(a), we plot the potential energy due to the interaction between the hydrogen and the IRMOF as a function of bulk pressure. Because the $\text{H}_2\text{-H}_2$ interaction energies in both

the bulk and adsorbed phases are much smaller than the H₂-IRMOF interaction energies, the interaction energies between the hydrogen and the IRMOF are approximately equal to the energies of adsorption. In Figure 2.6(a), we observe that this adsorption energy is not a function of loading at 300 K. This is consistent with a picture where the molecules are distributed through-out the cage at all loadings. This is also consistent with adsorption based on AV. The energies of adsorption range in magnitude from 1 to 3 kJ/mol, with IRMOF-7 having the largest adsorption energy and IRMOF-10 having the smallest adsorption energy.

In Figure 2.6(b), we observe that there is a loading-dependence to the energy of adsorption at 77 K. At the lower temperature, the first molecules preferentially occupy the energetically most favorable sites. Additional loading places molecules in less favorable places within the pore resulting in an increase in the average potential energy due to the interaction between the hydrogen and the IRMOF. The energies of adsorption range in magnitude from 2.5 to 5 kJ/mol, with IRMOF-7 again having the largest adsorption energy and IRMOF-10 again having the smallest adsorption energy.

2.3.4 Surface area and accessible volume

SAs and AVs for the IRMOFs studied in this work are listed in Table 2.2. The obtained results for AVs of IRMOF-1, IRMOF-7, IRMOF-8 and IRMOF-10 are in good agreement with simulation results reported by Frost *et al.*[18].

In calculating SAs, we note that the zero-volume probe will consistently yield higher SAs than experiment for MOFs [18]. Nevertheless, we use it as an unbiased and parameter-free estimate of the SA. The SA obtained for IRMOF-1 is within 1.7 % range with the experimentally calculated Langmuir SA by Saha *et al.* [16] and within 1.3% of experimentally calculated BET SA by Kaye *et al.* [52] . The results obtained for SA and AV were used to analyze the relationship with the hydrogen adsorption.

2.3.5 Correlation plots

The goal of this study is to develop clear relationships between structural characteristics and hydrogen uptake in IRMOFs. To create a better understanding, we calculated the correlation coefficients between various properties of the system. A correlation coefficient of two properties,

x and y , ρ_{xy} , is defined as the ratio of the covariance of x and y , σ_{xy} , over the product of the standard deviation of x , σ_x , with the standard deviation of y , σ_y ,

$$\rho_{xy} = \frac{\sigma_{xy}}{\sigma_x \sigma_y} \quad (4)$$

The correlation coefficient is a normalized variable bounded between negative and positive one. A value of zero for the correlation coefficient means that properties x and y are statistically independent of each other. A value greater than zero for the correlation coefficient means that properties x and y are positively correlated, with a limit of $\rho_{xy} = 1$ for $x=y$. A value less than zero for the correlation coefficient means that properties x and y are negatively correlated, with a limit of $\rho_{xy} = -1$ for $x=-y$.

As shown in Figure 2.7, we examine the correlation between SA (SA) and AV (AV) in two ways. First, the plot is presented on a per mass basis with the units of SA being m^2/g and the units of AV being cm^3/g . The correlation coefficient between the SA and AV is 0.663. Second, the plot is presented on a per cage basis with the units of SA being $\text{\AA}^2/\text{cage}$ and the units of AV being $\text{\AA}^3/\text{cage}$. The correlation coefficient between the SA and AV is 0.930. Thus by either the per mass or per cage basis, the SA and AV are positively correlated, although more strongly correlated on the per cage basis. This data is presented to make the point that it may not be easy to distinguish between regimes in which adsorption is dominated by AV and adsorption is dominated by available SA, since the two properties are highly correlated in these materials.

As shown in Figure 2.8, we plot the correlation coefficient on the y-axis as a function of bulk pressure on the x-axis. Each plot contains four curves representing two temperatures (77 K and 300 K) and two bases (per mass and per cage). Each data point in the plot represents a plot such as that given in Figure 2.7, from which a correlation coefficient was extracted. In Figure 2.8(a), the correlation coefficient between AV and energy of adsorption, ΔU_{ads} , is plotted. On either the per mass or per cage basis, we observe that the energy of adsorption at 300 K is highly positively correlated with the AV. This observation can be explained as follows. As the cage size increases, the AV increases. Also as the cage size increases, the overlap of energy wells decreases, resulting in a lower energy of adsorption. Since these energies are negative, a reduction in the magnitude of the energy of adsorption, yields an increase in the value of the energy of adsorption (less negative). Thus, we observe the positive correlation between AV and

ΔU_{ads} , since both increase with increasing cage size. In other words, because smaller pores typically have deeper energy wells, there is a positive correlation between AV and ΔU_{ads} . The correlation is not a function of loading at high temperature since the AV is independent of loading by definition and Figure 2.6(a) shows that ΔU_{ads} is not a strong function of loading.

As shown in Figure 2.8(a), the correlation coefficient between AV and ΔU_{ads} is also given at 77 K. At all pressures, the correlation between AV and ΔU_{ads} is positive, ranging from 0.7 to 0.9. At 77 K, the correlation is less positive than at 300 K and increases as the pressure increases. This is because ΔU_{ads} is loading-dependence at low temperature as observed in 6(b). We observe that the correlation is more positive at high pressures, because ΔU_{ads} increases with loading, as shown in Figure 2.6(b). From a physical point of view, Figure 2.8(a) tells us that at low loading, AV and ΔU_{ads} are correlated, but less so at low temperatures and low pressures, where one would expect the role of energetics to be more important.

In Figure 2.8(b), the correlation coefficient between SA and ΔU_{ads} is presented. At both temperatures and all pressures, the correlation between SA and ΔU_{ads} is positive, ranging from 0.2 to 0.8. The correlation between SA and ΔU_{ads} is stronger on a per cage than per mass basis since the addition of functional groups changes the molecular weight of the framework but does not change the SA or ΔU_{ads} to the same degree. The correlation between SA and ΔU_{ads} is independent of pressure at high temperature for the same reasons that the correlation between AV and ΔU_{ads} is independent of pressure, namely neither property individual is a function of pressure at high temperature.

In Figure 2.8(b), the correlation coefficient between SA and ΔU_{ads} is also given at 77 K. As was the case with the correlation between AV and ΔU_{ads} , this correlation increases as the pressure increases because ΔU_{ads} is loading-dependence at low temperature as observed in 6(b). Thus, In Figures 2.7 and 2.8, we observe positive correlations between these three properties,

AV, SA and ΔU_{ads} that are typically used to characterize regimes of diffusion. Below, we see how each property is correlated with hydrogen adsorption.

In Figure 2.9, the correlation coefficient between the amount of hydrogen adsorbed and AV (a), ΔU_{ads} (b) and SA (c) is presented as a function of temperature and pressure. The behavior exhibited in Figure 2.9 can be understood in terms of competing energetic and entropic contributions to the free energy

$$\Delta A_{ads} = \Delta U_{ads} - T\Delta S_{ads} \quad (5)$$

where the distribution of molecules between the bulk and adsorbed (*ads*) phases is given by

$$\frac{N_{ads}}{N_{bulk}} = \exp\left(-\frac{\Delta A_{ads}}{k_B T}\right) = \exp\left(\frac{\Delta S_{ads}}{k_B}\right) \exp\left(-\frac{\Delta U_{ads}}{k_B T}\right) \quad (6)$$

As temperature decreases, the entropic contribution to the free energy of adsorption, $-T\Delta S_{ads}$, diminishes. In the limit of absolute zero temperature, there is only an energetic effect. In the limit of infinite temperature, there is only an entropic effect. Between these asymptotes, the behavior shifts from one limit to the other. The energetic effect is captured by the energy of adsorption. The entropic effect is captured by the AV of the IRMOF.

The competition between energetic and entropic factors can also be understood as a function of bulk pressure. At low pressure, there is little adsorbate fluid in the pore. As the loading increases, the ability for molecules to pack within the pore space (an entropic contribution) becomes relevant. Therefore, one typically observes a decrease in importance of the energetic effect and an increase in the importance of the entropic effect with an increase in loading. Such behavior has been shown for simple fluids in idealized pores [53].

Furthermore, this simple competition can explain the relative preference for adsorption among pores of different sizes and shapes. Small and/or more curved pores have energetically deeper wells (due to more overlap of adsorbate-MOF interactions) and greater confinement. Large and/or less curved pores have energetically shallower wells and less confinement. Thus the energetic term favors small pores and the entropic term favors large pores. The relative preference for a given pore is determined by the balance between these two terms. The adsorption of hydrogen in the various MOFs as a function of temperature and pressure can be

understood in terms of the competition between energetic and entropic contributions to the free energy.

In terms of correlation coefficients, one should expect a positive correlation between the amount of hydrogen adsorbed and the AV in a regime where entropic effects dominate. A negative correlation between these two properties is a clear indication of an adsorption process dominated by energetic factors. One should also expect a negative correlation between the amount of hydrogen adsorbed and ΔU_{ads} in a regime where energetic effects dominate. A positive correlation between these two properties is a clear indication of an adsorption process dominated by entropic factors.

As shown in Figure 2.9(a), there is virtually a perfect correlation between the amount of hydrogen adsorbed and the AV for all pressures at 300 K on both the per mass and per cage bases. This positive correlation is another way to represent the isotherms presented in Figure 2.2(b). As the AV increases, the amount of material increases. This observation also is consistent with the idea that at 300 K, adsorption of hydrogen is governed by an entropic effect, which can be captured in the AV. We observe no influence of pressure on this correlation because 300 K is essentially already in the infinite temperature limit. Alternatively, the loadings are so low at 300 K that packing effects never become an issue.

As shown in Figure 2.9(a), a markedly different behavior is observed for the correlation between amount of H₂ adsorbed and AV at 77 K. At low pressures, there is a negative correlation between the amount of H₂ adsorbed and the AV. The correlation gradually becomes positive as the pressure is increased. This change in correlation corresponds to the conventional expectation that adsorption is governed by energetic effects at low loading and by entropic effects at high loadings. At low temperatures, the energy of adsorption dictates the amount adsorbed. Since the energy well deepens as the pores get smaller (less AV), we observe a negative correlation with respect to AV, when the energetic effect dominates. As the loading increases, packing effects (an entropic contribution) become important, and we observe a positive correlation with AV.

In Figure 2.9(b), the correlation coefficient between the amount of hydrogen adsorbed and ΔU_{ads} is presented as a function of temperature and pressure. At 300 K, we observe a very high positive correlation with ΔU_{ads} , indicative of adsorption governed by entropic processes. At

77 K, we observe that the adsorption is negatively correlated with ΔU_{ads} at low pressures and positively correlated with ΔU_{ads} at high pressures. Again, this is a consequence of the fact that energetic effects are more important at low temperature and packing effects only become significant at high loadings.

In Figure 2.9(c), the correlation coefficient between the amount of hydrogen adsorbed and SA is presented as a function of temperature and pressure. The role of SA is conceptually clear. More SA provides more secondary adsorption sites. It is clear from the density distributions in Figures 2.4 and 2.5, that the primary adsorption sites are located in front of the Zn carboxylate connectors. The number of these connectors does not change with cage size or functionalization of the linker. However, secondary adsorption sites with a less favorable energy of adsorption are located at other positions along the surface and their number increases with an increase in SA. With this understanding, SA should have no impact on adsorption at 300 K, where energetic arguments are not significant. That we observe a positive correlation in Figure 2.9(c) between the amount of H₂ adsorbed and the SA is strictly a consequence of the fact that SA is positively correlated with AV, as was apparent in Figure 2.7.

At 77 K, we observe little correlation between amount of H₂ adsorbed and SA at low loadings because the H₂ are adsorbing in the most favorable sites in front of the connectors. As the loading increases, we observe a positive correlation between the amount of H₂ adsorbed and the SA. One can naturally ask whether this positive correlation is (i) due to the presence of secondary adsorption sites on the additional SA or (ii) simply a consequence of the fact that SA is positively correlated with AV in these IRMOFs and as loading increases, larger pores are preferred due to packing effects. The MOF that is an outlier in many of the trends, IRMOF-7, can be used to answer this question. IRMOF-7 has a similar cage size to IRMOF-1, 2 and 3, but more SA. At 300 K, all four IRMOFs adsorb virtually the same amount of hydrogen on a per cage basis (Figure 2.2(a)), which is to be expected since at high temperature, adsorption is governed by entropic effects, as characterized by AV. At 77 K, IRMOF-7 adsorbs substantially more than the other three similarly sized IRMOFs in an intermediate pressure range. Therefore, we can conclude that at 77 K, where we expect energetic effects to be important, the presence of secondary adsorption sites is important in this pressure range. At very low pressure, the secondary adsorption sites are not important because the primary adsorption sites are available.

At high pressures, the packing effect, characterized by AV, become most significant. In this intermediate pressure regime, the difference between the IRMOF-7 adsorption isotherm and the IRMOF-1, 2 and 3 adsorption isotherms is greatest (Figure 2.3(b)).

2.3.6 Self-Diffusivity

Self-diffusivities of H₂ in the IRMOFs were obtained using MD simulation. This is the only property available from MD that is not available from the GCMC simulations. Several properties (such as energies of adsorption) are available from both methods. It was verified that the values of the energies of adsorption were the same for a given temperature, pressure and IRMOF from the MD and GCMC simulations. The self-diffusivities were obtained from the Einstein relation, which relates the mean square displacement (MSD) to the observation time,

$$D = \lim_{\tau \rightarrow \infty} \frac{\langle [\mathbf{r}_i(t + \tau) - \mathbf{r}_i(t)]^2 \rangle}{2d\tau} \quad (7)$$

where D is the self-diffusivity, \mathbf{r}_i is the position of particle i , τ is the observation time, d is the dimensionality of the system and where the angled brackets indicate an ensemble average over both particle i and time origin t . This relation requires that the simulations be run to the infinite-time limit, where this linear relationship between MSD and observation time is valid. Once the diffusivities are known for several temperatures, the activation energy can be calculated by the Arrhenius Equation

$$D(T, \rho) = D_o(\rho) \exp\left(-\frac{E_a(\rho)}{k_B T}\right) \quad (8)$$

As indicated in equation (8), there can be density dependence in the diffusivity. We did not explore the density dependence. All self-diffusivities reported here correspond to an infinite dilution density. We calculated self-diffusivity for the 10 different IRMOFs we selected at four temperatures: 300 K, 400 K, 500 K and 600 K. We verified that the MSDs were in the infinite time limit by computing the exponent relating the MSD to the observation time, which should be one in the linear, infinite-time limit. For the 40 MD simulations run here, the average value of this exponent was 1.004, with a minimum of 0.99 and a maximum of 1.03. Furthermore, the long time limit behavior can only be achieved if the MSDs are sufficiently long as to have traversed

through many cages. In Table 2.3, we also report the square root of the final MSD, which can be compared to the size of the cage. In all instances the distance traveled is many times larger than the cage size. Thus, the values of the self-diffusivities are valid. The values obtained for the self-diffusivities are presented in Table 2.3. Self-diffusivity values calculated for IRMOF 1, 8 and 10 are in good agreement with the calculations of Liu *et al.*[54] Average relative error is 4.9 %

The activation energies for each IRMOFs were calculated via a linear regression of equation (8). The activation energies calculated for IRMOF 1 and 8 are reported in Table 2.3 and are in agreement with the values simulated by Yang *et al.*[49] Average relative error is 12.2 %

The relationship of self-diffusivity at 300 K and activation energy with SA, AV and energy of adsorption are analyzed by calculating the correction coefficients. For the energy of adsorption, the lowest density, which is at 1 bar was used, since the self-diffusivities were computed at infinite dilution. The results are listed in Table 2.4. Self-diffusivity has a strong positive correlation with AV. When the pore size is large, the hydrogen diffuses more quickly. The self-diffusivity also has a positive correlation with the adsorption energy, since as the energy wells become more shallow, adsorption occurs more quickly These observations are consistent with the results obtained by Liu *et al.*[54] The self-diffusivity does not have a strong correlation with SA.

According to Equation (8), the activation energy for diffusion is negatively correlated with the self-diffusivity, if the prefactor, D_0 , is held constant. However, in these simulations, we surprisingly observe a positive correlation between the self-diffusivity and activation energy for diffusion. This can only be explained by the fact that the increase in the prefactor is a more dominant effect than the increase in the activation energy. The prefactor contains the entropic contribution to the free energy of activation, whereas the energetic contribution remains in the activation energy. Therefore, we can conclude that diffusion in larger IRMOFs is faster because of an entropic advantage and specifically not because of a lower activation energy for diffusion. The origin of this behavior lies in the fact that the activation energy is positively correlated with the energy of adsorption. In other words, contrary to conventional expectation, the shallower energy wells do not result in lower energy barriers to diffusion in these systems. As the pore cages become larger, the value of adsorption energy rises (shallower wells) but the energy of the transition state for diffusion rises even more, resulting in a net increase in the activation barrier.

2.4 Conclusions

For all of the MOFs studied here, the maximum average hydrogen adsorbed is less than 6% (as a weight percentage) at 77 K and 10 bar. Hydrogen adsorption within all cages is preferred at vertices at both low and high temperature in entire pressure range. Based on this work, we observe that at pressures up to 10 bar at 300 K, the adsorption process is virtually completely governed by entropic considerations, resulting in a strong correlation between the amount of hydrogen adsorbed and the AV of the adsorbent. In other words, the adsorbed hydrogen is distributed through-out the pore space, largely independent of the energy landscape within the pore. At 77 K, we observe more than one adsorption regime. At low pressures, the adsorption process is governed by energetic considerations, resulting in a strong correlation between the amount of hydrogen adsorbed and the energy of adsorption. Here the adsorbed hydrogen is located in the adsorption sites at the cage vertices. At the high end of the pressure range, the adsorption becomes a process dominated by entropic considerations, again resulting in a strong correlation between the amount of hydrogen adsorbed and the AV. Here the packing of hydrogen within the cage becomes important. Only in the intermediate regime, does one observe that an increase in SA results in an increase in the amount of hydrogen adsorbed. These secondary adsorption sites are important only in the intermediate regime because at lower loadings there are still primary adsorption sites available and at higher loadings, AV has become the dominant characteristic of the adsorbent in determining adsorption.

At 77 K energetic effects are dominant at low pressure (frameworks with deeper energy wells adsorb more hydrogen) and entropic effects become dominant at high pressures. The presence of secondary adsorption sites that provide more SA (as in IRMOF-7) becomes an important factor in intermediate pressures. At 300 K, adsorption of hydrogen is governed by an entropic effect, which is characterized by AV. Pressure does not influence on this correlation because 300 K is already in the infinite temperature limit; and also, the loadings are so low at 300 K that packing effects never become an issue.

Self-diffusivities and activation energies for diffusion at infinite dilution were calculated for all IRMOFs studied. The relationships with SA, AV and energy of adsorption were analyzed. Self-diffusivity is strongly correlated with both energy of adsorption and AV. The diffusion in

larger IRMOFs is faster because of an entropic advantage and specifically not because of a lower activation energy for diffusion.

Acknowledgements

This research was supported by the Sustainable Energy and Education Research Center at the University of Tennessee, by a grant from the National Science Foundation (DGE-0801470) and by the U.S. Department of Energy, Office of Basic Energy Sciences, Division of Materials Sciences and Engineering. This research project used resources of the National Institute for Computational Sciences (NICS) supported by NSF under agreement number: OCI 07-11134.5.

References

- [1] I.P. Jain, *Hydrogen the fuel for 21st century*, Int. J. Hydrog. Energy,34 (2009), pp. 7368-7378.
- [2] T.K. Mandal, and D.H. Gregory, *Hydrogen: a future energy vector for sustainable development*, Proc. Inst. Mech. Eng. Part C-J. Eng. Mech. Eng. Sci.,224 (2010), pp. 539-558.
- [3] N.A. Kelly, T.L. Gibson, M. Cai, J.A. Spearot, and D.B. Ouwerkerk, *Development of a renewable hydrogen economy: optimization of existing technologies*, Int. J. Hydrog. Energy,35 (2010), pp. 892-899.
- [4] S. Elnashaie, Z.X. Chen, and P. Prasad, *Efficient production and economics of clean-fuel hydrogen*, Int. J. Green Energy,4 (2007), pp. 249-282.
- [5] K.B. Lee, M.G. Beaver, H.S. Caram, and S. Sircar, *Reversible chemisorption of carbon dioxide: simultaneous production of fuel-cell grade H₂ and compressed CO₂ from synthesis gas*, Adsorpt.-J. Int. Adsorpt. Soc.,13 (2007), pp. 385-397.
- [6] K. Nath, and D. Das, *Production and storage of hydrogen: Present scenario and future perspective*, J. Sci. Ind. Res.,66 (2007), pp. 701-709.
- [7] E. Pasculete, F. Condrea, and C. Radulescu, *Hydrogen and sustainable energy. Research for hydrogen production*, Environ. Eng. Manag. J.,6 (2007), pp. 45-49.
- [8] K.L. Lim, H. Kazemian, Z. Yaakob, and W.R.W. Daud, *Solid-state Materials and Methods for Hydrogen Storage: A Critical Review*, Chem. Eng. Technol.,33 (2010), pp. 213-226.
- [9] *Targets for Onboard Hydrogen Storage Systems for Light-Duty Vehicles*, U. D. o. Energy ed., Office of Energy Efficiency and Renewable Energy and The FreedomCAR and Fuel Partnership (2009).
- [10] J. Yang, A. Sudik, C. Wolverton, and D.J. Siegel, *High capacity hydrogen storage materials: attributes for automotive applications and techniques for materials discovery*, Chem. Soc. Rev.,39 (2010), pp. 656-675.
- [11] J.L.C. Rowsell, A.R. Millward, K.S. Park, and O.M. Yaghi, *Hydrogen sorption in functionalized metal-organic frameworks*, J. Am. Chem. Soc.,126 (2004), pp. 5666-5667.

- [12] H. Li, M. Eddaoudi, M. O'Keeffe, and O.M. Yaghi, *Design and synthesis of an exceptionally stable and highly porous metal-organic framework*, *Nature*,402 (1999), pp. 276-279.
- [13] M. Eddaoudi, J. Kim, N. Rosi, D. Vodak, J. Wachter, M. O'Keeffe, and O.M. Yaghi, *Systematic design of pore size and functionality in isorecticular MOFs and their application in methane storage*, *Science*,295 (2002), pp. 469-472.
- [14] N.L. Rosi, J. Eckert, M. Eddaoudi, D.T. Vodak, J. Kim, M. O'Keeffe, and O.M. Yaghi, *Hydrogen storage in microporous metal-organic frameworks*, *Science*,300 (2003), pp. 1127-1129.
- [15] F.M. Mulder, T.J. Dingemans, H.G. Schimmel, A.J. Ramirez-Cuesta, and G.J. Kearley, *Hydrogen adsorption strength and sites in the metal organic framework MOF5: Comparing experiment and model calculations*, *Chem. Phys.*,351 (2008), pp. 72-76.
- [16] D.P. Saha, Z.J. Wei, and S.G. Deng, *Hydrogen adsorption equilibrium and kinetics in metal-organic framework (MOF-5) synthesized with DEF approach*, *Sep. Purif. Technol.*,64 (2009), pp. 280-287.
- [17] P. Ryan, L.J. Broadbelt, and R.Q. Snurr, *Is catenation beneficial for hydrogen storage in metal-organic frameworks*, *Chem. Commun.* (2008), pp. 4132-4134.
- [18] H. Frost, T. Duren, and R.Q. Snurr, *Effects of surface area, free volume, and heat of adsorption on hydrogen uptake in metal-organic frameworks*, *J. Phys. Chem. B*,110 (2006), pp. 9565-9570.
- [19] H. Frost, and R.Q. Snurr, *Design requirements for metal-organic frameworks as hydrogen storage materials*, *J. Phys. Chem. C*,111 (2007), pp. 18794-18803.
- [20] M. Fischer, F. Hoffmann, and M. Froba, *Molecular simulation of hydrogen adsorption in metal-organic frameworks*, *Colloid Surf. A-Physicochem. Eng. Asp.*,357 (2010), pp. 35-42.
- [21] K. Sillar, A. Hofmann, and J. Sauer, *Ab Initio Study of Hydrogen Adsorption in MOF-5*, *J. Am. Chem. Soc.*,131 (2009), pp. 4143-4150.

- [22] G. Garberoglio, A.I. Skoulidas, and J.K. Johnson, *Adsorption of gases in metal organic materials: Comparison of simulations and experiments*, J. Phys. Chem. B, 109 (2005), pp. 13094-13103.
- [23] J.L.C. Rowsell, and O.M. Yaghi, *Strategies for hydrogen storage in metal-organic frameworks*, Angewandte Chemie-International Edition, 44 (2005), pp. 4670-4679.
- [24] J.L.C. Rowsell, and O.M. Yaghi, *Effects of functionalization, catenation, and variation of the metal oxide and organic linking units on the low-pressure hydrogen adsorption properties of metal-organic frameworks*, J. Am. Chem. Soc., 128 (2006), pp. 1304-1315.
- [25] B. Kesanli, Y. Cui, M.R. Smith, E.W. Bittner, B.C. Bockrath, and W.B. Lin, *Highly interpenetrated metal-organic frameworks for hydrogen storage*, Angewandte Chemie-International Edition, 44 (2005), pp. 72-75.
- [26] D.H. Jung, D. Kim, T.B. Lee, S.B. Choi, J.H. Yoon, J. Kim, K. Choi, and S.H. Choi, *Grand canonical Monte Carlo simulation study on the catenation effect on hydrogen adsorption onto the interpenetrating metal-organic frameworks*, J. Phys. Chem. B, 110 (2006), pp. 22987-22990.
- [27] B.L. Chen, N.W. Ockwig, A.R. Millward, D.S. Contreras, and O.M. Yaghi, *High H₂ adsorption in a microporous metal-organic framework with open metal sites*, Angewandte Chemie-International Edition, 44 (2005), pp. 4745-4749.
- [28] P.M. Forster, J. Eckert, J.S. Chang, S.E. Park, G. Ferey, and A.K. Cheetham, *Hydrogen adsorption in nanoporous Nickel(II) phosphates*, J. Am. Chem. Soc., 125 (2003), pp. 1309-1312.
- [29] V.V. Simonyan, P. Diep, and J.K. Johnson, *Molecular simulation of hydrogen adsorption in charged single-walled carbon nanotubes*, Journal of Chemical Physics, 111 (1999), pp. 9778-9783.
- [30] A.K. Rappe, C.J. Casewit, K.S. Colwell, W.A. Goddard, and W.M. Skiff, *UFF, A Full Periodic-Table Force-Field for Molecular Mechanics and Molecular-Dynamics Simulations*, J. Am. Chem. Soc., 114 (1992), pp. 10024-10035.
- [31] D.J. Keffer, Molecular Simulation Images from the Computational Materials Research Group at the University of Tennessee Knoxville, TN.,
<http://utkstair.org/clausius/docs/atoms/explosivesensors/index.html>.

- [32] D. Frenkel, and B. Smit, *Understanding Molecular Simulation*, Academic Press, San Diego, 1996.
- [33] M.P. Allen, and D.J. Tildesley, *Computer Simulation of Liquids*, Oxford Science Publications Oxford 1987.
- [34] Q.Y. Wang, and J.K. Johnson, *Molecular simulation of hydrogen adsorption in single-walled carbon nanotubes and idealized carbon slit pores*, Journal of Chemical Physics,110 (1999), pp. 577-586.
- [35] R.P. Feynman, *Space- Time Approach to Non-Relativistic Quantum Mechanics*, Reviews of Modern Physics,20 (1948), pp. 367-387.
- [36] Q.Y. Wang, and J.K. Johnson, *Phase equilibrium of quantum fluids from simulation: Hydrogen and neon*, Fluid Phase Equilib.,132 (1997), pp. 93-116.
- [37] Q.Y. Wang, J.K. Johnson, and J.Q. Broughton, *Path integral grand canonical Monte Carlo*, Journal of Chemical Physics,107 (1997), pp. 5108-5117.
- [38] D. Landau, and K. Binder, *A Guide to Monte Carlo Simulations in Statistical Physics*, Cambridge University Press, Cambridge, UK, 2000.
- [39] M.E. Tuckerman, B.J. Berne, G.J. Martyna, and M.L. Klein, *Efficient Molecular-Dynamics And Hybrid Monte-Carlo Algorithms For Path-Integrals*, Journal of Chemical Physics,99 (1993), pp. 2796-2808.
- [40] M. Tuckerman, B.J. Berne, and G.J. Martyna, *Reversible Multiple Time Scale Molecular-Dynamics*, Journal of Chemical Physics,97 (1992), pp. 1990-2001.
- [41] S. Nose, *A Molecular-Dynamics Method for Simulations in the Canonical Ensemble*, Molecular Physics,52 (1984), pp. 255-268.
- [42] W.G. Hoover, *Canonical Dynamics - Equilibrium Phase-Space Distributions*, Physical Review A,31 (1985), pp. 1695-1697.
- [43] J.C. Liu, J.T. Culp, S. Natesakhawat, B.C. Bockrath, B. Zande, S.G. Sankar, G. Garberoglio, and J.K. Johnson, *Experimental and theoretical studies of gas adsorption in Cu-3(BTC)(2): An effective activation procedure*, J. Phys. Chem. C,111 (2007), pp. 9305-9313.

- [44] J. Liu, J.Y. Lee, L. Pan, R.T. Obermyer, S. Simizu, B. Zande, J. Li, S.G. Sankar, and J.K. Johnson, *Adsorption and diffusion of hydrogen in a new metal-organic framework material: [Zn(bdc)(ted)(0.5)]*, J. Phys. Chem. C, 112 (2008), pp. 2911-2917.
- [45] R.Q. Snurr, A.T. Bell, and D.N. Theodorou, *A Hierarchical Atomistic Lattice Simulation Approach For The Prediction Of Adsorption Thermodynamics Of Benzene In Silicalite*, Journal of Physical Chemistry, 98 (1994), pp. 5111-5119.
- [46] C. Chakravarty, *Fourier Path-Integral Simulations of Para-H-2 and Ortho-D-2 Clusters* Molecular Physics, 84 (1995), pp. 845-852.
- [47] J.W. Liu, N. Suraweera, D.J. Keffer, S.T. Cui, and S.J. Paddison, *On the Relationship between Polymer Electrolyte Structure and Hydrated Morphology of Perfluorosulfonic Acid Membranes*, J. Phys. Chem. C, 114 (2010), pp. 11279-11292.
- [48] R.C. Xiong, K. Odbadrakh, A. Michalkova, J.P. Luna, T. Petrova, D.J. Keffer, D.M. Nicholson, M.A. Fuentes-Cabrera, J.P. Lewis, and J. Leszczynski, *Evaluation of functionalized isoreticular metal organic frameworks (IRMOFs) as smart nanoporous preconcentrators of RDX*, Sens. Actuator B-Chem., 148 (2010), pp. 459-468.
- [49] Q.Y. Yang, and C.L. Zhong, *Molecular simulation of adsorption and diffusion of hydrogen in metal-organic frameworks*, J. Phys. Chem. B, 109 (2005), pp. 11862-11864.
- [50] S. Amirjalayer, and R. Schmid, *Mechanism of benzene diffusion in MOF-5: A molecular dynamics investigation*, Microporous Mesoporous Mat., 125 (2009), pp. 90-96.
- [51] R.C. Xiong, J.T. Fern, D.J. Keffer, M. Fuentes-Cabrera, and D.M. Nicholson, *Molecular simulations of adsorption and diffusion of RDX in IRMOF-1*, Molecular Simulation, 35 (2009), pp. 910-919.
- [52] S.S. Kaye, A. Dailly, O.M. Yaghi, and J.R. Long, *Impact of preparation and handling on the hydrogen storage properties of Zn₄O(1,4-benzenedicarboxylate)(3) (MOF-5)*, J. Am. Chem. Soc., 129 (2007), pp. 14176-14177.
- [53] D. Keffer, H.T. Davis, and A.V. McCormick, *The effect of nanopore shape on the structure and isotherms of adsorbed fluids*, Adsorpt.-J. Int. Adsorpt. Soc., 2 (1996), pp. 9-21.

[54] B. Liu, Q.Y. Yang, C.Y. Xue, C.L. Zhong, and B. Smit, *Molecular simulation of hydrogen diffusion in interpenetrated metal-organic frameworks*, *Physical Chemistry Chemical Physics*, 10 (2008), pp. 3244-3249.

Appendix A: Tables and Figures

Table 2.1. The Lennard-Jones parameters for the atoms in the frameworks of the IRMOFs.

Atom	σ (Å)	ϵ/k (K)
H	2.571	22.142
C	3.431	52.839
O	3.118	30.194
Zn	2.462	62.400
N	3.261	34.737
Br	3.732	126.364

Table 2.2. Unit cell length, unit cell masses, accessible surface areas and accessible volumes for the IRMOFs studied.

IRMOF	Unit Cell Length (Å)	Unit Cell Molecular Weight	Accessible Surface Area for H ₂ (m ² /g)	Accessible Volume (cm ³ /g)
IRMOF-1	25.8320	6159.256	3850.756	1.345
IRMOF-2	25.7718	8052.762	3311.908	0.988
IRMOF-3	25.7465	6519.616	3933.671	1.228
IRMOF-7	25.8280	7360.696	4120.030	1.038
IRMOF-8	30.0915	7360.696	4178.026	1.854
IRMOF-10	34.2807	7985.608	4313.344	2.647
IRMOF-10NH ₂ ²	34.2807	8345.968	4427.441	2.504
IRMOF-10NH ₂ ³	34.2807	8345.968	4389.968	2.507
IRMOF-10Br ²	34.2807	9879.114	3813.797	2.107
IRMOF-10Br ³	34.2807	9879.114	3802.979	2.108

Table 2.3. Self-Diffusivity and Activation Energy for IRMOFs

IRMOF	Temp (K)	Diffusivity (10^{-7} m ² /sec)	Standard Deviation (10^{-8} m ² /sec)	Exponential	Square root of Mean Square Displacement			cage size	Activation Energy (kcal/mol)
					x Direction	y Direction	z Direction		
IRMOF-1	300	2.41	0.58	1.0167	221.06	216.46	220.04	12.916	0.6018
	400	2.96	1.17	1.0078	243.97	239.20	248.79		
	500	3.60	0.26	1.0065	268.72	266.62	268.84		
	600	3.96	1.92	1.0022	288.99	282.17	275.57		
IRMOF-2	300	1.96	3.00	1.0178	180.15	201.20	209.30	12.886	0.5776
	400	2.40	3.88	1.0271	198.80	221.43	233.69		
	500	2.78	4.96	0.9910	209.31	247.43	247.12		
	600	3.22	5.28	1.0056	230.24	260.23	270.31		
IRMOF-3	300	1.85	0.59	1.0156	192.00	189.50	195.38	12.873	0.6489
	400	2.31	0.32	1.0044	215.06	214.76	214.36		
	500	2.86	1.21	1.0010	241.56	233.50	240.48		
	600	3.16	1.16	1.0052	248.54	249.62	256.31		
IRMOF-7	300	1.38	0.32	0.9922	169.16	164.15	166.04	12.914	0.6327
	400	1.73	0.76	1.0188	182.67	190.56	185.79		
	500	2.05	1.39	0.9984	208.67	196.18	202.77		
	600	2.37	1.05	1.0054	221.65	215.02	215.40		
IRMOF-8	300	3.16	2.57	1.0191	241.28	260.44	251.78	15.046	0.6535
	400	3.92	9.50	0.9987	282.42	274.75	281.87		
	500	4.74	1.73	0.9905	304.56	312.69	304.69		
	600	5.50	0.79	1.0065	334.40	331.54	329.49		
IRMOF-10	300	4.94	2.61	0.9921	319.39	314.45	306.73	17.140	0.6682
	400	6.26	1.92	1.0109	348.86	355.46	358.60		
	500	7.45	0.63	0.9977	386.97	382.91	389.30		
	600	8.75	0.47	1.0080	417.74	418.27	417.44		
IR-10Br ²	300	4.30	1.92	1.0006	299.48	292.75	288.20	17.140	0.6521
	400	5.32	2.06	0.9885	327.37	321.18	334.24		
	500	6.38	2.39	0.9858	364.16	353.29	358.89		
	600	7.52	0.65	1.0037	389.73	385.51	387.29		
IR-10Br ³	300	4.06	1.10	1.0120	281.43	289.11	283.66	17.140	0.6638
	400	5.35	0.31	1.0048	327.48	325.38	327.65		
	500	6.16	4.94	1.0024	337.91	362.19	353.35		
	600	7.19	1.04	1.0018	381.58	376.49	378.05		
IR-10NH ₂ ²	300	4.24	3.10	0.9893	300.51	282.31	288.04	17.140	0.6597
	400	5.52	1.53	1.0156	327.50	335.16	331.98		
	500	6.48	3.69	0.9947	369.96	349.22	362.51		
	600	7.42	4.73	1.0150	379.50	376.99	397.46		
IR-10NH ₂ ³	300	4.06	1.10	1.0120	281.43	289.11	283.66	17.140	0.7415
	400	5.38	2.19	0.9982	322.08	335.45	328.70		
	500	6.58	2.63	0.9908	366.31	354.26	368.15		
	600	7.59	2.20	1.0212	385.90	393.81	389.58		

Table 2.4. Correlation factors for the relationship of self-diffusivity (at 300 K) and activation energy with surface area, accessible volume and adsorbate-framework energy (at 300 K and 1 bar)

Property 1	Property 2	Correlation Coefficient
Self- Diffusivity	Accessible Volume	0.96
Self- Diffusivity	Surface Area	0.17
Self- Diffusivity	Adsorbate Framework Energy	0.95
Activation Energy	Accessible Volume	0.75
Activation Energy	Surface Area	0.61
Activation Energy	Adsorbate Framework Energy	0.58

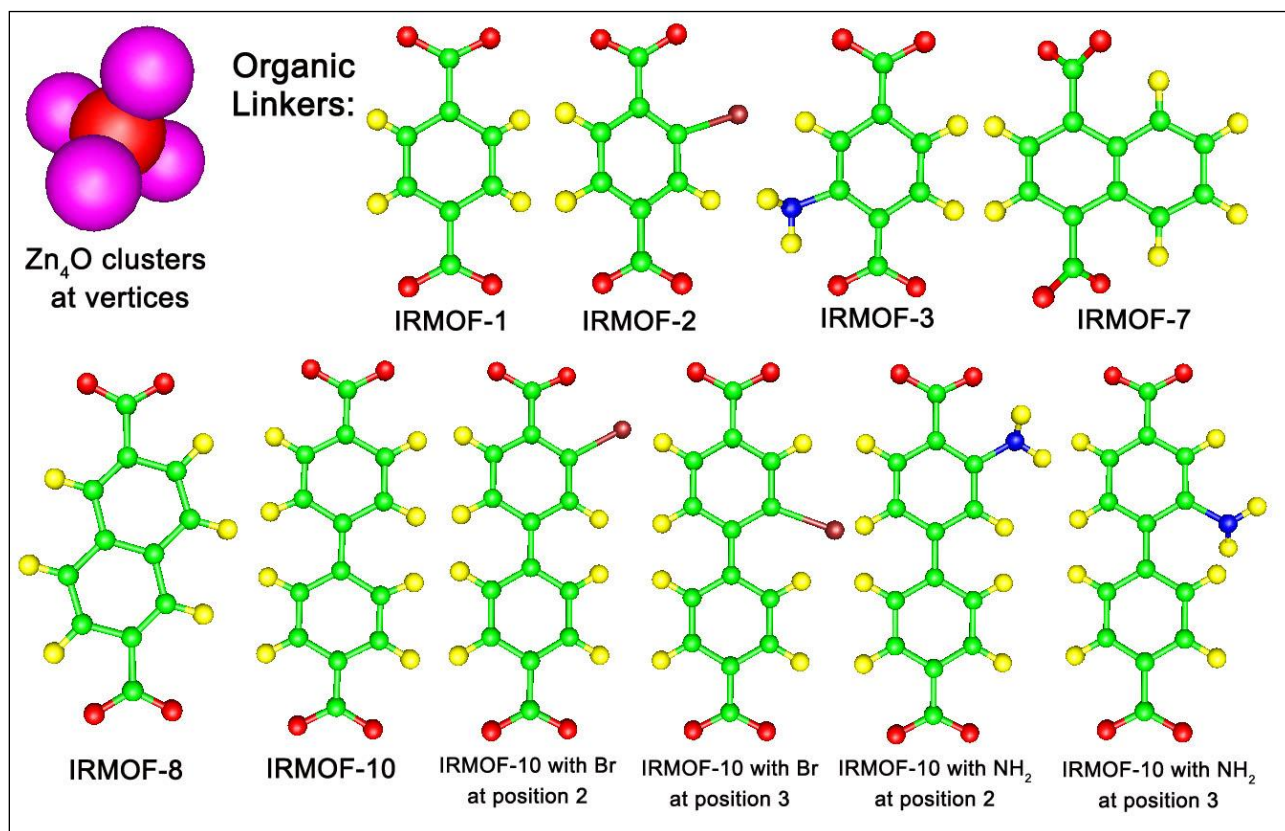


Figure 2.1. Structures of the 10 IRMOFs investigated in this work. The six structures on the left have been experimentally synthesized. The four structures on the right have not, to our knowledge, been synthesized, but the likelihood of synthesis is high based on the existence of functional analogs for the single ring connector. (legend: Zn-purple, O-red, C-green, H-yellow, Br-brown, N-blue)

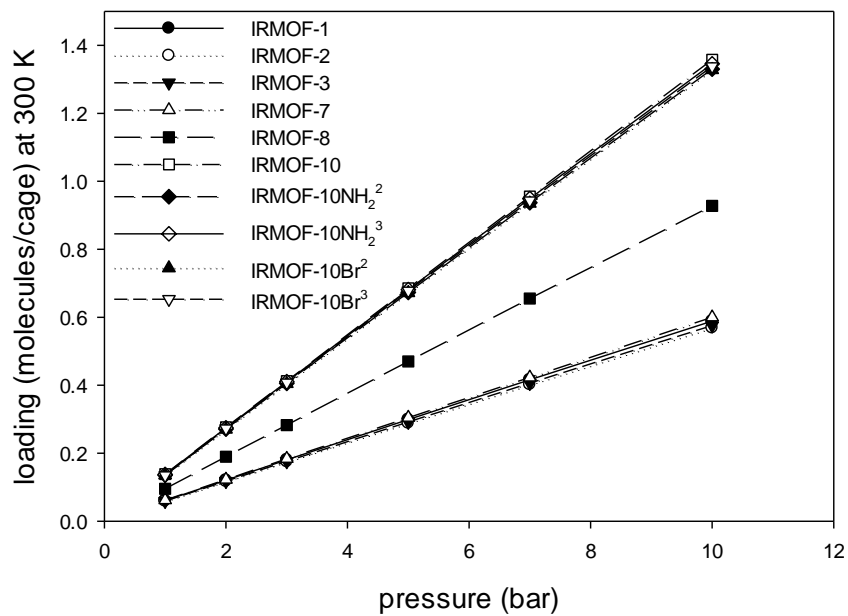
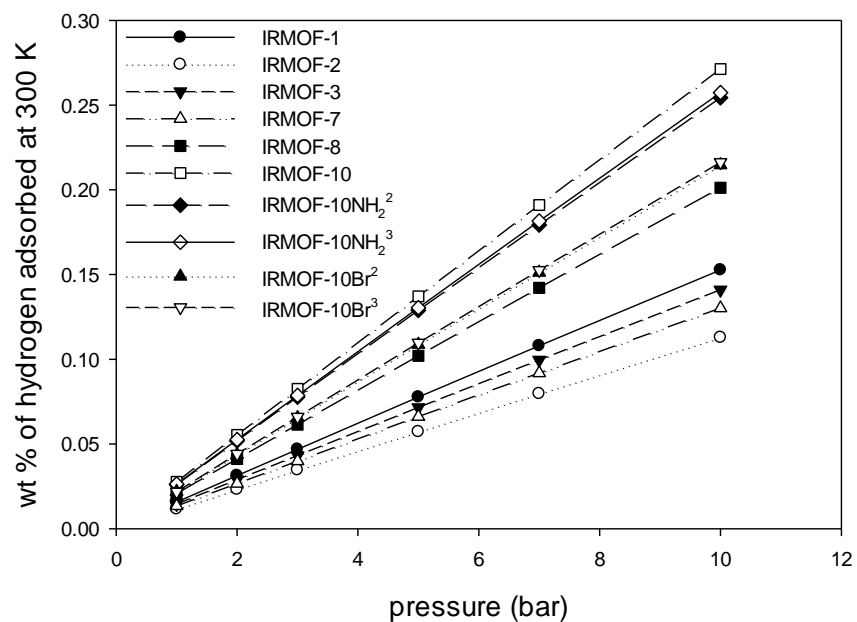


Figure 2.2. Hydrogen adsorption isotherms at 300 K on a weight percent basis (top) and on a molecules per cage basis (bottom).

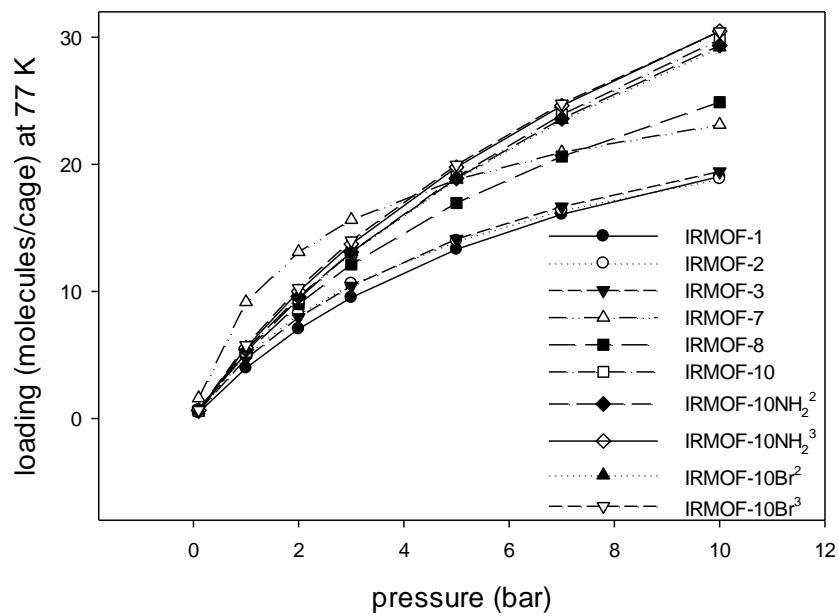
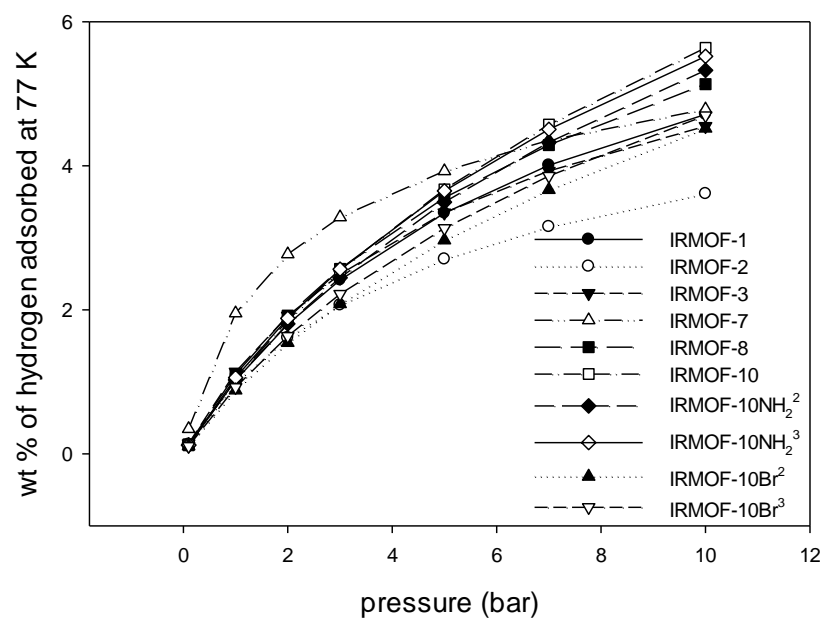


Figure 2.3. Hydrogen adsorption isotherms at 77 K on a weight percent basis (top) and on a molecules per cage basis (bottom).

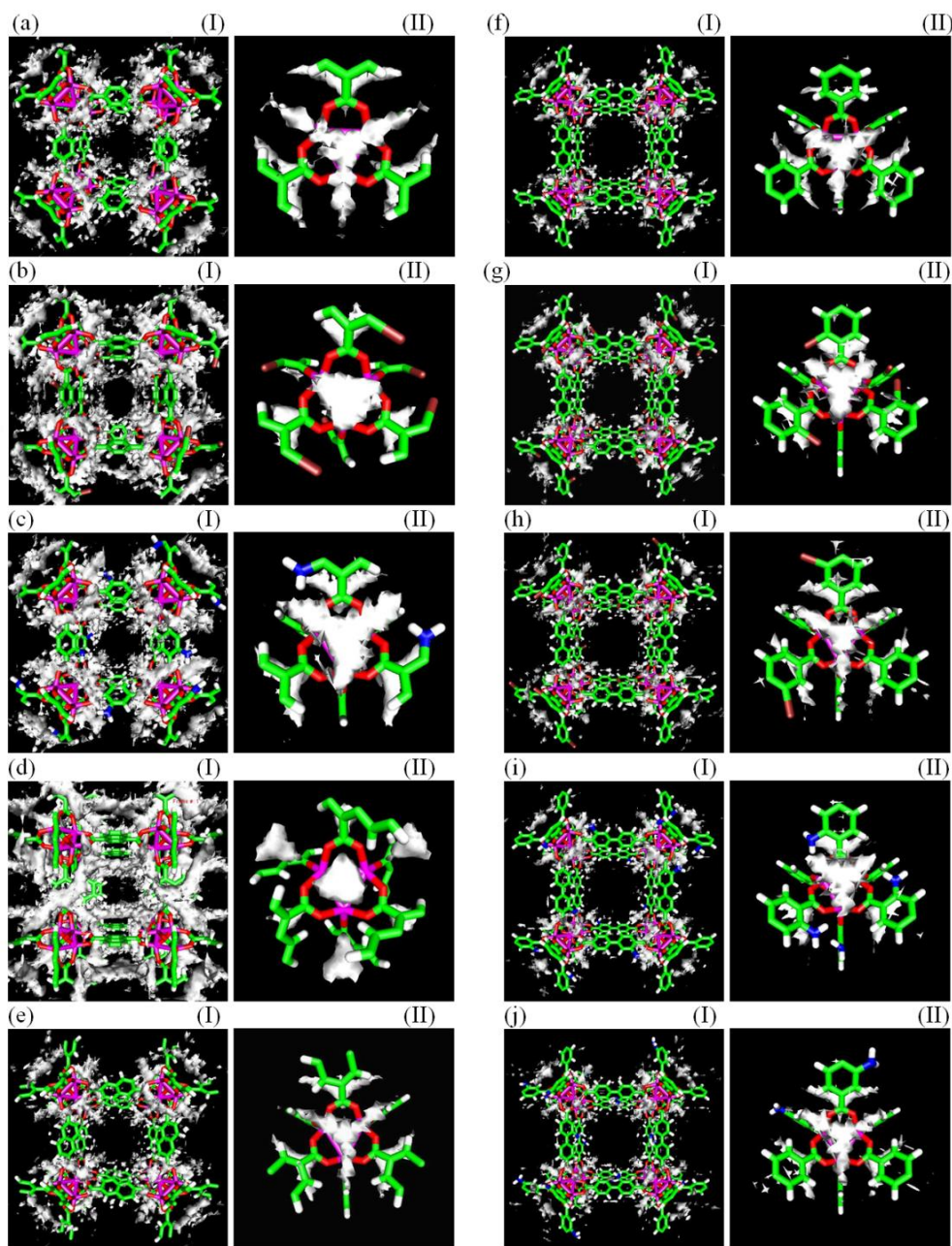


Figure 2.4. Density distributions at 300 K and 1 bar. The surface is drawn at a contour value of $0.0001 \text{ molecules}/\text{\AA}^3$. For each IRMOF, two views are shown, including (I) a view of the unit cell with a small cage in the center and (II) a vertex. IRMOF Legend: (a) IRMOF-1, (b) IRMOF-2, (c) IRMOF-3, (d) IRMOF-7, (e) IRMOF-8, (f) IRMOF-10, (g) IRMOF-10Br², (h) IRMOF-10Br³, (i) IRMOF-10NH₂², (j) IRMOF-10NH₂³. Color legend: violet-Zn, red-O, green-C, white-H, brown-Br, blue-N.

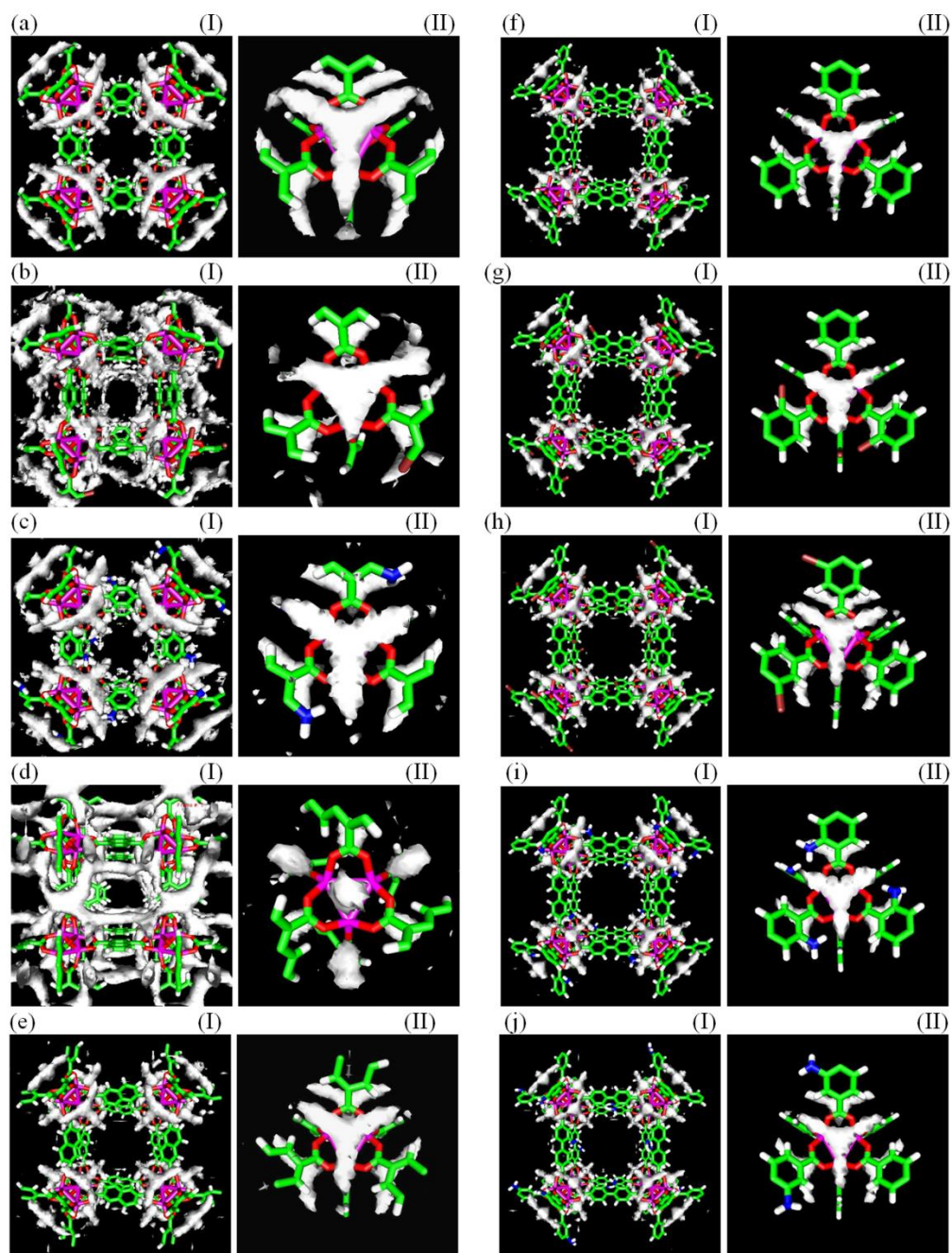


Figure 2.5. Density distributions at 77 K and 1 bar. The surface is drawn at a contour value of $0.015 \text{ molecules}/\text{\AA}^3$. For each IRMOF, two views are shown, including (I) a view of the unit cell with a small cage in the center and (II) a vertex. IRMOF Legend: (a) IRMOF-1, (b) IRMOF-2, (c) IRMOF-3, (d) IRMOF-7, (e) IRMOF-8, (f) IRMOF-10, (g) IRMOF-10Br², (h) IRMOF-10Br³, (i) IRMOF-10NH₂², (j) IRMOF-10NH₂³. Color legend: violet-Zn, red-O, green-C, white-H, brown-Br, blue-N.

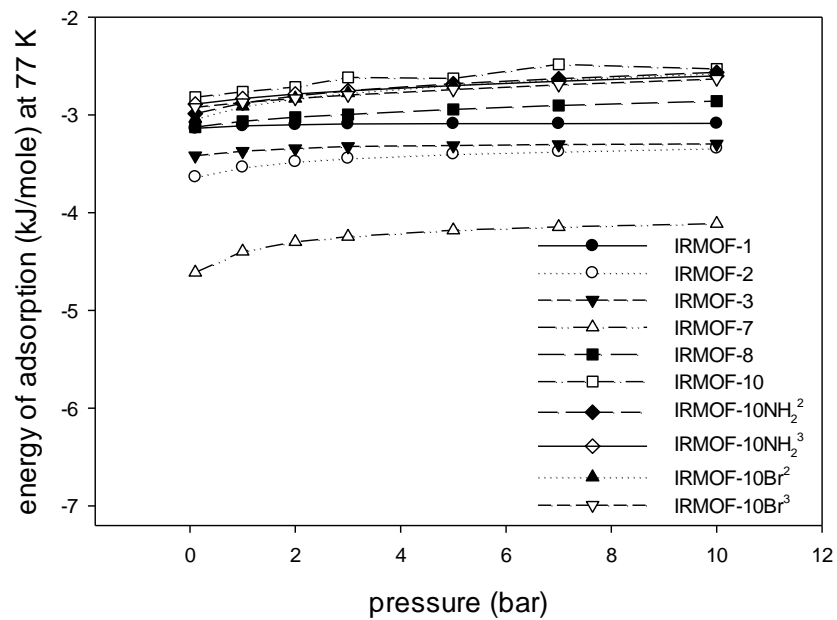
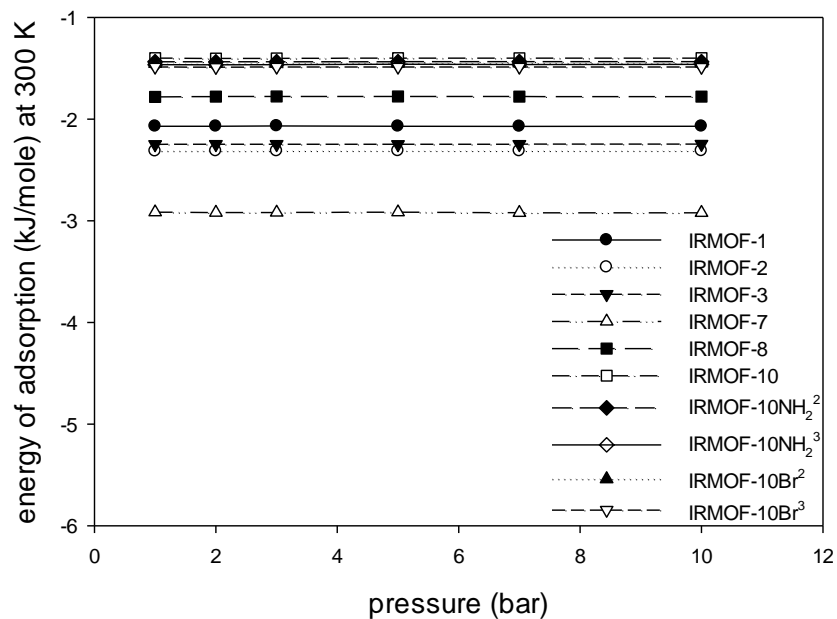


Figure 2.6. Adsorbate framework energy as a function of bulk pressure for 300 K (top) and 77 K (bottom).

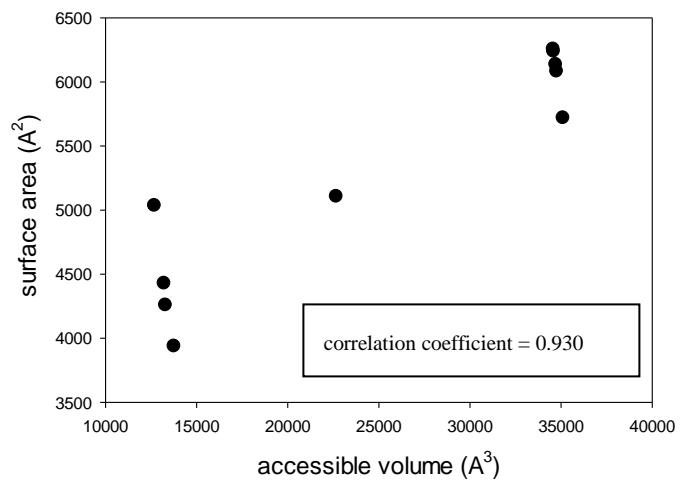
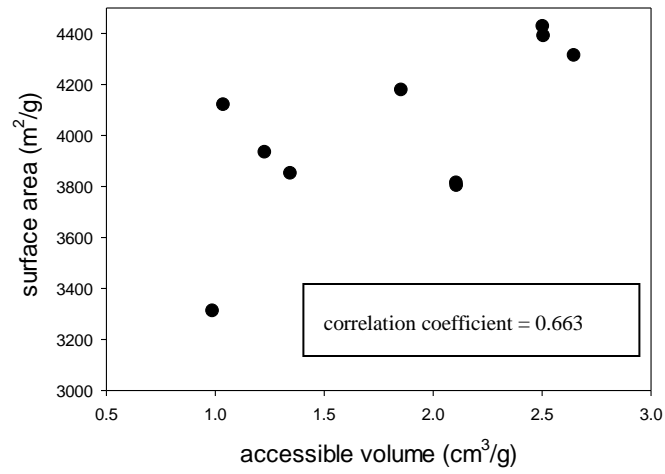


Figure 2.7. Relationship between surface area and accessible volume on a mass basis (top) and cage basis (bottom).

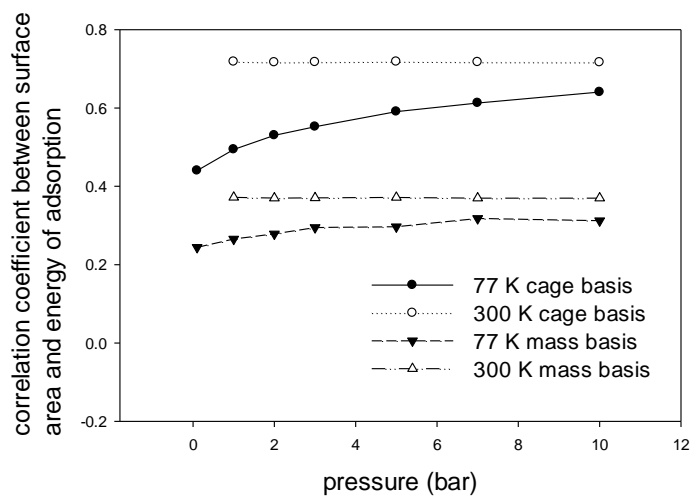
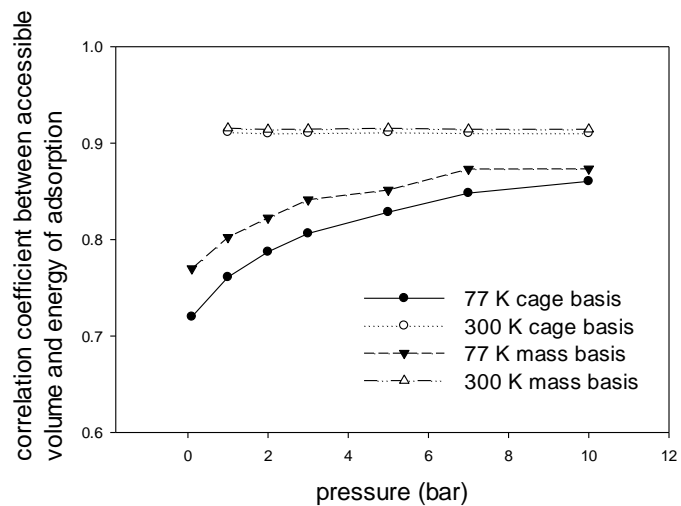


Figure 2.8. Correlation coefficients relating accessible volume (top) and surface area (bottom) to adsorbate-framework energy as a function of temperature and pressure.

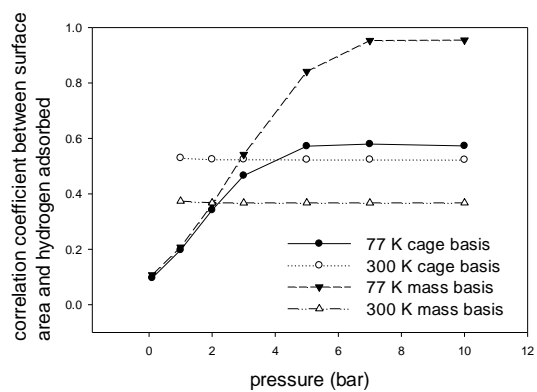
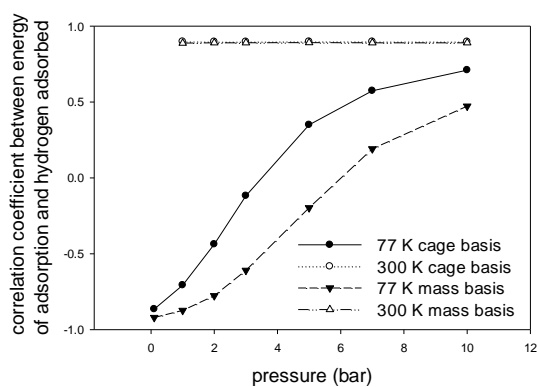
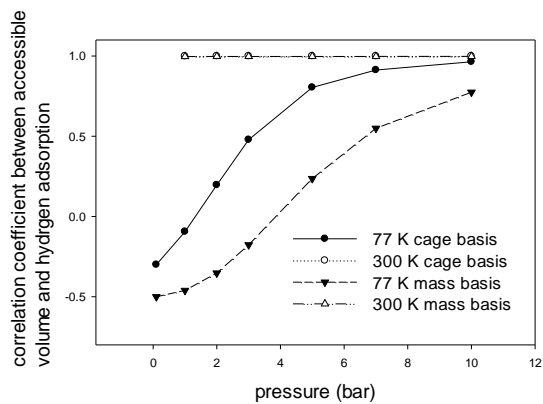


Figure 2.9. Correlation coefficients relating hydrogen adsorption to IRMOF properties as a function of temperature and pressure. (top) Correlation between hydrogen adsorption and free volume. (middle) Correlation between hydrogen adsorption and adsorbate-framework energy. (bottom) Correlation between hydrogen adsorption and surface area.

CHAPTER 3

Hydrogen Adsorption and Diffusion in Amorphous, Metal-Decorated Nano-Porous Silica

This chapter is a slightly revised version of a manuscript by the same title submitted to *International Journal of Hydrogen Energy* in 11/2013 by **Nethika S. Suraweera**, A.A. Albert, J.R. Humble, C.E. Barnes and D.J. Keffer:

Suraweera, N.S., Albert, A.A., Humble, J.R., Barnes, C.E., Keffer, D.J., “Hydrogen Adsorption and Diffusion in Amorphous, Metal-Decorated Nanoporous Silica”, *Int. J. Hydrogen Energy*, **under review**, 11/2013.

The use of “we” in this part refers to the co-authors and the author of this dissertation. My primary contributions to this paper include (1) all of the simulation work (2) analysis of data, and (3) most of the writing.

Reproduced with permission from *Int. J. Hydrogen Energy* (2013). Copyright © Elsevier Inc, 2013

Abstract

Amorphous, nanoporous adsorbents composed of spherosilicate building blocks and incorporating isolated metal sites were investigated for their ability to adsorb and desorb hydrogen. This novel adsorbent contains cubic silicate building blocks (spherosilicate units: Si_8O_{20}), which are cross-linked by SiCl_2O_2 bridges and decorated with either $-\text{OTiCl}_3$ or $-\text{OSiMe}_3$ groups. The models for the structures were generated to describe experimentally synthesized materials, based on physical properties including density, surface area, and accessible volume. Adsorption isotherms and energies at 77 K and 300 K for pressures up to 100 bar were generated via molecular simulation describing physisorption only. The maximum gravimetric capacity of these materials is 5.8 wt% H_2 , occurring at 77 K and 89.8 bar. A low density (high accessible volume) material with no $-\text{OTiCl}_3$ groups proved to be the best performing adsorbent. The presence of $-\text{OTiCl}_3$ did not enhance physisorption even on a volumetric basis, while the high molecular weight of Ti provided a strong penalty on a gravimetric basis. Pair correlation functions illustrate that the most favorable adsorption sites for hydrogen are located in front of the faces of the spherosilicate cubes. The self-diffusivity of hydrogen was reported and found to be highly correlated with accessible volume.

Keywords: Grand Canonical Monte Carlo simulation; spherosilicate; metal decorated silica; physisorption; hydrogen

3.1 Introduction

As depletion of fossil fuels becomes a challenge to our energy future and with the increasing concerns of their hazardous effects on the environment, hydrogen is often proposed as a sustainable energy carrier [1-4]. A variety of sources are used for hydrogen production including fossil fuels, renewables such as water with the aid of solar and wind energy, biomass and wastes [5-10]. However, its application particularly in on-board vehicles as an energy carrier is limited by hydrogen storage problems. Developing a reliable hydrogen storage system that meets the cost, safety, capacity and discharge rate requirements of the transportation sector is crucial. Some of the methods used and investigated for hydrogen storage include compressed gas, liquefaction, adsorption in metal hydrides, activated carbon, and metal organic frameworks (MOFs) [7, 11]. The Department of Energy (DOE) set the targets for onboard hydrogen storage systems for light-duty vehicles for gravimetric capacity of 5.5 wt.% hydrogen (1.8 kWh/kg system) and volumetric capacity of 0.04 kg hydrogen/L (1.3 kWh/L system) to be achieved by 2017 [12]. These targets will allow some hydrogen-fueled vehicle platforms to meet customer performance expectations, while the “ultimate full fleet” targets of 2.5 kWh/kg system (7.5 wt%), 2.3 kWh/L system (0.070 kg hydrogen/L), and \$8/kWh (\$266/kg H₂) are intended to facilitate the introduction of hydrogen-fueled propulsion systems across the majority of vehicle classes and models.

A good storage media for hydrogen should perform both as an efficient adsorber and desorber, because it is not only the storage capacity that matters, but also the discharge rate. Hydrogen storage adsorbents that have been investigated so far belong to two categories. First, the materials that adsorb hydrogen via chemisorption display high adsorptive capacities due to the large binding energies they possess, but their discharge rates are slow (e.g.: metal hydrides). Second, the materials that adsorb hydrogen via physisorption have smaller binding energies and consequently display lower adsorptive capacities, but discharge rates are better (e.g.: single-walled carbon nanotubes (SWNTs), metal organic frameworks (MOFs))[13]. Neither category currently meets both the adsorptive and desorptive requirements effectively. In 1997, Bushnell *et al.* [14] performed quantum mechanical studies to identify the favorable binding energies for both adsorption and desorption of hydrogen in the structures with isolated Ti centers. Ti metal

centers have binding energies that are between those associated with physisorption and chemisorption, making materials that incorporate them potentially interesting storage materials.

Motivated by this idea a synthetic strategy to make porous spherosilicate matrices that contain isolated titanium metal centers has been developed [15, 16]. These materials have an inorganic cross-linked polymer-like structure with atomically dispersed Ti acting as isolated metal centers. In a reduced state, the Ti metal centers provide catalytic sites, which mimic those described by Bushnell *et al.* [14]. In an oxidized state, the Ti metal centers appear as $-\text{OTiCl}_3$, which still impacts the adsorption of H_2 . In this study we computationally investigate the spherosilicate structures made up of polyhedral oligomeric silsesquioxane (POSS). It is in shape of a cube and has the empirical chemical formula $(\text{RSiO}_{3/2})_8$ where R is either a functional ending group or a cross linker which is connected to another spherosilicate unit. POSS are part of a large family of polycyclic compounds consist of silicon–oxygen bonds [17, 18].

Metal-containing POSS compounds have been experimentally studied as metal catalyst supports. [19] Numerous elements throughout the periodic table have been incorporated successfully into POSS[15, 16] opening paths to facilitate broad applications. Theoretical modeling of synthesis, assembly and properties for POSS systems have been previously investigated by McCabe *et al.*[20]. The adsorptive capability of POSS-based structures has been investigated in several studies. A Pd-POSS system has been analyzed by Maiti *et al.* [21] to investigate hydrogen catalysis and sequestration. They report density functional theory results on POSS binding energies at the Pd(110) surface, hydrogen storing ability of POSS and possible pathways of hydrogen radicals from the catalyst surface to unsaturated bonds away from the surface. Shanmugam *et al.* studied CO_2 adsorption [22], Xie *et al.* studied copper and nickel ions adsorption [23], Hongbo *et al.* studied N_2 adsorption [24], in different variations of POSS -based structures.

The family of cross-linked matrices of spherosilicate cubes used in this work has been prepared according to published procedures [15, 16, 19]. More details about experimental structures are included in our previous work on adsorption properties for methane and carbon dioxide in the same set of adsorbents[25]. Here we report the results of molecular-level simulations to study physisorption and diffusion of hydrogen in these materials, with the purpose of developing fundamental structure/property relationships. Particularly, we are interested in the

impact of surface area (SA), accessible volume (AV) and $-\text{OTiCl}_3$ content on the adsorptive and diffusive behavior of H_2 .

3.2 Simulation Methods

3.2.1 Model for Spherosilicate Structures

Developing an atomistic model of a novel amorphous adsorbent is more challenging than for a crystalline material, because in the latter case one can rely on atomic coordinates and unit cell parameters obtained from diffraction whereas in the former case, one must propose atomic coordinates and validate the resulting material through comparison to physical properties with those available from experiments (such as the chemical stoichiometry, pore size distribution, surface area, fraction of accessible volume and density of the material). In order to generate an atomistic structure for these amorphous, metal-decorated spherosilicate structures, we developed a multiscale procedure which includes a mesoscale level modeling step followed by a molecular level modeling step. A detailed description of this procedure is included in our previous work [25]. Briefly, in the mesoscale level modeling step, four different coarse grain beads representing four different atomic groups were placed in a $50 \times 50 \times 50 \text{ \AA}^3$ cubic simulation box according to the relevant distances and angles between connected beads, so as the system agrees with the experimentally determined stoichiometry, density, surface area and accessible volume. The four groups are spherosilicate cubes (Figure 3.1(a)), O_2SiCl_2 connecting bridges (Figure 3.1(b)) and two groups that terminally binds to the vertices of the spherosilicate cubes: $-\text{OTiCl}_3$ (Figure 3.1(c)) and $-\text{OSi}(\text{CH}_3)_3$ (trimethylsilyl or $-\text{OSiMe}_3$) (Figure 3.1(d)). A mesoscale level energy minimization in which the coarse grain beads were translated was performed using canonical Monte Carlo simulation to avoid overlap between the beads and to obtain a stable structure. In the molecular level modeling step the coarse grain beads were replaced with their relevant atomic descriptions and rotated to obtain the correct orientation using the downhill simplex method[26]. Figure 3.1(e) and Figure 3.1(f) illustrate a coarse grain structure and an atomistic structure respectively.

Using this procedure we modeled nine materials for this study, by varying two physical properties at three levels. The first property is density of the adsorbent. Of course, a change in density corresponds to a change in the fraction of accessible volume in the adsorbent as well as a

commensurate change in surface area. The second property is $-\text{OTiCl}_3$ content. As noted above there are two types of non-connecting end groups attached to the vertices of the spherosilicate cube, $-\text{OTiCl}_3$ and $-\text{OSi}(\text{CH}_3)_3$. Values of 0%, 50% and 100% Ti correspond to the fraction of end groups which were $-\text{OTiCl}_3$. For each level of $-\text{OTiCl}_3$ content, there are three levels of material density, designated low, medium and high. It is worth noting that the densities change as the name implies for a given $-\text{OTiCl}_3$ content, although there are examples where the density of a “low density” material with 100% $-\text{OTiCl}_3$ end groups has a higher density than a “medium density” material with 0% $-\text{OTiCl}_3$ end groups, due to the high molecular weight of Ti. Accessible volume and surface area for each structure were calculated using geometrical methods that have been used for MOFs[27] and polymer membranes[28, 29] in our previous studies. These geometrical methods are based on published approaches[30]. Additional details and physical properties of these structures are included in Table 3.1. Atomistic structures for adsorbents modeled are available at an online archive[31].

3.2.2 Grand Canonical Monte Carlo Simulation

Standard Grand Canonical Monte Carlo (GCMC) simulation [32, 33] was used for adsorption simulations, in which the chemical potential (μ), volume (V) and temperature (T) of the system are fixed and the simulation delivers the number of hydrogen molecules in the system and the potential energy. Three types of moves: (i) center-of-mass translation, (ii) molecule insertion and (iii) molecule deletion, were randomly attempted for hydrogen molecules in a ratio of 3:2:2. For each simulation, 20 million configurations were used with the last half of the configurations were performed to get the desired average ensemble properties. No electrostatic interactions were included as justified for H_2 adsorption in MOFs in literature [34]. Three dimensional standard periodic boundary conditions and the minimum image convention were employed. The size of the simulation box was chosen such that the average number of hydrogen molecules in the system is between 300 and 2000.

At cryogenic temperatures for light molecules like H_2 quantum effects become non-negligible [35, 36]. Even at 300 K, quantum effects could lead to an overestimation of adsorption by several percent [37]. To account for the quantum effects, we adopted the Feynman-Hibbs (FH) effective Buch potential method [38, 39] in the GCMC simulations. This is computationally

more efficient than the Path Integral MC method[40] , used in our earlier study for isoreticular metal organic frameworks (IRMOFs) [27]. The FH effective Buch potential is capable of accurately reproducing properties from Path Integral Monte Carlo [41, 42]. We previously validated that points on the isotherm could be reproduced using either the FH effective Buch potential or the PI method to within 0.06 % for H₂ in IRMOF-1 at 300 K and 1 bar [27].

Since we are interested in generating an isotherm as a function of T and pressure (p), the chemical potential of the bulk phase at a given temperature and pressure was estimated using the Lennard-Jones equation of state by Johnson *et al.*[43] To eliminate the error arising from the approximate nature of the equation of state, at each case for a choice of chemical potential and temperature, we performed two simulations: one in the bulk phase and one in the adsorbed phase. Adsorption isotherms were generated by plotting the amount of hydrogen in the system obtained from the adsorbed phase simulation as a function of the pressure obtained from the bulk phase.

The hydrogen molecule is treated as a single Lennard-Jones (LJ) particle (united atom model) and Buch Lennard-Jones parameters ($\sigma_{H_2} = 2.96 \text{ \AA}$ and $\epsilon_{H_2}/k_B = 34.2 \text{ K}$) were used to model the interaction potentials[44]. The framework atoms of the structures are assumed to be rigid, hence only the non-bonded interactions between the molecular hydrogen and the atoms of the adsorbent were calculated. The LJ parameters for the atoms in the framework were taken from universal force field (UFF) [45] (values are listed in Table 3.2). Interaction parameters between different types of atoms were determined using the Lorentz-Berthelot mixing rules[46]. Previous studies shows that the hydrogen adsorption capacities for MOFs calculated with UFF agree with experimental values and the calculated values with other force fields [27, 47].

3.2.3 Quantum Mechanical Calculations

We needed to make sure only physisorption of hydrogen occurs with -OTiCl₃ groups, not chemisorption. For this quantum mechanical calculations were performed making use of the B3LYP functional in combination with the standard 6-311G(d,p) basis set utilizing Gaussian 03[48] which is a level of theory used by other researchers [49] to calculate properties for similar structures. First we stabilized 2 molecules: (1) a spherosilicate cube with a -OTiCl₃ group attached into it (2) H₂ molecule. Then we placed the stabilized H₂ molecule near to the -OTiCl₃

group (with spherosilicate cube) and stabilized the entire system again. We made sure the stabilized H-H bond length of H₂ molecule in the system is equal to the H-H bond length of H₂ molecule when it is stabilized alone (at 3 decimal places 0.744024 and 0.744206). Hence we can assure there's no distortion occurred in H₂ molecule, therefore no chemisorption will result.

3.2.4 Molecular Dynamics Simulations

Classical equilibrium MD simulations in the canonical (NVT) ensemble were used to calculate transport properties of H₂ in the spherosilicate structures. The two-time step r-RESPA algorithm [50] was used to integrate equations of motion with 2 fs for a large time step and 0.2 fs for intramolecular interactions. The same interaction potentials were used in the GCMC and MD simulations. The Nosé-Hoover thermostat [51, 52] method was used to maintain the temperature at a constant value. The system was equilibrated for 2 ns and an additional 8 ns was simulated for data production. Self-diffusivities were calculated via the Einstein relation using the center-of-mass positions of the hydrogen molecules saved at 5 ps intervals during data production. The activation energy for each structure was calculated via linear regression of the Arrhenius Equation using the self-diffusivities calculated at four temperatures (300 K, 400 K, 500 K and 600 K). We did not explore the density dependence for the diffusivity. Instead, self-diffusivities correspond to an infinite dilution density were calculated.

3.3 Results and Discussion

3.3.1 Adsorption Isotherms

Adsorption isotherms were generated at 300 K and 77 K for a pressure range up to 100 bar. All the isotherms were analyzed on both gravimetric basis (weight percentage wt%) and volumetric basis (kg of hydrogen/l). Only gravimetric isotherms are included in this manuscript. A complete and analogous set of volumetric isotherms are available in the corresponding supplementary information (Appendix C). Adsorption isotherms can be understood in terms of the general thermodynamic considerations outlined in supplementary document, section C1 (Appendix C).

Gravimetric isotherms at 300 K are shown in Figure 3.2 for low density structures (Figure 3.2(a)), middle density structures (Figure 3.2 (b)) and high density structures (Figure 3.2 (c)). At 300 K, the highest weight percentage of hydrogen is less than 1.1 wt% for all the structures studied and volumetric quantity adsorbed is less than 0.007 kg of hydrogen/l. Adsorption up to 100 bar occurs within the linear regime for all structures. This relatively low adsorption capacity at room temperature is consistent with the physisorption mechanism included in the simulations. What is also obvious from these simulations is that the presence of Ti does not enhance adsorption on a gravimetric basis. Obviously, there is a gravimetric penalty associated with the inclusion of Ti based on its molecular weight. However, this is not the sole reason because an analysis of the volumetric isotherms shown in the supplementary information (Appendix C) also shows less adsorption with increasing $-\text{OTiCl}_3$ content. Considering the relevant thermodynamics (supplementary document - Appendix C), 300 K is already in infinite temperature limit and adsorption is governed by entropic effects, which is characterized by AV . Although $-\text{OTiCl}_3$ groups add relatively more free volume to the system, they can also add inaccessible volume. Therefore, the amount of H_2 adsorbed becomes lower in the frameworks with more $-\text{OTiCl}_3$. Further the value of well depth (ϵ) of the Lennard Jones potential for Ti is relatively low resulting less number of H_2 adsorbed by physisorption at $-\text{OTiCl}_3$ sites. The conclusion here is that the presence of Ti as $-\text{OTiCl}_3$ does not enhance physisorption. Of course, no conclusion can be drawn from the present work on the impact of reduced Ti on chemisorption.

Gravimetric isotherms at 77 K are shown in Figure 3.3 for low density structures (Figure 3.3(a)), middle density structures (Figure 3.3 (b)) and high density structures (Figure 3.3 (c)). At 77 K, the maximum weight percentage of hydrogen adsorbed is 5.8 wt% and maximum volumetric quantity adsorbed is 0.036 kg of hydrogen/l at the maximum bulk pressure studied (89.8 bar). The isotherms of all nine materials are clearly nonlinear. Again, it is clear that the addition replacement of $-\text{OSi}(\text{CH}_3)_3$ with $-\text{OTiCl}_3$ does not enhance physisorption at low temperature.

In order to better judge the impact of material density (or equivalently accessible volume) on the adsorption isotherms, some of the isotherms plotted in Figures 3.2 and 3.3 are re-plotted in Figure 3.4, grouped now according to $-\text{OTiCl}_3$ content, so that the impact of density is obvious

to the eye. Figure 3.4 presents isotherms for 0% -OTiCl₃ structures: gravimetric isotherms at 300 K (Figure 3.4(a)), gravimetric isotherms at 77 K (Figure 3.4 (b)) and volumetric isotherms at 77 K (Figure 3.4 (c)). In Figure 3.4(a), the gravimetric plots of the adsorption isotherms indicate that the structures with higher AV adsorb more hydrogen on a wt% basis at 300 K. For these materials, adsorption is already dominated by entropic factors (AV) at 300 K. The low density material contains a greater fraction of accessible volume, allowing for a higher adsorption capacity on both a gravimetric and volumetric basis at high temperature, although the difference is emphasized on a gravimetric basis.

At 77 K, the impact of material density is more complicated but still understandable in terms of the underlying thermodynamics (supplementary document - Appendix C). At low pressures, adsorption is dominated by energetic effects. Therefore, the high density materials, which present deeper energy wells at the walls of the pores, have an advantage. Therefore, on a volumetric basis, the high density materials adsorb more H₂ than do the low density materials, as shown in Figure 3.4(c). However, on a gravimetric basis, the low density materials are favored due to the lighter mass of the framework, as shown in Figure 3.4(b). Taking these two competing effects into account results in little impact of the density of the material on the gravimetric isotherm. At high pressures, adsorption is governed by entropic considerations, which is enhanced by the greater accessible volume of the low density adsorbent. Therefore, the low densities materials show a greater adsorption capacity on both gravimetric and volumetric bases at high pressure and low temperature.

Based on the analysis above, the best adsorbent for a physisorption process is a low density material with 0% -OTiCl₃ content.

Hydrogen was always adsorbed around the framework and in the pore areas. We never observed H₂ adsorbed inside the spherosilicate cubes. This observation also agrees with the studies done by Maiti *et al.* to analyze the stability of a H₂ molecule in a spherosilicate cube[21]. They found H₂ molecule inside the POSS cage is less stable than an H₂ outside the cage. The possibility of stabilization and trapping of hydrogen by POSS cages has been discussed in the literature more than a decade ago.[53]

3.3.2 Energies of adsorption

The impact of material density and $-\text{OTiCl}_3$ content on energies of adsorption are important in terms of understanding structure/property relationships in adsorbents. The energy of adsorption is the difference between the energy of the adsorbed phase and the energy of the bulk phase. In practice, the interaction energies between hydrogen molecules are negligible compared to the interaction energies between hydrogen and framework atoms. Therefore, in calculating energy of adsorption, ‘adsorbate-adsorbent interactions in the adsorbed phase’ is the dominant term on which we now focus. In Figure 3.5, the potential energy due to adsorbate-adsorbent interactions is plotted for three $-\text{OTiCl}_3$ contents in the low density material (a) and for three densities in the 0% $-\text{OTiCl}_3$ material (b) at 300 K. Both plots show only a weak loading-dependence on the energy of adsorption, due to the relatively low loadings at 300 K. Figure 3.5(a) clearly shows a more favorable energy for the low 0% $-\text{OTiCl}_3$ material; the presence of Ti does not enhance physisorption, as reflected in the isotherms. Figure 3.5(b) shows that the high density materials have deeper energy wells, as noted above but the energetic enhancement is not sufficient to overcome the entropic penalty of high-density materials due to the reduced accessible volume as shown in the isotherms. At 300 K the energies of adsorption range in magnitude from 1 to 5 kJ/mol.

In Figure 3.6, the potential energy due to adsorbate-adsorbent interactions is plotted for three $-\text{OTiCl}_3$ contents in the low density material (a) and for three densities in the 0% $-\text{OTiCl}_3$ material (b) at 77 K. The energies of adsorption are much stronger functions of pressure, since the loadings are now much higher. The deep sites near the walls are occupied first. Then the energetically less favorable pore interior is filled. Figure 3.6(a) again clearly shows a more favorable energy for the low 0% $-\text{OTiCl}_3$ material across the entire pressure range. Figure 3.6(b) shows that the high density materials have deeper energy wells across the entire pressure range and the difference increases with increasing pressure. At 77 K the energies of adsorption range in magnitude from 2 to 7 kJ/mol.

In Figure 3.7, the potential energy due to adsorbate-adsorbate interactions is plotted for three $-\text{OTiCl}_3$ contents in the low density material (a) and for three densities in the 0% $-\text{OTiCl}_3$ material (b) at both 77 and 300 K. Note that the adsorbate-adsorbate energies are measured in

Joules, while the adsorbate-adsorbent energies in Figures 3.5 and 3.6 were measured in kJ. At 300 K, the magnitude of the adsorbate-adsorbate energy never exceeds 0.05 kJ/mol, while at 77 K it never exceeds 0.5 kJ/mol. There is no significant structural impact on the adsorbate-adsorbate energy at 300 K. At 77 K, the 0% -OTiCl₃ material shows a more favorable adsorbate-adsorbate energy (a) and the high density material shows a more favorable adsorbate-adsorbate energy at low loadings only (b). Essentially, adsorbate-adsorbate energies reflect the same trends as visible in the volumetric isotherms, because under the conditions examined here, the adsorbate-adsorbate energies is strongly correlated to the concentration of the adsorbed phase.

3.3.3 Hydrogen adsorption sites

In this work, pair correlation functions (PCFs), which represent a conditional probability of finding two particles at a given separation, normalized to unity at long distances, were used to identify the adsorption sites in the spherosilicate structures.

$$g(r) = \frac{V}{\Delta V N^2} \left\langle \sum_i \sum_{j \neq i} \delta(r - r_{ij}) \right\rangle \quad (1)$$

V is the system volume, r is the separation distance between two particles i and j , and N is the number of particles in the system. The use of three-dimensional density distributions to identify adsorption sites in crystalline IRMOFs in our previous study [27] cannot be used for amorphous spherosilicate structures because they do not have periodic unit cells.

Pair correlation functions were generated for pair of particles of different types. The H₂-H₂, H₂-Si and H₂-Ti PCFs are show in Figures 3.8, 3.9 and 3.10 respectively. At the top of each figure, a snapshot of a configuration representative of the peak is provided. For each case PCFs for three materials are examined, to investigate the best adsorbent (low density and 0% -OTiCl₃), the impact of -OTiCl₃ content (low density and 100% -OTiCl₃) and the impact of material density (high density and 0% -OTiCl₃). Furthermore, in Figures 3.8, 3.9 and 3.10, three thermodynamic state points are examined, (a) low temperature and low pressure (77 K and 1 bar), (b) low temperature and high pressure (77 K and 89.84 bar) and (c) high temperature and high pressure (300 K and 99.39 bar).

Using these pair correlation functions we identified that the preferred adsorption sites are located in front the exterior faces of the spherosilicate cubes. In Figure 3.8, there are two prominent peaks in the H₂-H₂ PCF, centered at 3.2 Å and 7 Å. The first peak corresponds to the H₂-H₂ nearest neighbor distance when occupies in pore areas. The second peak corresponds to H₂ located on adjacent faces of the same spherosilicate cube. At low temperature and low pressure (a), we observe that the relative magnitude of the two peaks is impacted by the presence of Ti, but the position is not. Ti groups allow relatively more H₂ bindings near to the cubes at low pressure and low temperature. As the loading is increased at low temperature (Figure 3.8(b)), one obtains a PCF structure typical of a high-density gas or liquid. The impact of the adsorbent on the PCF has been drastically diminished as the H₂ orient themselves in the limited accessible volume. The peaks for the high density material are higher since the PCF is normalized by the total density (number of H₂ per simulation volume) but the accessible volume where H₂ may be found is lower in the high density material. At high temperature (Figure 3.8(c)), one obtains a PCF structure typical of a gas, capturing the low density of the adsorbed phase.

In Figure 3.9, there are two prominent peaks in the H₂-Si PCF, centered at 4 and 6.8 Å. The first peak corresponds to the H₂ interacting with a Si on the adsorbed face and the second peak corresponds to a Si located in the same spherosilicate cube but on a different face than the one on which the H₂ is adsorbed. At low temperature and low pressure (a), we observe that the relative magnitude of the two peaks is impacted by the presence of Ti, but the position is not. In 0% -OTiCl₃ structures Si is also provided by the -OSiMe₃ groups. Therefore, we see a peak at 5.1 Å which is correspond to the H₂ interacting with a Si in -OSiMe₃ group connected to the adsorbed face of the spherosilicate cube. The peaks for the 100% -OTiCl₃ structure are higher since the PCF is normalized by the total density (number of H₂ per simulation volume) but the accessible volume where H₂ may be found is lower in 100% -OTiCl₃ structures. Values for accessible volumes for all the structures are presented in Table 3.1. At high temperature and high pressure (Figure 3.9(c)), the relationship between the adsorbed hydrogen and framework atoms are relatively low because the adsorption is governed by entropic effects and H₂ is located in available pore area.

In Figure 3.10, there are two prominent peaks in the H₂-Ti PCF, centered at 4.9 and 9.1 Å. The first peak corresponds to the H₂ interacting with a Ti in a -OTiCl₃ group connected to the adsorbed face of the spherosilicate cube and the second peak corresponds to a Ti in a -OTiCl₃ group connected to the same spherosilicate cube but on a different face than the one on which the H₂ is adsorbed. At low temperature and low pressure we observe high probability for H₂ to stay near to the -OTiCl₃ groups, in other words near to the surface of the adsorbent. At high pressures effect of the presence of Ti diminishes, as in this entropically dominant area H₂ is adsorbed into pores and the binding to the surface of the adsorbent is minimum.

Additional PCFs, H₂-O H₂-Cl and Ti-Ti are presented in the supplementary information (Appendix C) in Figures 3.S5, 3.S6 and 3.S7 respectively. The Ti-Ti PCF demonstrates the atomistically dispersed nature of Ti within the matrix, which is a key feature that is important for an analogous material with reduced Ti, that can act as independent chemisorption sites for hydrogen molecules.

3.3.4 Self-Diffusivity

For each structure self-diffusivities were calculated at four temperatures: 300 K, 400 K, 500 K and 600 K. The values are presented in Table 3.3. Calculated self-diffusivities were validated using two methods. First, it was ensured that all the MD simulations were run to the infinite-time limit, where a linear relationship between MSD and observation time is observed. Second, long time limit behavior was verified by showing that the distance travelled by H₂ molecules is large enough compared to the pore size of the structure (Table 3.3; Average distance travelled is the square root of the final MSD).

In calculating diffusivities we observed there's a significant difference between the diffusivities in *x* direction component, *y* direction component and *z* direction component. (We confirmed the accuracy of these results by getting the same results with rotated structure) This happens due to the anisotropic effects of the structure. Being amorphous, these matrices have a structure with irregular pores in every direction. Our cubic simulation box with a side length of 50 Å has not been able to overcome the anisotropic effect. For example in one instance we get *x* component: $7.92 \times 10^{-07} \text{ (m}^2/\text{s)}$ with standard deviation of $8.82 \times 10^{-10} \text{ (m}^2/\text{s)}$, *y* component: $9.10 \times 10^{-07} \text{ (m}^2/\text{s)}$ with standard deviation of $3.90 \times 10^{-10} \text{ (m}^2/\text{s)}$, *z* component: $5.00 \times 10^{-07} \text{ (m}^2/\text{s)}$ with

standard deviation of 1.47×10^{-10} (m^2/s) and then the average diffusivity become 7.34×10^{-07} (m^2/s) with standard deviation of 2.11×10^{-07} (m^2/s). Therefore, in each case we see that the standard deviation of average diffusivity become significant while the standard deviation for a one direction component (x , y or z) is 3 orders of magnitudes less than the diffusivity component towards that direction.

The activation energies calculated are presented in Table 3.3. As expected from the Arrhenius equation, a negative correlation between the self-diffusivity and activation energy for diffusion is observed.

Similar to our previous studies [25, 27] we calculated correlation coefficients, a statistical property bounded between -1 (perfect negative correlation) and +1 (perfect positive correlation), to analyze the relationship between self-diffusivity and activation energy with SA, AV and energy of adsorption (at 1 bar to match with the infinite dilution conditions) at 300 K. Calculated values (Table 3.4) show a strong positive correlation between self-diffusivity and AV. When the pore size is large, the hydrogen diffuses faster. Since the SA is negatively correlated with the AV, the self-diffusivity is also negatively correlated with the SA. These observations are consistent with the results obtained by Liu *et al.*[54] and our previous study [27] for hydrogen diffusion in metal organic frameworks. The self-diffusivity increases as the molecules are more weakly bound, in large part due to a commensurate decrease in the activation energy.

3.3.5 Comparison with Experiments

Simulated hydrogen adsorption results were compared with experimental adsorption for two structures at 77 K up to 1 bar (100 kPa). The materials include the high density %0 -OTiCl₃ structure and the middle density 100% -OTiCl₃ structure. Physical properties of the experimental structures such as accessible volume, surface area and -OTiCl₃ content agreed with the selected modeled structures. The comparison of adsorption isotherms is shown in Figure 3.11. There is good agreement between the simulated and experimental isotherms for 100% -OTiCl₃ structure. The difference between the two experimental materials is within experimental error based on independent measurement of the isotherms across samples. (The primary purpose of the experimental isotherms was to distinguish between physisorption and chemisorption. These results clearly indicated physisorption for both materials.) The simulated H₂ adsorption for the

0% $-OTiCl_3$ structure is much higher than the experimental adsorption. This discrepancy must be attributed to failures in either the structure or potential of the model. Since our structure has been validated against available experimental characterization of structure, we suspect that a shortcoming in the UFF potential may be responsible for the discrepancy. The UFF well depth (ϵ) of the Lennard Jones potential for Si is relatively high (Table 3.2) resulting in more energetically favorable sites for H_2 adsorption associate in the material with $-OSiMe_3$ groups rather than $-OTiCl_3$ groups. Therefore, the simulations show high adsorption in this structure which is not observed experimentally.

3.4 Conclusions

In this work, we investigated the physisorption of H_2 in adsorbents containing cubic silicate building blocks (sphaerosilicate units: Si_8O_{20}), which are cross-linked by $SiCl_2O_2$ bridges and decorated with either $-OTiCl_3$ or $-OSiMe_3$ groups. At 300 K, the highest weight percentage of hydrogen is less than 1.1 wt% for all the structures studied and volumetric quantity adsorbed is less than 0.007 kg of hydrogen/l. At 77 K, the maximum weight percentage of hydrogen adsorbed is 5.8 wt% and maximum volumetric quantity adsorbed is 0.036 kg of hydrogen/l at the maximum bulk pressure studied (89.8 bar). The best adsorbent for a physisorption process studied herein is a low density material with 0% $-OTiCl_3$ content. The presence of Ti as $-OTiCl_3$ does not enhance physisorption. First there is a gravimetric penalty associated with the inclusion of Ti based on its molecular weight. Second Ti is surrounded by 3 Cl atoms limiting the attraction of Ti towards the adsorbed H_2 . However, for an analogous material, in which the Ti is reduced and can act as a chemisorption site for H_2 , inclusion of Ti catalytic sites is expected to yield significantly higher H_2 adsorption.

We observe that at 300 K and pressures up to 100 bar the adsorption process is governed by entropic considerations. At 77 K, there are more than one adsorption regimes. At low pressures, the adsorption process is governed by energetic considerations and at the high end of the pressure range the adsorption becomes a process dominated by entropic considerations. Based on the pair correlation functions we identified that favorable adsorption sites for hydrogen are located in front of the face of a sphaerosilicate cube. Self-diffusivity of hydrogen at infinite dilution is correlated with accessible volume (AV).

Acknowledgements

This research was supported by the Sustainable Energy and Education Research Center at the University of Tennessee, by a grant from the National Science Foundation (DGE-0801470). This research project used resources of the National Institute for Computational Sciences (NICS) supported by NSF under agreement number: OCI 07-11134.5.

References

- [1] Jain IP. Hydrogen the fuel for 21st century. *Int J Hydrog Energy*. 2009;34:7368-78.
- [2] Mandal TK, Gregory DH. Hydrogen: a future energy vector for sustainable development. *Proceedings of the Institution of Mechanical Engineers Part C-Journal of Mechanical Engineering Science*. 2010;224:539-58.
- [3] Kelly NA, Gibson TL, Cai M, Spearot JA, Ouwerkerk DB. Development of a renewable hydrogen economy: optimization of existing technologies. *Int J Hydrog Energy*. 2010;35:892-9.
- [4] Lee JY, Yoo M, Cha K, Lim TW, Hur T. Life cycle cost analysis to examine the economical feasibility of hydrogen as an alternative fuel. *Int J Hydrog Energy*. 2009;34:4243-55.
- [5] Elnashaie S, Chen ZX, Prasad P. Efficient production and economics of clean-fuel hydrogen. *International Journal of Green Energy*. 2007;4:249-82.
- [6] Lee KB, Beaver MG, Caram HS, Sircar S. Reversible chemisorption of carbon dioxide: simultaneous production of fuel-cell grade H₂ and compressed CO₂ from synthesis gas. *Adsorption-Journal of the International Adsorption Society*. 2007;13:385-97.
- [7] Nath K, Das D. Production and storage of hydrogen: Present scenario and future perspective. *Journal of Scientific & Industrial Research*. 2007;66:701-9.
- [8] Pasculete E, Condrea F, Radulescu C. Hydrogen and sustainable energy. Research for hydrogen production. *Environmental Engineering and Management Journal*. 2007;6:45-9.

- [9] Mantz RJ, De Battista H. Hydrogen production from idle generation capacity of wind turbines. *Int J Hydrog Energy*. 2008;33:4291-300.
- [10] Steinfeld A. Solar thermochemical production of hydrogen - a review. *Sol Energy*. 2005;78:603-15.
- [11] Lim KL, Kazemian H, Yaakob Z, Daud WRW. Solid-state Materials and Methods for Hydrogen Storage: A Critical Review. *Chemical Engineering & Technology*. 2010;33:213-26.
- [12] Fuel Cell Technologies Office Multi-Year Research, Development and Demonstration Plan. Available from: <http://www1.eere.energy.gov/hydrogenandfuelcells/mypp/> US Dept. of Energy, Energy Efficiency and Renewable Energy-Fuel Cell Technologies Office; Updated July 2013, Accessed November 2013.
- [13] Yang J, Sudik A, Wolverton C, Siegel DJ. High capacity hydrogen storage materials: attributes for automotive applications and techniques for materials discovery. *Chemical Society Reviews*. 2010;39:656-75.
- [14] Bushnell JE, Maitre P, Kemper PR, Bowers MT. Binding energies of Ti+(H₂)(1-6) clusters: Theory and experiment. *J Chem Phys*. 1997;106:10153-67.
- [15] Clark JC, Barnes CE. Reaction of the Si₈O₂₀(SnMe₃)₈ building block with silyl chlorides: A new synthetic methodology for preparing nanostructured building block solids. *Chemistry of Materials*. 2007;19:3212-8.
- [16] Clark JC, Saengkerdsub S, Eldridge GT, Campana C, Barnes CE. Synthesis and structure of functional spherosilicate building block molecules for materials synthesis. *Journal of Organometallic Chemistry*. 2006;691:3213-22.
- [17] Cordes DB, Lickiss PD, Rataboul F. Recent Developments in the Chemistry of Cubic Polyhedral Oligosilsesquioxanes. *Chemical Reviews*. 2010;110:2081-173.
- [18] Jaroentomeechai T, Yingsukkamol PK, Phurat C, Somsook E, Osotchan T, Ervithayasuporn V. Synthesis and Reactivity of Nitrogen Nucleophiles-Induced Cage-Rearrangement Silsesquioxanes. *Inorganic Chemistry*. 2012;51:12266-72.

- [19] Ghosh NN, Clark JC, Eldridge GT, Barnes CE. Building block syntheses of site-isolated vanadyl groups in silicate oxides. *Chemical Communications*. 2004:856-7.
- [20] McCabe C, Glotzer SC, Kieffer J, Neurock M, Cummings PT. Multiscale simulation of the synthesis, assembly and properties of nanostructured organic/inorganic hybrid materials. *Journal of Computational and Theoretical Nanoscience*. 2004;1:265-79.
- [21] Maiti A, Gee RH, Maxwell R, Saab AP. Hydrogen catalysis and scavenging action of Pd-POSS nanoparticles. *Chemical Physics Letters*. 2007;440:244-8.
- [22] Shanmugam N, Lee KT, Cheng WY, Lu SY. Organic-Inorganic Hybrid Polyaspartimide Involving Polyhedral Oligomeric Silsesquioxane via Michael Addition for CO₂ Capture. *Journal of Polymer Science Part a-Polymer Chemistry*. 2012;50:2521-6.
- [23] Xie KL, Jing LX, Zhao WG, Zhang YL. Adsorption Removal of Cu²⁺ and Ni²⁺ from Waste Water Using Nano-Cellulose Hybrids Containing Reactive Polyhedral Oligomeric Silsesquioxanes. *Journal of Applied Polymer Science*. 2011;122:2864-8.
- [24] Ren HB, Qin YC, Shang CW, Bi YT, Zhang L. Adsorption and Desorption Properties of Hybrid Aerogels Derived from MPMS-SSO at 77 K. *Rare Metal Materials and Engineering*. 2010;39:475-8.
- [25] Suraweera NS, Albert AA, Peretich ME, Abbott J, Humble JR, Barnes CE, et al. Methane and Carbon Dioxide Adsorption and Diffusion in Amorphous, Metal-Decorated Nanoporous Silica. *Molec Sim*. 2013;in press.
- [26] Press WH, Flannery BP, Teukolsky SA, Vetterling WT. *Numerical Recipes: The Art of Scientific Computing*. New York: Cambridge University Press; 1986.
- [27] Suraweera NS, Xiong RC, Luna JP, Nicholson DM, Keffer DJ. On the relationship between the structure of metal-organic frameworks and the adsorption and diffusion of hydrogen. *Molecular Simulation*. 2011;37:621-39.

- [28] Liu JW, Suraweera N, Keffer DJ, Cui ST, Paddison SJ. On the Relationship between Polymer Electrolyte Structure and Hydrated Morphology of Perfluorosulfonic Acid Membranes. *Journal of Physical Chemistry C*. 2010;114:11279-92.
- [29] Wang QF, Suraweera NS, Keffer DJ, Deng SX, Mays J. Atomistic and Coarse-Grained Molecular Dynamics Simulation of a Cross-Linked Sulfonated Poly(1,3-cyclohexadiene)-Based Proton Exchange Membrane. *Macromolecules*. 2012;45:6669-85.
- [30] Frost H, Duren T, Snurr RQ. Effects of surface area, free volume, and heat of adsorption on hydrogen uptake in metal-organic frameworks. *Journal of Physical Chemistry B*. 2006;110:9565-70.
- [31] Keffer DJ. Molecular Simulation Images from the Computational Materials Research Group at the University of Tennessee, Knoxville, TN. Available from: <https://trace.lib.utk.edu/home/davidkeffer/sites/atoms/animmn.html>. 2013.
- [32] Allen MP, Tildesley DJ. *Computer Simulation of Liquids*: Oxford Science Publications, Oxford; 1987.
- [33] Frenkel D, Smit B. *Understanding Molecular Simulation*: Academic Press, San Diego, CA; 1996.
- [34] Jhung SH, Yoon JW, Kim HK, Chang JS. Low temperature adsorption of hydrogen on nanoporous materials. *Bulletin of the Korean Chemical Society*. 2005;26:1075-8.
- [35] Basmadjian D. Adsorption Equilibria of Hydrogen, Deuterium, and Their Mixtures .1. *Canadian Journal of Chemistry-Revue Canadienne De Chimie*. 1960;38:141-8.
- [36] Freeman MP. The Quantum Mechanical Correction for the High Temperature Van Der Waals Interaction of Light Gases and Surfaces- A New Method of Determining Surface Area. *Journal of Physical Chemistry*. 1960;64:32-7.
- [37] Wang QY, Johnson JK. Molecular simulation of hydrogen adsorption in single-walled carbon nanotubes and idealized carbon slit pores. *J Chem Phys*. 1999;110:577-86.

- [38] Feynman RP. *Statistical Mechanics: A Set Of Lectures*. . Reading MA: W. A. Benjamin; 1972.
- [39] Feynman RP. *Quantum Mechanics and Path Integrals*. New York: McGraw-Hill Companies; 1965.
- [40] Feynman RP. Space-Time Approach to Non-Relativistic Quantum Mechanics. *Reviews of Modern Physics*. 1948;20:367-87.
- [41] Liu JC, Culp JT, Natesakhawat S, Bockrath BC, Zande B, Sankar SG, et al. Experimental and theoretical studies of gas adsorption in Cu-3(BTC)(2): An effective activation procedure. *Journal of Physical Chemistry C*. 2007;111:9305-13.
- [42] Liu J, Lee JY, Pan L, Obermyer RT, Simizu S, Zande B, et al. Adsorption and diffusion of hydrogen in a new metal-organic framework material: [Zn(bdc)(ted)(0.5)]. *Journal of Physical Chemistry C*. 2008;112:2911-7.
- [43] Johnson JK, Zollweg JA, Gubbins KE. The Lennard-Jones Equation of State Revisited. *Molecular Physics*. 1993;78:591-618.
- [44] Buch V. Path-Integral Simulations of Mixed Para-D2 and Ortho-D2 Clusters: The Orientational Effects. *J Chem Phys*. 1994;100:7610-29.
- [45] Rappe AK, Casewit CJ, Colwell KS, Goddard WA, Skiff WM. Uff, a Full Periodic-Table Force-Field for Molecular Mechanics and Molecular-Dynamics Simulations. *Journal of the American Chemical Society*. 1992;114:10024-35.
- [46] Prausnitz JM, Lichtenthaler RN, Avezedo EG. *Molecular Thermodynamics of Fluid-Phase Equilibria*. New Jersey: Prentice-Hall International Series; 1998.
- [47] Garberoglio G, Skoulidas AI, Johnson JK. Adsorption of gases in metal organic materials: Comparison of simulations and experiments. *Journal of Physical Chemistry B*. 2005;109:13094-103.

- [48] Frisch MJ, Trucks GW, Schlegel HB, Scuseria GE, Robb MA, Cheeseman JR, et al. Gaussian 03, Revision C.02. Gaussian, Inc., Wallingford CT2004.
- [49] Chiacchio MA, Borrello L, Di Pasquale G, Pollicino A, Bottino FA, Rescifina A. Synthesis of functionalized polyhedral oligomeric silsesquioxane (POSS) macromers by microwave assisted 1,3-dipolar cycloaddition. *Tetrahedron*. 2005;61:7986-93.
- [50] Tuckerman M, Berne BJ, Martyna GJ. Reversible Multiple Time Scale Molecular-Dynamics. *J Chem Phys*. 1992;97:1990-2001.
- [51] Nose S. A Molecular-Dynamics Method for Simulations in the Canonical Ensemble. *Molecular Physics*. 1984;52:255-68.
- [52] Hoover WG. Canonical Dynamics- Equilibrium Phase-Space Distributions. *Physical Review A*. 1985;31:1695-7.
- [53] Sasamori R, Okaue Y, Isobe T, Matsuda Y. Stabilization of Atomic-Hydrogen in Both Solution and Crystal at Room-Temperature. *Science*. 1994;265:1691-3.
- [54] Liu B, Yang QY, Xue CY, Zhong CL, Smit B. Molecular simulation of hydrogen diffusion in interpenetrated metal-organic frameworks. *Physical Chemistry Chemical Physics*. 2008;10:3244-9.

Appendix B: Tables and Figures

Table 3.1. Structural details for selected spherosilicate structures

Structure	Number of groups in a 50×50×50 Å ³ simulation box				Volume fraction	Density (g/cc)	Accessible Volume		Surface Area	
	Cubes	Bridges	TiCl ₃	TMS			(cm ³ /g)	Å ³ per simulation box	(m ² /g)	Å ² per simulation box
0 % -OTiCl ₃ low density	40	41	0	248	0.73	0.59	1.23	90800	4810	35500
50 % -OTiCl ₃ low density	40	41	124	124	0.74	0.72	1.02	92100	4090	37000
100 % -OTiCl ₃ low density	40	41	248	0	0.75	0.86	0.88	94200	3350	35900
0 % -OTiCl ₃ medium density	50	51	0	308	0.66	0.73	0.90	82400	4790	44000
50 % -OTiCl ₃ medium density	50	51	154	154	0.67	0.90	0.75	84400	3990	44900
100 % -OTiCl ₃ medium density	50	51	308	0	0.69	1.07	0.65	86800	3320	44200
0 % -OTiCl ₃ high density	60	61	0	368	0.59	0.88	0.68	74400	4680	51400
50 % -OTiCl ₃ high density	60	61	184	184	0.61	1.08	0.57	76500	3970	53400
100 % -OTiCl ₃ high density	60	61	368	0	0.64	1.27	0.50	79500	3270	52000

Table 3.2. The Lennard-Jones parameters for the atoms in the frameworks of the sphaerosilicate structures.

Atom	σ (Å)	ϵ/k (K)
H	2.571	22.142
C	3.431	52.839
O	3.118	30.194
Si	3.826	202.43
Cl	3.516	114.31
Ti	2.829	8.5604

Table 3.3. Self-Diffusivity and Activation Energies

Structure	Temperature (K)	Diffusivity (10^{-7} m ² /s)	Standard Deviation (10^{-7} m ² /s)	Average of square root of mean square displacement (Å)	Activation Energy (kcal/mol)
0 % -OTiCl ₃ low density	300	3.60	0.98	265	0.850
	400	5.05	1.38	315	
	500	6.33	2.03	351	
	600	7.34	2.11	380	
50 % -OTiCl ₃ low density	300	2.57	0.74	226	0.798
	400	3.57	1.09	264	
	500	4.28	1.25	290	
	600	5.10	1.53	316	
100 % -OTiCl ₃ low density	300	3.99	2.50	269	0.712
	400	5.41	3.35	314	
	500	6.52	4.25	344	
	600	7.20	4.70	361	
0 % -OTiCl ₃ medium density	300	1.82	0.35	190	0.861
	400	2.61	0.51	227	
	500	3.18	0.60	251	
	600	3.80	0.75	274	
50 % -OTiCl ₃ medium density	300	1.50	0.60	170	0.803
	400	2.08	1.07	200	
	500	2.50	1.29	219	
	600	2.98	1.50	239	
100 % -OTiCl ₃ medium density	300	2.07	1.65	186	0.812
	400	2.72	2.18	213	
	500	3.32	2.67	235	
	600	4.19	3.46	262	
0 % -OTiCl ₃ high density	300	0.93	0.41	134	0.861
	400	1.36	0.63	161	
	500	1.62	0.74	177	
	600	1.94	0.93	193	
50 % -OTiCl ₃ high density	300	0.47	0.19	95	0.775
	400	0.66	0.24	113	
	500	0.77	0.28	123	
	600	0.91	0.31	134	
100 % -OTiCl ₃ high density	300	1.01	0.86	128	0.755
	400	1.40	1.16	151	
	500	1.67	1.40	165	
	600	1.91	1.57	177	

Table 3.4. Correlation factors for the relationship of self-diffusivity (at 300 K) and activation energy with surface area, accessible volume and adsorbate-framework energy (at 300 K and 1 bar)

Property 1	Property 2	Correlation Coefficient
Self- Diffusivity	Accessible Volume	0.92
Self- Diffusivity	Surface Area	-0.95
Self- Diffusivity	Adsorbate Framework Energy	0.63
Activation Energy	Accessible Volume	-0.30
Activation Energy	Surface Area	0.06
Activation Energy	Adsorbate Framework Energy	-0.67

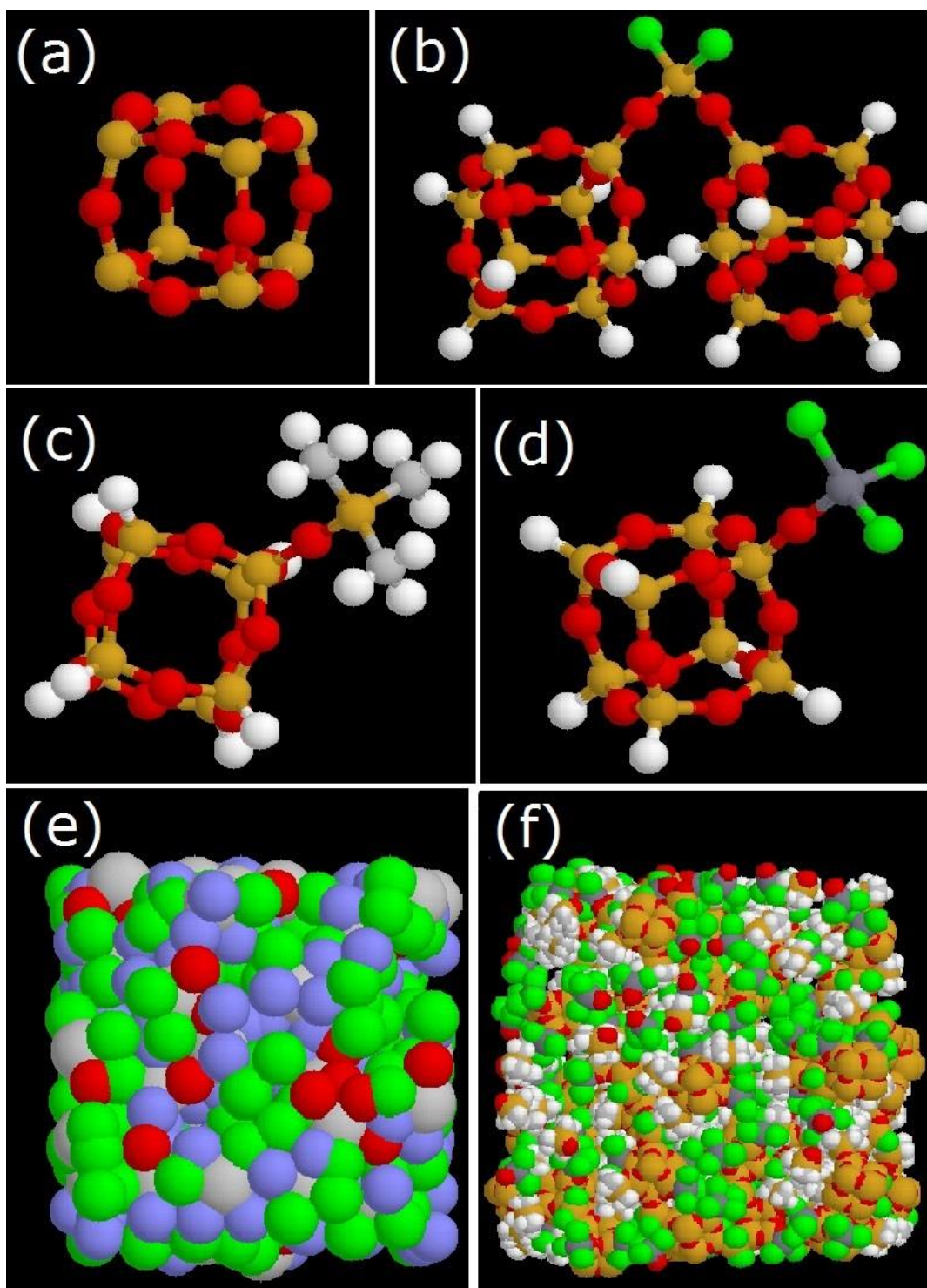


Figure 3.1. (a) spherosilicate cube, (b) O_2SiCl_2 bridge, (c) $-OSiMe_3$ end group and (d) $-OTiCl_3$ end group. (e) Course grain structure (Cubes: grey, bridges: red, $-OTiCl_3$:green, $-OSiMe_3$: blue) (f) Atomic structure. (Cl-green, Ti-dark grey, Si-yellow/orange, O-red, C-light grey, H- white)

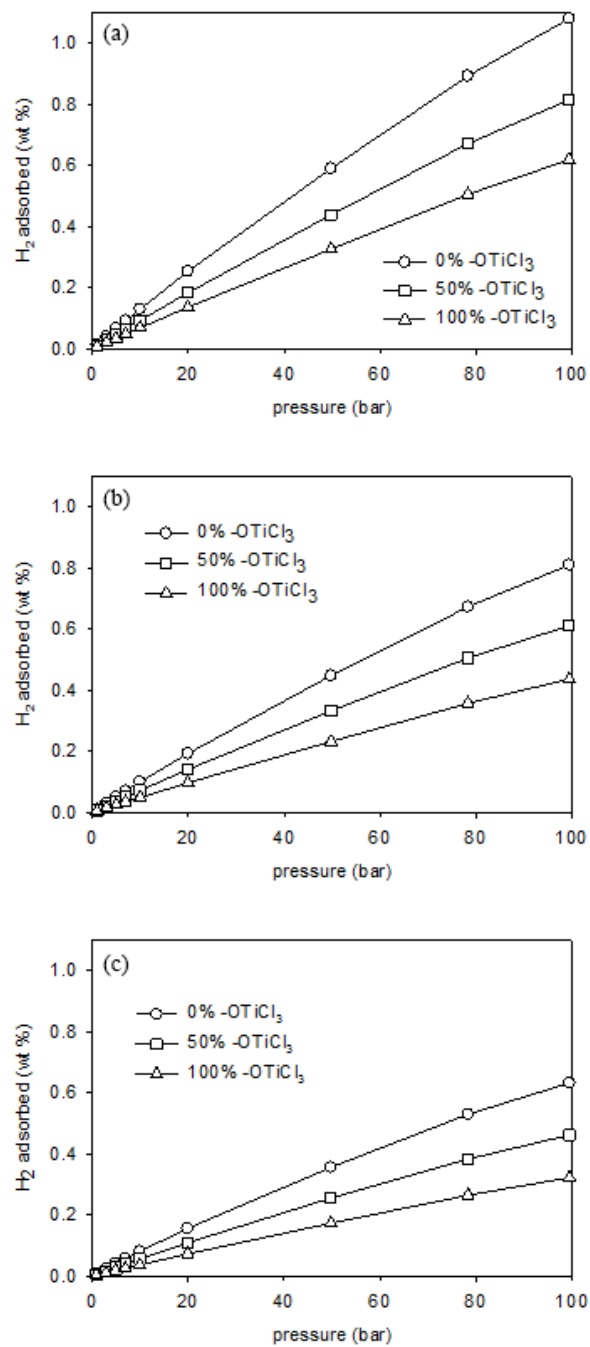


Figure 3.2. Gravimetric H₂ adsorption isotherms at 300 K (a) low density structure.(b) middle density structure.(c)high density structure.

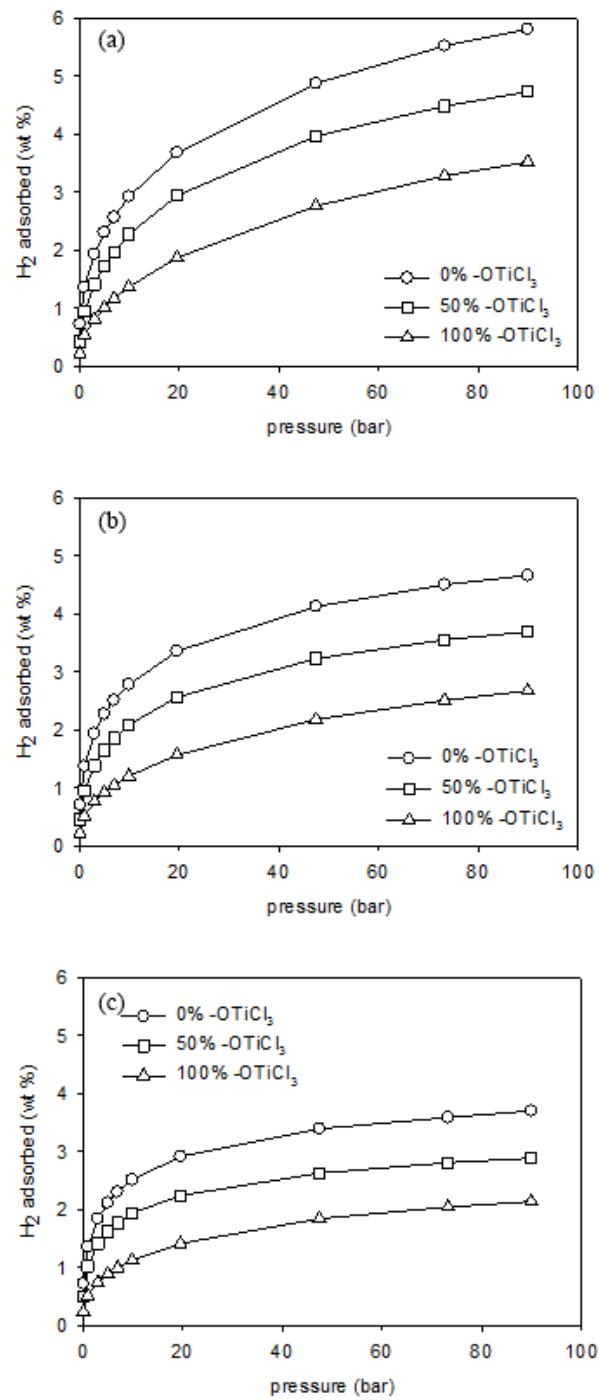


Figure 3.3. Gravimetric H₂ adsorption isotherms at 77 K (a) low density structure.(b) middle density structure.(c)high density structure.

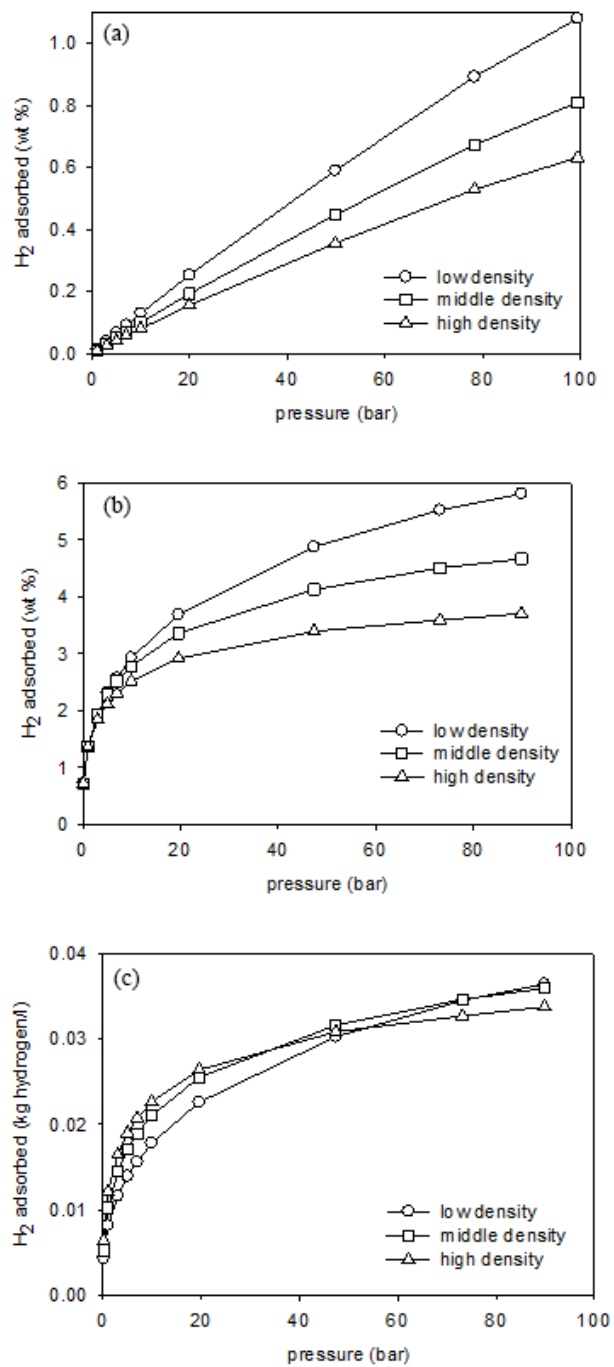


Figure 3.4. H₂ adsorption isotherms for 0 % -OTiCl₃ structure (a) Gravimetric H₂ adsorption isotherms at 300 K.(b) Gravimetric H₂ adsorption isotherms at 77 K.(c) Volumetric H₂ adsorption isotherms at 77 K.

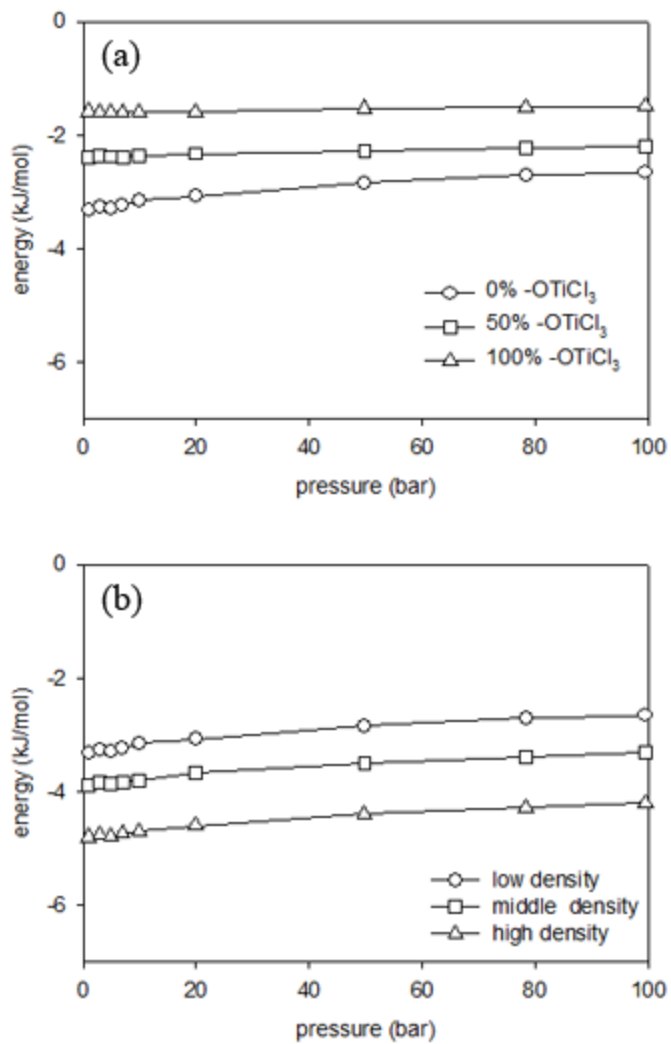


Figure 3.5. Energy between H₂ and framework at 300 K (a) low density structure (b) for 0 % - OTiCl₃ structure

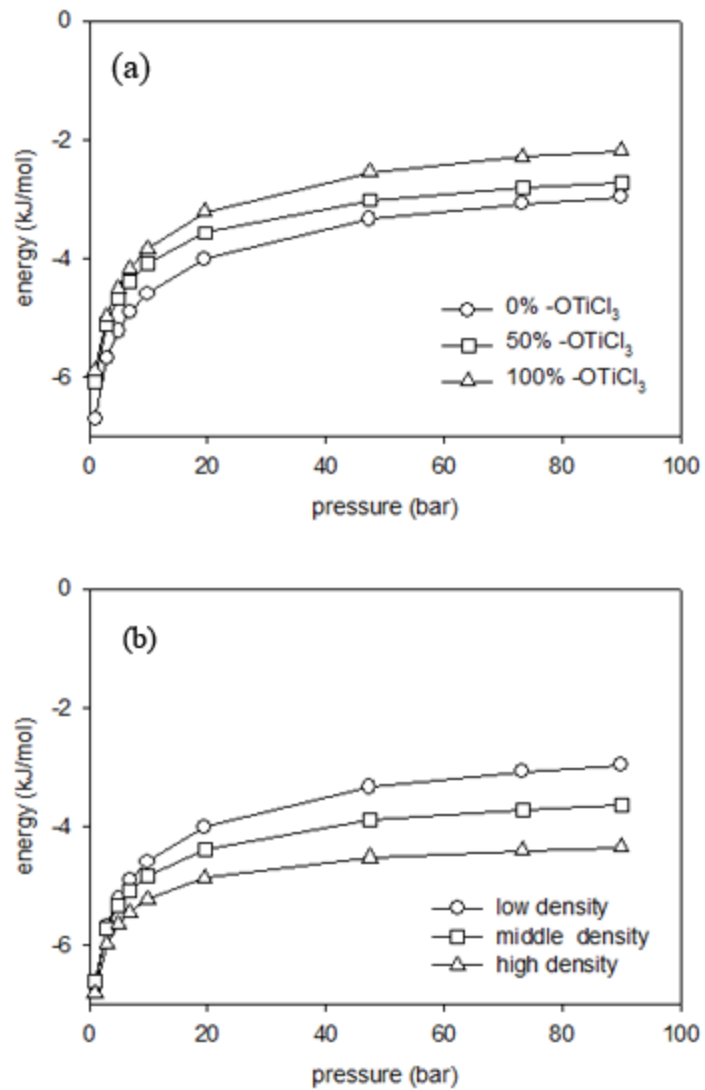


Figure 3.6. Energy between H₂ and framework at 77 K (a) low density structure (b) for 0 % - OTiCl₃ structure

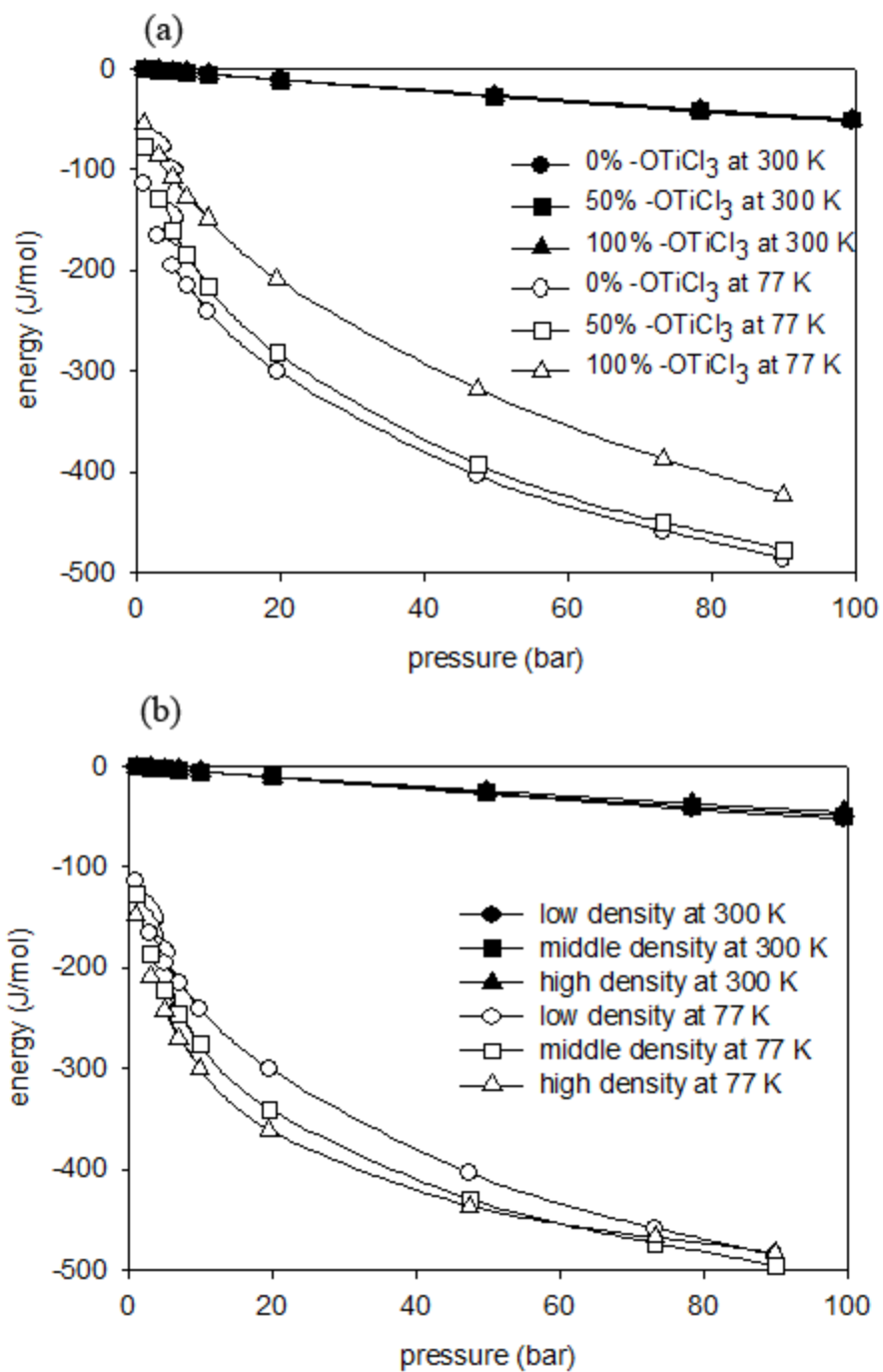


Figure 3.7. Energy between adsorbed H₂ (a) low density structures (b) for 0 % -OTiCl₃ structure.

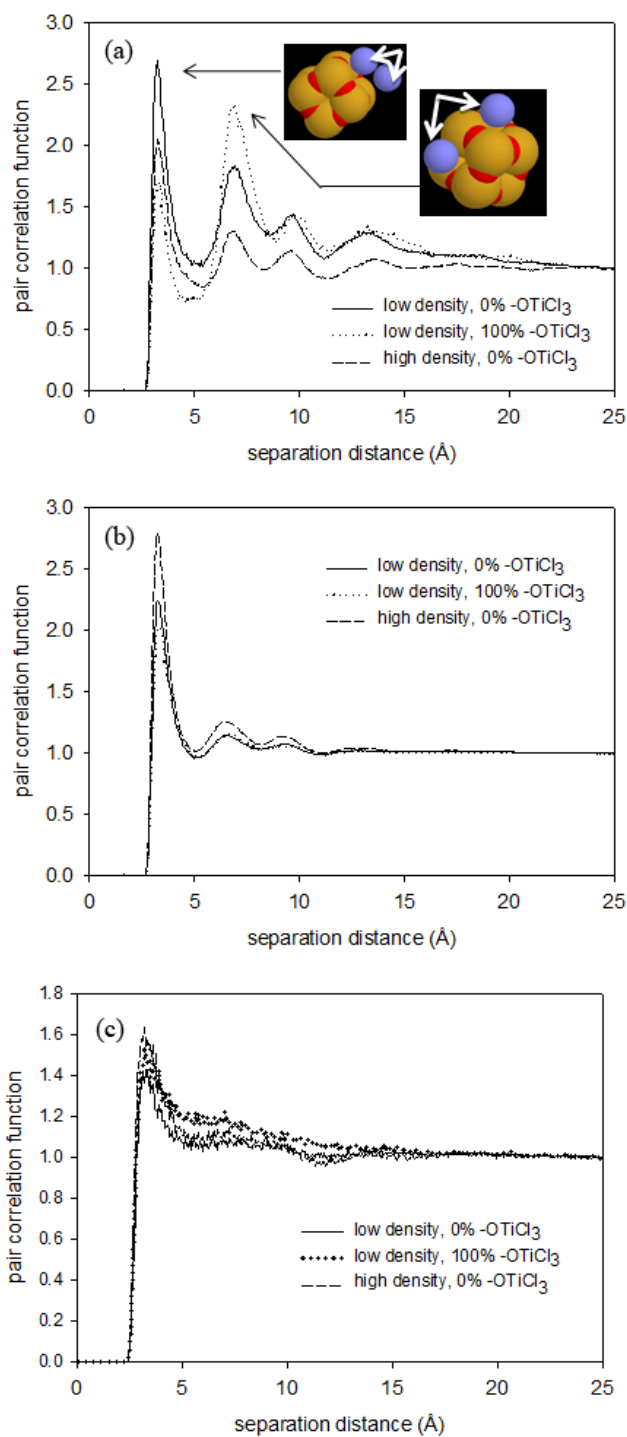


Figure 3.8. Pair correlation function between H₂-H₂. (a) at 77 K and 1 bar, (b) at 77 K and 100 bar, (c) at 300 K and 100 bar.

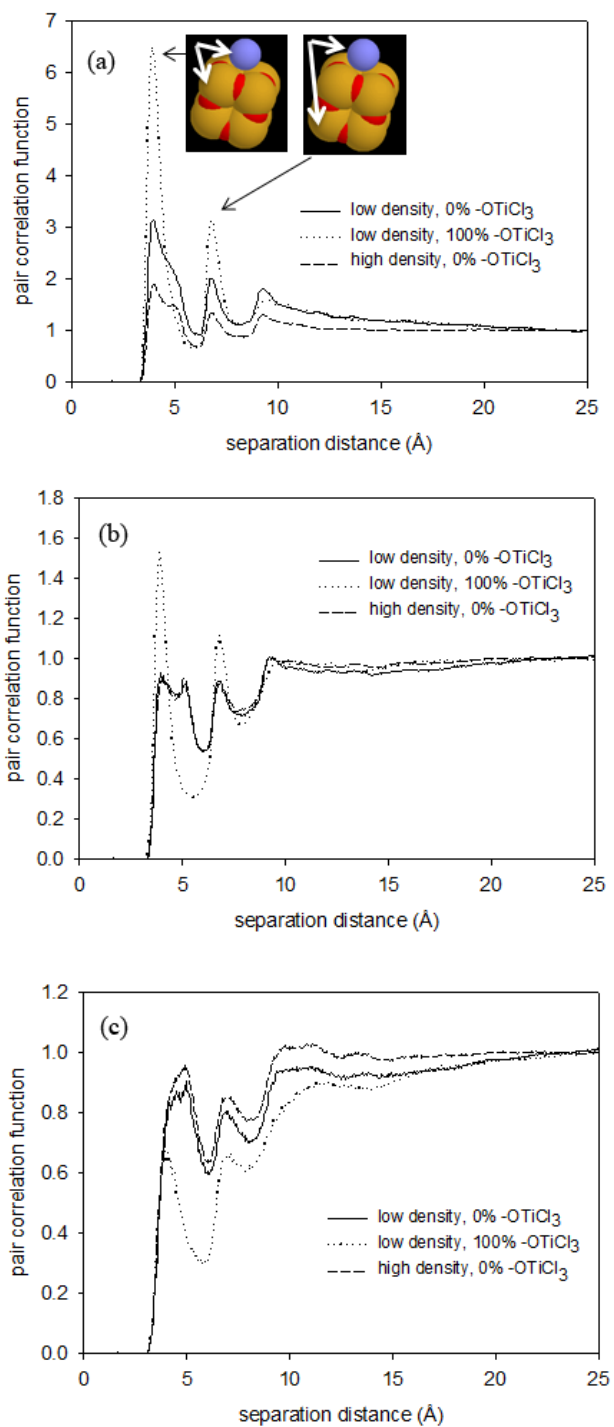


Figure 3.9. Pair correlation function between H₂-Si. (a) at 77 K and 1 bar, (b) at 77 K and 100 bar, (c) at 300 K and 100 bar.

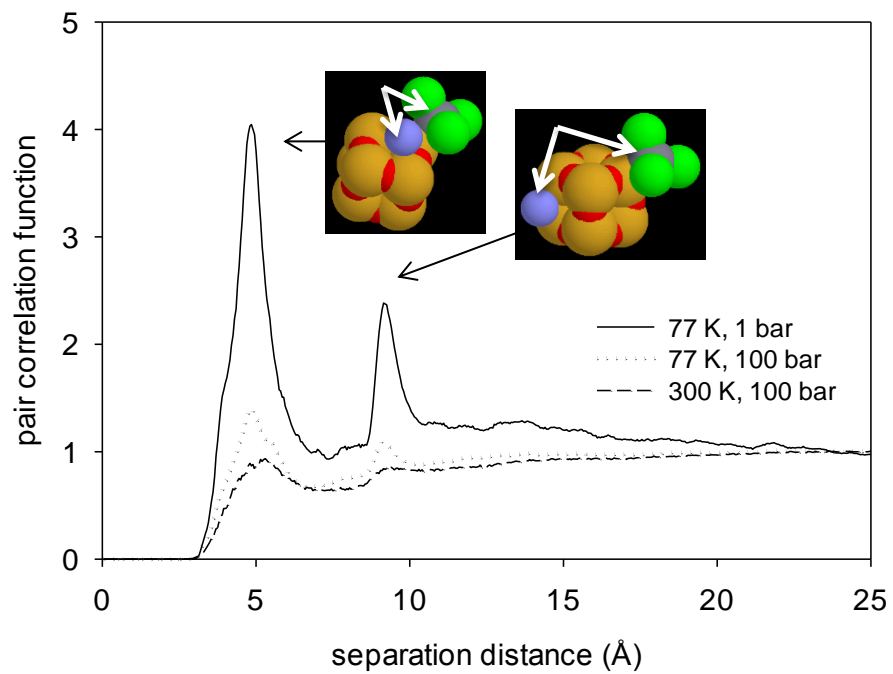


Figure 3.10. Pair correlation function between H₂-Ti for low density 100% -OTiCl₃ structure.

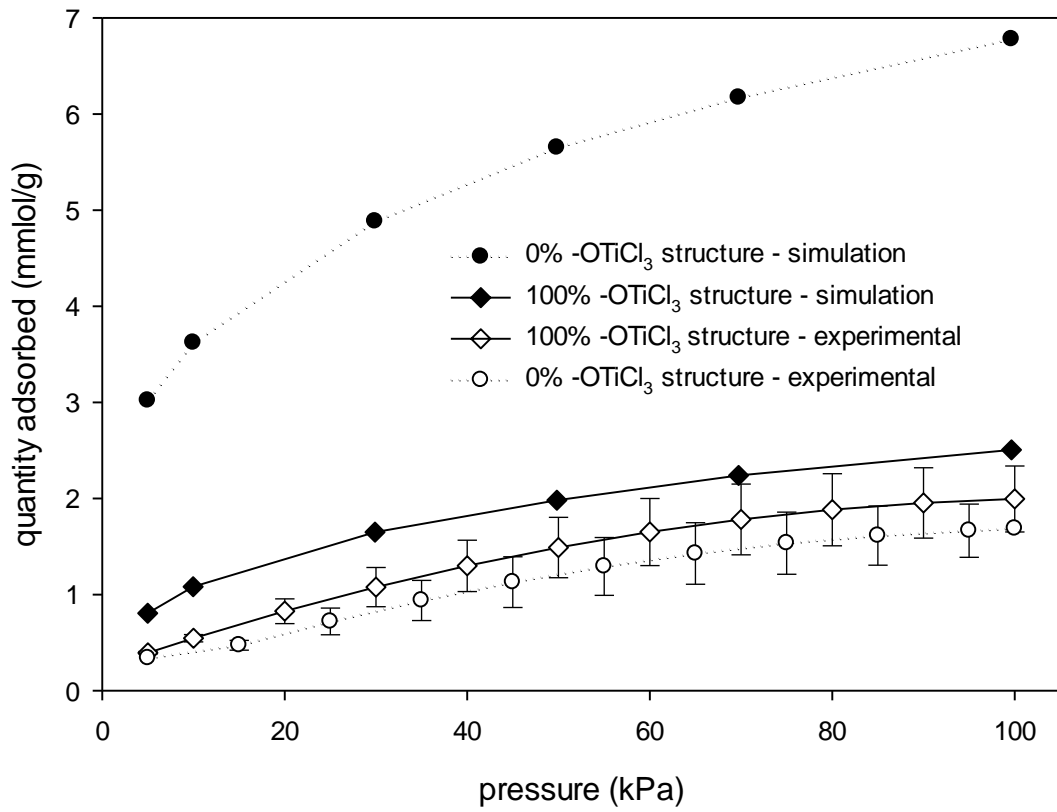


Figure 3.11. Experimental and Simulation Isotherms comparison.

Appendix C: Supplementary Document

C1. Thermodynamics considerations for Adsorption of Hydrogen

Adsorption of hydrogen in the various adsorbents as a function of temperature and pressure can be understood in terms of the competition between energetic and entropic contributions to the free energy.

$$\Delta A_{ads} = \Delta U_{ads} - T\Delta S_{ads} \quad (1)$$

The distribution of molecules between the bulk and adsorbed (*ads*) phases can be expressed by:

$$\frac{N_{ads}}{N_{bulk}} = \exp\left(-\frac{\Delta A_{ads}}{k_B T}\right) = \exp\left(\frac{\Delta S_{ads}}{k_B}\right) \exp\left(-\frac{\Delta U_{ads}}{k_B T}\right) \quad (2)$$

The term $-T\Delta S_{ads}$ in equation (1), the entropic contribution to the free energy of adsorption, diminishes as temperature decreases. There is only an energetic effect in the limit of absolute zero temperature. There is only an entropic effect in the limit of infinite temperature. The behavior shifts from one limit to the other, between these asymptotes. The energetic effect is captured by the energy of adsorption while the entropic effect is captured by the accessible volume of the structures.

This behavior can also be understood as a function of pressure. There is little adsorbate fluid in the pores at low pressure and when the loading increases, the ability for molecules to pack within the pore space (an entropic contribution) becomes relevant. Hence, as the pressure increases, a decrease in importance of the energetic effect and an increase in the importance of the entropic effect are observed. Same behavior has been shown for simple fluids in idealized pores*.

The competition between energetic and entropic effects can explain the relative preference for adsorption among pores of different sizes and shapes. Small pores have

energetically deeper wells (due to more overlap of adsorbate-framework interactions) and greater confinement. Large pores have energetically shallower wells and less confinement. Thus the energetic effects favor small pores and the entropic effects favor large pores. The relative preference for a given pore is determined by the balance between them.

*Keffer, D., H.T. Davis, and A.V. McCormick, *The effect of nanopore shape on the structure and isotherms of adsorbed fluids*. Adsorption-Journal of the International Adsorption Society, 1996. **2**(1): p. 9-21.

C2. Figures

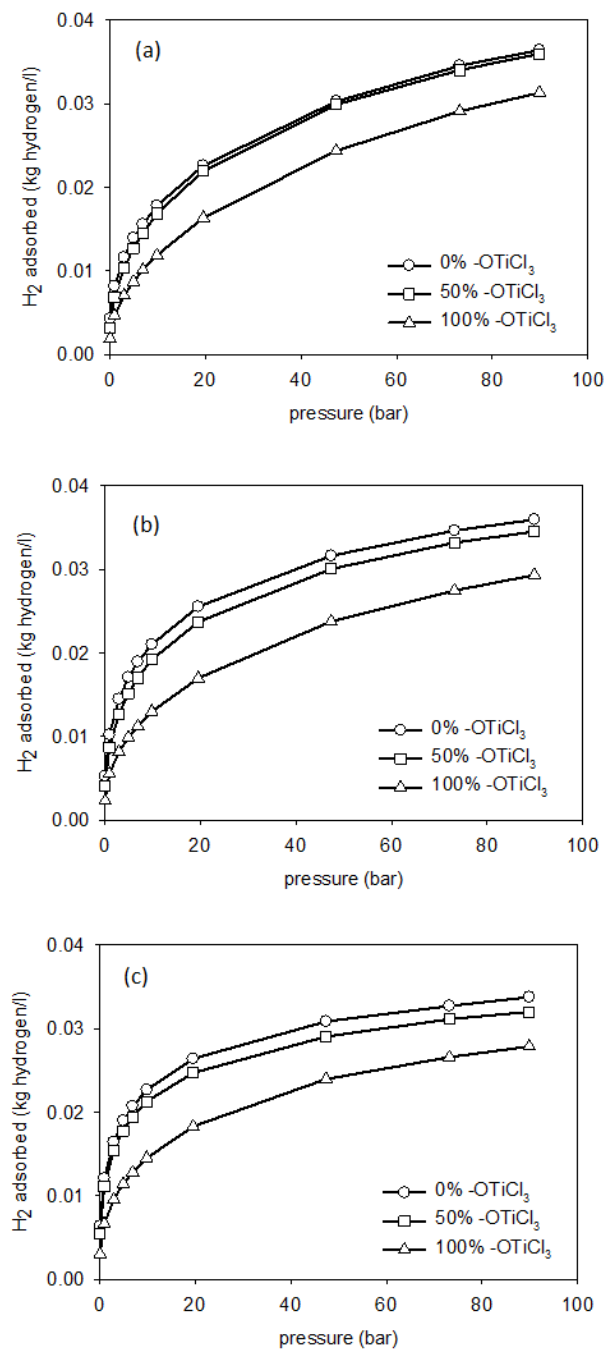


Figure 3.S1 Volumetric H₂ adsorption isotherms at 77 K (a) low density structure.(b) middle density structure.(c) high density structure.

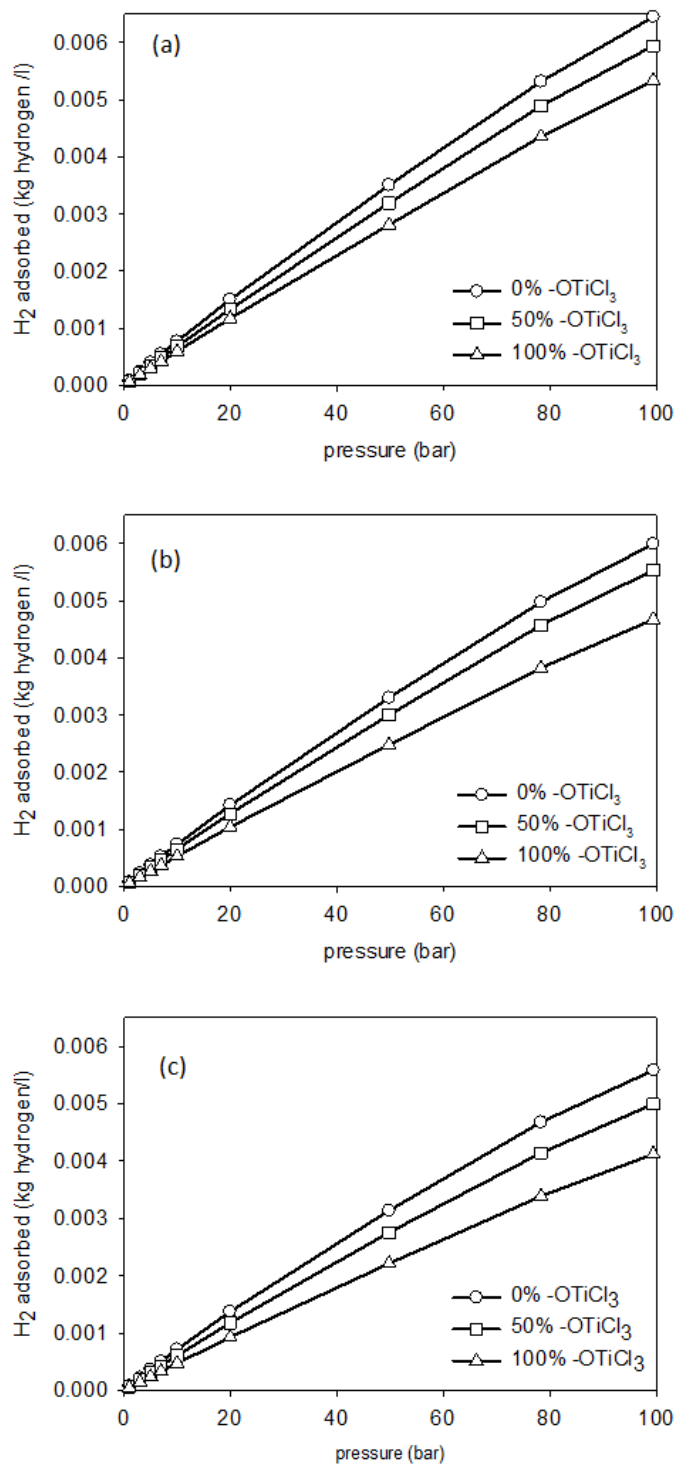


Figure 3.S2 Volumetric H₂ adsorption isotherms at 300 K (a) low density structure.(b) middle density structure.(c) high density structure.

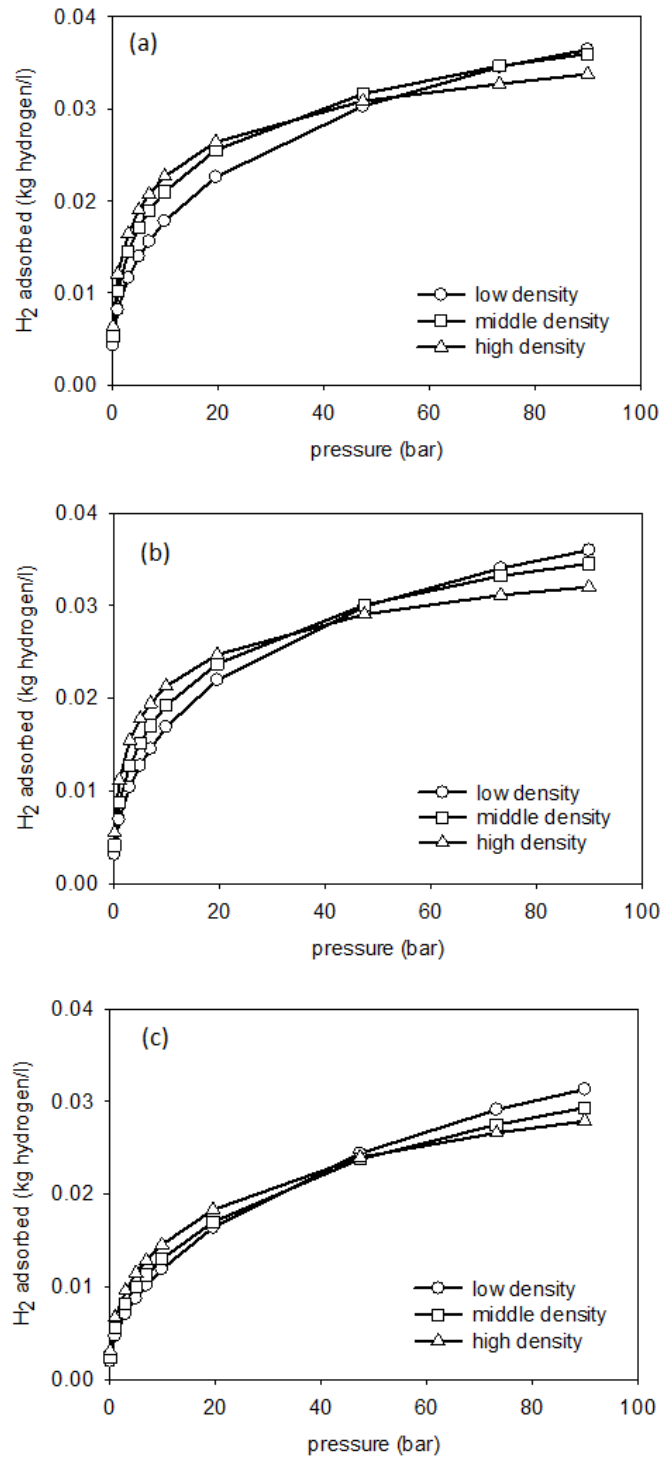


Figure 3.S3 Volumetric H_2 adsorption isotherms at 77 K (a) for 0 % $TiCl_3$ structure (b) for 50 % $TiCl_3$ structure (c) for 100 % $TiCl_3$ structure.

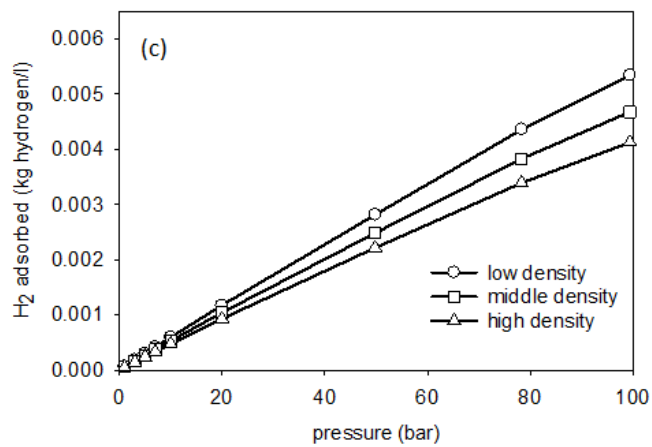
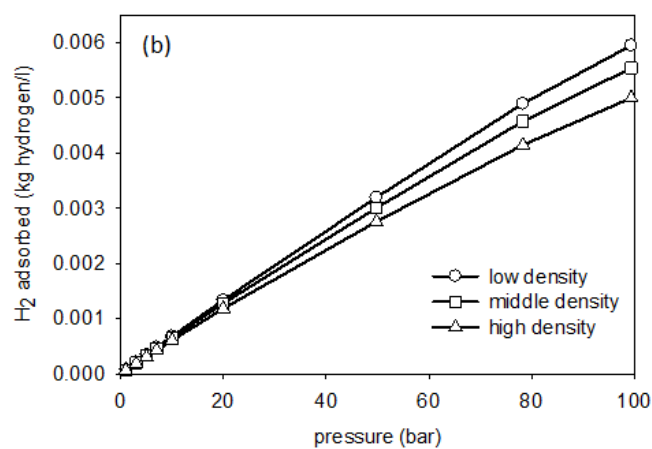
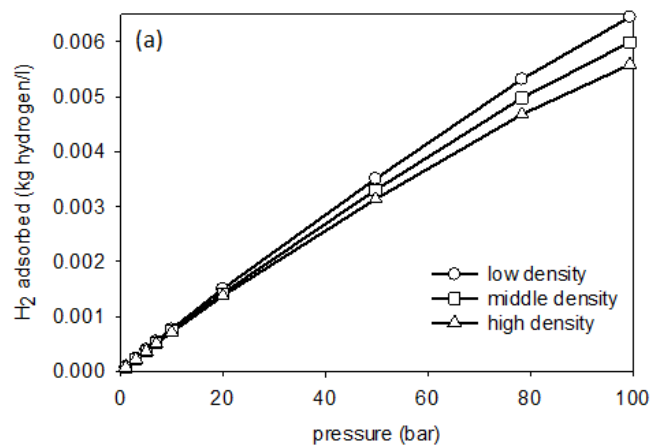


Figure 3.S4 Volumetric H₂ adsorption isotherms at 300 K for 0 % TiCl₃ structure (a) for 50 % TiCl₃ structure (b) for 100 % TiCl₃ structure (c)

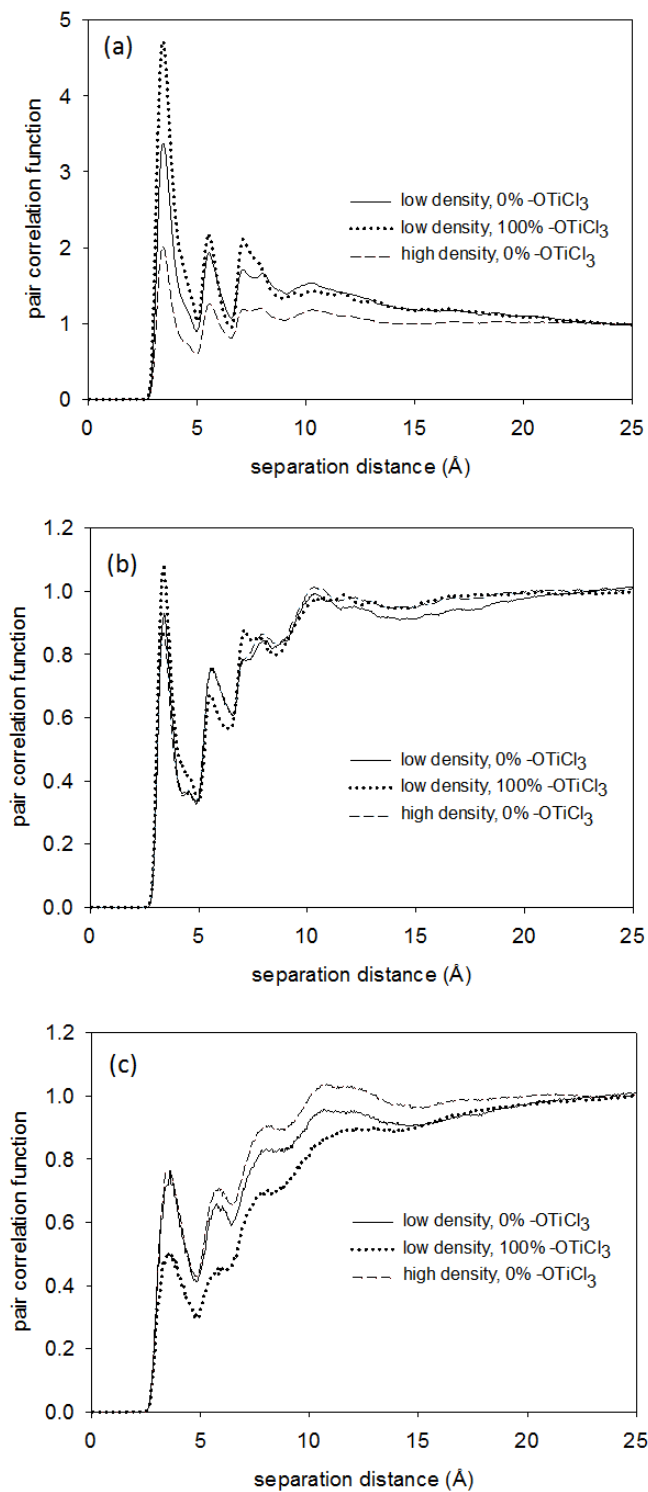


Figure 3.S5 Pair correlation function between H₂-O. (a) at 77 K and 1 bar, (b) at 77 K and 100 bar, (c) at 300 K and 100 bar.

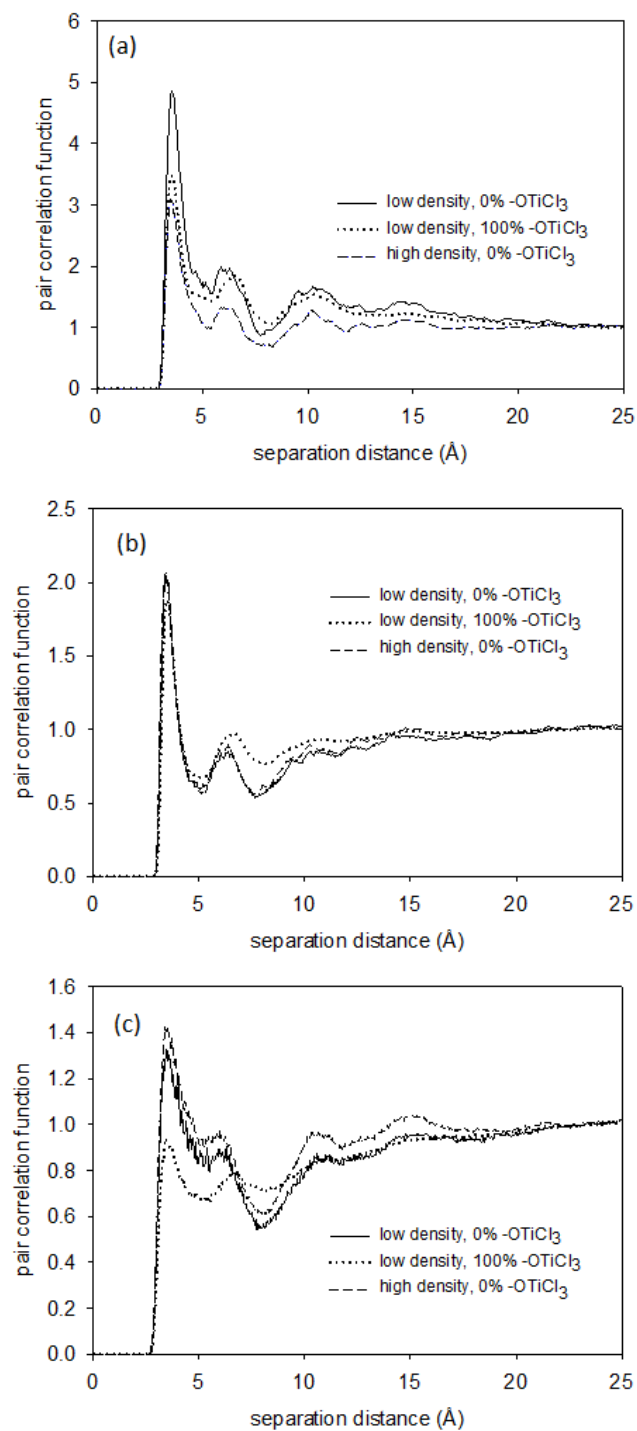


Figure 3.S6 . Pair correlation function between H₂-Cl. (a) at 77 K and 1 bar, (b) at 77 K and 100 bar, (c) at 300 K and 100 bar.

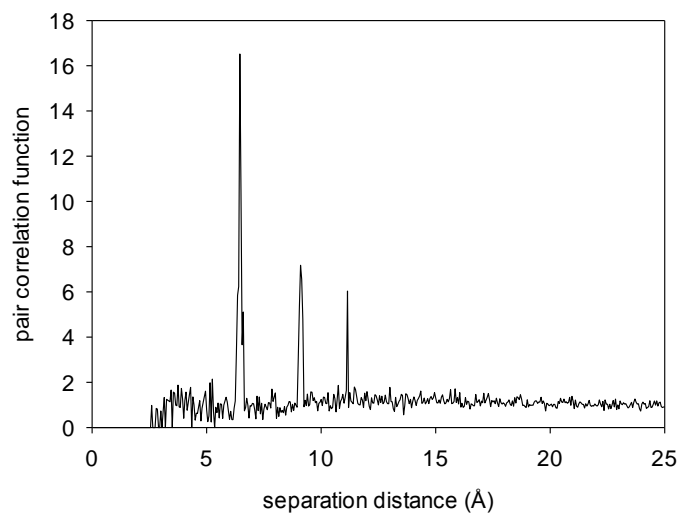


Figure 3.S7 Pair correlation function between Ti-Ti for low density 100% -OTiCl₃ structure.

CHAPTER 4

Methane and Carbon Dioxide Adsorption and Diffusion in Amorphous, Metal- Decorated Nano-Porous Silica

This chapter is a slightly revised version of a paper by the same title accepted by *Journal of Molecular Simulations* in 05/2013 by **Nethika S. Suraweera**, A.A. Albert, M.E. Peretich, J. Abbott, J.R. Humble, C.E. Barnes and D.J. Keffer:

Suraweera, N.S., Albert, A.A., Peretich, M.E., Abbott, J., Humble, J.R., Barnes, C.E., Keffer, D.J., “Methane and Carbon Dioxide Adsorption and Diffusion in Amorphous, Metal-Decorated Nanoporous Silica”, *Molec. Simul.*, **in press**, 05/2013

The use of “we” in this part refers to the co-authors and the author of this dissertation. My primary contributions to this paper include (1) all of the simulation work (2) analysis of data, and (3) most of the writing

Reproduced with permission from *Molec. Simul.* 2013. Copyright © Taylor and Francis, 2013.

Abstract

The adsorptive and diffusive behavior of methane and carbon dioxide in amorphous nanoporous adsorbents composed of spherosilicate building blocks, in which isolated metal sites have been distributed, is examined. The adsorbent contains cubic silicate building blocks (spherosilicate units: Si_8O_{20}), which are cross-linked by SiCl_2O_2 bridges and decorated with either $-\text{OTiCl}_3$ or $-\text{OSiMe}_3$ groups off of the other cube corners. The model structures were generated to correspond to experimentally synthesized materials, matching physical properties including density, surface area, and accessible volume. It is shown that both methane and carbon dioxide adsorb via physisorption only in the modeled materials. Adsorption isotherms and energies at 300 K for pressures up to 100 bar were generated via molecular simulation. The maximum gravimetric capacity of CH_4 is 16.9 wt%, occurring at 300 K and 97 bar. The maximum gravimetric capacity of CO_2 is 50.3 wt%, occurring at 300 K and 51.6 bar. The best performing adsorbent was a low density (high accessible volume) material with no $-\text{OTiCl}_3$ groups. The presence of $-\text{OTiCl}_3$ did not enhance physisorption even on a volumetric basis, and the high molecular weight of $-\text{OTiCl}_3$ groups is a significant penalty on a gravimetric basis. Based on the pair correlation functions, the most favorable adsorption sites for both adsorbates are located in front of the faces of spherosilicate cubes. The self-diffusivity and activation energy for diffusion are also reported.

Keywords: Grand Canonical Monte Carlo simulation; spherosilicate; metal decorated silica; physisorption.

4.1 Introduction

The burning of non-renewable fossil fuels as an energy source produces a steady increase of carbon dioxide in the atmosphere with uncertain but potentially significant impacts on global ecosystems [1]. Numerous solutions for mitigating the impact of CO₂ are being investigated including capture and storage of CO₂ [2-4]. Development of new, cost-effective, advanced technologies for CO₂ sequestration remains a challenge. Porous materials are continually being tested to optimize as efficient adsorbents and storage media for CO₂ [5-7].

At the same time, identifying and developing new, cleaner and sustainable energy sources is a current on-going research topic. Utilization of natural gas (NG) [8, 9] and hydrogen [10-12] as cleaner fuels are continually being investigated. Even though NG produces CO₂, it is comparatively less than that from other fossil fuels. The bottleneck for commercialization of these fuels in automobiles is the lack of efficient methods to separate, capture and store these energy carriers. Storage of energy-related gases in porous materials has been investigated in a variety of materials [13, 14]. Compressed natural gas (CNG) vehicles already exist but the gas is stored in high-pressure (greater than 200 atm) tanks, which are an explosive hazard and add extra weight to vehicles. To address the need for better methane-storage technologies, the US DOE has set the target for methane storage systems at 180 v(STP)/v(STP equivalent of methane per volume of adsorbent material storage system) under 35 bar and near ambient temperature [15]. Current research has been able to develop porous materials that can absorb CH₄ even beyond these targets [16].

There remains interest in developing low-cost but high-performance adsorbents for both carbon sequestration and energy storage applications. The amorphous metal-decorated nanoporous silica adsorbents investigated here were motivated by quantum mechanical studies done by Bushnell *et al.* [17] showing that there exist favorable binding energies for adsorption and desorption of gases in the structures with isolated Ti centers. The calculated binding energies fell between those associated with physisorption and chemisorptions, implying strong but reversible adsorption. In order to test this effect a synthetic strategy was developed to make porous spherosilicate matrices that contain isolated titanium metal centers [18, 19]. These spherosilicate materials have an inorganic cross-linked polymer-like structure and atomically dispersed -OTiCl₃ groups that approximate isolated metal centers. While in a reduced state, the

Ti metal centers predicted to bind hydrogen, as described by Bushnell *et al.* [17]. In an oxidized state, the Ti metal centers appear as $-\text{OTiCl}_3$, which may still impact the adsorption of gases. The amorphous spherosilicate matrix provides a nanoporous, high-surface-area support to the structure.

The framework of these adsorbents is composed of spherosilicate or silsesquioxane units, cage-like structures in the shape of cubes, hexagonal prisms, octagonal prisms, and decagonal or dodecagonal prisms [20, 21]. In this study we consider cubical polyhedral oligomeric silsesquioxanes (POSS), comprised of 8 Si atoms, with formula $(\text{RSiO}_{1.5})_8$ where R is either a functional ending group or a cross linker which is connected to another spherosilicate unit. They belong to the family of polycyclic compounds consisting of silicon–oxygen bonds and the ability to incorporate numerous elements throughout the periodic table has been experimentally reported [18, 19]. Applications are being developed for the metal–POSS compounds as metal catalyst supports [22]. Theoretical modeling studies have been previously done by McCabe *et al.* for POSS systems [23].

POSS structures have been studied for their adsorption capability. An organic–inorganic hybrid porous polymer namely polyaspartimide (PAI) was tested as a solid CO_2 adsorbent by Shanmugam *et al.*[24]. Adsorption of copper and nickel ions in aqueous solution using nanocellulose hybrids containing R-POSS, as a novel biosorbent was studied by Xie *et al.* [25]. Hongbo *et al.* observed strong adsorption energies between N_2 molecules, resulting in high adsorptive capacities in the study of adsorption and desorption properties of hybrid aerogels derived from methacryloxypropyltrimethoxysilane based silsesquioxane [26]. Maiti *et al.* investigated hydrogen catalysis and sequestration in Pd-POSS systems [27].

The class of adsorbents studied in this work have been synthesized in a manner in which the surface area and free volume of the silica matrix and amount of titanium present (as $-\text{OTiCl}_3$) in the material can be controlled [18, 19, 22]. A family of cross-linked matrices of silicate cubes has been prepared according to published procedures. Briefly, the tin functionalized cube, $\text{Si}_8\text{O}_{20}(\text{SnMe}_3)_8$ is reacted with SiCl_4 to produce an amorphous matrix of Si_8O_{20} cubes randomly linked together by a variety of $\text{SiCl}_{4-x}\text{O}_x$ groups (Figure 4.1(a)). The number of cross links can be controlled by the stoichiometric ratio of tin cube to SiCl_4 and was adjusted to obtain an average of 2.5 bonds to different cubes from a linking silicon center. The

average number of trimethyl tin groups left in the matrix at this stage is $\sim 2.0/\text{cube}$. These could be quantitatively exchanged for trimethylsilyl (TMS) or TiCl_3 groups through exposure to the chloride reagents, ClSiMe_3 or TiCl_4 , respectively (Figure 4.1(b)). The surface areas for the TMS and TiCl_3 containing matrices were measured (BET analysis, N_2 adsorption) and found to be 566 and 621 m^2/g respectively and the pore volumes found to be 0.638 and 0.648 cm^3/g respectively. In this paper we report the results of molecular-level simulations to study physisorption of CO_2 and CH_4 in these materials.

4.2 Simulation Methods

4.2.1 Model for Spherosilicate Structures

Generating an atomistic model for the amorphous, nanoporous silica structure is more involved than for a crystalline structure, given the absence of a periodic unit cell. For a crystalline material one can use atomic coordinates and unit cell parameters obtained from diffraction to model the structure. In contrast, for an amorphous structure one must first propose atomic coordinates and then validate the resulting model through comparison to physical properties that are available from experiment, such as the chemical stoichiometry, pore size distribution, surface area, fraction of accessible volume and density of the material. In order to generate an atomistic structure for these amorphous, metal-decorated spherosilicate structures, we developed the following procedure.

In the first step, a coarse-grained model was constructed for the amorphous matrix. The use of the initial coarse-grained model facilitates the process of developing an amorphous model that matches macroscopic experimental measures of surface area and pore volume, because it reduces the number of degrees of freedom and thus the corresponding computational effort of the structure generation process. Four different spherical coarse-grained bead types were identified based on the groups present in these matrices. As shown in Figure 4.2, the four groups include silicate cubes (consisting of 8 Si atoms and 12 O's), O_2SiCl_2 bridges (that connect the cubes to each other), and two groups that terminally bind to the vertices of the silicate cubes, $-OTiCl_3$ and $-OSi(CH_3)_3$ (trimethyl silicon oxide or $-OSiMe_3$). Relevant distances and angles between the connected beads were derived from equilibrated geometries of the atoms composing the beads. The distribution of bead types was chosen to match the experimentally determined stoichiometry and the number of beads per unit volume was chosen to match the experimentally determined matrix density. The beads were randomly placed to satisfy the appropriate distances between connected beads and angles between sequences of three beads. An illustration of a coarse-grained model of the framework developed in this manner is shown in Figure 4.3(a).

Since this procedure resulted in some overlap of unconnected beads, in the next step a mesoscale level energy minimization was performed for the coarse grain structure using canonical Monte Carlo simulation (in which beads were translated) in order to obtain a stable structure. The potential energies used in the energy minimization included (i) non-bonded

repulsion, (ii) bead “bond stretching” and (iii) bead “angle bending”. The functional form of the non-bonded interaction was an inverse twelfth relation. The functional forms of the bonded interactions were harmonic. The parameters of the coarse-grained potentials were chosen on an *ad hoc* basis so as to maintain non-bonded bead overlap less than 1% of the mixed diameter, bond distances within 0.04 Å and bond angles within 0.06°.

In the final step of model generation, the beads were replaced with the relevant atomic descriptions. The atomic groups were placed at the corresponding bead center of mass. Each of the four units shown in Figure 4.2 was considered to have an internally rigid structure. The internal structures were obtained from optimized first principles calculations or literature values[28]. The downhill simplex method [29], was used to rotate the fragments to obtain the correct values for orientation of the atomic bond distances and bond angles involved in the connection of bead fragments. The resulting framework was used as a rigid structure in our adsorption simulations. An example of the final atomistic structure is shown in Figure 4.3 (b). Each vertex of a spherosilicate cube is bound to either a bridge (Figure 4.2(b)) or one of two terminal end groups, -OTiCl₃ groups or -OSiMe₃ (Figures 4.2(c) and (d)). Atomistic structures for all adsorbents simulated here are available at an online archive [30].

In this work we developed and studied nine structures obtained by varying two physical properties at three levels. The first is the density of the adsorbent and the second is -OTiCl₃ content. The three levels of density are low, medium and high. A change in density corresponds to a change in the fraction of accessible volume as well as a commensurate change in surface area. The three levels of -OTiCl₃ content corresponded to 0%, 50% and 100% corresponding to the fraction of end groups which were -OTiCl₃ (as opposed to -OSiMe₃). Additional details of these 9 structures are included in Table 4.1. Note that the densities change as the name implies for a given Ti content. However there are examples where the density of a “low density” material with 100% Ti end groups has a higher density than a “medium density” material with 0% Ti end groups, due to the high molecular weight of the -OTiCl₃ group.

The accessible volume (AV) in the adsorbents was determined using a geometrical method that has been used in the past for calculating accessible volumes in MOFs [31, 32] and polymer membranes [33]. Briefly, the space within the framework is divided into a three-dimensional grid with a resolution of 0.05 Å. A zero-volume probe was inserted into each box

and tested for overlap with the atoms of the framework. The surface area (SA) of the framework was also calculated by a previously established geometrical method [31-33]. A two-dimensional grid was created on the spherical surface of each framework atom and a point probe was inserted onto each small surface block and tested for overlap with other framework atoms. This probe also has zero-volume, making the calculation purely geometric and consistent with the AV calculation.

4.2.2 Grand Canonical Monte Carlo Simulation

Adsorption simulations were performed using standard Grand Canonical Monte Carlo (GCMC) simulation [34, 35] in which the chemical potential (μ), volume (V) and temperature (T) of the system are fixed. The simulation delivers the number of particles in the system and the potential energy among other properties. Four types of moves included in the GCMC simulations: (i) center-of-mass translation, (ii) center-of-mass rotation (iii) molecule insertion and (iv) molecule deletion, which are randomly attempted in a ratio of 3:3:2:2. For each simulation, 10 million configurations were performed for system equilibrium and another 10 million configurations were performed for data production. Three dimensional standard periodic boundary conditions and the minimum image convention were employed.

The molecular model assumes a rigid framework structure. Lennard-Jones parameters for the atoms in the structure are taken from the UFF force fields [36] (values are listed in Table 4.2). CH₄ adsorption simulations do not include electrostatic interactions. The united-atom TraPPE force field [37] was used to model the CH₄ molecule (Table 4.2). Individual CO₂ molecules are considered to be rigid and linear. The interactions among CO₂ molecules are modeled with the TraPPE force field [38]. CO₂ adsorption simulations account for electrostatic interactions between CO₂ molecules by placing point charges on each atom (parameter values are listed in Table 4.2). Similar models have been used for calculating adsorption of CO₂ in MOFs [5]. LJ cross-interaction parameters were determined by the Lorentz-Berthelot mixing rules [34]. A spherical cut-off distance of 15 Å was used in calculating intermolecular potentials and a long-range correction was used to account for the cut-off error beyond the cut-off distance. The electrostatic energies were evaluated using the spherically truncated, charge neutralized method of Wolf *et al.*[39].

In order to better understand the effect of charge separation in the adsorbent on the adsorption of carbon dioxide, we performed two sets of GCMC simulations in a charged and uncharged framework. In both cases, the electrostatic interactions between CO₂ molecules were retained. The method for determining charge distribution in the framework is discussed below.

The Lennard-Jones equation of state by Johnson *et al.*[40] was used to estimate the chemical potential of the bulk phase at a given temperature and pressure. At each case for a given choice of chemical potential and temperature, we performed two simulations: one in the bulk phase and one in the adsorbed phase. Performing bulk simulations eliminates the error of approximate nature of the equation of state. Adsorption isotherms were generated by plotting the fractional loading obtained from the adsorbed phase simulation as a function of the pressure obtained from the bulk phase simulation. We chose the volume of the bulk and adsorbed phases such that the average number of adsorbate molecules in the system turned out to be bound by 500 and 2500.

For adsorbents with periodic crystalline structures, three-dimensional density distributions can be plotted to show the adsorption sites [32]. However, since amorphous materials do not have periodic units, this method cannot be used here. Therefore in this study we used pair correlation functions (PCFs) to identify the adsorption sites in the spherosilicate structure. The pair correlation function is a *conditional probability* of finding two particles at a given separation, normalized to unity at long distances.

$$g(r) = \frac{V}{\Delta V N^2} \left\langle \sum_i \sum_{j \neq i} \delta(r - r_{ij}) \right\rangle \quad (1)$$

where V is the system volume, r is the separation distance between two particles i and j , and N is the number of particles in the system. Pair correlation functions can be generated for pairs of particles of any type. In our simulations we developed PCFs between adsorbate molecules and each type of atoms in the framework (Si, Ti, O and Cl). Adsorbate-adsorbate and Ti-Ti PCFs were also generated.

4.2.3 Quantum Mechanical Calculations

4.2.3.1 Validation of Physisorption

It has been predicted that in a reduced state, isolated Ti atoms will cause gases to chemisorb [17]. In these materials, the Ti appears in an oxidized state, as $-\text{OTiCl}_3$. Therefore, we performed quantum mechanical simulations to determine whether CO_2 and CH_4 would chemisorb in the presence $-\text{OTiCl}_3$. Density Functional Theory (DFT) calculations were performed using the B3LYP functional in combination with the standard 6-311G(d,p) basis set, utilizing the Gaussian03 set of programs [41]. An initial geometry optimization of an isolated spherosilicate cube with one $-\text{OTiCl}_3$ group attached to it was performed. Next, a single molecule of either CH_4 or CO_2 was placed near the $-\text{OTiCl}_3$ group on the spherosilicate cube and a second geometry optimization was performed. We judged that no chemisorptions took place on the basis of no change in the internal molecular structure of the adsorbate molecules. The C-H bond length of the CH_4 molecule was changed by only 0.01% to 0.02% between the adsorbed and isolated states. The H-C-H bond angle in CH_4 was changed by only 0.09% to 0.2%. The C-O bond length of the CO_2 molecule differed by only 1.3% to 1.6% and O-C-O bond angle differed by only 0.28%. These DFT calculations validate the use of the non-reactive potentials in the classical GCMC and MD simulations.

4.2.3.2 Calculating partial charges of the framework atoms.

In order to determine the importance of charge distribution in the framework on the adsorption of CO_2 , we generated a set of framework charges from DFT calculations. The charge distribution for spherosilicate structures was calculated based on geometries of fragments optimized using B3LYP/6-311G(d,p) in Gaussian 03 [41]. The electron distributions were mapped onto point charges centered at atom positions using Natural Bond Orbital (NBO) Analysis method [42, 43]. This approach has also been used by other researchers [44, 45] to calculate the charge distributions for porous structures. The resulting partial charges are shown in Table 4.2. The sum of the charges were set to zero for each of the four units shown in Figure 4.2, allowing for a feasible building-block approach that did not violate electrostatic neutrality.

4.2.4 Molecular Dynamics Simulations

Classical equilibrium MD simulations in the canonical (NVT) ensemble were used to calculate diffusivities of CH₄ and CO₂ in each adsorbent. Equations of motion were integrated using the Two-time step r-RESPA algorithm of Tuckerman and co-workers[46]. Intramolecular degrees of freedom were accounted for in the short time loop, with a step size of 0.2 fs. 10 short steps were performed per long time step. Temperature was controlled by the Nosé-Hoover thermostat [47, 48] method. An equilibration time of 2 ns was employed followed by an additional 8 ns of data production. During data production, positions of the center-of-mass of adsorbate molecules were saved every 5 ps and were used to calculate the self-diffusivity via the Einstein relation. Uncertainties in the self-diffusivity are reported as the standard deviation of the x, y, and z components of the diffusivity. The interaction potentials used in MD simulations are same as in GCMC simulations.

The self-diffusivities were obtained from the Einstein relation shown in Equation 2. It relates the mean square displacement (MSD) to the observation time:

$$D = \lim_{\tau \rightarrow \infty} \frac{\langle [\mathbf{r}_i(t + \tau) - \mathbf{r}_i(t)]^2 \rangle}{2d\tau} \quad (2)$$

where D is the self-diffusivity, \mathbf{r}_i is the position of particle i , τ is the observation time, d is the dimensionality of the system and the angled brackets indicate an ensemble average over both particle i and time origin t . The MD simulations were run until to the infinite-time limit, where the linear relationship between MSD and observation time is valid. The activation energy was calculated by the Arrhenius equation (Equation 3) using diffusivities at 4 temperatures: 300 K, 400 K, 500 K and 600 K.

$$D(T, \rho) = D_o(\rho) \exp\left(-\frac{E_a(\rho)}{k_B T}\right) \quad (3)$$

We did not explore the density dependence for the diffusivity indicated in Equation (3), as we calculated all the self-diffusivities correspond to an infinitely dilute concentration of adsorbates.

4.3 Results and Discussion

4.3.1 CH₄ Adsorption

4.3.1.1 Adsorption Isotherms

Adsorption isotherms for CH₄ were calculated at 300 K for a pressure range up to 100 bar for the nine structures studied. All the isotherms were analyzed on both gravimetric basis (weight percentage wt%) and volumetric basis (kg of methane/l). While only gravimetric isotherms are shown in this manuscript, an analogous set of volumetric isotherms are available in the corresponding supplementary information (Appendix E). The general thermodynamic considerations that can be used to understand adsorption isotherms are also outlined in the supplementary document (Appendix E).

Calculated gravimetric isotherms at 300 K are shown in Figure 4.4 for low density structures (Figure 4.4(a)), middle density structures (Figure 4.4 (b)) and high density structures (Figure 4.4 (c)). The isotherms of all nine materials are nonlinear. The highest weight percentage of methane is 16.9 wt% for all the structures studied and maximum volumetric quantity adsorbed is 0.12 kg /l at the maximum bulk pressure studied (97 bar). We can see in these simulations that the presence of Ti does not enhance adsorption on a gravimetric basis. Furthermore there is a gravimetric penalty associated with the inclusion of Ti based on its molecular weight. An analysis of the volumetric isotherms found in the supplementary information: Figure 4.S2 (Appendix E) also shows less adsorption with increasing Ti content, due to the smaller well depth (ϵ) of the Lennard Jones potential for Ti. The conclusion here is that the presence of Ti as -OTiCl₃ does not enhance physisorption of CH₄. Of course, no conclusion can be drawn from the present work on the impact of a matrix that contains reduced Ti, for which chemisorption would likely be the dominant mechanism of adsorption. Therefore as a next step for this study, the effect of chemisorption with reduced Ti in the structures could be investigated. In comparison to the DOE targets of 180 v(STP)/v (under 35 bar and near ambient temperature), the maximum CH₄ adsorption calculated is 110.6 v(STP)/v at 34.75 bar. Future studies could investigate improving the adsorption capacity to meet the DOE targets using the suggested method above.

In order to better judge the impact of material density (or equivalently accessible volume) on the adsorption isotherms, gravimetric isotherms plotted in Figure 4.4 are re-plotted in Figure

4.S1 (volumetric isotherms plotted in Figure 4.S2 are re-plotted in Figure 4.S3), grouped now according to Ti content, so that the impact of density is obvious to the eye. We see for all Ti contents and all pressures, the low density material adsorbs more CH₄ on a gravimetric basis, due to the lighter mass of the framework. At low pressures, adsorption is dominated by energetic effects. Therefore, the high density materials, which present deeper energy wells at the walls of the pores, have an advantage at low pressure. This advantage is seen only on a volumetric basis, where the high density materials adsorb more CH₄ than do the low density materials at low pressure, as shown in Figure 4.S3. At high pressures, adsorption is governed by entropic considerations, which is enhanced by the greater accessible volume of the low density adsorbent. Therefore, the low density materials show a greater adsorption capacity on both gravimetric and volumetric bases as pressure increases. In Figure 4.S3 this cross-over from the energetic to the entropic regimes is shown in the volumetric isotherms.

4.3.1.2 Energies of adsorption

Herein, the energy of adsorption is the difference between the energy of the adsorbed phase and the energy of the isolated bulk gas and adsorbent phases. In practice, the dominant contribution to the energy of adsorption is the potential energy due to adsorbate-adsorbent interactions in the adsorbed phase. In Figure 4.5, the potential energy due to adsorbate-adsorbent interactions is plotted for three Ti contents in the low density material (a) and for three densities in the 0% Ti material (b) at 300 K. The energies of adsorption are functions of pressure: at low pressures binding energies are stronger. The deep sites near the walls are occupied first. Then the energetically less favorable pore interior is filled. Figure 4.5(a) clearly shows a more favorable energy for the low 0% Ti material across the entire pressure range. Figure 4.5(b) shows that the high density materials have deeper energy wells across the entire pressure range and the difference increases with increasing pressure. Energy of adsorption for methane varies from 6 to 22 kJ/mol in magnitude at 300 K.

In Figure 4.6, the potential energy due to adsorbate-adsorbate interactions is plotted for three Ti contents in the low density material (a) and for three densities in the 0% Ti material (b) at 300 K. At 300 K, the magnitude of the adsorbate-adsorbate energy increases up to 2 kJ/mol. The 0% Ti material shows more favorable adsorbate-adsorbate energy; see Figure 4.6(a). Over most of the pressure range, the high density material shows more favorable adsorbate-adsorbate

energy; see Figure 4.6(b). At both extremes of the pressure range, the difference in energy between high density and low density becomes less.

4.3.1.3 CH₄ adsorption sites

PCFs at 300 K and 100 bar were generated between CH₄-CH₄, CH₄-Si, CH₄-Ti and Ti-Ti PCFs (shown in Figures 4.7 and 4.S5). Additional PCFs, including CH₄-O and CH₄-Cl are presented in the supplementary information (Appendix E). A snapshot of a configuration representative of the peak is provided at the top of each figure. In each plot (except for Ti-Ti and CH₄-Ti), PCFs for three materials are examined, to investigate the best adsorbent (low density and 0% Ti), the impact of Ti content (low density and 100% Ti) and the impact of material density (high density and 0% Ti). As expected, CH₄ was always adsorbed around the framework and in the pore areas. Adsorption of either CH₄ or CO₂ inside the spherosilicate cubes was not observed because the Si₈O₁₂ frame is too small to accommodate either adsorbate.

Using these pair correlation functions we identified that the preferred adsorption sites are located in front the exterior faces of the spherosilicate cubes. In Figure 4.7(a), there are two prominent peaks in the CH₄-CH₄ PCF, centered at 4.8 Å and 7.8 Å. The first peak corresponds to the CH₄-CH₄ nearest neighbor distance in a bulk phase. The second peak corresponds to CH₄-CH₄ pairs located on adjacent faces of the same spherosilicate cube. At the high loadings at 300 K we observe a PCF structure more typical of a high-density gas or liquid. CH₄ molecules orient themselves in the limited accessible volume and the impact of the adsorbent on the CH₄-CH₄ PCF is less significant. The peaks for the high density material are higher since the PCF is normalized by the total density (number of CH₄ per simulation volume, not accessible volume) but the accessible volume is lower in the high density material.

In Figure 4.7(b), there are two prominent peaks in the CH₄-Si PCF, centered at 4.8 and 7.5 Å. The first peak corresponds to the CH₄ interacting with a Si atom on the adsorbed face and the second peak corresponds to a Si located in the same spherosilicate cube but on a different face than the one on which the CH₄ is adsorbed. In 0% -OTiCl₃ structures Si is also provided by the -OSiMe₃ groups. Therefore we see a peak at 5.5 Å which is correspond to the CH₄ interacting with a Si in -OSiMe₃ group connected to a vertex of the adsorbed face of the spherosilicate cube. The peaks for the 100% -OTiCl₃ structure are higher since the PCF is normalized by the total density (number of CH₄ per simulation volume) but the accessible volume where CH₄ may be

found is lower in 100% -OTiCl₃ structures. Values for accessible volumes for all the structures are presented in Table 4.1.

In Figure 4.7(c), there are two prominent peaks in the CH₄-Ti PCF, centered at 5.4 and 9.7 Å. The first peak corresponds to the CH₄ interacting with a Ti in a -OTiCl₃ group connected to the adsorbed face of the spherosilicate cube and the second peak corresponds to a Ti in a -OTiCl₃ group connected to the same spherosilicate cube but on a different face than the one on which the CH₄ is adsorbed.

In Figure 4.S5, we provide a Ti-Ti PCF, which demonstrates that the Ti are atomistically dispersed in the matrix, a key feature of these materials. The impact of this dispersion is perhaps not exploited by a material that relies on physisorption. However, for an analogous material, in which the Ti is reduced and can act as a chemisorption site for adsorbates, the atomistic dispersion is important to maintain the chemical nature of the site [17].

4.3.1.4 Self-Diffusivity and Activation Energy

Self-diffusion coefficients for CH₄ at infinite dilution were calculated using standard MD simulations employing Einstein relation. MD Simulations were run at 300K, 400 K, 500 K and 600K for all 9 structure and in each case we computed the exponent relating the MSD to the observation time, which should be equal to “one” in the linear, infinite-time limit to verify that the MSDs were in this regime. The resulting average value of this exponent was 1.003, with a minimum of 0.98 and a maximum of 1.02. Furthermore, we clarified the long time limit behavior is achieved by observing MSDs are sufficiently long as to have travelled through the structure. In all instances the root mean square distance traveled was large compared to the pore size, indicating that inter-pore transport was being probed. The values obtained for the self-diffusivities are listed in Table 4.3, which are in the same order of magnitude with the diffusivity of CH₄ in MOFs[49].

We observed significant differences between the diffusivities in the x, y and z direction components (accuracy of these results was confirmed by obtaining the same results with a rotated structure). This anomalously large variance in the x, y and z components of the self-diffusivity is an acceptable artifact of the finite size of the simulation volume. Experimentally, the materials are amorphous with irregular pores but isotropic on the macroscale. The finite size of the cubic simulation (side length of 50 Å) exaggerates the anisotropy. To our knowledge the

only impact of finite simulation volume in this work is this larger uncertainty on the self-diffusivities.

The activation energies for CH₄ diffusion at infinite dilution in each structure were calculated via a linear regression of the Arrhenius equation (Equation (3)). The activation energies calculated are presented in Table 4.3. As expected we observe a negative correlation between the self-diffusivity and activation energy for diffusion, in accordance to the Arrhenius equation.

The relationship of self-diffusivity at 300 K and activation energy with SA, AV and energy of adsorption are analyzed by calculating the statistical correlation coefficients, a statistical property bounded between -1 (a perfect negative correlation between x and y, e.g. $y=-x$) and 1 (a perfect positive correlation between x and y, e.g. $y=x$). For the energy of adsorption, the lowest density, which is at 1 bar was used, since the self-diffusivities were computed at infinite dilution. The results are listed in Table 4.4. As the potential energy becomes stronger (more negative), the activation energy increases and the self-diffusivity decreases. As the AV increases, the self-diffusivity increases, with little change to the activation energy. As the surface area increases, we observe a combination of the two effects above, resulting in a statistical decrease in the activation energy and an increase in the self-diffusivity.

4.3.2 CO₂ Adsorption

4.3.2.1 Adsorption Isotherms

Adsorption isotherms for CO₂ were generated at 300 K for a pressure range up to 51.6 bar for the nine structures studied. Because the bulk critical point for CO₂ at 300 K is 67.131 bar [50] we did not simulate at higher pressures. All the isotherms were analyzed on both a gravimetric basis (weight percentage wt%) and volumetric basis (kg of carbon dioxide/l). The gravimetric isotherms are shown here and volumetric isotherms are available in the corresponding supplementary information (Appendix E).

For CO₂ two sets of adsorption isotherms were generated, which either included or excluded electrostatic charges on the framework. Based on comparison between models and experimental data we chose to present the results for the isotherms that exclude electrostatic charges on the framework. Experimental data for CO₂ adsorption in a material at 273.15 K up to

1 bar was generated for a material comparable with modeled high density material with 0% -OTiCl₃. Physical characteristics of the modeled structure agree with the experimental material. The accessible volume of the experimental sample and the 0% -OTiCl₃ high density model were respectively 0.64 cm³/g and 0.68 cm³/g. The density of the experimental sample and the 0% -OTiCl₃ high density model were respectively 0.87 and 0.88 g/cm³. The surface area calculated for modeled structure has a higher value than for the measured BET surface area of the experimental structure (experimental: 565 m²/g, modeled: 4679.17 m²/g). This calculated surface area of the model is high because of the choice of a zero-volume probe for calculations in the modeled structure, which is attractive because it is a purely geometric calculation, independent of energy, which yields correct trends when comparing different materials but which overestimates surface area. The experimental surface area is calculated using N₂ adsorption. The calculated surface area for the model using a N₂ probe was 221.99 m²/g for atomistic structure and 449.93 m²/g for coarse grain structure. The experimental isotherm is presented as an excess adsorption isotherm (cm³/g at STP) in Figure 4.8. The relevant simulated isotherms (with and without framework charge) have been converted to excess isotherms and also plotted. The experimental excess adsorption at 273.15 K, 740.31 mmHg is 15.54 cm³/g at STP. The simulated excess adsorption at 300 K, 742.45 mmHg, with framework charges is 255.60 cm³/g at STP and without framework charges is 46.46 cm³/g at STP. The simulated adsorption without framework charges is on the same order of magnitude with the experiments. It was on this basis that we decided not to use framework charges in our simulations. CO₂ adsorption studies in IRMOF-1 done by Walton *et al.*[5] also showed that simulations with electrostatic interaction between CO₂-CO₂ but without the electrostatic interaction between CO₂-framework better agreed with comparable experimental data.

An example of the isotherms in which electrostatic charges on the framework atoms was included is shown in Figure 4.S6. The presence of the charges enhances adsorption and the CO₂ quickly reaches a maximum capacity by about 10 bar. The dramatic effect of charge distribution on polar molecules [51] and on CO₂ in particular [5] has previously been seen.

As noted above, here we discuss the results for the simulated isotherms that exclude electrostatic charges on the framework. In all cases, the electrostatic interactions between CO₂-CO₂ are included.

Gravimetric isotherms at 300 K are shown in Figure 4.9 for low density structures (Figure 4.9(a)), middle density structures (Figure 4.9(b)) and high density structures (Figure 4.9(c)). The isotherms of all nine materials are nonlinear. The highest weight percentage of CO₂ adsorbed is 50.3 wt% and the maximum volumetric quantity adsorbed is 0.67 kg/l at 51.6 bar. Again, the presence of -OTiCl₃ groups does not enhance adsorption on a gravimetric basis because of the gravimetric penalty associated with their molecular weight. The volumetric isotherms shown in the supplementary information: Figure 4.S8 (Appendix E) also shows less adsorption with increasing Ti content. Again, this is primarily due to the low well depth (ϵ) of the Lennard Jones potential for Ti. Therefore the presence of Ti in the form of -OTiCl₃ does not enhance physisorption. Calculated CO₂ adsorption capacities were compared with the CO₂ adsorption simulation studies done by Babarao *et. al.* [52] for MOFs. Comparison shows at low pressure (1 bar) Si structures adsorb more CO₂ than IRMOF-1 and less CO₂ than single-walled carbon nanotubes (SWNT). But at high pressure (up to 50 bar) Si structures adsorb less CO₂ than IRMOF-1 and considerably more CO₂ than SWNT. Future studies will investigate enhancing the adsorption capacity with improvements to Si structures (reduced Ti, inclusion of chemisorption effect).

In order to better judge the impact of material density (or equivalently accessible volume) on the adsorption isotherms, gravimetric isotherms plotted in Figure 4.9 are re-plotted in Figure 4.S7 (volumetric isotherms plotted in Figures 4.S8 are re-plotted in Figure 4.S9), grouped now according to Ti content, so that the impact of density is more obvious. At low pressures, adsorption is dominated by energetic effects. Therefore, the high density materials, which present deeper energy wells at the walls of the pores, have an advantage. Therefore, on a volumetric basis, we observe that the high density materials adsorb more CO₂ than do the low density materials at low pressures, as shown in Figure 4.S9. However, on a gravimetric basis, we cannot see this effect clearly since the low density materials are favored due to the lighter mass of the framework, as shown in Figure 4.S7.

We observe an inflection behavior in CO₂ isotherms (Figure 4.9 and Figure 4.S7). These inflections become more defined with the increase of pore volume. Low density materials with higher pore volume have higher inflection compared to middle density and high density materials with same -OTiCl₃ content (Figure 4.S7). 100% -OTiCl₃ materials with higher pore volume have more inflection compared to 50% -OTiCl₃ and 0% -OTiCl₃ materials with the same

density (Figure 4.9). Below the inflection CO_2 adsorb near to the adsorbent (this is the regime governed by energetic effects) and along the inflection CO_2 starts to fill the pores (this is the regime governed by entropic effects). This agrees with the studies done by Walton *et al.*[5] where they obtained an inflection point both experimentally and in simulations for CO_2 adsorption in IRMOF-1. They also observed more defined inflection with the increase of effective pore size and justified the positions of CO_2 adsorbed along the inflection similar to this study.

As was seen for CH_4 , at high pressures, adsorption is governed by entropic considerations, which is enhanced by the greater accessible volume of the low density adsorbent. Therefore, the low density materials show a greater adsorption capacity on both gravimetric and volumetric basis at high pressures. We can see in Figure 4.S9 that there is a cross over in the volumetric isotherms as the pressure increases and low density materials start to adsorb more in high pressure. Also in gravimetric isotherms (Figure 4.S7) we can see a clear difference at high pressures.

4.3.2.2 Energies of adsorption

In Figure 4.10, the potential energy due to adsorbate-adsorbent interactions is plotted for three Ti contents in the low density material (a) and for three densities in the 0% Ti material (b) at 300 K. The energies of adsorption are functions of pressure. At low pressures binding energies are stronger and the deep sites near the walls are occupied first. Next the energetically less favorable pore interior is filled. Figure 4.10(a) shows a more favorable energy for the low 0% Ti material. Figure 4.10(b) shows that the high density materials have deeper energy wells and the difference increases with increasing pressure. Energies of adsorption range in magnitude from 5 to 27 kJ/mol. The inflection behavior is also observed in the adsorption energies.

In Figure 4.11, the potential energy due to adsorbate-adsorbate interactions is plotted for three Ti contents in the low density material (a) and for three densities in the 0% Ti material (b) at 300 K. Adsorbate-adsorbate interactions play a more significant role in adsorption of CO_2 than in the adsorption of CH_4 or H_2 . We can see the crossover of energies at around 25 bars illustrating the change of regimes from energetic dominated to entropic dominated. At 300 K, the magnitude of the adsorbate-adsorbate energy increases up to 10 kJ/mol.

4.3.2.3 CO₂ adsorption sites

PCFs at 300 K and 20 bar were generated between CO₂-CO₂, CO₂-Si and CO₂-Ti PCFs (shown in Figure 4.12). CO₂-O and CO₂-Cl PCFs are presented in the supplementary information (Appendix E). In each plot case (except for CH₄-Ti), PCFs for three materials are examined, to investigate the best adsorbent (low density and 0% Ti), the impact of Ti content (low density and 100% Ti) and the impact of material density (high density and 0% Ti).

As was the case for CH₄, the CO₂ pair correlation functions indicate that the preferred adsorption sites are located in front the exterior faces of the spherosilicate cubes. In Figure 4.12(a), there are two prominent peaks in the CO₂-CO₂ PCF, centered at 3.9 Å and 7.5 Å. The first peak corresponds to the CO₂-CO₂ nearest neighbor distance in bulk. The second peak corresponds to CO₂-CO₂ located on adjacent faces of the same spherosilicate cube.

In Figure 4.12(b), there are two prominent peaks in the CO₂-Si PCF, centered at 4.5 and 7.3 Å. The first peak corresponds to the CO₂ molecule interacting with a Si atom on the adsorbed face and the second peak corresponds to a Si located in the same spherosilicate cube but on a different face than the one on which the CO₂ is adsorbed. In the 0% -OTiCl₃ structures, Si is also provided by the -OSiMe₃ groups. Therefore we see a peak at 5.1 Å which is correspond to the CO₂ interacting with a Si in -OSiMe₃ group connected to the adsorbed face of the spherosilicate cube. As observed earlier the peaks for the 100% -OTiCl₃ structure are higher since the accessible volume may be lower in 100% -OTiCl₃ structures.

In Figure 4.12(c), there are two prominent peaks in the CO₂-Ti PCF, centered at 5.1 and 9.8 Å. The first peak corresponds to the CO₂ interacting with a Ti in a -OTiCl₃ group connected to the adsorbed face of the spherosilicate cube and the second peak corresponds to a Ti in a -OTiCl₃ group connected to the same spherosilicate cube but on a different face than the one on which the CO₂ is adsorbed.

4.4 Conclusions

In this work, we used molecular simulation tools to examine the adsorptive and diffusive properties of methane and carbon dioxide in amorphous nanoporous adsorbents composed of spherosilicate building blocks, in which isolated metal sites have been distributed. We found via quantum mechanical calculations, that when Ti is present in an oxidized state as $-OTiCl_3$, that physisorption is strictly observed for both CH_4 and CO_2 .

At 300 K, the highest weight percentage of methane is 16.9 wt% and volumetric quantity adsorbed is less than 0.12 kg of methane/l at the maximum bulk pressure studied (97 bar). For carbon dioxide the maximum weight percentage is 50.3 wt% and the maximum volumetric quantity adsorbed is 0.67 kg/l at 51.6 bar. The strongest adsorbent for a physisorption process is a low density material with 0% Ti content. The presence of oxidized Ti as $-OTiCl_3$ does not enhance physisorption. There is a gravimetric penalty associated with the inclusion of as $-OTiCl_3$ groups based on their molecular weight. Furthermore, the non-bonding well-depth associated with Ti in the Lennard-Jones potential is weak.

We observe that at 300 K, there are two adsorption regimes. At low pressures, the adsorption process is governed by energetic considerations and at the high end of the pressure range the adsorption becomes a process dominated by entropic considerations. Based on the pair correlation functions we identified that favorable adsorption sites for adsorbents are located in front of a face of a spherosilicate cube. Self-diffusivities and activation energies for diffusion for CH_4 are reported and found to be similar to that in MOFs.

Acknowledgements

This research was supported by the Sustainable Energy and Education Research Center at the University of Tennessee, by a grant from the National Science Foundation (DGE-0801470). This research project used resources of the National Institute for Computational Sciences (NICS) supported by NSF under agreement number: OCI 07-11134.5.

References

- [1] T.A. Boden, G. Marland, and R.J. Andres, *Global, Regional, and National Fossil-Fuel CO₂ Emissions.*, Carbon Dioxide Information Analysis Center, Oak Ridge National Laboratory, U.S. Department of Energy, Oak Ridge, Tenn., (USA).
- [2] P.F. N Florin, *Carbon capture technology: future fossil fuel use and mitigating climate change*, Grantham Institute for Climate Change, London (UK), 2010.
- [3] C. Ehlig-Economides and M.J. Economides, *Sequestering carbon dioxide in a closed underground volume*, Journal of Petroleum Science and Engineering. 70 (2010), pp. 118-125.
- [4] J.D. Figueroa, T. Fout, S. Plasynski, H. McIlvried and R.D. Srivastava, *Advances in CO₂ capture technology - The US Department of Energy's Carbon Sequestration Program*, International Journal of Greenhouse Gas Control. 2 (2008), pp. 9-20.
- [5] K.S. Walton, A.R. Millward, D. Dubbeldam, H. Frost, J.J. Low, O.M. Yaghi and R.Q. Snurr, *Understanding inflections and steps in carbon dioxide adsorption isotherms in metal-organic frameworks*, J Am Chem Soc. 130 (2008), pp. 406-+.
- [6] A.R. Millward and O.M. Yaghi, *Metal-organic frameworks with exceptionally high capacity for storage of carbon dioxide at room temperature*, J Am Chem Soc. 127 (2005), pp. 17998-17999.
- [7] M. Sevilla and A.B. Fuertes, *Sustainable porous carbons with a superior performance for CO₂ capture*, Energy & Environmental Science. 4 (2011), pp. 1765-1771.
- [8] W.M. Frota, J.A.S. Sa, S.S.B. Moraes, B.R.P. Rocha and K.A.R. Ismail, *Natural gas: The option for a sustainable development and energy in the state of Amazonas*, Energy Policy. 38 (2010), pp. 3830-3836.
- [9] M. Taniewski, *Sustainable chemical technologies in production of clean fuels from fossil fuels*, Clean-Soil Air Water. 36 (2008), pp. 393-398.
- [10] I.P. Jain, *Hydrogen the fuel for 21st century*, International Journal of Hydrogen Energy. 34 (2009), pp. 7368-7378.
- [11] T.K. Mandal and D.H. Gregory, *Hydrogen: a future energy vector for sustainable development*, Proceedings of the Institution of Mechanical Engineers Part C-Journal of Mechanical Engineering Science. 224 (2010), pp. 539-558.
- [12] N.A. Kelly, T.L. Gibson, M. Cai, J.A. Spearot and D.B. Ouwerkerk, *Development of a renewable hydrogen economy: optimization of existing technologies*, International Journal of Hydrogen Energy. 35 (2010), pp. 892-899.
- [13] Q.F. Zhang, E. Uchaker, S.L. Candelaria and G.Z. Cao, *Nanomaterials for energy conversion and storage*, Chemical Society Reviews. 42 (2013), pp. 3127-3171.
- [14] S.Q. Ma and L. Meng, *Energy-related applications of functional porous metal-organic frameworks*, Pure and Applied Chemistry. 83 (2011), pp. 167-188.
- [15] M.R. Tim Burchell, *Low pressure storage of natural gas for vehicular applications*, SAE, Washington, D.C., 2000.

- [16] S. Ma, D. Sun, J.M. Simmons, C.D. Collier, D. Yuan and H.-C. Zhou, *Metal-organic framework from an anthracene derivative containing nanoscopic cages exhibiting high methane uptake*, J Am Chem Soc. 130 (2008), pp. 1012-1016.
- [17] J.E. Bushnell, P. Maitre, P.R. Kemper and M.T. Bowers, *Binding energies of Ti+(H₂)(1-6) clusters: Theory and experiment*, J Chem Phys. 106 (1997), pp. 10153-10167.
- [18] J.C. Clark, S. Saengkerdsub, G.T. Eldridge, C. Campana and C.E. Barnes, *Synthesis and structure of functional spherosilicate building block molecules for materials synthesis*, Journal of Organometallic Chemistry. 691 (2006), pp. 3213-3222.
- [19] J.C. Clark and C.E. Barnes, *Reaction of the Si₈O₂₀(SnMe₃)₈ building block with silyl chlorides: A new synthetic methodology for preparing nanostructured building block solids*, Chemistry of Materials. 19 (2007), pp. 3212-3218.
- [20] D.B. Cordes, P.D. Lickiss and F. Rataboul, *Recent developments in the chemistry of cubic polyhedral oligosilsesquioxanes*, Chemical Reviews. 110 (2010), pp. 2081-2173.
- [21] T. Jaroentomeechai, P.K. Yingsukkamol, C. Phurat, E. Somsook, T. Osotchan and V. Ervithayasuporn, *Synthesis and reactivity of nitrogen nucleophiles-induced cage-rearrangement silsesquioxanes*, Inorganic Chemistry. 51 (2012), pp. 12266-12272.
- [22] N.N. Ghosh, J.C. Clark, G.T. Eldridge and C.E. Barnes, *Building block syntheses of site-isolated vanadyl groups in silicate oxides*, Chemical Communications. (2004), pp. 856-857.
- [23] C. McCabe, S.C. Glotzer, J. Kieffer, M. Neurock and P.T. Cummings, *Multiscale simulation of the synthesis, assembly and properties of nanostructured organic/inorganic hybrid materials*, J. Comput. Theor. Nanosci. 1 (2004), pp. 265-279.
- [24] N. Shanmugam, K.T. Lee, W.Y. Cheng and S.Y. Lu, *Organic-inorganic hybrid polyaspartimide involving polyhedral oligomeric silsesquioxane via Michael addition for CO₂ capture*, J. Polym. Sci. Pol. Chem. 50 (2012), pp. 2521-2526.
- [25] K.L. Xie, L.X. Jing, W.G. Zhao and Y.L. Zhang, *Adsorption removal of Cu₂₊ and Ni₂₊ from waste water using nano-cellulose hybrids containing reactive polyhedral oligomeric silsesquioxanes*, J. Appl. Polym. Sci. 122 (2011), pp. 2864-2868.
- [26] H.B. Ren, Y.C. Qin, C.W. Shang, Y.T. Bi and L. Zhang, *Adsorption and desorption properties of hybrid aerogels derived from MPMS-SSO at 77 K*, Rare Metal Materials and Engineering. 39 (2010), pp. 475-478.
- [27] A. Maiti, R.H. Gee, R. Maxwell and A.P. Saab, *Hydrogen catalysis and scavenging action of Pd-POSS nanoparticles*, Chem. Phys. Lett. 440 (2007), pp. 244-248.
- [28] K.W. Tornroos, *Octahydridosilasesquioxane determined by neutron-diffraction*, Acta Crystallographica Section C-Crystal Structure Communications. 50 (1994), pp. 1646-1648.
- [29] B.P.F. William H. Press, Saul A. Teukolsky, William T. Vetterling *Numerical recipes: the art of scientific computing*, Cambridge University Press, New York, 1986.

- [30] D.J. Keffer, *Molecular Simulation Images from the Computational Materials Research Group at the University of Tennessee, Knoxville, TN*, Available at: <https://trace.lib.utk.edu/home/davidkeffer/sites/atoms/animmn.html>
- [31] H. Frost, T. Duren and R.Q. Snurr, *Effects of surface area, free volume, and heat of adsorption on hydrogen uptake in metal-organic frameworks*, *J. Phys. Chem. B.* 110 (2006), pp. 9565-9570.
- [32] N.S. Suraweera, R.C. Xiong, J.P. Luna, D.M. Nicholson and D.J. Keffer, *On the relationship between the structure of metal-organic frameworks and the adsorption and diffusion of hydrogen*, *Mol Simulat.* 37 (2011), pp. 621-639.
- [33] J.W. Liu, N. Suraweera, D.J. Keffer, S.T. Cui and S.J. Paddison, *On the relationship between polymer electrolyte structure and hydrated morphology of perfluorosulfonic acid membranes*, *J Phys Chem C.* 114 (2010), pp. 11279-11292.
- [34] M.P. Allen and D.J. Tildesley, *Computer Simulation of Liquids*, Oxford Science Publications, Oxford, 1987.
- [35] D. Frenkel and B. Smit, *Understanding Molecular Simulation*, Academic Press, San Diego, CA, 1996.
- [36] A.K. Rappe, C.J. Casewit, K.S. Colwell, W.A. Goddard and W.M. Skiff, *UFF, a full periodic-table force-field for molecular mechanics and molecular-dynamics simulations*, *J Am Chem Soc.* 114 (1992), pp. 10024-10035.
- [37] M.G. Martin and J.I. Siepmann, *Transferable potentials for phase equilibria. 1. United-atom description of n-alkanes*, *J Phys Chem B.* 102 (1998), pp. 2569-2577.
- [38] J.J. Potoff and J.I. Siepmann, *Vapor-liquid equilibria of mixtures containing alkanes, carbon dioxide, and nitrogen*, *Aiche Journal.* 47 (2001), pp. 1676-1682.
- [39] D. Wolf, P. Keblinski, S.R. Phillpot and J. Eggebrecht, *Exact method for the simulation of Coulombic systems by spherically truncated, pairwise $r(-1)$ summation*, *J Chem Phys.* 110 (1999), pp. 8254-8282.
- [40] J.K. Johnson, J.A. Zollweg and K.E. Gubbins, *The Lennard-Jones equation of state revisited*, *Molecular Physics.* 78 (1993), pp. 591-618.
- [41] M.J. Frisch, G. W. Trucks, H. B. Schlegel, G. E. Scuseria, M. A. Robb, J. R. Cheeseman, J. A. Montgomery, Jr., T. Vreven, K. N. Kudin, J. C. Burant, J. M. Millam, S. S. Iyengar, J. Tomasi, V. Barone, B. Mennucci, M. Cossi, G. Scalmani, N. Rega, G. A. P and H.B.S. G. W. Trucks, G. E. Scuseria, M. A. Robb, J. R. Cheeseman, J. A. Montgomery, Jr., T. Vreven, K. N. Kudin, J. C. Burant, J. M. Millam, S. S. Iyengar, J. Tomasi, V. Barone, B. Mennucci, M. Cossi, G. Scalmani, N. Rega, G. A. Petersson, H. Nakatsuji, M. Hada, M. Ehara, K. Toyota, R. Fukuda, J. Hasegawa, M. Ishida, T. Nakajima, Y. Honda, O. Kitao, H. Nakai, M. Klene, X. Li, J. E. Knox, H. P. Hratchian, J. B. Cross, V. Bakken, C. Adamo, J. Jaramillo, R. Gomperts, R. E. Stratmann, O. Yazyev, A. J. Austin, R. Cammi, C. Pomelli, J. W. Ochterski, P. Y. Ayala, K. Morokuma, G. A. Voth, P. Salvador, J. J. Dannenberg, V. G. Zakrzewski, S. Dapprich, A. D. Daniels, M. C. Strain, O. Farkas, D. K. Malick, A. D. Rabuck, K. Raghavachari, J. B. Foresman, J. V. Ortiz, Q. Cui, A. G. Baboul, S. Clifford, J. Cioslowski, B. B. Stefanov, G. Liu, A. Liashenko, P. Piskorz, I. Komaromi, R. L. Martin, D. J. Fox, T. Keith, M. A. Al-Laham, C. Y. Peng, A.

- Nanayakkara, M. Challacombe, P. M. W. Gill, B. Johnson, W. Chen, M. W. Wong, C. Gonzalez, and J. A. Pople, *Gaussian 03, Revision C.02*, Gaussian, Inc., Wallingford CT, 2004.
- [42] J.P. Foster and F. Weinhold, *Natural hybrid orbitals*, J Am Chem Soc. 102 (1980), pp. 7211-7218.
- [43] A.E. Reed, L.A. Curtiss and F. Weinhold, *Intermolecular interactions from a natural bond orbital, donor-acceptor viewpoint*, Chemical Reviews. 88 (1988), pp. 899-926.
- [44] M.A. Chiacchio, L. Borrello, G. Di Pasquale, A. Pollicino, F.A. Bottino and A. Rescifina, *Synthesis of functionalized polyhedral oligomeric silsesquioxane (POSS) macromers by microwave assisted 1,3-dipolar cycloaddition*, Tetrahedron. 61 (2005), pp. 7986-7993.
- [45] A.O. Yazaydin, R.Q. Snurr, T.-H. Park, K. Koh, J. Liu, M.D. LeVan, A.I. Benin, P. Jakubczak, M. Lanuza, D.B. Galloway, J.J. Low and R.R. Willis, *Screening of Metal-Organic Frameworks for carbon dioxide capture from flue gas using a combined experimental and modeling approach*, J Am Chem Soc. 131 (2009), pp. 18198-+.
- [46] M. Tuckerman, B.J. Berne and G.J. Martyna, *Reversible Multiple Time Scale Molecular-Dynamics*, Journal of Chemical Physics. 97 (1992), pp. 1990-2001.
- [47] S. Nose, *A molecular-dynamics method for simulations in the canonical ensemble*, Molecular Physics. 52 (1984), pp. 255-268.
- [48] W.G. Hoover, *Canonical dynamics - equilibrium phase-space distributions*, Physical Review A. 31 (1985), pp. 1695-1697.
- [49] D. Saha, Z.B. Bao, F. Jia and S.G. Deng, *Adsorption of CO₂, CH₄, N₂O, and N₂ on MOF-5, MOF-177, and Zeolite 5A*, Environmental Science & Technology. 44 (2010), pp. 1820-1826.
- [50] R. Span and W. Wagner, *A new equation of state for carbon dioxide covering the fluid region from the triple-point temperature to 1100 K at pressures up to 800 MPa*, Journal of Physical and Chemical Reference Data. 25 (1996), pp. 1509-1596.
- [51] R.C. Xiong, D.J. Keffer, M. Fuentes-Cabrera, D.M. Nicholson, A. Michalkova, T. Petrova, J. Leszczynski, K. Odbadrakh, B.L. Doss and J.P. Lewis, *Effect of charge distribution on RDX adsorption in IRMOF-10*, Langmuir. 26 (2010), pp. 5942-5950.
- [52] R. Babarao and J.W. Jiang, *Molecular screening of metal-organic frameworks for CO₂ storage*, Langmuir. 24 (2008), pp. 6270-6278.

Appendix D: Tables and Figures

Table 4.1. Structural details for selected spherosilicate structures

Structure	Number of groups in a 50×50×50 Å ³ simulation box				Volume fraction	Density (g/cc)	Accessible Volume		Surface Area	
	Cubes	Bridges	TiCl ₃	TMS			(cm ³ /g)	Å ³ per simulation box	(m ² /g)	Å ² per simulation box
0 % -OTiCl ₃ low density	40	41	0	248	0.73	0.59	1.23	90800	4810	35500
50 % -OTiCl ₃ low density	40	41	124	124	0.74	0.72	1.02	92100	4090	37000
100 % -OTiCl ₃ low density	40	41	248	0	0.75	0.86	0.88	94200	3350	35900
0 % -OTiCl ₃ medium density	50	51	0	308	0.66	0.73	0.90	82400	4790	44000
50 % -OTiCl ₃ medium density	50	51	154	154	0.67	0.90	0.75	84400	3990	44900
100 % -OTiCl ₃ medium density	50	51	308	0	0.69	1.07	0.65	86800	3320	44200
0 % -OTiCl ₃ high density	60	61	0	368	0.59	0.88	0.68	74400	4680	51400
50 % -OTiCl ₃ high density	60	61	184	184	0.61	1.08	0.57	76500	3970	53400
100 % -OTiCl ₃ high density	60	61	368	0	0.64	1.27	0.50	79500	3270	52000

Table 4.2. The Lennard-Jones parameters and partial atomic charges for absorbent and adsorbate atoms.

Atom	σ (Å)	ϵ/k (K)	q (e)
framework atoms			
H	2.571	22.142	0.22
C	3.431	52.839	-1.08
O	3.118	30.194	-1.26 (O in bridge) -1.00 (O in -OTiCl ₃) -1.25 (O in -OSiMe ₃) -1.26 (O in cube)
Si	3.826	202.43	2.53 (Si in bridge) 1.87 (Si in -OSiMe ₃) 1.94 (Si in cube)
Cl	3.516	114.31	-0.35
Ti	2.829	8.5604	1.42
adsorbate atoms and united-atom			
CH ₄	3.81	148.2	0
C	2.80	27.0	0.70
O	3.05	79.0	-0.35

Table 4.3 Self-Diffusivity and Activation Energies for CH₄ and CO₂

Structure	Temperature (K)	CH ₄		
		Diffusivity (10 ⁻⁸ m ² /s)	Standard Deviation (10 ⁻⁸ m ² /s)	Activation Energy (kcal/mol)
0 % -OTiCl ₃ low density	300	0.14	0.07	5.81
	400	5.44	1.38	
	500	12.31	3.44	
	600	16.35	4.54	
50 % -OTiCl ₃ low density	300	0.60	0.11	3.55
	400	5.99	1.11	
	500	9.25	2.76	
	600	11.25	3.24	
100 % -OTiCl ₃ low density	300	6.32	3.49	1.38
	400	12.36	7.78	
	500	16.14	10.57	
	600	20.31	13.52	
0 % -OTiCl ₃ medium density	300	0.26	0.09	4.16
	400	2.41	0.12	
	500	5.50	0.68	
	600	8.03	1.14	
50 % -OTiCl ₃ medium density	300	0.53	0.08	2.99
	400	2.82	1.00	
	500	4.86	2.23	
	600	6.33	2.93	
100 % -OTiCl ₃ medium density	300	2.83	2.19	1.56
	400	6.11	5.03	
	500	8.64	7.28	
	600	10.36	8.85	
0 % -OTiCl ₃ high density	300	0.22	0.04	3.36
	400	1.34	0.46	
	500	2.57	0.97	
	600	3.67	1.69	
50 % -OTiCl ₃ high density	300	0.12	0.07	2.68
	400	0.49	0.33	
	500	0.78	0.54	
	600	1.10	0.83	
100 % -OTiCl ₃ high density	300	0.99	0.83	1.77
	400	2.56	2.39	
	500	3.46	3.30	
	600	4.41	4.31	

Table 4.4. Correlation factors for the relationship of self-diffusivity (at 300 K) and activation energy with surface area, accessible volume and adsorbate-framework energy (at 300 K and 1 bar) for CH₄ and CO₂

Property 1	Property 2	Correlation Coefficient
Self- Diffusivity	Accessible Volume	0.55
Self- Diffusivity	Surface Area	-0.42
Self- Diffusivity	Adsorbate Framework Energy	0.79
Activation Energy	Accessible Volume	0.07
Activation Energy	Surface Area	-0.32
Activation Energy	Adsorbate Framework Energy	-0.81

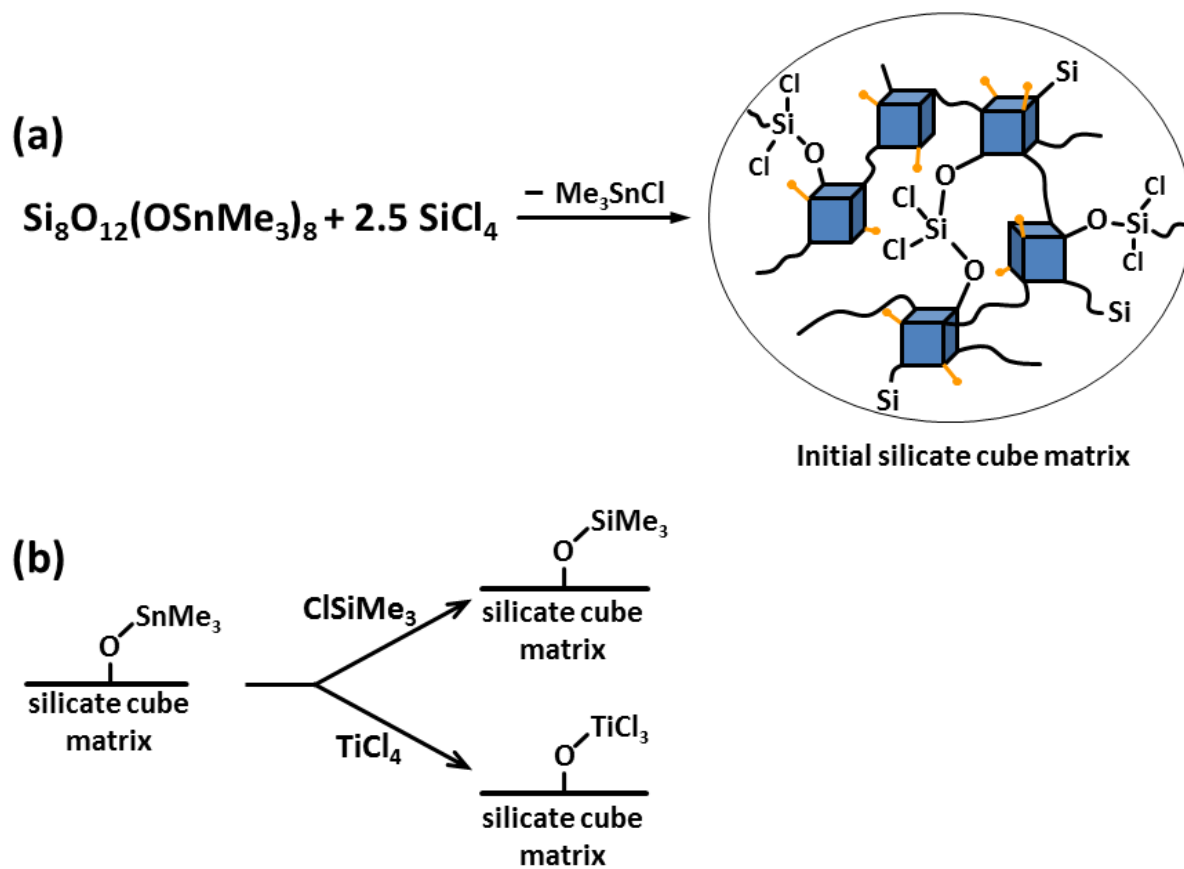


Figure 4.1. (a) Silicate cube matrix after initial cross linking with SiCl_4 . Golden termini are residual SnMe_3 groups in the matrix that are exchanged in final functionalization of the matrix (b).

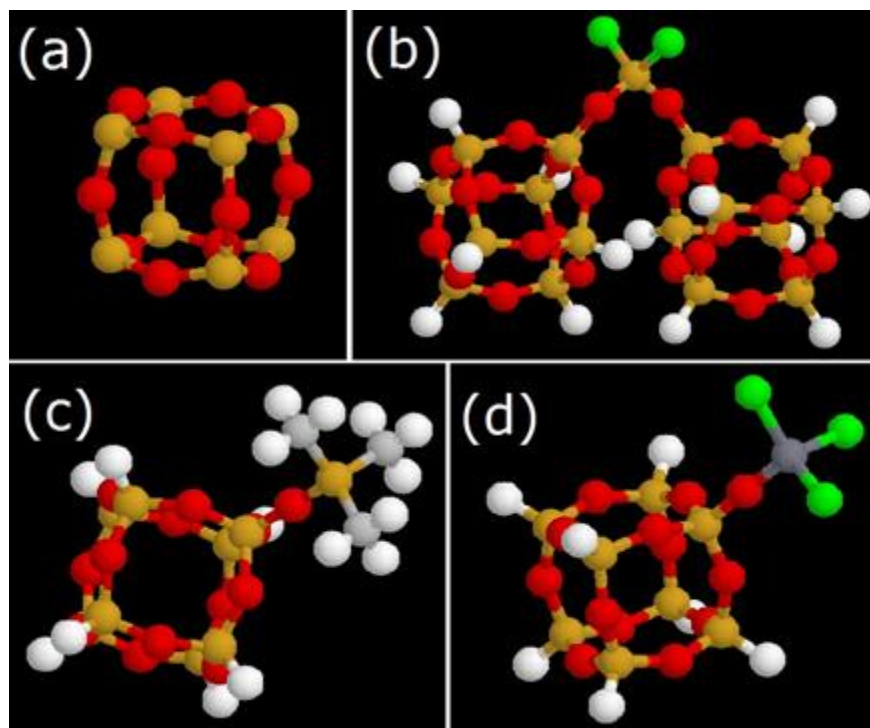


Figure 4.2. Coarse grain beads. (a) spherosilicate cube, (b) O_2SiCl_2 bridge, (c) $-OSiMe_3$ end group and (d) $-OTiCl_3$ end group. (Cl-green, Ti-dark grey, Si-yellow/orange, O-red, C-light gray, H- white).

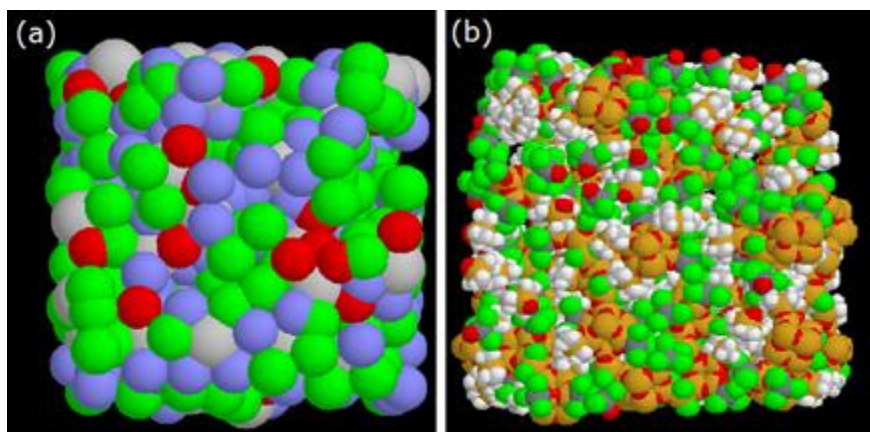


Figure 4.3. (a) Course grain structure (Cubes: grey, bridges: red, -OTiCl₃ :green, -OSiMe₃: blue)
(b) Atomic structure. Atomic color legend as in Figure 4.2.

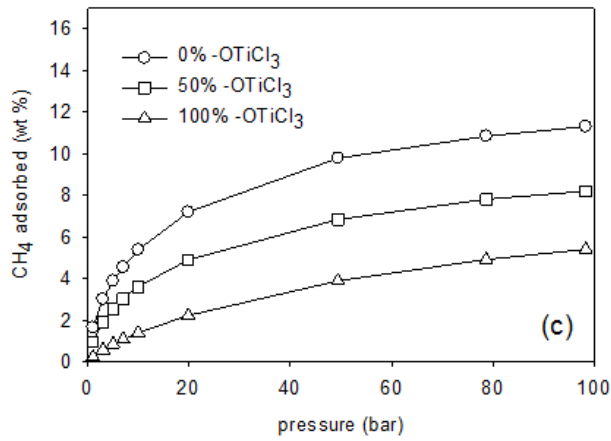
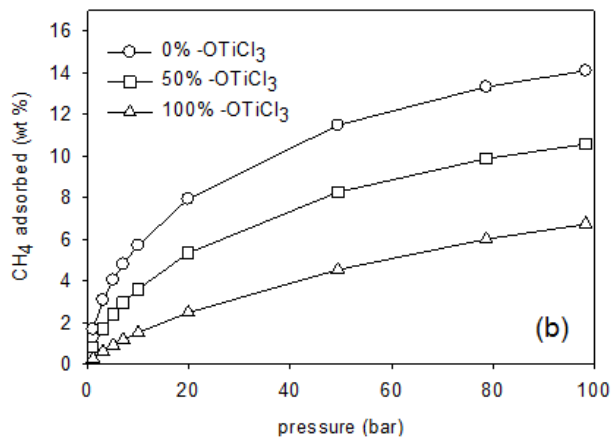
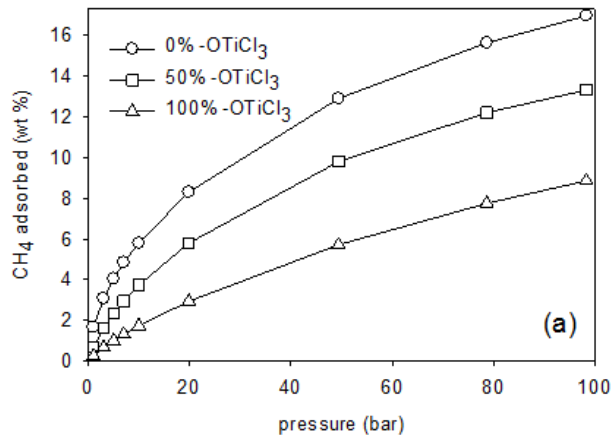


Figure 4.4. Gravimetric CH₄ adsorption isotherms at 300 K. (a) low density structure.(b) middle density structure.(c) high density structure.

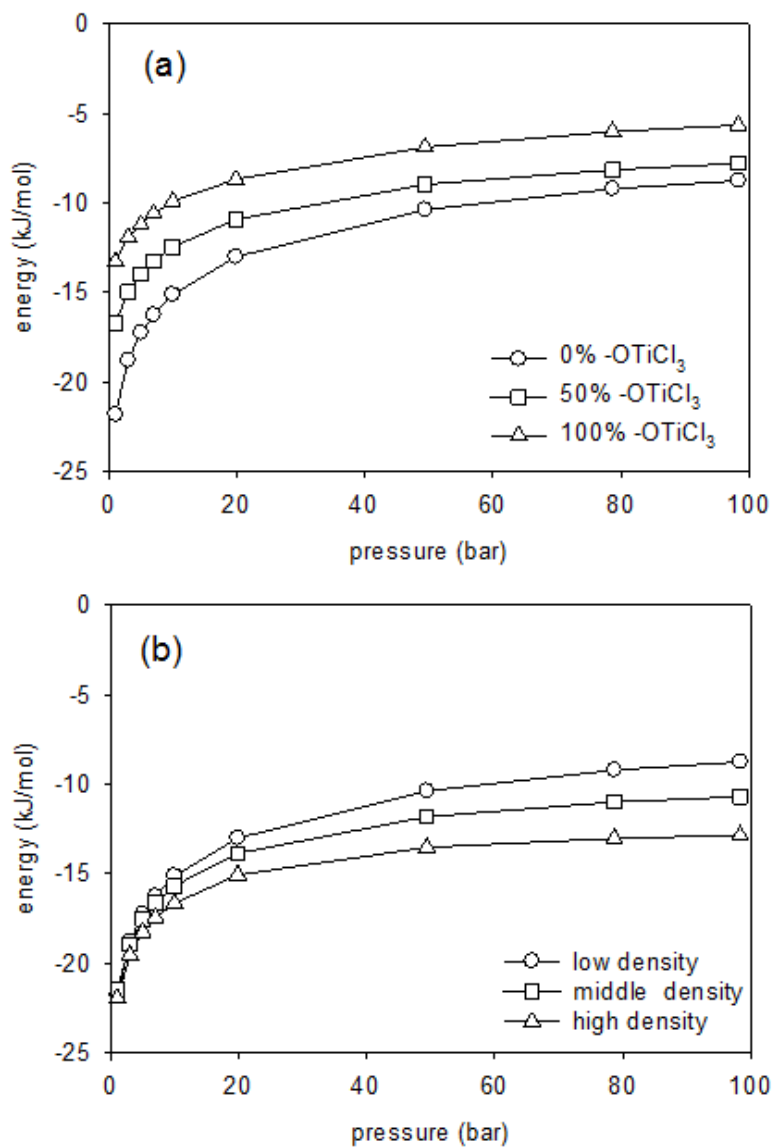


Figure 4.5. Energy between CH₄ and framework at 300 K. (a) low density structure with varying TiCl₃ content. (b) for 0 % -OTiCl₃ structure with varying density.

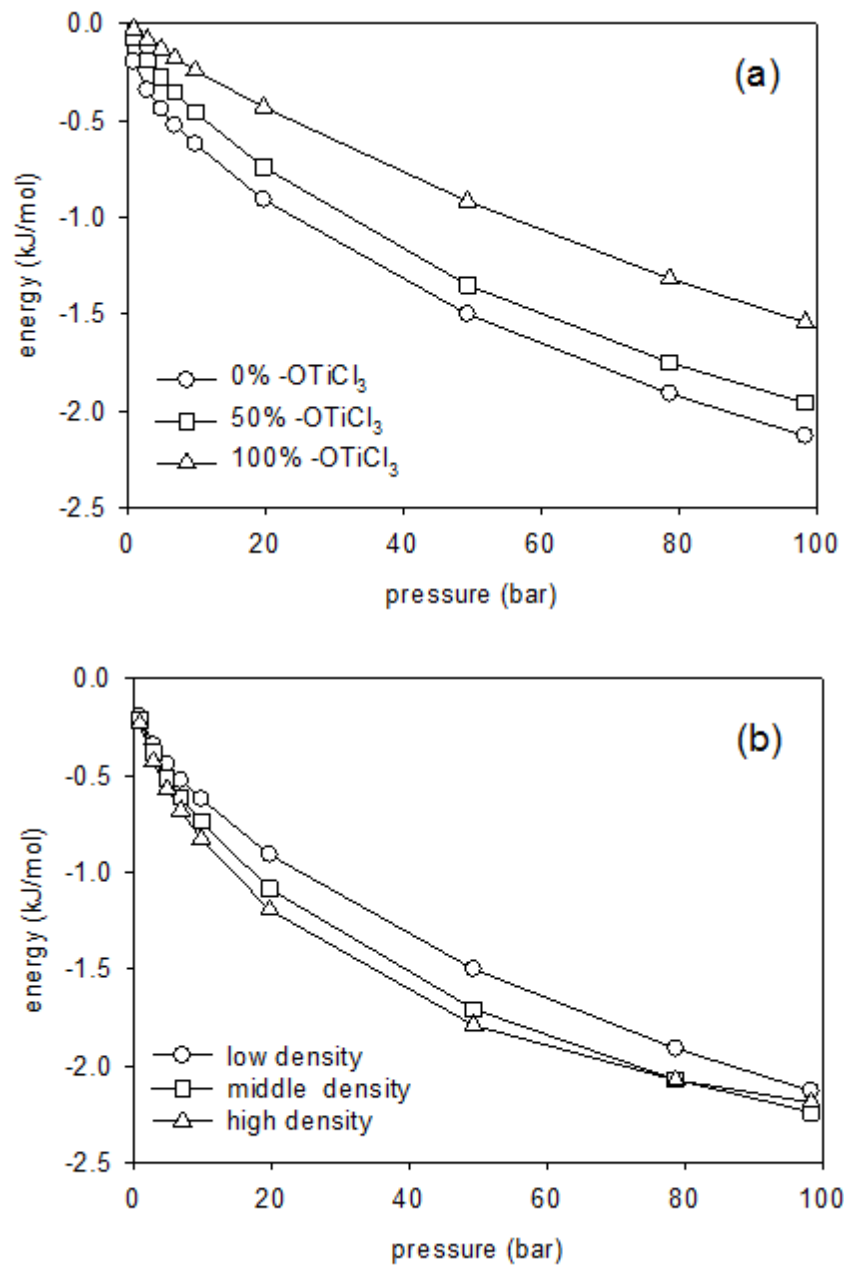


Figure 4.6. Energy between adsorbed CH₄ (a) low density structure with varying -OTiCl₃ content. (b) for 0 % -OTiCl₃ structure with varying density.

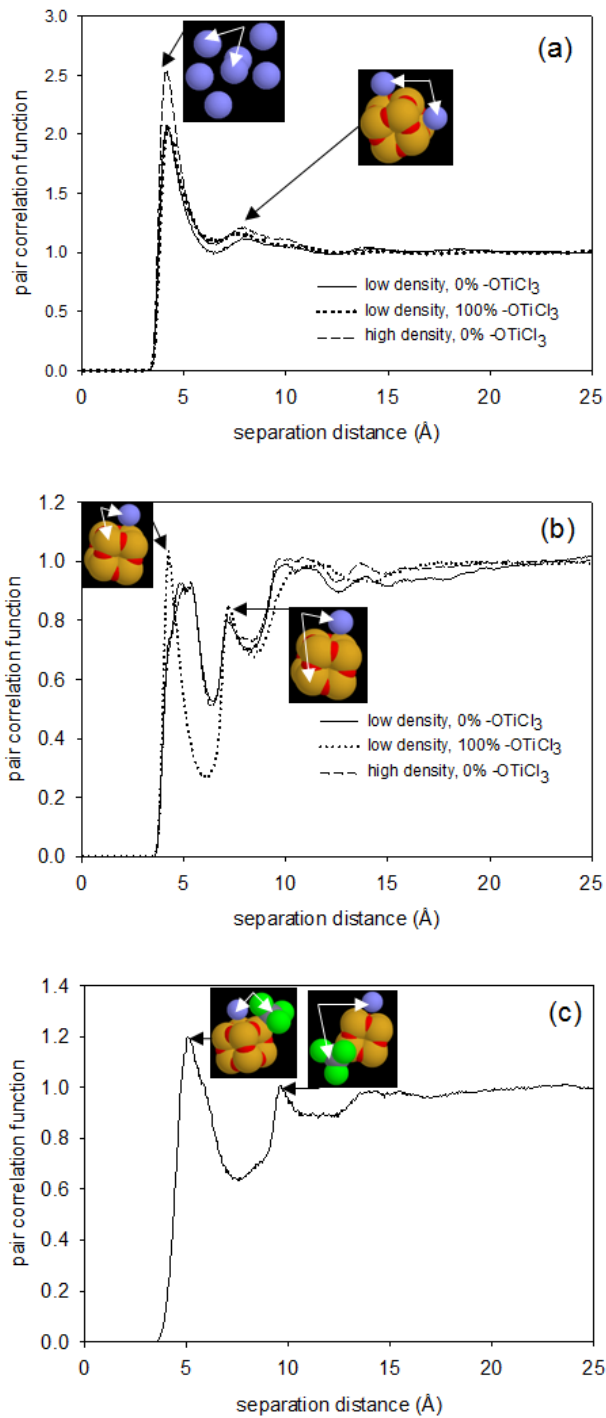


Figure 4.7. Pair correlation functions at 300 K and 100 bar. (a) between CH_4 - CH_4 (b) between CH_4 -Si (c) between CH_4 -Ti for low density 100 % - OTiCl_3 structure.

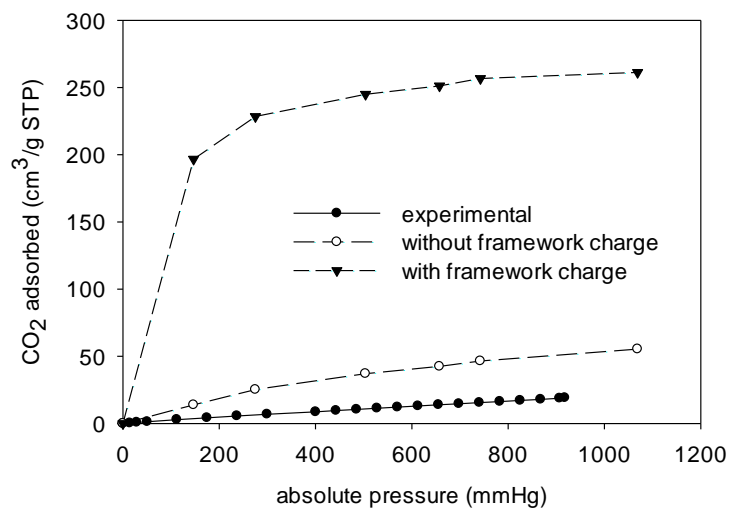


Figure 4.8. Comparison of experimental CO₂ adsorption isotherm at 273.15 K with simulated CO₂ adsorption isotherms at 300 K with and without framework charges for high density 0% - OTiCl₃ structure.

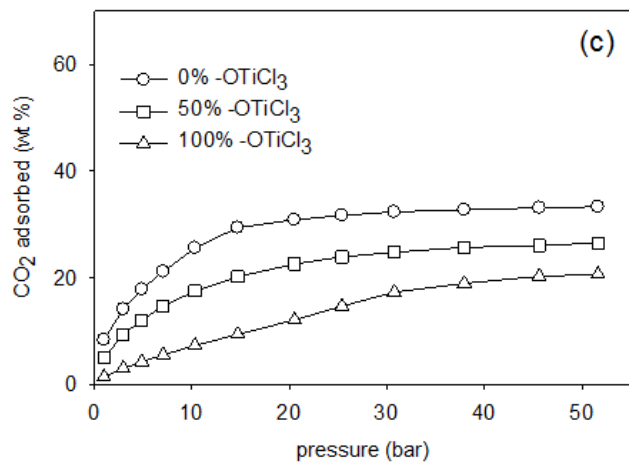
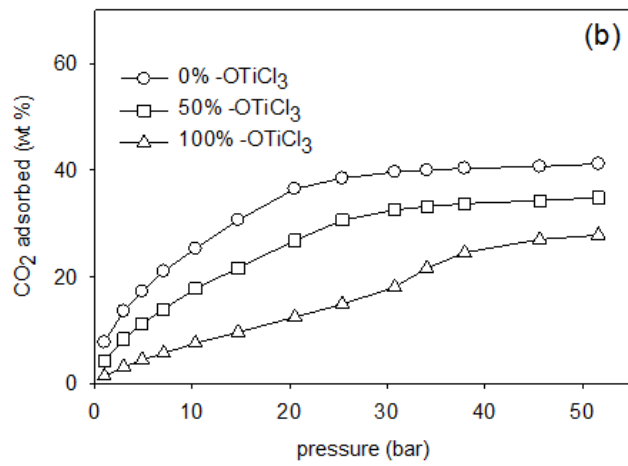
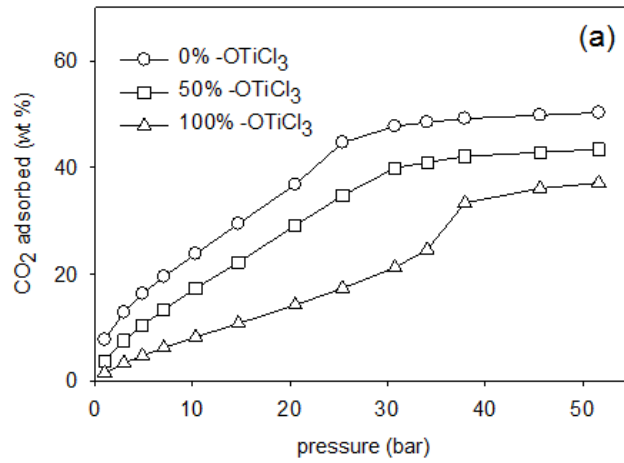


Figure 4.9. Gravimetric CO₂ adsorption isotherms at 300 K. (a) low density structure.(b) middle density structure.(c) high density structure.

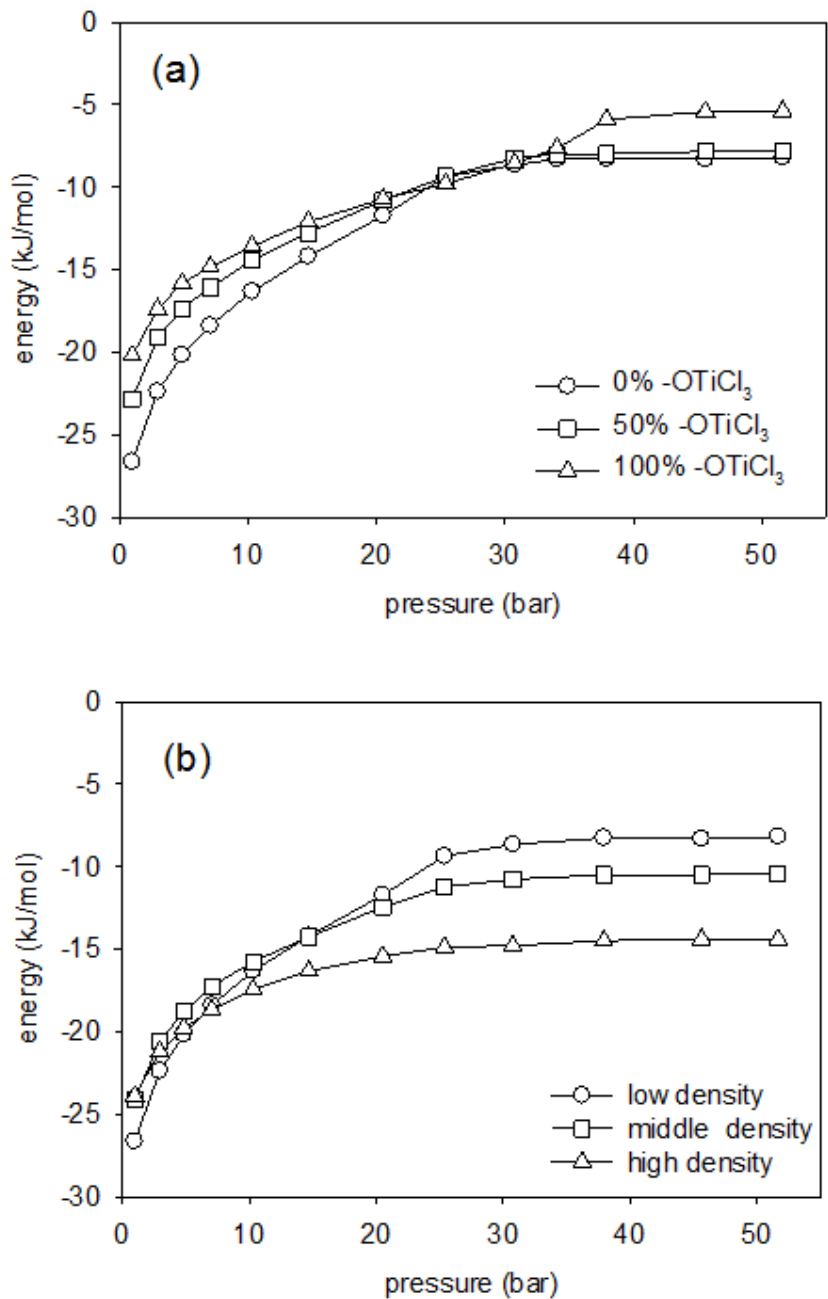


Figure 4.10. Energy between CO₂ and framework at 300 K. (a) low density structure with varying -OTiCl₃ content. (b) for 0% -OTiCl₃ structure with varying density.

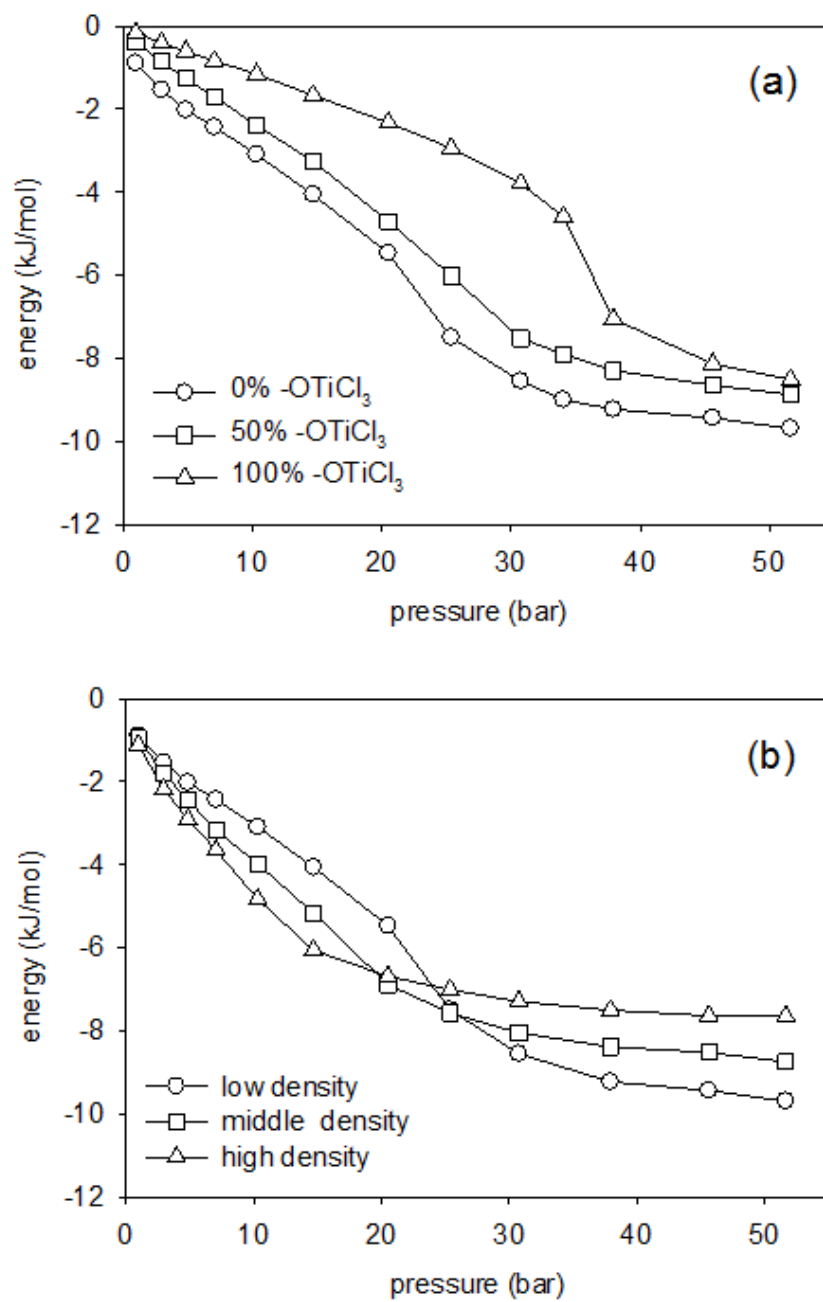


Figure 4.11. Energy between adsorbed CO₂. (a) low density structure with varying -OTiCl₃ content. (b) for 0 % -OTiCl₃ structure with varying density.

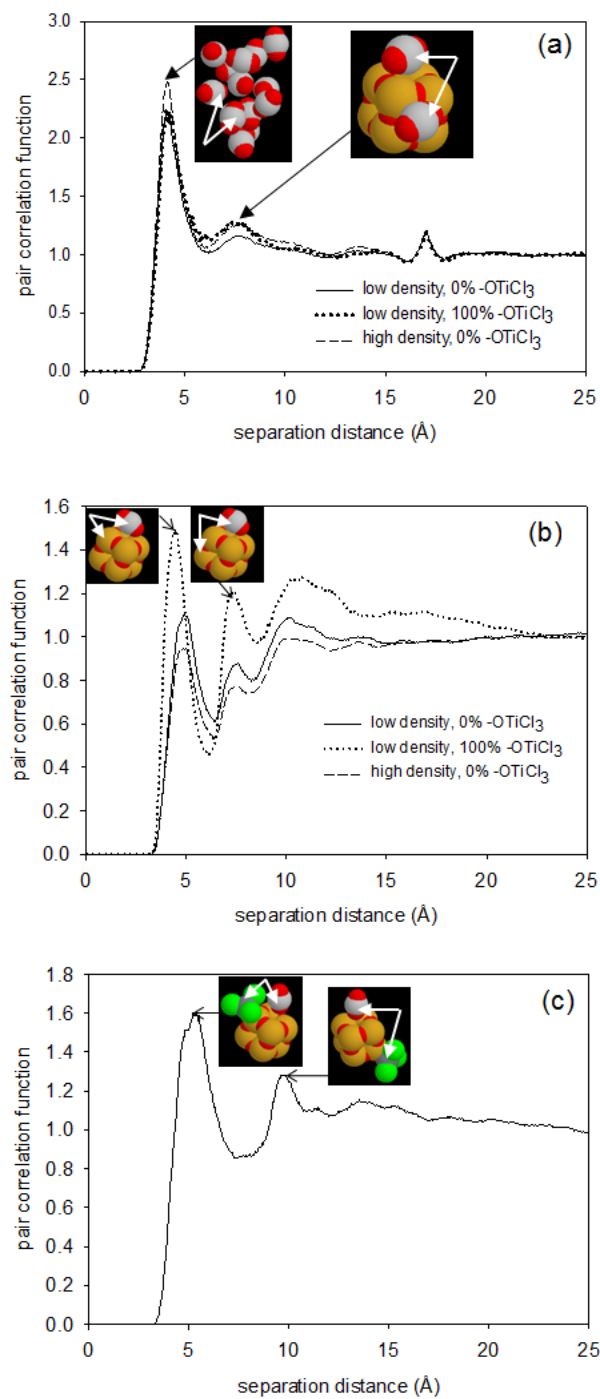


Figure 4.12. Pair correlation functions at 300 K and 20 bars. (a) between CO₂- CO₂ (b) between CO₂-Si (c) between CO₂-Ti for low density 100 % -OTiCl₃ structure.

Appendix E: Supplementary Document

E1. Thermodynamics considerations for Adsorption of Hydrogen

In general, the adsorption of hydrogen in the various structures as a function of temperature and pressure can be understood in terms of the competition between energetic and entropic contributions to the free energy.

$$\Delta A_{ads} = \Delta U_{ads} - T\Delta S_{ads} \quad (1)$$

where the distribution of molecules between the bulk and adsorbed (*ads*) phases is given by

$$\frac{N_{ads}}{N_{bulk}} = \exp\left(-\frac{\Delta A_{ads}}{k_B T}\right) = \exp\left(\frac{\Delta S_{ads}}{k_B}\right) \exp\left(-\frac{\Delta U_{ads}}{k_B T}\right) \quad (2)$$

As temperature decreases the entropic contribution to the free energy of adsorption, $-T\Delta S_{ads}$, diminishes. In the limit of absolute zero temperature, there is only an energetic effect. In the limit of infinite temperature, there is only an entropic effect. Between these asymptotes, the behavior shifts from one limit to the other. The energetic effect is captured by the energy of adsorption. The entropic effect is captured by the AV of the structures.

The competition between energetic and entropic factors can also be understood as a function of bulk pressure. At low pressure, there is little adsorbate fluid in the pore. As the loading increases, the ability for molecules to pack within the pore space (an entropic contribution) becomes relevant. Therefore, one typically observes a decrease in importance of the energetic effect and an increase in the importance of the entropic effect with an increase in loading. Such behavior has been shown for simple fluids in idealized pores*.

Furthermore, this simple competition can explain the relative preference for adsorption among pores of different sizes and shapes. Small and/or more curved pores have energetically deeper wells (due to more overlap of adsorbate-framework interactions) and greater confinement. Large and/or less curved pores have energetically shallower wells and less confinement. Thus the

energetic term favors small pores and the entropic term favors large pores. The relative preference for a given pore is determined by the balance between these two terms.

*Keffer, D., H.T. Davis, and A.V. McCormick, *The effect of nanopore shape on the structure and isotherms of adsorbed fluids*. Adsorption-Journal of the International Adsorption Society, 1996. **2**(1): p. 9-21.

E2. Figures

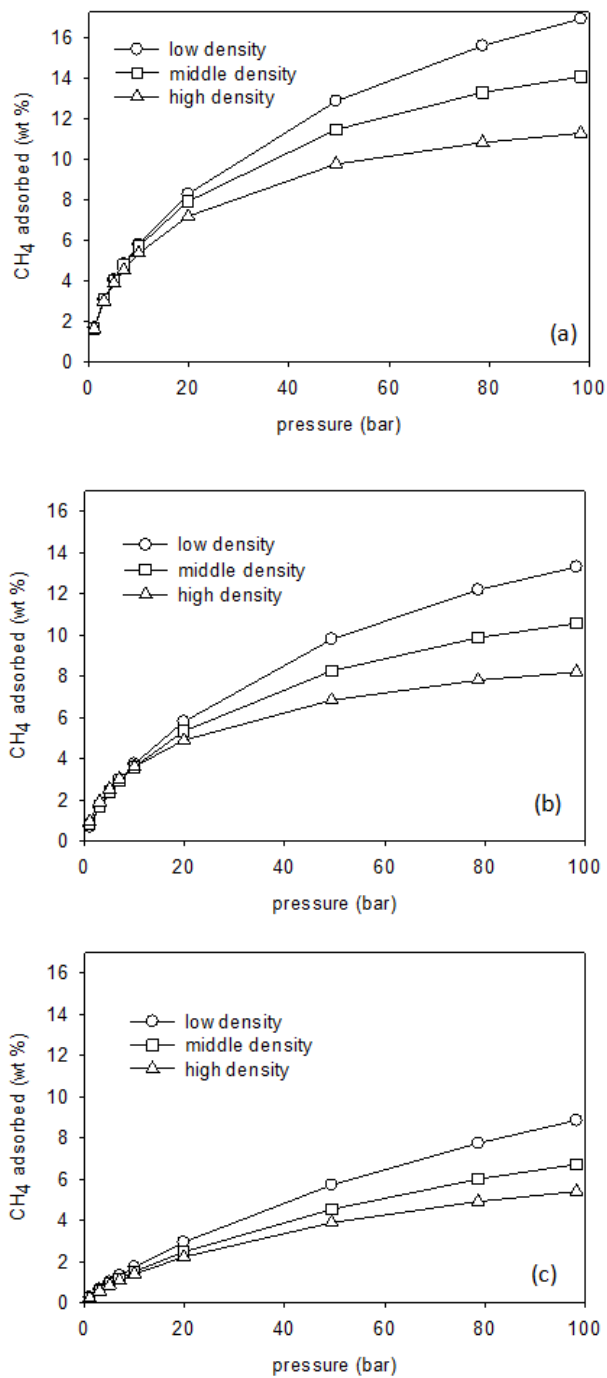


Figure 4.S1. Gravimetric CH₄ adsorption isotherms at 300 K. (a) 0 % -OTiCl₃ structure (b) 50 % -OTiCl₃ structure.(c) 100 % -OTiCl₃ structure.

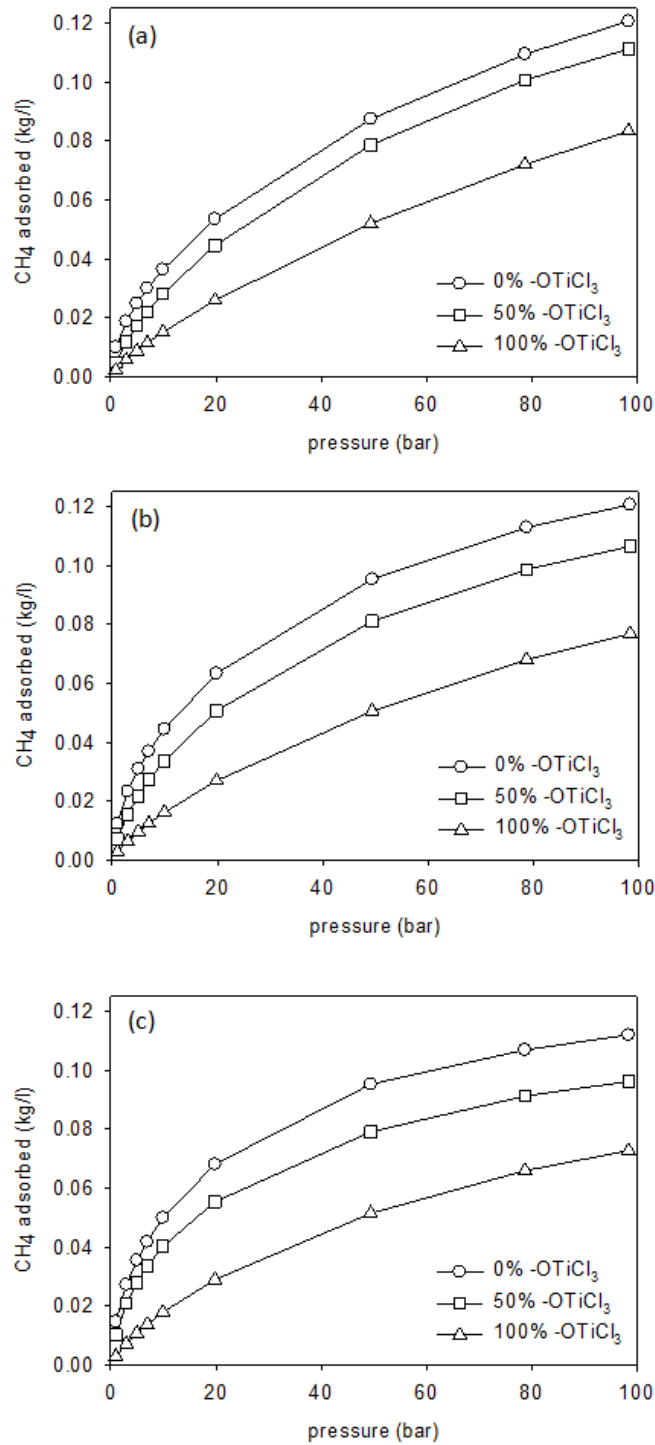


Figure 4.S2. Volumetric CH_4 adsorption isotherms at 300 K (a) low density structure.(b) middle density structure.(c) high density structure.

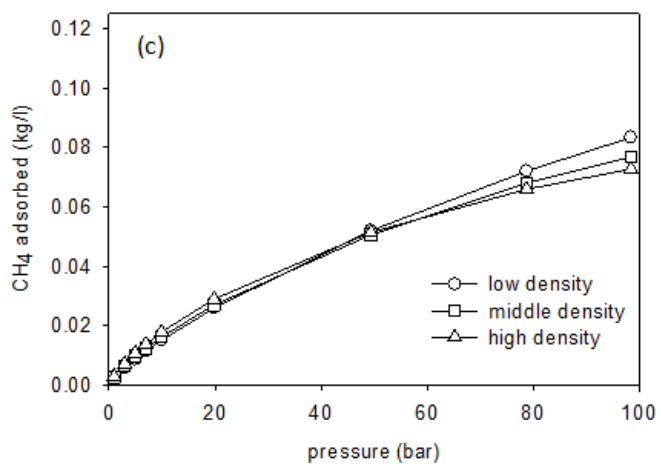
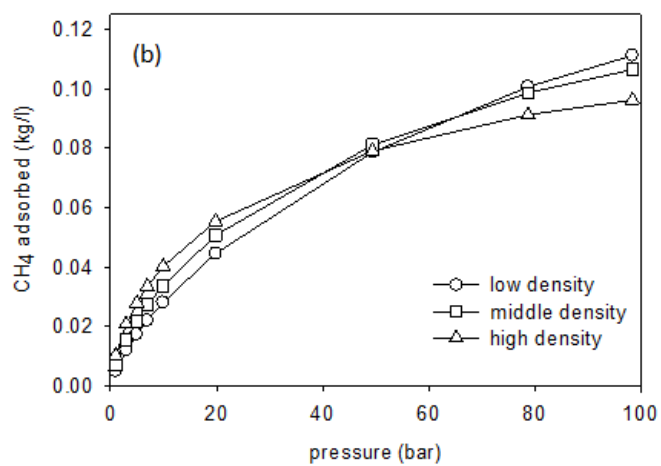
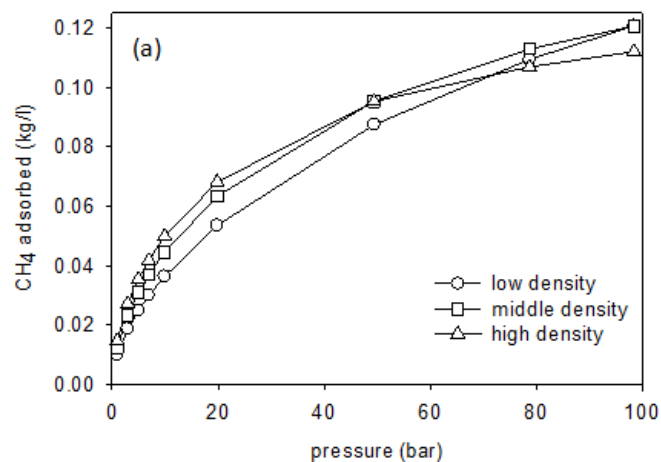


Figure 4.S3. Volumetric CH₄ adsorption isotherms at 300 K for 0 % -OTiCl₃ structure (a) for 50 % -OTiCl₃ structure (b) for 100 % -OTiCl₃ structure (c).

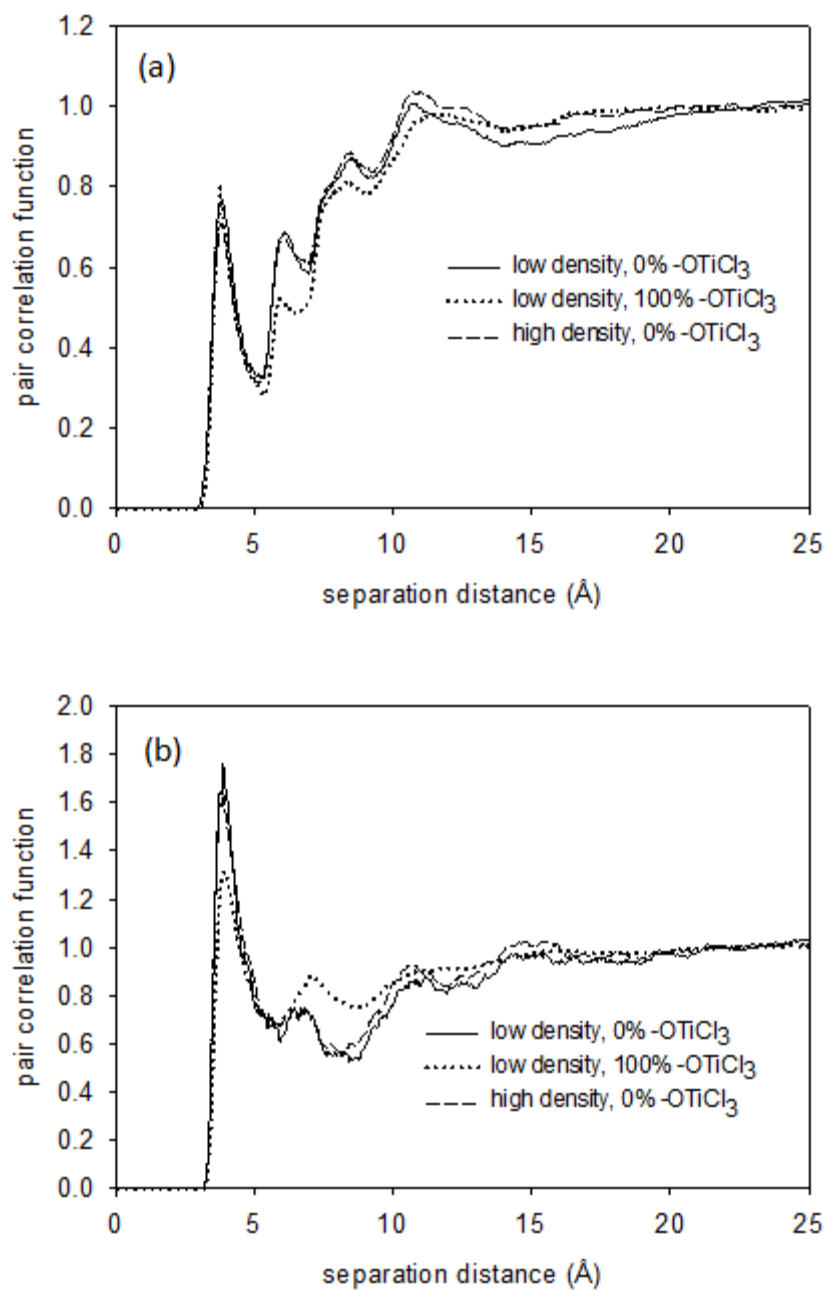


Figure 4.S4. Pair correlation functions at 300 K and 100 bars. (a) between CH₄-O (b) between CH₄-Cl.

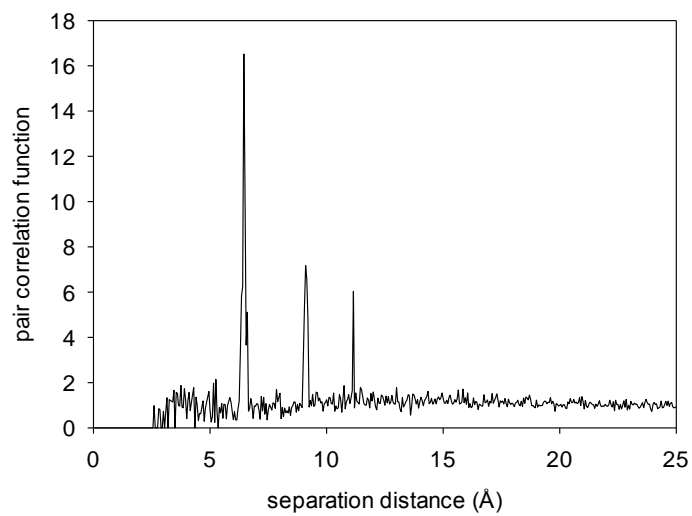


Figure 4.S5. Pair correlation function between Ti-Ti for the low density 100% -OTiCl₃ structure.

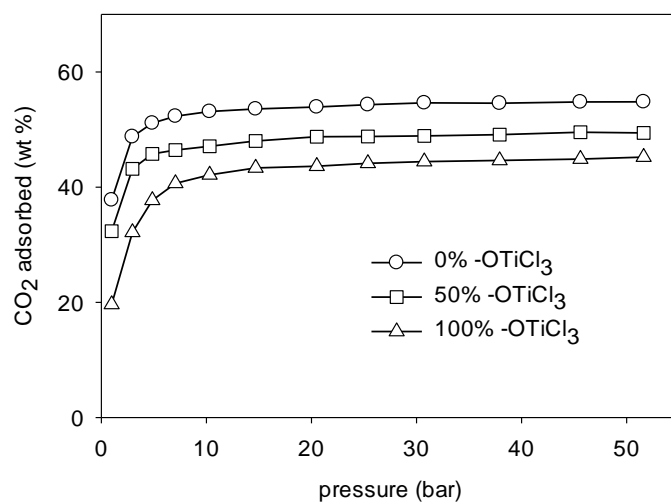


Figure 4.S6. Gravimetric CO₂ adsorption isotherms at 300 K. with framework charges for low density structure.

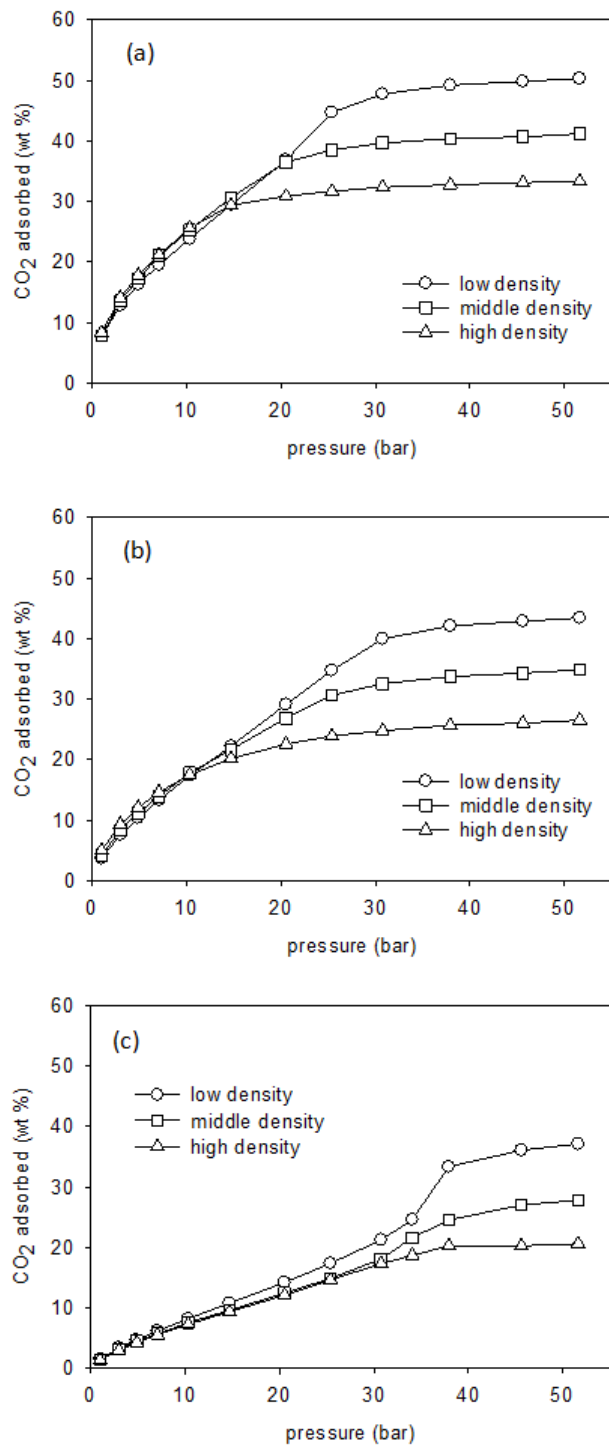


Figure 4.S7. Gravimetric CO₂ adsorption isotherms at 300 K. (a) 0 % -OTiCl₃ structure (b) 50 % -OTiCl₃ structure.(c) 100 % -OTiCl₃ structure.

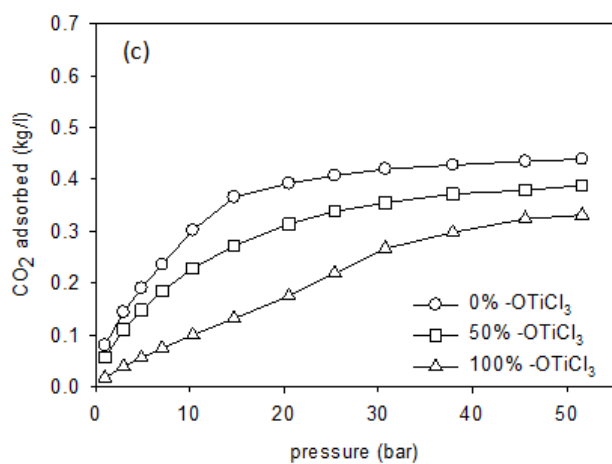
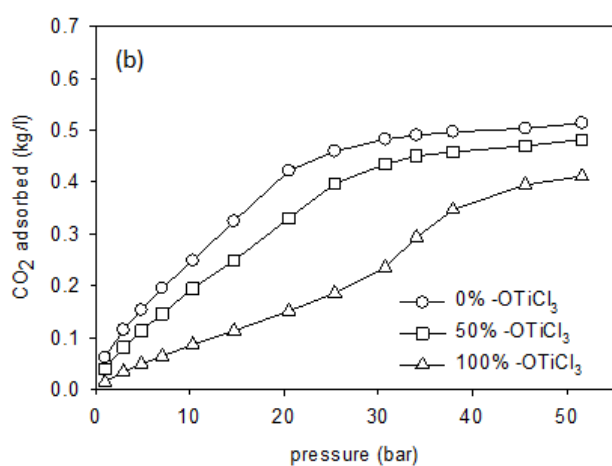
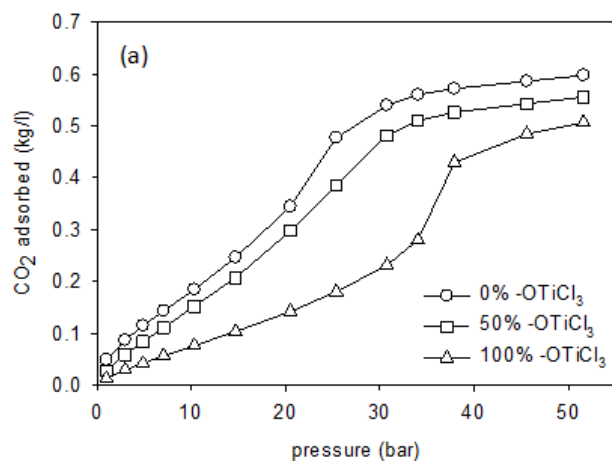


Figure 4.S8. Volumetric CO₂ adsorption isotherms at 300 K (a) low density structure.(b) middle density structure.(c) high density structure.

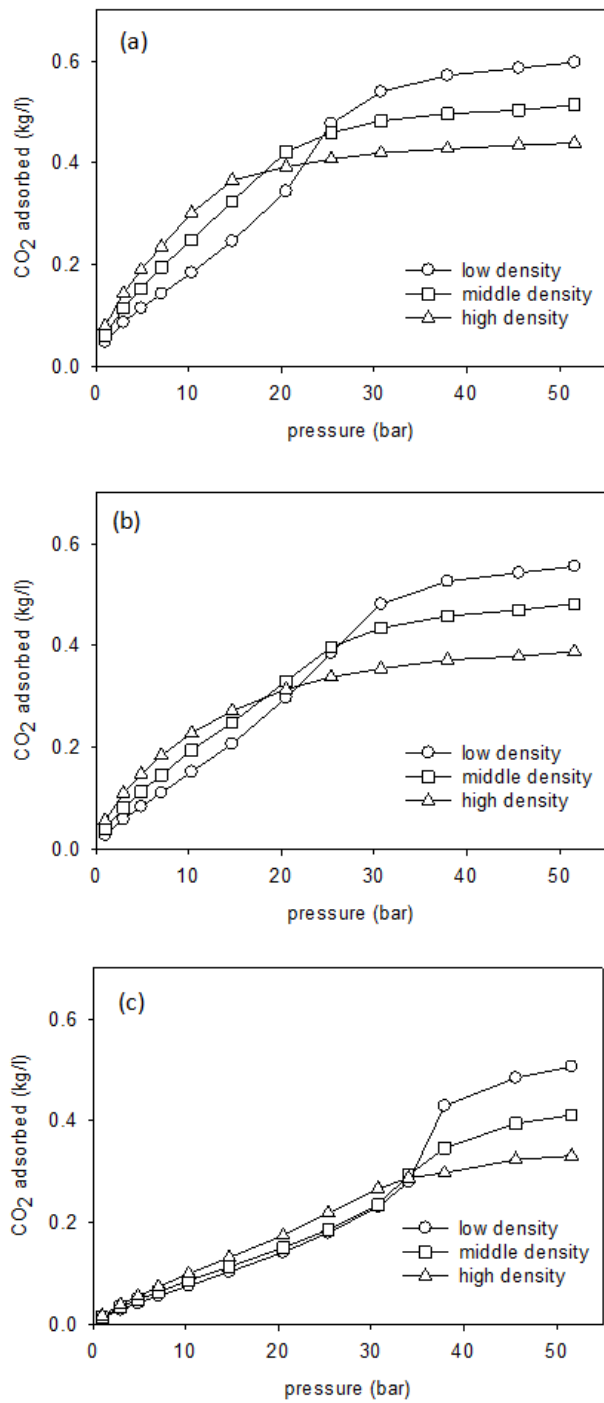


Figure 4.S9. Volumetric CO₂ adsorption isotherms at 300 K for 0 % -OTiCl₃ structure (a) for 50 % -OTiCl₃ structure (b) for 100 % -OTiCl₃ structure (c).

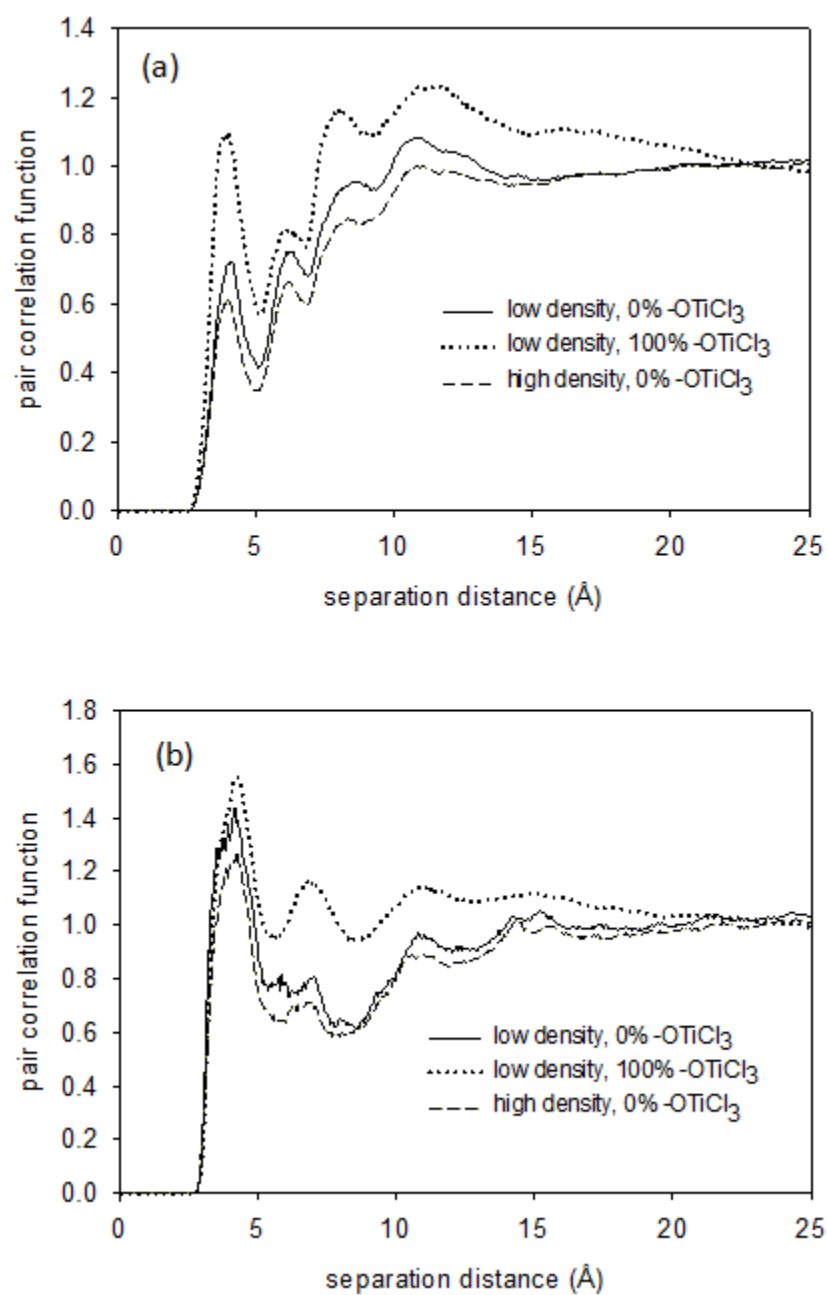


Figure 4.S10. Pair correlation functions at 300 K and 100 bars. (a) between CO₂-O (b) between CO₂-Cl.

CHAPTER 5

The Adsorption Properties of Amorphous, Metal-Decorated Nanoporous Silica for Mixtures of Carbon Dioxide, Methane and Hydrogen

This chapter is a slightly revised version of a paper under preparation by **Nethika S. Suraweera**, C.E. Barnes and D.J. Keffer:

Suraweera, N.S., Barnes, C.E., Keffer, D.J., “The Adsorption Properties of Amorphous, Metal-Decorated Nanoporous Silica for Mixtures of Carbon Dioxide, Methane and Hydrogen”, **In preparation**. Potential journal: *J. Phys. Chem C*

The use of “we” in this part refers to the co-authors and the author of this dissertation. My primary contributions to this paper include (1) all of the simulation work (2) analysis of data, and (3) most of the writing

Abstract

Amorphous, nanoporous adsorbents composed of spherosilicate building blocks and incorporating isolated metal sites were investigated for their ability to separate equimolar binary gas mixtures of CH₄/H₂, CO₂/H₂ and CO₂/CH₄. This novel adsorbent contains cubic silicate building blocks (spherosilicate units: Si₈O₂₀), which are cross-linked by SiCl₂O₂ bridges and decorated with either -OTiCl₃ or -OSiMe₃ groups. Adsorption isotherms, selectivity and energies at 300 K for pressures up to 100 bar for CH₄/H₂ and pressures up to 50 bar for CO₂/H₂ and CO₂/CH₄ were generated via molecular simulation describing physisorption using the Grand Canonical Monte Carlo (GCMC) method. Selectivity was also predicted using ideal adsorbed solution theory (IAST). A high density material with no -OTiCl₃ groups proved to be the best performing separator for the gas mixtures (among the spherosilicate structures studied in this work), with selectivity between 10 and 35 from high to low pressures for CH₄/H₂ mixtures, selectivity between 45 and 65 for CO₂/H₂ mixtures and selectivity between 2 to 4 for CO₂/CH₄ mixtures.

Keywords: Grand Canonical Monte Carlo simulation; spherosilicate; metal decorated silica; physisorption, hydrogen, methane, carbon dioxide

5.1 Introduction

Separation of gas mixtures containing CH_4 , CO_2 and H_2 is currently an interesting topic of studies due to modern developments of clean energy productions and addressing environmental issues like greenhouse gas emissions. Technologies for utilization of methane [1-3] and hydrogen [4-6] as cleaner fuels are currently being employed and improved. CH_4 is obtained mainly from natural gas (NG). Industrial and municipal landfill gas is also a source of CH_4 [3]. In both cases CH_4 should be separated from CO_2 and other impurities in order to increase the energy density and to protect methane transportation pipelines and tanks from corrosion caused by CO_2 .

For use as a clean fuel in fuel cells, hydrogen is mainly produced by steam re-forming of natural gas [7]. The synthetic gas produced by this process contains impurities like CO_2 and CH_4 and need to be removed before hydrogen can be used effectively. Due to rising levels of greenhouse gas emissions, separation of CO_2 from mixtures of gases such as the gas emitted from burning of non-renewable fossil fuels is of great importance [8]. Flue gas, which is the exhaust of fossil-fuel-based power plants, accounts for roughly 33–40% of global CO_2 emissions [9]. Therefore industrial carbon capture technologies are vital in environmental safety. Development of new, cost-effective, advanced technologies for CO_2 sequestration is continually being pursued.

Adsorption separation, using porous materials is a process that generally consumes low energy, and therefore is an attractive technology to use in gas separation applications. A variety of nanoporous materials, such as carbonaceous materials, zeolites and metal-organic frameworks (MOFs) have been investigated experimentally and computationally for the adsorptive separation of binary gas mixtures of CH_4 - CO_2 , H_2 - CH_4 and CO_2 - CH_4 [9-13]. In this work we investigate the adsorption of these three binary mixtures in a novel porous material made up of metal decorated spherosilicate matrices.

A synthetic strategy has been developed to make porous spherosilicate matrices that contain isolated titanium metal centers [14, 15]. These spherosilicate materials have an inorganic cross-linked polymer-like structure and atomically dispersed $-\text{OTiCl}_3$ groups. While in a reduced state, the Ti metal centers are predicted to bind hydrogen, as described by Bushnell *et al.* [16]. In an oxidized state, as is the case in this study, the Ti metal centers appear as $-\text{OTiCl}_3$, which have

been shown to interact with H₂, CH₄ and CO₂ through a physisorption, rather than chemisorption mechanism.[17, 18]

The framework of these adsorbents is composed of spherosilicate or silsesquioxane units, cage-like structures in the shape of cubes, hexagonal prisms, octagonal prisms, and decagonal or dodecagonal prisms [19, 20]. In this study we consider cubical polyhedral oligomeric silsesquioxane (POSS), comprised of 8 Si atoms, with formula (RSiO_{1.5})₈ where R is either a functional ending group or a cross linker which is connected to another spherosilicate unit. They belong to the family of polycyclic compounds consisting of silicon–oxygen bonds. The amorphous spherosilicate matrix provides a nanoporous, high-surface-area support to the structure. The ability to incorporate numerous elements throughout the periodic table has been experimentally reported [14, 15]. Applications are being developed for the metal–POSS compounds as metal catalyst supports [21]. Theoretical modeling studies have been previously done by McCabe *et al.* for POSS systems [22].

POSS structures have been studied for their adsorption capability. An organic–inorganic hybrid porous polymer namely polyaspartimide (PAI) was tested as a solid CO₂ adsorbent by Shanmugam *et al.*[23]. Adsorption of copper and nickel ions in aqueous solution using nano-cellulose hybrids containing R-POSS, as a novel biosorbent was studied by Xie *et al.* [24]. Hongbo *et al.* observed strong adsorption energies for N₂ molecules, resulting in high adsorptive capacities in the study of adsorption and desorption properties of hybrid aerogels derived from methacryloxypropyltrimethoxysilane based silsesquioxane [25]. Maiti *et al.* investigated hydrogen catalysis and sequestration in Pd-POSS systems [26].

The class of adsorbents studied in this work has been synthesized in a manner in which the surface area and free volume of the silica matrix and amount of titanium present (as -OTiCl₃) in the material can be controlled [14, 15, 21]. In our previous work [17, 18] we computationally investigated pure component gas adsorption of H₂, CH₄ and CO₂ and the results were compared with the experimental observations. In this paper we report the results of molecular-level simulations to study physisorption of the equimolar binary mixture of CH₄/H₂, CO₂/H₂ and CO₂/CH₄ in these materials.

5.2 Simulation Methods

Models for spherosilicate structures were generated using a coarse grain method and detailed description about this procedure is included in our previous work [17, 18]. To summarize, 4 distinct groups were identified in these amorphous materials to represent as 4 different coarse grain beads, which are silicate cubes (consisting of 8 Si atoms and 12 O's), O_2SiCl_2 bridges (that connect the cubes to each other), and two groups that terminally bind to the vertices of the silicate cubes, $-OTiCl_3$ and $-OSi(CH_3)_3$ (trimethylsilyl: $-OSiMe_3$) (Figure 5.1:(a),(b),(c) and (d)). The beads were placed in a cubic simulation box to satisfy the appropriate distances between connected beads and angles between sequences of three beads while the system agrees with the experimentally determined stoichiometry and density along with the surface area and fraction of accessible volume. A mesoscale level energy minimization was performed for the coarse grain structure using canonical Monte Carlo simulation (in which beads were translated) in order to avoid overlap between beads and to obtain a stable structure. Next the coarse grain beads were replaced with the relevant atomic descriptions and rotated into correct orientations using the downhill simplex method [27]. A coarse gain structure and an atomistic structure are shown in Figure 5.1 (e) and (f).

We developed and studied nine structures obtained by varying two physical properties at three levels. First the density of the adsorbent and the second is $-OTiCl_3$ content. The three levels of density are low, medium and high. The three levels of $-OTiCl_3$ content corresponded to 0%, 50% and 100%. The accessible volume (AV) and surface area (SA) were calculated for each structure using geometrical methods that has been used in the past for calculating SA and AV in MOFs [28, 29] and polymer membranes [30]. Details of these nine structures are included in Table 5.1.

Grand Canonical Monte Carlo Simulations were used to perform adsorption simulations in which the chemical potential (μ), volume (V) and temperature (T) of the system are fixed. Four types of moves were included in the GCMC simulations: (i) center-of-mass translation, (ii) center-of-mass rotation (iii) molecule insertion and (iv) molecule deletion, which are randomly attempted in a ratio of 3:3:2:2. For each simulation, 10 million configurations were performed for system equilibrium and another 10 million configurations were performed for data production. Three dimensional standard periodic boundary conditions and the minimum image

convention were employed. Additional details of GCMC simulations are included in our previous studies [17, 18].

The framework is considered to have a rigid structure. Lennard-Jones (LJ) parameters for the atoms in the framework are taken from the UFF potential [31] (values are listed in Table 5.2). A LJ potential was used model H₂. The hydrogen molecule is treated as a single LJ particle (united atom model) and parameters are taken from the universal force field (UFF)[31] (parameter values are listed in Table 5.2). Our previous study for hydrogen adsorption in IRMOFs[29] shows that the potential with these parameters has been shown to be able to reproduce results obtained from the Silvera-Goldman (SG) [32] potential within 5% [33]. Individual CO₂ molecules are considered to be rigid and linear. The interactions among CO₂ molecules are modeled with the TraPPE force field [34]. CO₂ adsorption simulations account for electrostatic interactions between CO₂ molecules by placing point charges on each atom (parameter values are listed in Table 5.2). The united-atom TraPPE force field [35] was used to model the CH₄ molecule (Table 5.2). Both H₂ and CH₄ adsorption simulations do not account for electrostatic interactions. LJ cross-interaction parameters were determined by the Lorentz-Berthelot mixing rules [36].

The Lennard-Jones equation of state by Johnson *et al.*[37] was used to estimate the chemical potential of the bulk phase at a given temperature and pressure. In order to obtain bulk phase equimolar binary gas mixtures, an iterative series of bulk phase simulations were performed, in which the chemical potential of each species were adjusted until the mole fraction of each species converged to 0.5 (an equimolar binary mixture). Once the correct chemical potentials were determined, they were used for the adsorbed phase simulations to generate gas mixture adsorption properties in the sphaerosilicate adsorbents. Performing bulk simulations eliminates the error of approximate nature of the equation of state. Adsorption isotherms were generated by plotting the fractional loading obtained from the adsorbed phase simulation as a function of the pressure obtained from the bulk phase simulation. We chose the volume of the bulk and adsorbed phases such that the average number of adsorbate molecules in the system turned out to be bound by 500 and 2500.

Quantum mechanical calculations were used for validation of physisorption. It has been predicted that in a reduced state, isolated Ti atoms will cause gases to chemisorb [16]. In these materials, the Ti appears in an oxidized state, as -OTiCl₃. Therefore, we performed quantum

mechanical simulations to determine whether H₂, CO₂ and CH₄ would chemisorb in the presence of -OTiCl₃. Density Functional Theory (DFT) calculations were performed using the B3LYP functional in combination with the standard 6-311G(d,p) basis set, utilizing the Gaussian03 set of programs [38]. An initial geometry optimization of an isolated spherosilicate cube with one -OTiCl₃ group attached to it was performed. Next, a single molecule of either H₂, CH₄ or CO₂ was placed near the -OTiCl₃ group on the spherosilicate cube and a second geometry optimization was performed. We judged that no chemisorption took place on the basis of no change in the internal molecular structure of the adsorbate molecules. The H-H bond length of the H₂ molecule was changed by only 0.02% between the adsorbed and isolated states. The C-H bond length of the CH₄ molecule was changed by only 0.01% to 0.02% between the adsorbed and isolated states. The H-C-H bond angle in CH₄ was changed by only 0.09% to 0.2%. The C-O bond length of the CO₂ molecule differed by only 1.3% to 1.6% and O-C-O bond angle differed by only 0.28%. These DFT calculations validate the use of the non-reactive potentials in the classical GCMC and MD simulations.

Quantum mechanical calculations were also used for calculating partial charges of the framework atoms. This was useful in determining the importance of charge distribution in the framework on the adsorption of CO₂. The charge distribution for spherosilicate structures was calculated based on geometries of fragments optimized using DFT calculations in DFT calculations utilizing the B3LYP functional and standard 6-311G(d,p) basis set [38]. The electron distributions were mapped onto point charges centered at atom positions using Natural Bond Orbital (NBO) Analysis method [39, 40]. The resulting partial charges are shown in Table 5.2. Our previous work suggested that simulations with electrostatic interaction between CO₂-CO₂ but without the electrostatic interaction between CO₂-framework better agreed with comparable experimental data [18]. CO₂ adsorption studies in IRMOF-1 done by Walton *et al.* [41] also showed that simulations with electrostatic interaction between CO₂-CO₂ but without the electrostatic interaction between CO₂-framework better agreed with comparable experimental data. Therefore we decided to include the electrostatic charges only between CO₂-CO₂ in this study.

5.3 Results and Discussion

Adsorption isotherms were computed using GCMC simulations for equimolar binary mixtures of CH₄/H₂, CO₂/H₂ and CO₂/CH₄ at 300 K for all 9 structures studied. (pressure up to 100 bars for CH₄/H₂ and pressure up to 50 bars for CO₂/H₂ and CO₂/CH₄). Selectivity was calculated to get a better view of the ability for separation of gas mixtures in the porous materials. The selectivity for component A relative to component B is defined by

$$S = \frac{(x_A/x_B)}{(y_A/y_B)} \quad (1)$$

where x_A and x_B are the mole fractions of component A and B in the adsorbed phase respectively, and y_A and y_B are the mole fractions for A and B in the bulk phase respectively. Selectivity was also predicted using ideal adsorbed solution theory (IAST) [42] based on the single component gas adsorption data for H₂, CO₂ and CH₄ extracted from our past studies [17, 18]. Past research have proved the reliability of IAST predictions for gas mixtures adsorbed in porous materials [11, 43].

This discussion section is organized as follows. We begin with a thorough analysis of a single mixture, CO₂/H₂, in a single adsorbent, the 0% -OTiCl₃ low density structure. In this analysis, the selectivity, pure and mixture adsorption isotherms, energies and adsorption sites are specifically identified. This analysis provides a molecular-level understanding for the nanoscale structural characteristics governing macroscopic observables such as selectivity. After demonstrating the complete analysis for one combination of gas and adsorbent, we next provide a more general analysis, providing only selectivities and mixture isotherms, for all three binary mixtures in nine different adsorbents, in which density and Ti content are varied.

Figure 5.2 provides a comparison between selectivity for CO₂/H₂ in 0% -OTiCl₃ low density structure calculated using GCMC and IAST. In the low pressure regime, as pressure increases a quick decrease of selectivity is observed. Due to the dominating energetic effects, CO₂, which is energetically favored relative to H₂, preferably adsorbs at low pressure. However, when the pressure increases, entropic effects come into play and the smaller H₂ molecules are easily adsorbed into available pores, resulting in a decrease in the selectivity of CO₂ over H₂. At much higher pressures, due to strong electrostatic interactions between CO₂ molecules, the

selectivity for CO₂ over H₂ again increases. IAST predictions agree with the trend of selectivity calculated from GCMC in low pressure, but fail to predict the increasing selectivity with increasing pressure at high loadings for CO₂/H₂ mixtures. (Additional comparison plots for CO₂/H₂ mixtures are in Figure 5.S1, supplementary document, Appendix G). Yang et al. also reported poor agreement between IAST and GCMC selectivity for CO₂/H₂ in Cu-BTC, while the selectivity for other gas mixtures (CH₄/H₂, CO₂/CH₄) in Cu-BTC has a good agreement [11]. (Similarly for CH₄/H₂ (Figure 5.S2) and CO₂/CH₄ (Figure 5.S3) we observed good agreement between IAST and GCMC selectivity.)

Figure 5.3(a) presents CO₂ and H₂ adsorption isotherms for both equimolar mixture and pure component gases. In the equimolar mixture of CO₂/H₂, as the more favorable adsorbate CO₂ adsorbs at pressure x , approximately the same amount as pure component CO₂ adsorbs at pressure $x/2$. This observation re-establishes the accuracy of our calculations, because in an equimolar mixture the partial pressure of CO₂ is half of the total pressure, and adsorbs nearly the same amount of CO₂ as a pure component at same pressure. (while the amount of H₂ adsorbed is much less compared to CO₂ in CO₂/H₂ mixture). We observe the similar behavior for every different mixture of gases in every structure.

Figures 5.3(b) and 5.3(c) show the energies of adsorption for CO₂ and H₂ respectively. The energy of adsorption is the difference between the energy of the adsorbed phase and the energy of the bulk phase. In practice, it is the contribution of the potential energy due to adsorbate-adsorbent interactions in the adsorbed phase, which is the dominant term. It is clear that CO₂ energies (Figure 5.3(b)) are significantly stronger than H₂ (Figure 5.3(c)) both in terms of adsorbate-framework and adsorbate-adsorbate components. The CO₂-framework interactions increase (become less favorable) with pressure, while H₂-framework interactions increase with pressure at low loadings, but remain almost constant at higher loadings. We can see some noise in H₂-framework interactions. Considering the very low H₂ adsorption compared to CO₂, this level of noise is acceptable. The complete, tabulated isotherm data and energy data for all 27 systems are also included in supplementary document, Appendix G (Tables 5.S1, 5.S2, 5.S3 and 5.S4).

In our previous studies for pure component adsorption of H₂, CO₂ and CH₄, using pair correlation functions (PCFs), we identified the favorable adsorption sites for gases in the

spherosilicate structures are located in front of a spherosilicate cube [17, 18]. This observation remains true for the gas mixtures. Figure 5.4 illustrates the snapshots of gas mixtures adsorbed in 0% -OTiCl₃ low density structure. Examples of adsorbates bound in the most energetically favorable sites are circled.

Having discussed the selectivity, isotherms, adsorption energy and adsorption sites observed in the 0%-OTiCl₃ low density structure, we next discuss the comparison of adsorption behavior in different structures based on -OTiCl₃ content and density for each gas mixture

5.3.1 CH₄/H₂ Binary Mixtures

A comparison of selectivity, as obtained from GCMC simulations, for CH₄ over H₂ in structures in which the framework density and -OTiCl₃ content vary is presented in Figure 5.5(a) and Figure 5.6(a) respectively. As expected based on the LJ well-depth, CH₄ is preferentially adsorbed over H₂. In every structure, adsorption selectivity for CH₄ decreases with the increase of pressure at two steps: a quick decrease at pressure lower than about 10 bar, followed by a slow decrease with further increasing pressure. At low pressure energetic effects dominate, resulting in the preferential adsorption of the more energetically favorable CH₄. As pressure increases, entropic effects becomes significant and small H₂ molecules can be adsorbed easily into available pores, resulting in the decreased adsorption selectivity for CH₄.

In Figure 5.5(a) we see an increase in the density of the structure results in an increase in selectivity for CH₄. The pores are smaller in the higher density structures than the pores of low density structures and therefore have deeper energy wells. Structures with small pores exhibit higher CH₄/H₂ adsorption selectivity than the structures with large pores due to stronger adsorption of CH₄ over H₂ in smaller pores compared with large pores.

Figure 5.6(a) shows that CH₄/H₂ selectivity increases with a decrease in -OTiCl₃ content. The reason is two-fold. First, the energetic well-depth associated with Ti is lower than that for Si, reducing the energetic advantage of CH₄. Second, the presence of -OTiCl₃ groups results in slightly larger pores than structures with -OSiMe₃, again reducing the weight of the energetic contribution to the free energy.

The calculated adsorption selectivity with IAST for CH₄/H₂ agrees well with the GCMC simulations qualitatively for entire pressure range and quantitatively at low pressure (Figure

5.S2). The best CH₄/H₂ selectivity is obtained for high density 0% -OTiCl₃ structure which is between 10 and 35 from high to low pressure respectively. Separation of an equimolar mixture of hydrogen and methane has been performed in other porous materials; for example, at room temperature the selectivity is around 5 for MOF-5, between 10 and 20 for Cu-BTC[11], between 2 and 4 for ZIF-68 and between 1 and 3 for ZIF-70 [43]. Compared to these, the spherosilicate structures are promising for CH₄-H₂ separation.

The observed selectivity for CH₄ over H₂ has its origin in the mixture isotherms. A comparison of gravimetric adsorption isotherms for CH₄ and H₂ is presented in Figure 5.7(a) for materials with varying density. When the selectivity of CH₄ over H₂ is high at low pressure, the wt% CH₄ adsorbed is almost same for low density, middle density and high density structures with same -OTiCl₃ content. When pressure increases, the wt% CH₄ adsorbed increases to the greatest extent for low density structures. While the 0% -TiCl₃ high density structure has the best selectivity for gas mixtures, the 0% -OTiCl₃ low density structure has the best gravimetric adsorption capability. As the high density adsorbent is heavier than the low density adsorbent there is a gravimetric penalty added when the adsorption capacity is measured in wt%.

The volumetric basis version of the isotherms are included in supplementary document (Appendix G) Figure 5.S4(a) for materials with varying density. When the isotherms are considered on a volumetric basis, we observe that the high density structures adsorb more CH₄ than low density structures. As CH₄ adsorption is favored by energetic effects, high density materials, which present deeper energy wells at the walls of the pores, have an advantage that can be seen only on a volumetric basis, where the high density materials adsorb more CH₄ than do the low density materials.

When different -OTiCl₃ contents are considered for the same density structures, low Ti structures adsorb more gas both gravimetrically (Figure 5.8(a)) and volumetrically (Figure 5.S5(a)). This observation agrees with our prior finding for pure component gas adsorption that inclusion of Ti sites in the adsorbent does not enhance gas storage capacity. On a gravimetric basis, there is a penalty for including Ti. On a volumetric basis, the energetic interaction of the adsorbates with Ti is much less than that with Si.

5.3.2 CO₂/H₂ Binary Mixtures

A comparison of selectivity, as obtained from GCMC simulations, for CO₂ over H₂ in structures with the framework density and -OTiCl₃ content vary is presented in Figure 5.5(b) and Figure 5.6(b) respectively. Energetically more favorable, CO₂ adsorbs preferably relative to the energetically less favorable H₂ as expected. The complete analysis of adsorption selectivity (both from GCMC and IAST) from the equimolar binary mixture of CO₂ and H₂ at 300 K for all nine structures is reported in supplementary document, Appendix G (Figure 5.S1). In most of the structures we see two distinct features in the changes of CO₂/H₂ selectivity. The first feature is a decrease of carbon dioxide selectivity at the low-pressure region, and the second is an increase of its selectivity with further increasing pressure. The first feature is caused by the same reason as that for CH₄/H₂, while the second feature is caused by the strong electrostatic interactions between carbon dioxide molecules at higher loadings. The structure with the smallest pores, which is the high density 0% -OTiCl₃ structure has a third feature added into its CO₂/H₂ selectivity plot: a slow decrease of selectivity at high pressures. This additional feature is due to the fact that at higher pressures, the entropic/packing effect starts dominating the adsorption, with easily adsorbed H₂ molecules, leading to a shape similar to that for the methane-hydrogen system.

Structures with small pores exhibit higher CO₂/H₂ adsorption selectivity than the structures with large pores due to the same reason as for CH₄/H₂, namely that the energetic interaction with the framework is enhanced in small pores. This observation is evident in the comparison presented in Figure 5.5(b) and Figure 5.6(b), where the pore size decreases with increasing density and decreasing -OTiCl₃ content.

The discrepancy between the calculated adsorption selectivity with IAST and with GCMC simulations is more significant for CO₂/H₂ (Figure 5.S1) as CO₂ and H₂ are much more different to each other in both size and chemistry. IAST does not predict the increase of CO₂ selectivity due to the strong interactions between CO₂ molecules at high pressure.

The best CO₂/H₂ selectivity obtained for spherosilicate structures is for high density 0% -OTiCl₃ structure, in which the selectivity is between 45 and 65. Separation of equimolar mixtures of hydrogen and carbon dioxide for other porous materials has been studied and the values of

selectivity at room temperature are reported. The selectivity is between 10 and 30 for MOF-5, between 100 and 150 for Cu-BTC[11],

In Figure 5.7(b), gravimetric isotherms for CO₂ show nearly the same wt% adsorption of CO₂ for all the density levels for structures with same -OTiCl₃ content at low pressure. However, at high pressure, the low density material shows more adsorption, due to the gravimetric penalty described in the previous section. Volumetric isotherms for CO₂ (Figure 5.S4(b)) show that high density structures adsorb more CO₂ than low density structures, as was the case for CH₄.

In Figure 5.8(b), where gravimetric adsorption isotherms for CO₂ and H₂ is presented as a comparison between the materials with varying -OTiCl₃ content, we note that CO₂ adsorption decreases with increasing -OTiCl₃ content, due to the low LJ well-depth of Ti. This is true for the volumetric (Figure 5.S5(b)) case as well.

Adsorption isotherms for the entropically favored H₂ shows that low density structures have better H₂ adsorption than high density structures, as shown in Figure 5.7(b). In Figure 5.8(b), we observe that the presence of Ti in the framework does not enhance H₂ adsorption either, except at very high loadings, where the secondary effect of larger pores of the higher -OTiCl₃ content materials entropically favors H₂ adsorption..

5.3.3 CO₂/CH₄ Binary Mixtures

A comparison of selectivity, as obtained from GCMC simulations, for CO₂ over CH₄ in structures in which the framework density and -OTiCl₃ content vary is presented in Figure 5.5(c) and Figure 5.6(c) respectively. The value of selectivity of CO₂ over CH₄ does not vary in a significant range (only between 2 and 4) and is low compared with the other two mixtures as CO₂ is only slightly more energetically favorable than CH₄. The selectivity of CO₂/CH₄ has very different behavior from both CH₄/H₂ system and CO₂/H₂ mixtures. Most of the structures show a slight increase with increasing pressure in the low pressure region, followed by a nearly pressure independent plateau at high pressure. Since the dynamic sizes of both CH₄ and CO₂ are similar, the packing effect is nearly identical for both gases. Therefore the energetic effects are dominant in the entire pressure range.

At low pressures, both gases are adsorb in the energetically favorable sites, and the strong electrostatic interactions between the CO₂ molecules enhance the adsorption of carbon dioxide

greatly, leading to a slight increase on carbon dioxide selectivity. As the pressure increases, both gases are packed in the available pores leading to nearly pressure independent carbon dioxide selectivity behavior. As shown in Figure 5.5(c), structures with small pores exhibit higher CO₂/CH₄ adsorption selectivity, due to the enhanced energetic interaction with the framework in small pores. As shown in Figure 5.6(c), -OTiCl₃ content has very little impact on CO₂/CH₄ selectivity.

Calculated adsorption selectivities from IAST for CO₂/CH₄ agree well with the GCMC simulations both qualitatively and quantitatively for entire pressure range. (The complete analysis of adsorption selectivity (both from GCMC and IAST) from the equimolar binary mixture of CO₂ and CH₄ at 300 K for all nine structures is reported in supplementary document, Appendix G (Figure 5.S3).)

Calculated adsorption selectivity values of CO₂/CH₄ vary between 2 to 4. Adsorption selectivity of carbon dioxide from the equimolar binary mixture of methane and carbon dioxide has been previously calculated. At room temperature for Cu-BTC, MOF-5, ZIF-68 and ZIF-70, the values are between 6 to 10, 2 to 4 [11], 12 to 20 and 8 to 20 [43] respectively.

A comparison of gravimetric adsorption isotherms for CO₂ and CH₄ is presented in Figure 5.7(c) for materials with varying density. The gravimetric isotherms for CO₂ show that framework density has little impact on CO₂ from this mixture. Volumetric isotherms (supplementary document, Appendix G Figure 5.S4(c)) for CO₂ show that high density structures adsorb more CO₂ than low density ones. In Figure 5.7(c), gravimetric CH₄ adsorption isotherms shows that low density structures have better CH₄ adsorption than high density structures. Volumetric isotherms for CH₄ (Figure 5.S4(c)) exhibit a cross-over in terms of the relative favorability of framework density with pressure. At low pressure high density materials adsorb more CH₄ and at high pressure low density materials adsorb more CH₄.

With the comparison of different -OTiCl₃ contents for the same density structures (gravimetric: Figure 5.8(c), volumetric: Figure 5.S5(c)), we observe that the Ti-free structures adsorb more gas, emphasizing that the inclusion of Ti sites in the adsorbent does not contribute to enhance gas storage capacity.

5.4. Conclusions

In this work, we investigated the adsorption of equimolar binary mixtures of CH₄/H₂, CO₂/H₂ and CO₂/CH₄ in adsorbents containing cubic silicate building blocks (sphaerosilicate units: Si₈O₂₀), which are cross-linked by SiCl₂O₂ bridges and decorated with either -OTiCl₃ or -OSiMe₃ groups. Nine different sphaerosilicate structures, in which framework density and -OTiCl₃ content were varied, were generated using a multiscale method combining mesoscale step and a molecular level modeling step. GCMC simulations were used to generate adsorption properties for the three different gas mixtures at 300 K and pressures up to 100 bar for the CH₄/H₂ mixture and pressures up to 50 bar for the CO₂/H₂ and CO₂/CH₄ mixtures.

For all three mixtures studied, the best selectivity by the physisorption process studied herein is a high density material with 0% -OTiCl₃ content. The presence of Ti as -OTiCl₃ does not enhance adsorption capacity or selectivity. Selectivity of CH₄/H₂ for the best gas separating sphaerosilicate structures ranges from 10 to 35 from high to low pressure, proving to be a good CH₄/H₂ separator compared to other materials. Selectivity of CO₂/H₂ is between 45 and 65 acting as a middle range separator compared to other materials. Selectivity of CO₂/CH₄ is between 2 to 4, a relatively poor result compared to other materials.

IAST calculations predict the selectivity calculated using GCMC to a good extent for the mixtures of CH₄/H₂, CO₂/CH₄. But for CO₂/H₂ mixtures, IAST is not a reliable prediction method for this non-ideal mixture at higher pressures.

Acknowledgements

This research was supported by the Sustainable Energy and Education Research Center at the University of Tennessee, by a grant from the National Science Foundation (DGE-0801470). This research project used resources of the National Institute for Computational Sciences (NICS) supported by NSF under agreement number: OCI 07-11134.5.

References

- [1] W.M. Frota, J.A.S. Sa, S.S.B. Moraes, B.R.P. Rocha and K.A.R. Ismail, *Natural gas: The option for a sustainable development and energy in the state of Amazonas*, Energy Policy. 38 (2010), pp. 3830-3836.
- [2] M. Taniowski, *Sustainable chemical technologies in production of clean fuels from fossil fuels*, Clean-Soil Air Water. 36 (2008), pp. 393-398.
- [3] H.R. Amini and D.R. Reinhart, *Regional prediction of long-term landfill gas to energy potential*, Waste Manage. 31 (2011), pp. 2020-2026.
- [4] I.P. Jain, *Hydrogen the fuel for 21st century*, International Journal of Hydrogen Energy. 34 (2009), pp. 7368-7378.
- [5] T.K. Mandal and D.H. Gregory, *Hydrogen: a future energy vector for sustainable development*, Proceedings of the Institution of Mechanical Engineers Part C-Journal of Mechanical Engineering Science. 224 (2010), pp. 539-558.
- [6] N.A. Kelly, T.L. Gibson, M. Cai, J.A. Spearot and D.B. Ouwerkerk, *Development of a renewable hydrogen economy: optimization of existing technologies*, International Journal of Hydrogen Energy. 35 (2010), pp. 892-899.
- [7] J.R. Hufton, S. Mayorga and S. Sircar, *Sorption-enhanced reaction process for hydrogen production*, Aiche Journal. 45 (1999), pp. 248-256.
- [8] T.A. Boden, G. Marland, and R.J. Andres, *Global, Regional, and National Fossil-Fuel CO₂ Emissions.*, Carbon Dioxide Information Analysis Center, Oak Ridge National Laboratory, U.S. Department of Energy, Oak Ridge, Tenn., (USA).
- [9] H.Q. Yang, Z.H. Xu, M.H. Fan, R. Gupta, R.B. Slimane, A.E. Bland and I. Wright, *Progress in carbon dioxide separation and capture: A review*, J. Environ. Sci. 20 (2008), pp. 14-27.
- [10] C.E. Wilmer, O.K. Farha, Y.S. Bae, J.T. Hupp and R.Q. Snurr, *Structure-property relationships of porous materials for carbon dioxide separation and capture*, Energy & Environmental Science. 5 (2012), pp. 9849-9856.
- [11] Q.Y. Yang and C.L. Zhong, *Molecular simulation of carbon dioxide/methane/hydrogen mixture adsorption in metal-organic frameworks*, J Phys Chem B. 110 (2006), pp. 17776-17783.
- [12] D. Wu, C.C. Wang, B. Liu, D.H. Liu, Q.Y. Yang and C.L. Zhong, *Large-scale computational screening of metal-organic frameworks for CH₄/H₂ separation*, Aiche Journal. 58 (2012), pp. 2078-2084.
- [13] P.F. N Florin, *Carbon capture technology: future fossil fuel use and mitigating climate change*, Grantham Institute for Climate Change, London (UK), 2010.
- [14] J.C. Clark, S. Saengerkdsb, G.T. Eldridge, C. Campana and C.E. Barnes, *Synthesis and structure of functional spherosilicate building block molecules for materials synthesis*, Journal of Organometallic Chemistry. 691 (2006), pp. 3213-3222.
- [15] J.C. Clark and C.E. Barnes, *Reaction of the Si₈O₂₀(SnMe₃)₈ building block with silyl chlorides: A new synthetic methodology for preparing nanostructured building block solids*, Chemistry of Materials. 19 (2007), pp. 3212-3218.
- [16] J.E. Bushnell, P. Maitre, P.R. Kemper and M.T. Bowers, *Binding energies of Ti+(H-2)(1-6) clusters: Theory and experiment*, J Chem Phys. 106 (1997), pp. 10153-10167.

- [17] N.S. Suraweera, A.A. Albert, J.R. Humble, C.E. Barnes and D.J. Keffer, *Hydrogen Adsorption and Diffusion in Amorphous, Metal-Decorated Nanoporous Silica*, Int. J. Hydrogen Energy. under review (2013).
- [18] N.S. Suraweera, A.A. Albert, M.E. Peretich, J. Abbott, J.R. Humble, C.E. Barnes and D.J. Keffer, *Methane and Carbon Dioxide Adsorption and Diffusion in Amorphous, Metal-Decorated Nanoporous Silica*, Mol Simulat. in press (2013).
- [19] D.B. Cordes, P.D. Lickiss and F. Rataboul, *Recent developments in the chemistry of cubic polyhedral oligosilsesquioxanes*, Chemical Reviews. 110 (2010), pp. 2081-2173.
- [20] T. Jaroentomeechai, P.K. Yingsukkamol, C. Phurat, E. Somsook, T. Osotchan and V. Ervithayasuporn, *Synthesis and reactivity of nitrogen nucleophiles-induced cage-rearrangement silsesquioxanes*, Inorganic Chemistry. 51 (2012), pp. 12266-12272.
- [21] N.N. Ghosh, J.C. Clark, G.T. Eldridge and C.E. Barnes, *Building block syntheses of site-isolated vanadyl groups in silicate oxides*, Chemical Communications. (2004), pp. 856-857.
- [22] C. McCabe, S.C. Glotzer, J. Kieffer, M. Neurock and P.T. Cummings, *Multiscale simulation of the synthesis, assembly and properties of nanostructured organic/inorganic hybrid materials*, Journal of Computational and Theoretical Nanoscience. 1 (2004), pp. 265-279.
- [23] N. Shanmugam, K.T. Lee, W.Y. Cheng and S.Y. Lu, *Organic-inorganic hybrid polyaspartimide involving polyhedral oligomeric silsesquioxane via Michael addition for CO₂ capture*, J. Polym. Sci. Pol. Chem. 50 (2012), pp. 2521-2526.
- [24] K.L. Xie, L.X. Jing, W.G. Zhao and Y.L. Zhang, *Adsorption removal of Cu²⁺ and Ni²⁺ from waste water using nano-cellulose hybrids containing reactive polyhedral oligomeric silsesquioxanes*, J. Appl. Polym. Sci. 122 (2011), pp. 2864-2868.
- [25] H.B. Ren, Y.C. Qin, C.W. Shang, Y.T. Bi and L. Zhang, *Adsorption and desorption properties of hybrid aerogels derived from MPMS-SSO at 77 K*, Rare Metal Materials and Engineering. 39 (2010), pp. 475-478.
- [26] A. Maiti, R.H. Gee, R. Maxwell and A.P. Saab, *Hydrogen catalysis and scavenging action of Pd-POSS nanoparticles*, Chem. Phys. Lett. 440 (2007), pp. 244-248.
- [27] B.P.F. William H. Press, Saul A. Teukolsky, William T. Vetterling *Numerical recipes: the art of scientific computing*, Cambridge University Press, New York, 1986.
- [28] H. Frost, T. Duren and R.Q. Snurr, *Effects of surface area, free volume, and heat of adsorption on hydrogen uptake in metal-organic frameworks*, J Phys Chem B. 110 (2006), pp. 9565-9570.
- [29] N.S. Suraweera, R.C. Xiong, J.P. Luna, D.M. Nicholson and D.J. Keffer, *On the relationship between the structure of metal-organic frameworks and the adsorption and diffusion of hydrogen*, Mol Simulat. 37 (2011), pp. 621-639.
- [30] J.W. Liu, N. Suraweera, D.J. Keffer, S.T. Cui and S.J. Paddison, *On the relationship between polymer electrolyte structure and hydrated morphology of perfluorosulfonic acid membranes*, J Phys Chem C. 114 (2010), pp. 11279-11292.
- [31] A.K. Rappe, C.J. Casewit, K.S. Colwell, W.A. Goddard and W.M. Skiff, *UFF, a full periodic-table force-field for molecular mechanics and molecular-dynamics simulations*, J Am Chem Soc. 114 (1992), pp. 10024-10035.
- [32] R.Q. Snurr, A.T. Bell and D.N. Theodorou, *A Hierarchical Atomistic Lattice Simulation Approach For The Prediction Of Adsorption Thermodynamics Of Benzene In Silicalite*, Journal of Physical Chemistry. 98 (1994), pp. 5111-5119.

- [33] C. Chakravarty, *Fourier Path-Integral Simulations of Para-H₂ and Ortho-D₂ Clusters* Molecular Physics. 84 (1995), pp. 845-852.
- [34] J.J. Potoff and J.I. Siepmann, *Vapor-liquid equilibria of mixtures containing alkanes, carbon dioxide, and nitrogen*, Aiche Journal. 47 (2001), pp. 1676-1682.
- [35] M.G. Martin and J.I. Siepmann, *Transferable potentials for phase equilibria. 1. United-atom description of n-alkanes*, J Phys Chem B. 102 (1998), pp. 2569-2577.
- [36] M.P. Allen and D.J. Tildesley, *Computer Simulation of Liquids*, Oxford Science Publications, Oxford, 1987.
- [37] J.K. Johnson, J.A. Zollweg and K.E. Gubbins, *The Lennard-Jones equation of state revisited*, Molecular Physics. 78 (1993), pp. 591-618.
- [38] M.J. Frisch, G. W. Trucks, H. B. Schlegel, G. E. Scuseria, M. A. Robb, J. R. Cheeseman, J. A. Montgomery, Jr., T. Vreven, K. N. Kudin, J. C. Burant, J. M. Millam, S. S. Iyengar, J. Tomasi, V. Barone, B. Mennucci, M. Cossi, G. Scalmani, N. Rega, G. A. P and H.B.S. G. W. Trucks, G. E. Scuseria, M. A. Robb, J. R. Cheeseman, J. A. Montgomery, Jr., T. Vreven, K. N. Kudin, J. C. Burant, J. M. Millam, S. S. Iyengar, J. Tomasi, V. Barone, B. Mennucci, M. Cossi, G. Scalmani, N. Rega, G. A. Petersson, H. Nakatsuji, M. Hada, M. Ehara, K. Toyota, R. Fukuda, J. Hasegawa, M. Ishida, T. Nakajima, Y. Honda, O. Kitao, H. Nakai, M. Klene, X. Li, J. E. Knox, H. P. Hratchian, J. B. Cross, V. Bakken, C. Adamo, J. Jaramillo, R. Gomperts, R. E. Stratmann, O. Yazyev, A. J. Austin, R. Cammi, C. Pomelli, J. W. Ochterski, P. Y. Ayala, K. Morokuma, G. A. Voth, P. Salvador, J. J. Dannenberg, V. G. Zakrzewski, S. Dapprich, A. D. Daniels, M. C. Strain, O. Farkas, D. K. Malick, A. D. Rabuck, K. Raghavachari, J. B. Foresman, J. V. Ortiz, Q. Cui, A. G. Baboul, S. Clifford, J. Cioslowski, B. B. Stefanov, G. Liu, A. Liashenko, P. Piskorz, I. Komaromi, R. L. Martin, D. J. Fox, T. Keith, M. A. Al-Laham, C. Y. Peng, A. Nanayakkara, M. Challacombe, P. M. W. Gill, B. Johnson, W. Chen, M. W. Wong, C. Gonzalez, and J. A. Pople, *Gaussian 03, Revision C.02*, Gaussian, Inc., Wallingford CT, 2004.
- [39] J.P. Foster and F. Weinhold, *Natural hybrid orbitals*, J Am Chem Soc. 102 (1980), pp. 7211-7218.
- [40] A.E. Reed, L.A. Curtiss and F. Weinhold, *Intermolecular interactions from a natural bond orbital, donor-acceptor viewpoint*, Chemical Reviews. 88 (1988), pp. 899-926.
- [41] K.S. Walton, A.R. Millward, D. Dubbeldam, H. Frost, J.J. Low, O.M. Yaghi and R.Q. Snurr, *Understanding inflections and steps in carbon dioxide adsorption isotherms in metal-organic frameworks*, J Am Chem Soc. 130 (2008), pp. 406-+.
- [42] A.L. Myers and J.M. Prausnitz, *THERMODYNAMICS OF MIXED-GAS ADSORPTION*, Aiche Journal. 11 (1965), pp. 121-+.
- [43] J.C. Liu, S. Keskin, D.S. Sholl and J.K. Johnson, *Molecular Simulations and Theoretical Predictions for Adsorption and Diffusion of CH₄/H₂ and CO₂/CH₄ Mixtures in ZIFs*, J Phys Chem C. 115 (2011), pp. 12560-12566.

Appendix F: Tables and Figures

Table 5 1. Structural details for selected spherosilicate structures

Structure	Number of groups in a 50×50×50 Å ³ simulation box				Volume fraction	Density (g/cc)	Accessible Volume		Surface Area	
	Cubes	Bridges	TiCl ₃	TMS			(cm ³ /g)	Å ³ per simulation box	(m ² /g)	Å ² per simulation box
0 % -OTiCl ₃ low density	40	41	0	248	0.73	0.59	1.23	90800	4810	35500
50 % -OTiCl ₃ low density	40	41	124	124	0.74	0.72	1.02	92100	4090	37000
100 % -OTiCl ₃ low density	40	41	248	0	0.75	0.86	0.88	94200	3350	35900
0 % -OTiCl ₃ medium density	50	51	0	308	0.66	0.73	0.90	82400	4790	44000
50 % -OTiCl ₃ medium density	50	51	154	154	0.67	0.90	0.75	84400	3990	44900
100 % -OTiCl ₃ medium density	50	51	308	0	0.69	1.07	0.65	86800	3320	44200
0 % -OTiCl ₃ high density	60	61	0	368	0.59	0.88	0.68	74400	4680	51400
50 % -OTiCl ₃ high density	60	61	184	184	0.61	1.08	0.57	76500	3970	53400
100 % -OTiCl ₃ high density	60	61	368	0	0.64	1.27	0.50	79500	3270	52000

Table 5 2. The Lennard-Jones parameters and partial atomic charges for absorbent and adsorbate atoms.

Atom	σ (Å)	ϵ/k (K)	q (e)
framework atoms			
H	2.571	22.142	0.22
C	3.431	52.839	-1.08
O	3.118	30.194	-1.26 (O in bridge) -1.00 (O in -OTiCl ₃) -1.25 (O in -OSiMe ₃) -1.26 (O in cube)
Si	3.826	202.43	2.53 (Si in bridge) 1.87 (Si in -OSiMe ₃) 1.94 (Si in cube)
Cl	3.516	114.31	-0.35
Ti	2.829	8.5604	1.42
adsorbate atoms and united-atom			
H ₂	2.96	34.2	0
CH ₄	3.81	148.2	0
C in CO ₂	2.80	27.0	0.70
O in CO ₂	3.05	79.0	-0.35

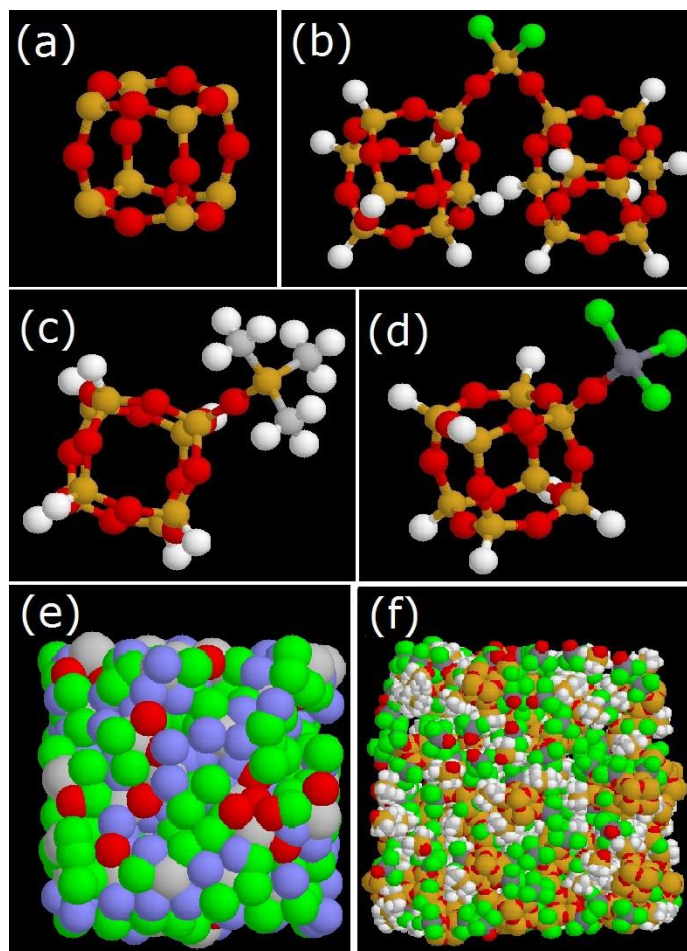


Figure 5.1. (a) spherosilicate cube, (b) O_2SiCl_2 bridge, (c) $-\text{OSiMe}_3$ end group and (d) $-\text{OTiCl}_3$ end group. (e) Course grain structure (Cubes: grey, bridges: red, $-\text{OTiCl}_3$:green, $-\text{OSiMe}_3$: blue) (f) Atomic structure. (Cl-green, Ti-dark grey, Si-yellow/orange, O-red, C-light gray, H- white)

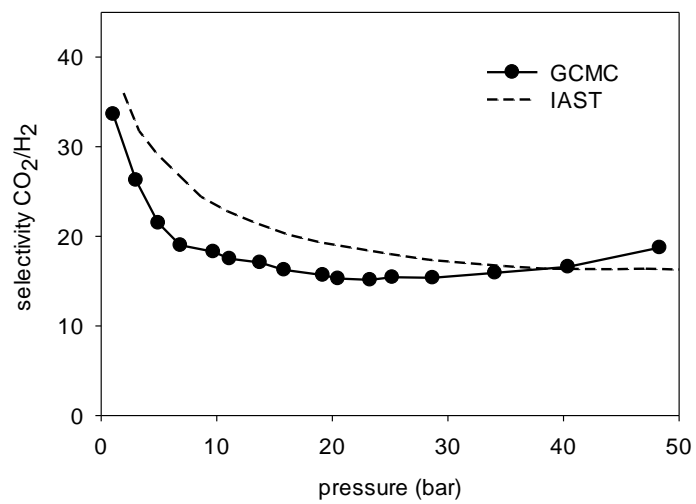


Figure 5.2. Selectivity comparison for CO₂/H₂ mixture adsorption in 0% -OTiCl₃ low density structure

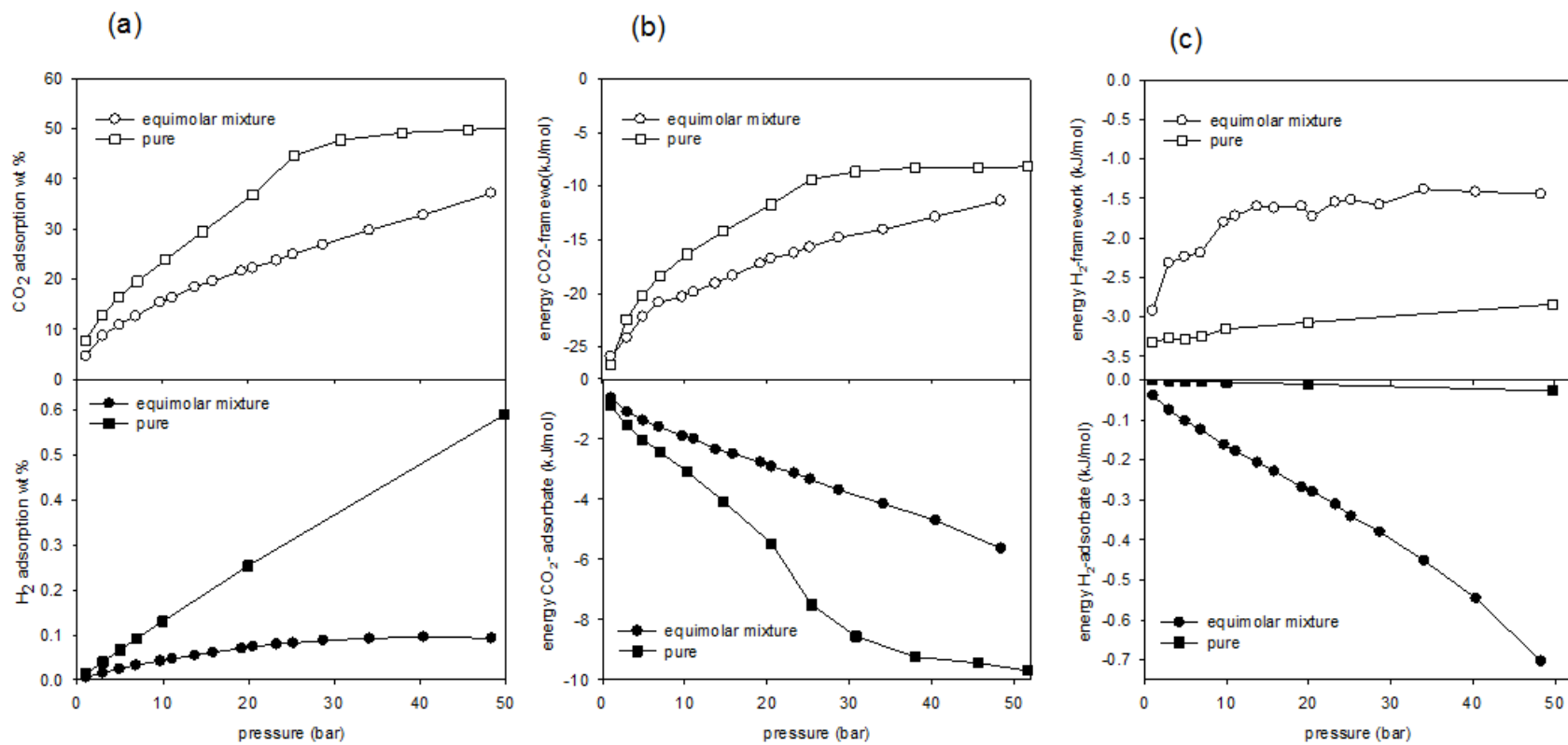


Figure 5.3. CO₂/H₂ mixture adsorption in 0% -OTiCl₃ low density structure (a) Isotherms, (b) Energy for CO₂, (c) Energy for H₂.

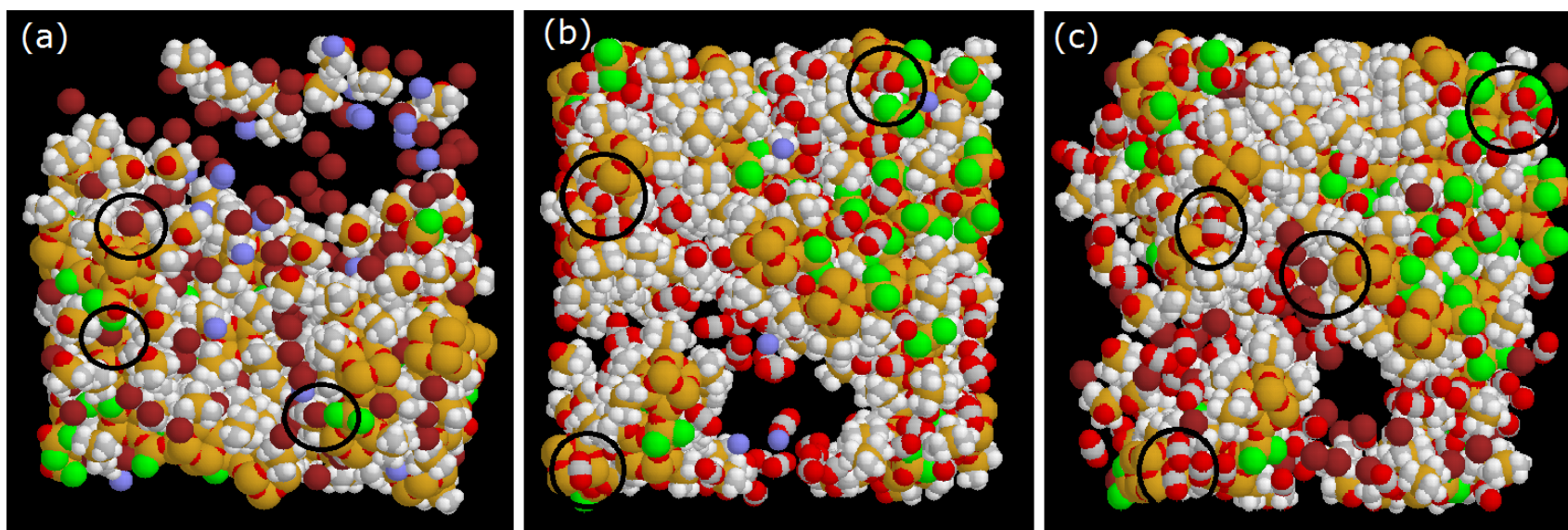


Figure 5.4. Snap shots for gas mixture adsorption (a) CH₄/H₂, (b) CO₂/H₂, (c) CO₂/CH₄. (adsorbed CH₄ molecules-maroon, adsorbed H₂ molecules-blue, Cl-green, Ti-dark grey, Si-yellow/orange, O-red, C-light gray, H- white)

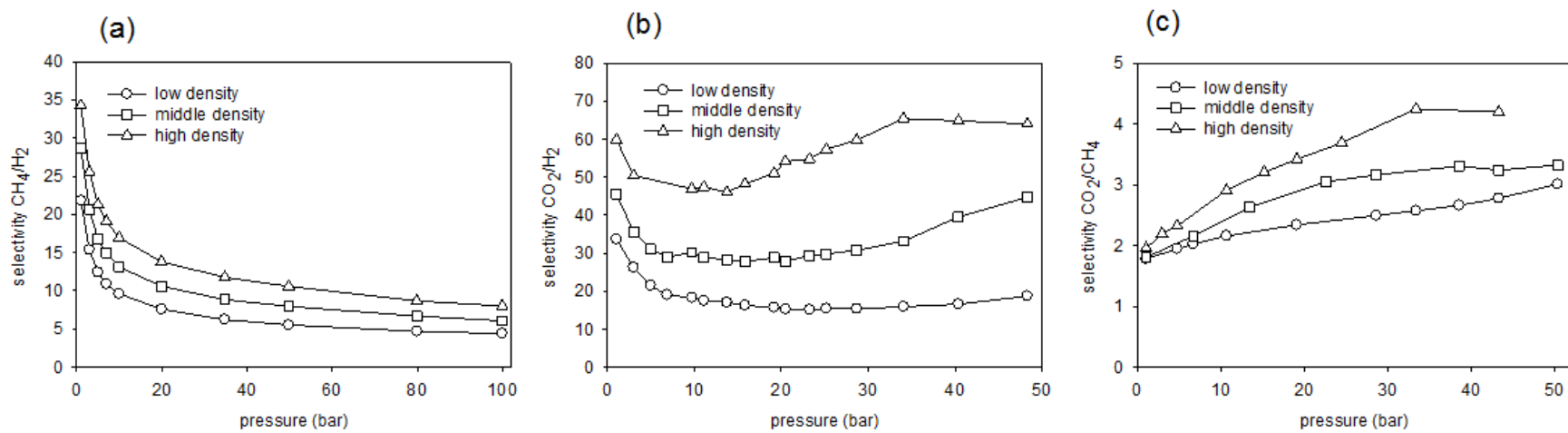


Figure 5.5. Selectivity comparison based on effect of density for 0% Ti structure (a) CH_4/H_2 , (b) CO_2/H_2 , (c) CO_2/CH_4

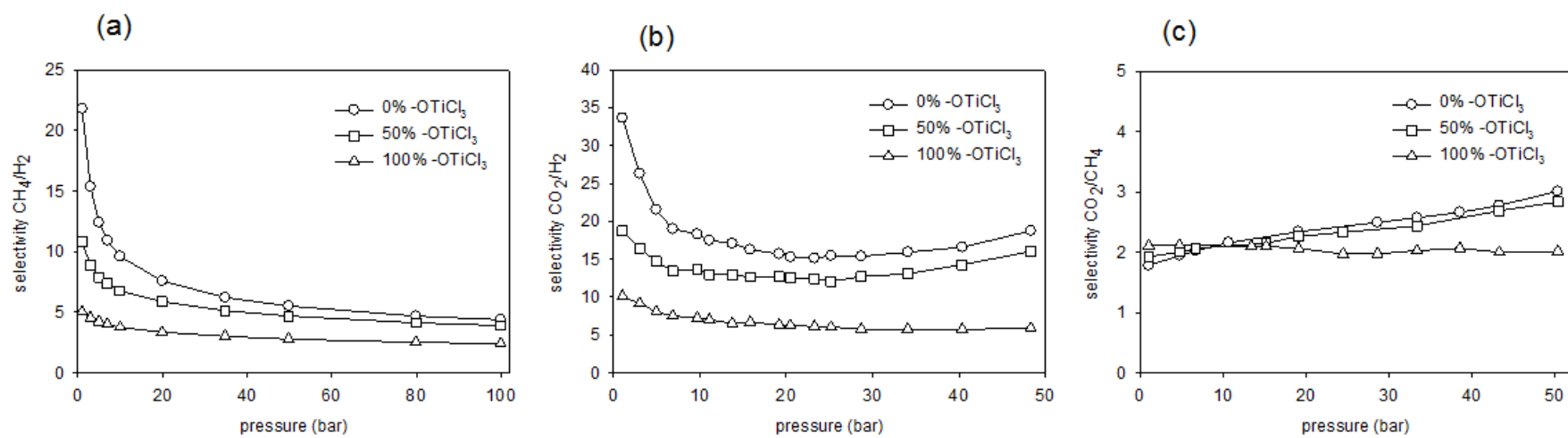


Figure 5.6. Selectivity comparison based on effect of Ti content for low density structure (a) CH₄/H₂, (b) CO₂/H₂, (c) CO₂/CH₄

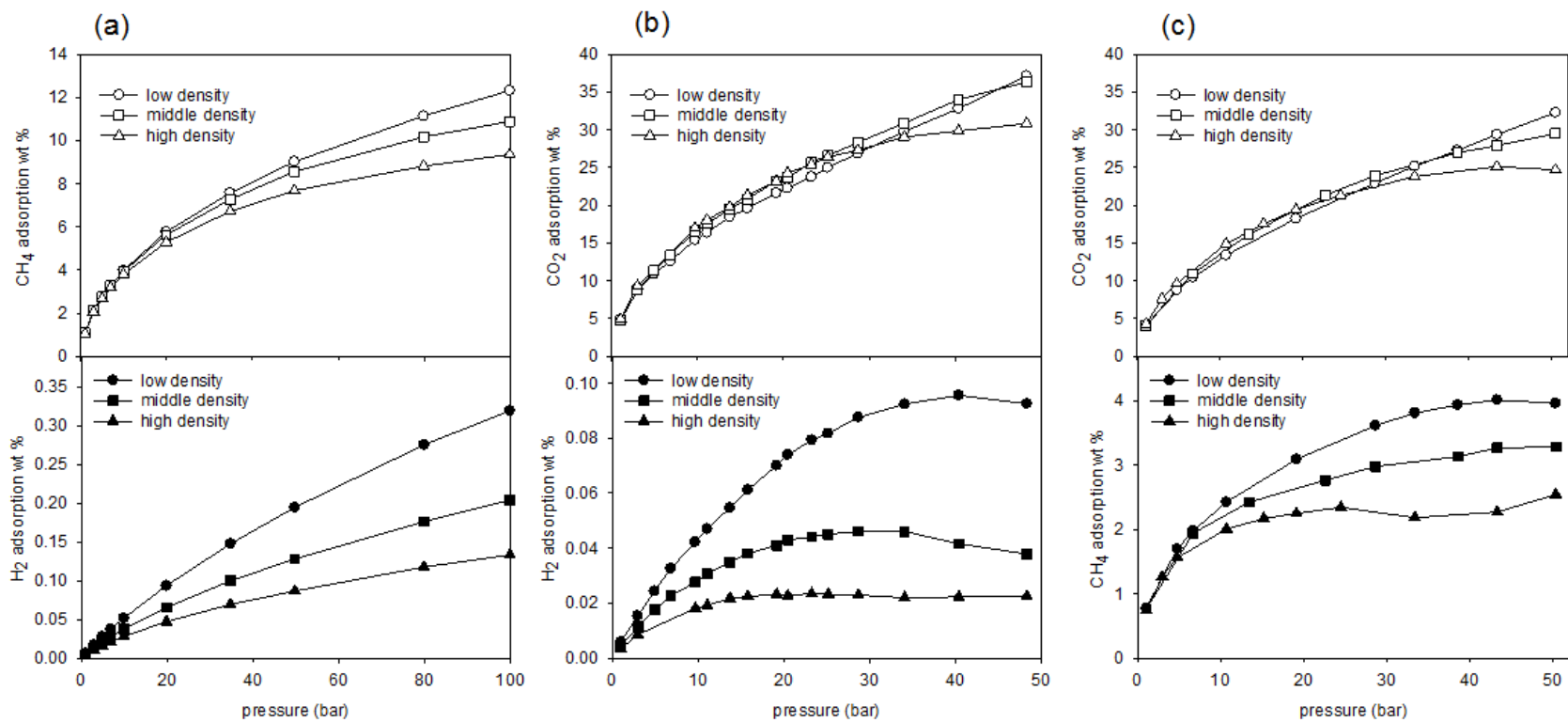


Figure 5.7. Gravimetric isotherms comparison based on effect of density for 0% Ti structure (a) CH₄/H₂, (b) CO₂/H₂, (c) CO₂/CH₄

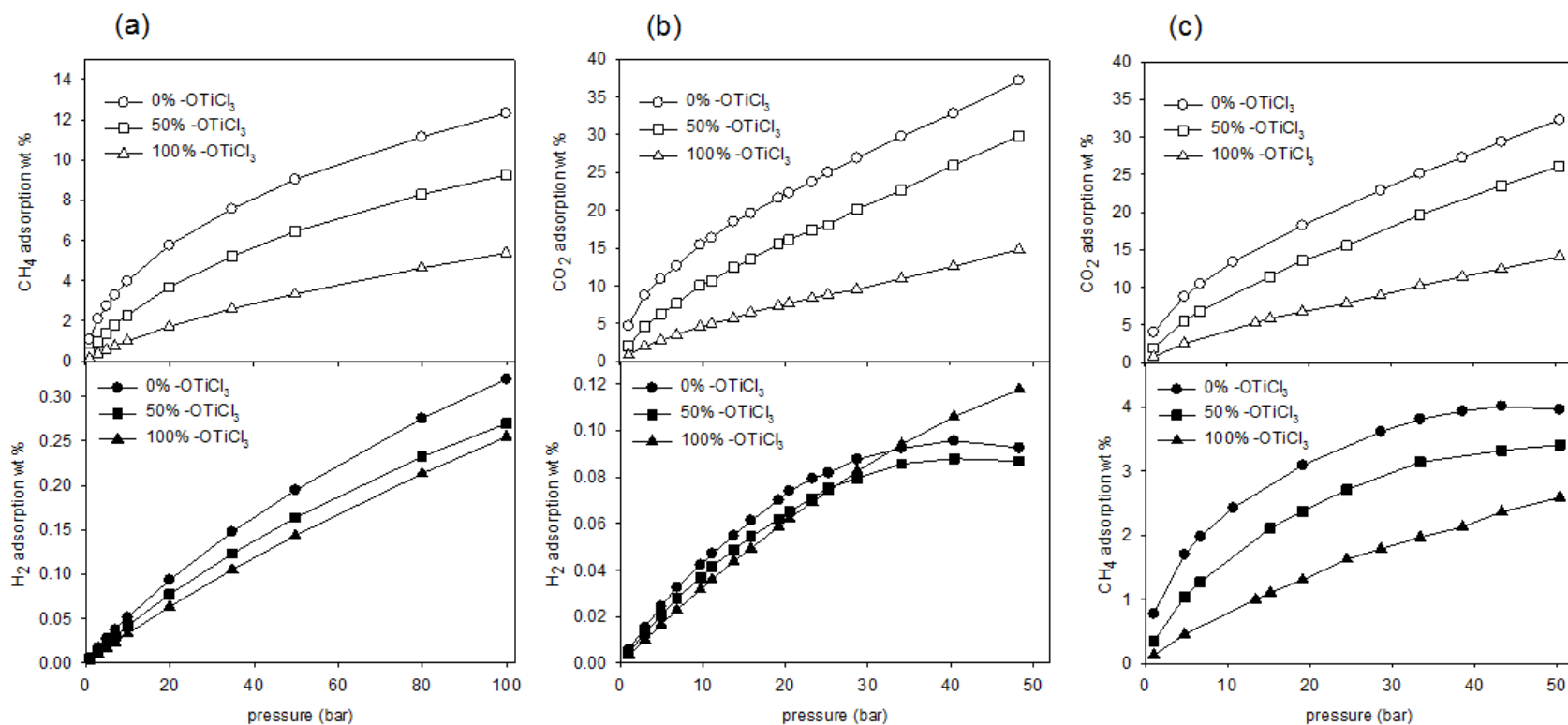


Figure 5.8. Gravimetric isotherms comparison based on effect of Ti content for low density structure (a) CH₄/H₂, (b) CO₂/H₂, (c) CO₂/CH₄

Appendix G: Supplementary Document

Table 5.S1 .Isotherm and energy data for CO₂/H₂ equimolar mixture adsorption

Pressure (bar)	Structure	CO ₂ adsorbed (wt%)	CO ₂ adsorbed (kg/l)	Energy CO ₂ -adsorbent (kJ/mol)	Energy CO ₂ -adsorbate (kJ/mol)	H ₂ adsorbed (wt%) x 10 ²	H ₂ adsorbed (kg/l) x 10 ³	Energy H ₂ -adsorbent (kJ/mol)	Energy H ₂ -adsorbate (kJ/mol)	
1.04	Low density 0% -OTiCl ₃	4.70	0.03	-25.84	-0.62	0.59	0.04	-2.92	-0.04	
4.94		10.90	0.07	-22.15	-1.37	2.43	0.16	-2.24	-0.10	
9.70		15.42	0.11	-20.30	-1.89	4.22	0.29	-1.80	-0.16	
13.74		18.46	0.13	-19.03	-2.34	5.47	0.40	-1.60	-0.21	
19.18		21.63	0.16	-17.21	-2.76	7.01	0.53	-1.60	-0.27	
28.67		26.90	0.22	-14.79	-3.69	8.76	0.71	-1.58	-0.38	
40.39		32.82	0.29	-12.86	-4.70	9.56	0.84	-1.41	-0.55	
48.31		37.16	0.35	-11.35	-5.63	9.26	0.87	-1.44	-0.70	
1.04		Low density 50% -OTiCl ₃	2.04	0.02	-21.89	-0.22	0.46	0.03	-2.30	-0.02
4.94			6.29	0.05	-18.95	-0.75	2.05	0.16	-2.02	-0.08
9.70	10.02		0.08	-17.71	-1.22	3.66	0.29	-1.72	-0.13	
13.74	12.39		0.10	-16.54	-1.57	4.86	0.40	-1.63	-0.17	
19.18	15.50		0.13	-15.21	-2.11	6.19	0.53	-1.53	-0.23	
28.67	20.13		0.18	-13.46	-2.89	7.95	0.72	-1.45	-0.34	
40.39	25.95		0.25	-11.78	-4.05	8.79	0.86	-1.32	-0.49	
48.31	29.83		0.31	-10.68	-4.87	8.69	0.90	-1.30	-0.62	
1.04	Low density 100% -OTiCl ₃		0.83	0.01	-19.51	-0.10	0.35	0.03	-1.59	-0.01
4.94			2.77	0.02	-17.54	-0.34	1.66	0.15	-1.42	-0.04
9.70		4.57	0.04	-16.35	-0.59	3.16	0.28	-1.29	-0.06	
13.74		5.66	0.05	-15.08	-0.76	4.38	0.40	-1.26	-0.09	
19.18		7.31	0.07	-14.16	-1.05	5.87	0.54	-1.19	-0.12	
28.67		9.51	0.09	-12.64	-1.41	8.25	0.78	-1.12	-0.17	
40.39		12.57	0.12	-11.36	-2.03	10.60	1.04	-1.09	-0.24	
48.31		14.79	0.15	-10.61	-2.46	11.77	1.19	-1.01	-0.30	
1.04		Mid density 0% O-TiCl ₃	4.76	0.04	-25.28	-0.63	0.44	0.03	-3.48	-0.05
4.94			11.33	0.09	-21.69	-1.60	1.75	0.14	-3.01	-0.15
9.70	16.61		0.15	-20.06	-2.36	2.76	0.24	-2.24	-0.25	
13.74	19.51		0.18	-18.49	-2.91	3.49	0.32	-2.26	-0.31	
19.18	23.24		0.22	-17.16	-3.57	4.10	0.39	-2.08	-0.41	
28.67	28.32		0.29	-15.07	-4.71	4.61	0.47	-2.00	-0.59	
40.39	34.00		0.38	-13.17	-6.16	4.16	0.46	-2.05	-0.87	
48.31	36.32		0.42	-12.41	-6.85	3.79	0.44	-2.18	-1.02	
1.04	Mid density 50% -OTiCl ₃		2.42	0.02	-23.26	-0.32	0.34	0.03	-2.99	-0.03
4.94			6.71	0.06	-20.20	-0.91	1.49	0.14	-2.72	-0.10
9.70		10.54	0.11	-18.94	-1.53	2.52	0.25	-2.29	-0.18	
13.74		13.15	0.14	-17.80	-2.01	3.19	0.33	-2.09	-0.24	
19.18		15.89	0.17	-16.47	-2.60	3.95	0.42	-1.97	-0.31	
28.67		20.14	0.23	-14.82	-3.55	4.75	0.54	-1.83	-0.44	
40.39		24.42	0.29	-13.18	-4.60	5.11	0.61	-1.81	-0.62	
48.31		27.19	0.34	-12.23	-5.37	4.92	0.61	-1.86	-0.76	
1.04		Mid density 100% -OTiCl ₃	0.81	0.01	-21.00	-0.11	0.25	0.03	-2.05	-0.01
4.94			2.60	0.03	-18.59	-0.38	1.16	0.13	-1.86	-0.04
9.70	4.10		0.05	-17.30	-0.63	2.20	0.25	-1.72	-0.08	
13.74	5.22		0.06	-16.26	-0.86	3.01	0.34	-1.64	-0.10	
19.18	6.62		0.08	-15.50	-1.14	4.00	0.46	-1.55	-0.14	
28.67	8.73		0.10	-14.17	-1.59	5.53	0.65	-1.45	-0.20	
40.39	11.05		0.13	-12.68	-2.16	7.05	0.84	-1.39	-0.27	
48.31	12.69		0.15	-12.06	-2.52	7.82	0.96	-1.34	-0.33	
1.04	High density 0% -OTiCl ₃		4.93	0.05	-25.46	-0.75	0.35	0.03	-4.51	-0.07
4.94			11.56	0.11	-22.03	-1.85	1.28	0.13	-4.09	-0.20
9.70		16.98	0.18	-20.60	-2.76	1.81	0.19	-3.13	-0.34	
13.74		19.75	0.22	-19.44	-3.36	2.18	0.24	-3.05	-0.44	
19.18		23.18	0.26	-18.00	-4.14	2.31	0.26	-2.87	-0.60	
28.67		27.31	0.33	-16.30	-5.38	2.29	0.28	-3.16	-0.82	
40.39		29.85	0.37	-15.29	-6.41	2.23	0.28	-3.83	-0.92	
48.31		30.83	0.39	-15.09	-6.78	2.25	0.29	-4.26	-0.93	
1.04		High density 50% -OTiCl ₃	3.01	0.03	-23.55	-0.48	0.25	0.03	-3.84	-0.05
4.94			7.86	0.09	-21.06	-1.36	0.99	0.12	-3.44	-0.16
9.70	11.54		0.14	-19.96	-2.05	1.58	0.19	-3.04	-0.25	
13.74	13.57		0.17	-18.84	-2.53	1.96	0.24	-3.03	-0.32	
19.18	15.70		0.20	-18.02	-3.04	2.32	0.30	-2.84	-0.40	
28.67	18.64		0.25	-16.90	-3.79	2.69	0.36	-2.77	-0.52	
40.39	21.38		0.29	-15.75	-4.70	2.86	0.39	-2.99	-0.65	
48.31	22.84		0.32	-15.35	-5.07	2.82	0.39	-2.96	-0.74	
1.04	High density 100% -OTiCl ₃		0.79	0.01	-21.70	-0.10	0.18	0.02	-2.71	-0.01
4.94			2.51	0.03	-19.36	-0.39	0.86	0.11	-2.48	-0.05
9.70		4.14	0.05	-18.27	-0.70	1.58	0.21	-2.28	-0.10	
13.74		5.22	0.07	-17.36	-0.94	2.14	0.29	-2.21	-0.13	
19.18		6.40	0.09	-16.38	-1.22	2.83	0.38	-2.15	-0.17	
28.67		8.31	0.12	-14.83	-1.75	3.81	0.53	-2.07	-0.25	
40.39		10.73	0.15	-13.57	-2.46	4.62	0.66	-2.01	-0.35	
48.31		12.34	0.18	-12.56	-2.99	4.97	0.72	-2.04	-0.43	

Table 5.S2. Isotherm and energy data for CH₄/H₂ equimolar mixture adsorption

Pressure (bar)	Structure	CH ₄ adsorbed (wt%)	CH ₄ adsorbed (kg/l) x 10 ⁻¹	Energy CH ₄ -adsorbate (kJ/mol)	Energy CH ₄ -adsorbate (kJ/mol)	H ₂ adsorbed (wt%)	H ₂ adsorbed (kg/l) x 10 ⁻³	Energy H ₂ -adsorbate (kJ/mol)	Energy H ₂ -adsorbate (kJ/mol)
1.00	Low density 0% -OTICl ₃	1.08	0.06	-23.31	-0.13	0.01	0.04	-2.83	-0.02
2.99		2.11	0.13	-20.79	-0.24	0.02	0.10	-2.43	-0.04
4.98		2.75	0.17	-19.18	-0.32	0.03	0.17	-2.38	-0.06
6.96		3.28	0.20	-18.16	-0.36	0.04	0.23	-2.30	-0.07
9.95		3.98	0.24	-17.19	-0.45	0.05	0.32	-2.20	-0.09
19.89		5.76	0.36	-15.21	-0.64	0.09	0.59	-2.00	-0.14
34.77		7.57	0.48	-13.48	-0.84	0.15	0.94	-1.84	-0.21
49.76		9.02	0.59	-12.49	-1.04	0.19	1.26	-1.77	-0.26
79.85		11.14	0.74	-11.13	-1.33	0.28	1.83	-1.72	-0.36
99.90		12.31	0.83	-10.62	-1.49	0.32	2.16	-1.64	-0.41
1.00	Low density 50% -OTICl ₃	0.41	0.03	-18.64	-0.04	0.00	0.03	-2.30	-0.01
2.99		0.97	0.07	-16.47	-0.11	0.01	0.10	-2.23	-0.03
4.98		1.40	0.10	-15.27	-0.17	0.02	0.16	-2.16	-0.04
6.96		1.80	0.13	-14.66	-0.21	0.03	0.22	-2.10	-0.05
9.95		2.30	0.17	-13.83	-0.28	0.04	0.31	-2.07	-0.07
19.89		3.68	0.28	-12.56	-0.46	0.08	0.58	-1.88	-0.12
34.77		5.22	0.40	-11.29	-0.69	0.12	0.94	-1.80	-0.18
49.76		6.44	0.50	-10.50	-0.88	0.16	1.27	-1.73	-0.24
79.85		8.29	0.66	-9.50	-1.18	0.23	1.84	-1.68	-0.32
99.90		9.25	0.74	-9.11	-1.34	0.27	2.16	-1.62	-0.37
1.00	Low density 100% -OTICl ₃	0.14	0.01	-13.94	-0.02	0.00	0.03	-1.62	0.00
2.99		0.37	0.03	-13.01	-0.05	0.01	0.09	-1.55	-0.01
4.98		0.57	0.05	-12.31	-0.07	0.02	0.15	-1.51	-0.02
6.96		0.75	0.07	-11.80	-0.10	0.02	0.20	-1.49	-0.03
9.95		1.00	0.09	-11.25	-0.14	0.03	0.29	-1.45	-0.04
19.89		1.72	0.15	-10.11	-0.25	0.06	0.55	-1.40	-0.07
34.77		2.61	0.23	-9.02	-0.40	0.11	0.93	-1.31	-0.11
49.76		3.34	0.30	-8.26	-0.54	0.14	1.27	-1.28	-0.15
79.85		4.63	0.42	-7.32	-0.80	0.21	1.92	-1.24	-0.22
99.90		5.37	0.49	-6.90	-0.95	0.25	2.31	-1.22	-0.27
1.00	Mid density 0% O-TICl ₃	1.08	0.08	-22.66	-0.14	0.00	0.04	-3.53	-0.03
2.99		2.13	0.16	-20.77	-0.27	0.01	0.10	-3.14	-0.05
4.98		2.75	0.21	-19.35	-0.34	0.02	0.15	-3.06	-0.08
6.96		3.29	0.25	-18.42	-0.42	0.03	0.21	-2.95	-0.09
9.95		3.94	0.30	-17.51	-0.51	0.04	0.28	-2.91	-0.12
19.89		5.62	0.44	-15.74	-0.74	0.07	0.51	-2.66	-0.19
34.77		7.27	0.58	-14.32	-1.00	0.10	0.79	-2.55	-0.27
49.76		8.56	0.69	-13.46	-1.21	0.13	1.03	-2.46	-0.34
79.85		10.17	0.83	-12.42	-1.52	0.18	1.44	-2.48	-0.43
99.90		10.89	0.90	-11.99	-1.66	0.20	1.68	-2.46	-0.47
1.00	Mid density 50% -OTICl ₃	0.47	0.04	-20.07	-0.05	0.00	0.03	-3.07	-0.01
2.99		1.06	0.10	-18.08	-0.13	0.01	0.09	-2.92	-0.03
4.98		1.53	0.14	-17.00	-0.20	0.02	0.15	-2.83	-0.05
6.96		1.88	0.17	-16.30	-0.26	0.02	0.20	-2.76	-0.07
9.95		2.37	0.22	-15.58	-0.34	0.03	0.28	-2.68	-0.09
19.89		3.57	0.33	-14.06	-0.55	0.05	0.51	-2.47	-0.15
34.77		4.81	0.46	-12.82	-0.74	0.09	0.81	-2.39	-0.21
49.76		5.79	0.55	-12.10	-0.97	0.11	1.06	-2.35	-0.27
79.85		7.14	0.69	-11.14	-1.26	0.16	1.51	-2.32	-0.35
99.90		7.85	0.77	-10.79	-1.41	0.18	1.76	-2.29	-0.40
1.00	Mid density 100% -OTICl ₃	0.14	0.01	-23.05	-0.15	0.00	0.03	-2.30	-0.01
2.99		2.05	0.18	-21.25	-0.29	0.01	0.09	-2.23	-0.03
4.98		2.68	0.24	-19.94	-0.39	0.02	0.14	-2.16	-0.04
6.96		3.19	0.29	-19.08	-0.47	0.02	0.19	-2.10	-0.05
9.95		3.80	0.35	-18.21	-0.57	0.03	0.25	-2.07	-0.07
19.89		5.29	0.49	-16.68	-0.83	0.05	0.44	-1.88	-0.12
34.77		6.72	0.63	-15.47	-1.11	0.07	0.65	-1.80	-0.18
49.76		7.68	0.73	-14.80	-1.32	0.09	0.82	-1.73	-0.24
79.85		8.82	0.85	-14.02	-1.61	0.12	1.13	-1.68	-0.32
99.90		9.35	0.91	-13.71	-1.74	0.13	1.29	-1.62	-0.37
1.00	High density 0% -OTICl ₃	0.58	0.06	-20.66	-0.08	0.00	0.03	-2.30	-0.01
2.99		1.26	0.14	-19.11	-0.19	0.01	0.08	-2.23	-0.03
4.98		1.69	0.19	-18.11	-0.27	0.01	0.13	-2.16	-0.04
6.96		2.03	0.22	-17.52	-0.33	0.02	0.18	-2.10	-0.05
9.95		2.49	0.28	-16.90	-0.43	0.02	0.24	-2.07	-0.07
19.89		3.56	0.40	-15.80	-0.64	0.04	0.41	-1.88	-0.12
34.77		4.57	0.52	-14.85	-0.86	0.06	0.62	-1.80	-0.18
49.76		5.26	0.60	-14.26	-1.03	0.07	0.81	-1.73	-0.24
79.85		6.14	0.71	-13.58	-1.25	0.10	1.12	-1.68	-0.32
99.90		6.53	0.75	-13.27	-1.36	0.11	1.30	-1.62	-0.37
1.00	High density 50% -OTICl ₃	0.13	0.02	-16.89	-0.02	0.00	0.02	-2.76	-0.01
2.99		0.32	0.04	-15.42	-0.05	0.01	0.07	-2.68	-0.02
4.98		0.49	0.06	-14.79	-0.08	0.01	0.11	-2.62	-0.03
6.96		0.64	0.08	-14.34	-0.12	0.01	0.16	-2.58	-0.04
9.95		0.83	0.11	-13.70	-0.16	0.02	0.22	-2.55	-0.05
19.89		1.37	0.18	-12.64	-0.29	0.03	0.42	-2.43	-0.09
34.77		1.98	0.26	-11.52	-0.46	0.05	0.68	-2.38	-0.14
49.76		2.48	0.32	-10.92	-0.60	0.07	0.91	-2.31	-0.18
79.85		3.27	0.43	-10.08	-0.85	0.10	1.32	-2.28	-0.25
99.90		3.66	0.48	-9.66	-1.00	0.12	1.57	-2.28	-0.29

Table 5.S3. Isotherm and energy data for CO₂/CH₄ equimolar mixture adsorption

Pressure (bar)	Structure	CO ₂ adsorbed (wt%)	CO ₂ adsorbed (kg/l) x 10 ²	Energy CO ₂ -adsorbent (kJ/mol)	Energy CO ₂ -adsorbate (kJ/mol)	CH ₄ adsorbed (wt%)	CH ₄ adsorbed (kg/l) x 10 ²	Energy CH ₄ -adsorbent (kJ/mol)	Energy CH ₄ -adsorbate (kJ/mol)	
1.07	Low density 0% -OTfCl ₃	4.07	2.53	-24.79	-0.68	0.77	0.48	-22.14	-0.33	
4.79		8.78	5.79	-20.61	-1.37	1.70	1.12	-17.41	-0.68	
6.73		10.45	7.05	-19.52	-1.62	1.98	1.33	-16.00	-0.81	
10.71		13.37	9.38	-18.36	-2.02	2.43	1.70	-13.88	-1.05	
19.14		18.25	13.70	-15.87	-2.81	3.09	2.32	-11.68	-1.52	
28.66		22.92	18.42	-13.77	-3.71	3.62	2.91	-10.21	-1.98	
38.59		27.26	23.39	-11.98	-4.61	3.94	3.38	-9.28	-2.45	
50.41		32.26	29.86	-10.47	-5.63	3.96	3.67	-8.15	-3.13	
1.07		Low density 50% -OTfCl ₃	1.95	1.44	-21.38	-0.25	0.34	0.25	-17.02	-0.14
4.79			5.50	4.26	-18.13	-0.82	1.03	0.80	-13.71	-0.45
6.73	6.84		5.39	-17.26	-1.06	1.27	1.00	-12.65	-0.58	
10.71	9.50		7.74	-16.73	-1.45	1.67	1.36	-11.00	-0.82	
19.14	13.56		11.67	-14.20	-2.25	2.37	2.04	-9.73	-1.28	
28.66	17.34		15.75	-12.40	-3.08	2.98	2.71	-8.82	-1.72	
38.59	21.29		20.43	-11.09	-3.94	3.28	3.15	-7.99	-2.21	
50.41	26.11		26.81	-9.96	-5.01	3.41	3.50	-7.39	-2.81	
1.07	Low density 100% -OTfCl ₃		0.80	0.69	-18.94	-0.12	0.13	0.11	-13.06	-0.06
4.79			2.54	2.24	-16.84	-0.41	0.45	0.40	-10.65	-0.22
6.73		3.16	2.81	-15.87	-0.53	0.60	0.53	-10.01	-0.29	
10.71		4.56	4.13	-15.38	-0.75	0.82	0.74	-8.29	-0.43	
19.14		6.76	6.31	-13.35	-1.21	1.30	1.21	-7.29	-0.71	
28.66		8.96	8.61	-11.78	-1.70	1.79	1.72	-6.54	-1.02	
38.59		11.43	11.34	-10.81	-2.23	2.13	2.11	-5.54	-1.35	
50.41		14.11	14.52	-9.45	-2.94	2.59	2.67	-5.31	-1.74	
1.07		Mid density 0% O-TfCl ₃	4.07	3.14	-24.35	-0.67	0.76	0.59	-21.56	-0.36
4.79			9.27	7.64	-20.66	-1.56	1.62	1.33	-17.12	-0.81
6.73	10.94		9.22	-19.42	-1.93	1.94	1.64	-16.16	-1.00	
10.71	15.21		13.51	-19.03	-2.56	2.07	1.84	-13.45	-1.42	
19.14	19.32		18.21	-16.19	-3.57	2.79	2.63	-12.63	-1.94	
28.66	23.92		24.02	-14.31	-4.60	2.98	2.99	-11.69	-2.48	
38.59	26.95		28.31	-13.22	-5.41	3.13	3.29	-11.03	-2.99	
50.41	29.50		32.23	-11.97	-6.34	3.29	3.59	-11.55	-3.35	
1.07	Mid density 50% -OTfCl ₃		2.23	2.06	-22.68	-0.35	0.37	0.34	-18.52	-0.18
4.79			5.85	5.65	-19.30	-1.05	1.03	0.99	-15.43	-0.55
6.73		7.10	6.97	-18.29	-1.31	1.26	1.23	-14.49	-0.70	
10.71		9.72	9.86	-17.85	-1.78	1.56	1.58	-12.77	-1.00	
19.14		13.62	14.53	-15.80	-2.65	2.02	2.16	-11.06	-1.53	
28.66		17.02	18.99	-14.19	-3.54	2.32	2.59	-10.11	-2.00	
38.59		19.99	23.21	-13.20	-4.27	2.50	2.90	-9.28	-2.47	
50.41		22.49	27.06	-11.73	-5.15	2.72	3.27	-9.62	-2.89	
1.07		Mid density 100% -OTfCl ₃	0.78	0.84	-20.41	-0.13	0.13	0.14	-16.12	-0.07
4.79			2.36	2.58	-17.86	-0.45	0.40	0.44	-12.39	-0.24
6.73	2.92		3.22	-16.98	-0.57	0.52	0.58	-11.71	-0.32	
10.71	4.13		4.62	-16.58	-0.81	0.72	0.80	-10.10	-0.48	
19.14	6.15		7.07	-14.93	-1.28	1.06	1.21	-8.53	-0.79	
28.66	7.92		9.31	-13.26	-1.84	1.43	1.68	-8.01	-1.08	
38.59	9.79		11.79	-12.28	-2.30	1.70	2.05	-7.08	-1.42	
50.41	11.77		14.55	-10.91	-2.94	2.00	2.47	-6.56	-1.80	
1.07	High density 0% -OTfCl ₃		4.28	3.95	-24.80	-0.75	0.74	0.69	-22.12	-0.41
4.79			9.63	9.52	-21.32	-1.84	1.56	1.54	-18.26	-0.97
6.73		10.83	10.89	-20.03	-2.17	1.89	1.90	-17.66	-1.13	
10.71		14.90	15.74	-19.60	-2.89	2.01	2.12	-15.66	-1.59	
19.14		19.41	21.76	-17.61	-4.03	2.25	2.52	-13.96	-2.31	
28.66		22.48	26.26	-16.19	-5.05	2.33	2.72	-13.45	-2.87	
38.59		23.88	28.42	-15.72	-5.46	2.35	2.80	-13.31	-3.15	
50.41		24.69	29.80	-15.09	-5.98	2.54	3.07	-13.99	-3.25	
1.07		High density 50% -OTfCl ₃	2.79	3.10	-23.20	-0.53	0.42	0.47	-19.28	-0.26
4.79			6.77	7.89	-20.63	-1.42	0.98	1.14	-16.33	-0.74
6.73	7.93		9.39	-19.79	-1.70	1.18	1.40	-15.71	-0.92	
10.71	10.35		12.62	-19.40	-2.20	1.38	1.69	-14.23	-1.26	
19.14	13.31		16.84	-17.72	-3.02	1.66	2.10	-13.47	-1.69	
28.66	15.46		20.12	-16.59	-3.72	1.82	2.36	-12.66	-2.07	
38.59	16.58		21.91	-15.94	-4.06	2.01	2.65	-12.67	-2.31	
50.41	18.00		24.22	-15.42	-4.56	2.06	2.78	-12.43	-2.57	
1.07	High density 100% -OTfCl ₃		0.77	0.99	-21.46	-0.12	0.12	0.15	-16.04	-0.07
4.79			2.33	3.05	-19.05	-0.45	0.37	0.48	-13.23	-0.27
6.73		2.81	3.70	-17.98	-0.59	0.48	0.64	-12.56	-0.35	
10.71		4.01	5.36	-17.60	-0.85	0.64	0.86	-10.87	-0.54	
19.14		5.82	7.96	-15.53	-1.41	0.96	1.31	-9.92	-0.88	
28.66		7.55	10.55	-14.19	-1.99	1.24	1.73	-9.07	-1.25	
38.59		9.31	13.29	-13.14	-2.60	1.43	2.04	-8.41	-1.64	
50.41		11.08	16.16	-12.03	-3.32	1.60	2.33	-8.00	-2.05	

Table 5.S4. Isotherm and Energy data for pure component adsorption

Adsorbate	Pressure (bar)	Structure	Amount Adsorbed (wt%)	Amount Adsorbed (kg/l)	Energy adsorbate-adsorbent (kJ/mole)	Structure	Amount Adsorbed (wt%)	Amount Adsorbed (kg/l)	Energy adsorbate-adsorbent (kJ/mole)	Structure	Amount Adsorbed (wt%)	Amount Adsorbed (kg/l)	Energy adsorbate-adsorbent (kJ/mole)			
														Only for H ₂	Only for H ₂	Only for H ₂
Hydrogen (H ₂)	1.00	Low density 0% -OTFC3	0.01	0.08	-3.32	Low density 50% -OTFC3	0.01	0.07	-2.40	Low density 100% -OTFC3	0.01	0.06	-1.58			
	2.99		0.04	0.24	-3.27		-0.17	0.03	0.21		-2.36	-0.17	0.02	0.18	-1.59	-0.16
	4.98		0.07	0.39	-3.28		-0.29	0.05	0.34		-2.37	-0.29	0.03	0.30	-1.59	-0.28
	6.98		0.09	0.55	-3.24		-0.41	0.07	0.48		-2.39	-0.40	0.05	0.41	-1.59	-0.38
	9.97		0.13	0.77	-3.15		-0.57	0.09	0.68		-2.36	-0.57	0.07	0.59	-1.59	-0.55
	19.93		0.25	1.50	-3.07		-1.13	0.18	1.33		-2.32	-1.12	0.14	1.17	-1.59	-1.08
	49.76		0.59	3.50	-2.84		-2.78	0.44	3.19		-2.27	-2.70	0.33	2.81	-1.53	-2.62
	78.32		0.89	5.32	-2.70		-4.30	0.67	4.89		-2.22	-4.18	0.51	4.35	-1.51	-4.04
	99.40		1.08	6.45	-2.66		-5.22	0.81	5.94		-2.18	-5.07	0.62	5.34	-1.49	-5.01
	1.00	Mid density 0% -OTFC3	0.01	0.08	-3.88	Mid density 50% -OTFC3	0.01	0.07	-3.18	Mid density 100% -OTFC3	0.00	0.05	-2.08	-0.05		
	2.99		0.03	0.22	-3.83		-0.17	0.02	0.20		-3.15	-0.16	0.01	0.16	-2.08	-0.15
	4.98		0.05	0.37	-3.85		-0.28	0.04	0.33		-3.15	-0.26	0.02	0.26	-2.07	-0.26
	6.98		0.07	0.52	-3.83		-0.38	0.05	0.46		-3.15	-0.36	0.03	0.37	-2.08	-0.35
	9.97		0.10	0.73	-3.79		-0.55	0.07	0.65		-3.12	-0.52	0.05	0.52	-2.09	-0.50
	19.93		0.19	1.42	-3.66		-1.10	0.14	1.27		-3.09	-1.03	0.10	1.04	-2.07	-0.98
	49.76		0.45	3.30	-3.50		-2.65	0.33	3.00		-3.01	-2.47	0.23	2.48	-2.01	-2.40
	78.32		0.67	4.98	-3.39		-4.06	0.51	4.57		-2.95	-3.81	0.36	3.82	-1.97	-3.71
	99.40		0.81	5.99	-3.32		-4.91	0.61	5.53		-2.91	-4.58	0.44	4.67	-1.95	-4.51
1.00	High density 0% -OTFC3	0.01	0.07	-4.80	High density 50% -OTFC3	0.01	0.06	-4.04	High density 100% -OTFC3	0.00	0.05	-2.73	-0.04			
2.99		0.02	0.22	-4.76		-0.16	0.02	0.18		-3.99	-0.13	0.01	0.14	-2.73	-0.14	
4.98		0.04	0.36	-4.79		-0.27	0.03	0.31		-4.00	-0.24	0.02	0.24	-2.73	-0.23	
6.98		0.06	0.50	-4.74		-0.38	0.04	0.43		-3.99	-0.33	0.03	0.33	-2.72	-0.31	
9.97		0.08	0.71	-4.70		-0.54	0.06	0.60		-3.98	-0.45	0.04	0.47	-2.73	-0.45	
19.93		0.16	1.37	-4.60		-1.05	0.11	1.18		-3.95	-0.90	0.07	0.93	-2.71	-0.88	
49.76		0.36	3.14	-4.40		-2.44	0.26	2.75		-3.87	-2.12	0.17	2.21	-2.66	-2.13	
78.32		0.53	4.68	-4.28		-3.74	0.38	4.14		-3.81	-3.20	0.27	3.39	-2.61	-3.27	
99.40		0.63	5.58	-4.19		-4.54	0.46	4.99		-3.79	-3.85	0.32	4.12	-2.60	-3.97	
Methane (CH ₄)	0.99	Low density 0% -OTFC3	1.67	0.01	-21.82	Low density 50% -OTFC3	0.69	0.01	-16.75	Low density 100% -OTFC3	0.26	0.00	-13.28	-0.03		
	2.98		3.08	0.02	-18.78		-0.34	1.63	0.01		-14.96	-0.19	0.66	0.01	-11.92	-0.08
	4.97		4.05	0.02	-17.26		-0.44	2.34	0.02		-13.97	-0.28	1.01	0.01	-11.21	-0.13
	6.95		4.85	0.03	-16.26		-0.53	2.96	0.02		-13.28	-0.35	1.32	0.01	-10.61	-0.18
	9.93		5.80	0.04	-15.12		-0.62	3.74	0.03		-12.46	-0.46	1.74	0.02	-9.91	-0.24
	19.81		8.31	0.05	-13.01		-0.91	5.80	0.04		-10.92	-0.74	2.94	0.03	-8.68	-0.43
	49.38		12.90	0.09	-10.39		-1.50	9.80	0.08		-8.98	-1.35	5.71	0.05	-6.89	-0.92
	78.72		15.63	0.11	-9.21		-1.91	12.20	0.10		-8.15	-1.75	7.75	0.07	-6.02	-1.32
	98.38		16.96	0.12	-8.76		-2.13	13.31	0.11		-7.79	-1.96	8.86	0.08	-5.66	-1.54
	0.99	Mid density 0% -OTFC3	1.67	0.01	-21.48	Mid density 50% -OTFC3	0.80	0.01	-18.77	Mid density 100% -OTFC3	0.25	0.00	-15.66	-0.03		
	2.98		3.08	0.02	-18.93		-0.38	1.70	0.02		-16.51	-0.23	0.60	0.01	-13.62	-0.09
	4.97		4.04	0.03	-17.55		-0.51	2.37	0.02		-15.55	-0.33	0.90	0.01	-12.75	-0.14
	6.95		4.79	0.04	-16.62		-0.61	2.94	0.03		-14.85	-0.42	1.16	0.01	-12.10	-0.19
	9.93		5.71	0.04	-15.68		-0.74	3.61	0.03		-13.97	-0.54	1.50	0.02	-11.34	-0.26
	19.81		7.94	0.06	-13.87		-1.09	5.33	0.05		-12.50	-0.84	2.47	0.03	-10.08	-0.46
	49.38		11.48	0.10	-11.82		-1.71	8.26	0.08		-10.64	-1.43	4.53	0.05	-8.24	-0.93
	78.72		13.32	0.11	-11.00		-2.07	9.87	0.10		-9.87	-1.78	6.00	0.07	-7.38	-1.30
	98.38		14.11	0.12	-10.70		-2.24	10.58	0.11		-9.58	-1.95	6.72	0.08	-7.02	-1.50
0.99	High density 0% -OTFC3	1.65	0.01	-21.95	High density 50% -OTFC3	0.95	0.01	-19.64	High density 100% -OTFC3	0.23	0.00	-15.82	-0.04			
2.98		3.01	0.03	-19.55		-0.43	1.90	0.02		-17.83	-0.31	0.56	0.01	-14.42	-0.10	
4.97		3.89	0.04	-18.28		-0.57	2.52	0.03		-16.89	-0.42	0.84	0.01	-13.64	-0.16	
6.95		4.54	0.04	-17.45		-0.68	3.02	0.03		-16.32	-0.52	1.08	0.01	-13.08	-0.21	
9.93		5.38	0.05	-16.65		-0.83	3.60	0.04		-15.70	-0.64	1.39	0.02	-12.53	-0.28	
19.81		7.20	0.07	-15.08		-1.19	4.89	0.06		-14.47	-0.92	2.22	0.03	-11.22	-0.50	
49.38		9.78	0.10	-13.54		-1.79	6.84	0.08		-13.14	-1.39	3.88	0.05	-9.59	-0.99	
78.72		10.85	0.11	-13.03		-2.07	7.81	0.09		-12.61	-1.64	4.92	0.07	-8.90	-1.34	
98.38		11.31	0.11	-12.86		-2.19	8.20	0.10		-12.40	-1.76	5.40	0.07	-8.64	-1.51	
Carbon dioxide (CO ₂)	0.99	Low density 0% -OTFC3	7.73	0.05	-26.66	Low density 50% -OTFC3	3.75	0.03	-22.85	Low density 100% -OTFC3	1.51	0.01	-20.22	-0.16		
	2.96		12.84	0.09	-22.39		-1.54	7.58	0.06		-19.15	-0.86	3.35	0.03	-17.40	-0.42
	4.85		16.33	0.12	-20.19		-2.02	10.41	0.08		-17.37	-1.27	4.71	0.04	-15.84	-0.61
	10.32		23.83	0.18	-16.34		-3.09	17.38	0.15		-14.44	-2.39	8.20	0.08	-13.59	-1.16
	14.69		29.46	0.25	-14.22		-4.06	22.24	0.21		-12.77	-3.26	10.77	0.10	-12.11	-1.67
	20.51		36.84	0.34	-11.73		-5.47	29.14	0.30		-10.82	-4.71	14.21	0.14	-10.72	-2.33
	30.74		47.75	0.54	-8.66		-8.55	39.93	0.48		-8.25	-7.52	21.25	0.23	-8.57	-3.80
	37.91		49.20	0.57	-8.28		-9.24	42.09	0.53		-7.98	-8.30	33.36	0.43	-5.91	-7.06
	51.62		50.29	0.60	-8.20		-9.70	43.42	0.56		-7.79	-8.88	37.13	0.51	-5.41	-8.52
	0.99	Mid density 0% -OTFC3	7.78	0.06	-26.07	Mid density 50% -OTFC3	4.28	0.04	-24.15	Mid density 100% -OTFC3	1.37	0.01	-20.98	-0.17		
	2.96		13.58	0.12	-21.95		-1.80	8.34	0.08		-20.61	-1.10	3.15	0.03	-18.52	-0.46
	4.85		17.27	0.15	-19.75		-2.44	11.23	0.11		-18.79	-1.64	4.46	0.05	-17.32	-0.68
	10.32		25.29	0.25	-16.27		-3.98	17.80	0.19		-15.77	-3.00	7.54	0.09	-15.00	-1.30
	14.69		30.66	0.32	-14.27		-5.17	21.66	0.25		-14.25	-3.84	9.63	0.11	-13.62	-1.76
	20.51		36.49	0.42	-12.41		-6.89	26.83	0.33		-12.45	-5.20	12.44	0.15	-12.19	-2.44
	30.74		39.66	0.48	-11.64		-8.05	32.55	0.43		-10.77	-7.09	18.09	0.24	-9.85	-3.92
	37.91		40.36	0.50	-11.46		-8.39	33.72	0.46		-10.50	-7.62	24.54	0.35	-7.82	-6.08
	51.62		41.16	0.51	-11.32		-8.76	34.86	0.48		-10.43	-8.03	27.84	0.41	-7.16	-7.49
0.99	High density 0% -OTFC3	8.35	0.08	-26.47	High density 50% -OTFC3	5.04	0.06	-23.93	High density 100% -OTFC3	1.38	0.02	-22.00	-0.06			
2.96		14.13	0.14	-22.50		-2.19	9.33	0.11		-21.22	-1.57	3.01	0.04	-19.31	-0.46	
4.85		17.83	0.19	-20.55		-2.91	12.10	0.15		-19.79	-2.15	4.24	0.06	-17.92	-0.25	
10.32		25.59	0.30	-16.95		-4.84	17.50	0.23		-17.45	-3.50	7.28	0.10	-15.78	-0.48	
14.69		29.41	0.37	-15.81		-6.06	20.18	0.27		-16.33	-4.27	9.39	0.13	-14.36	-0.68	
20.51		30.88	0.39	-15.29		-6.69	22.59	0.31		-15.45	-4.97	12.09	0.18	-12.80	-0.94	
30.74		32.35	0.42	-15.07		-7.30	24.80	0.35		-14.79	-5.78	17.31	0.27	-10.71	-1.54	
37.91		32.75	0.43	-14.89		-7.51	25.69	0.37		-14.50	-6.20	18.95	0.30	-10.07	-1.79	
51.62		33.33	0.44	-14.95		-7.66	26.54	0.39		-14.41	-6.49	20.62	0.33	-9.90	-2.02	

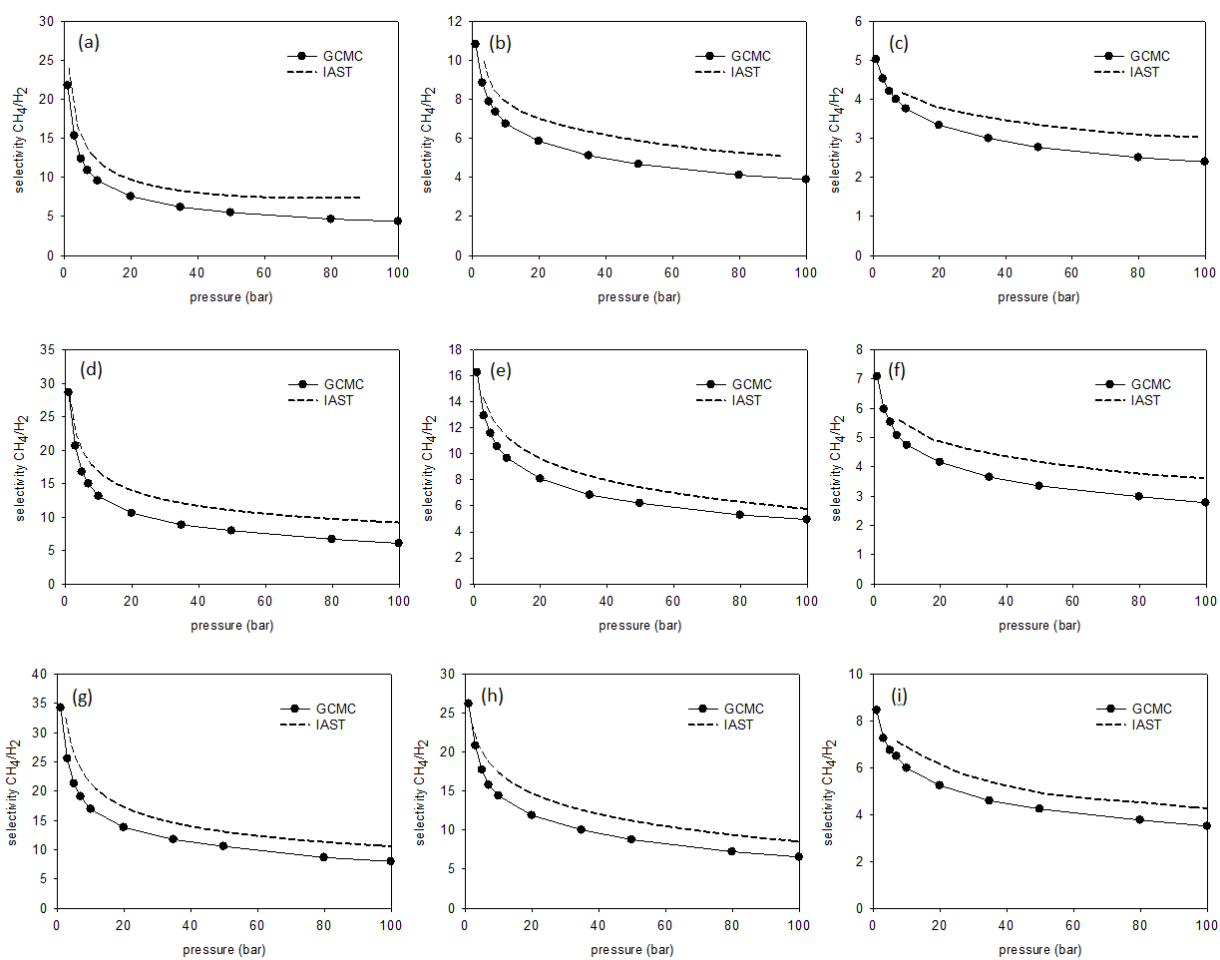


Figure 5.S1. Selectivity comparison between GCMC and IAST for equimolar binary mixture of CH_4/H_2 (a) low density 0 % - OTiCl_3 structure. (b) low density 50 % - OTiCl_3 structure. (c) low density 100 % - OTiCl_3 structure (d) middle density 0 % - OTiCl_3 structure. (e) middle density 50 % - OTiCl_3 structure. (f) middle density 100 % - OTiCl_3 structure. (g) high density 0 % - OTiCl_3 structure. (h) high density 0 % - OTiCl_3 structure. (i) high density 0 % - OTiCl_3 structure.

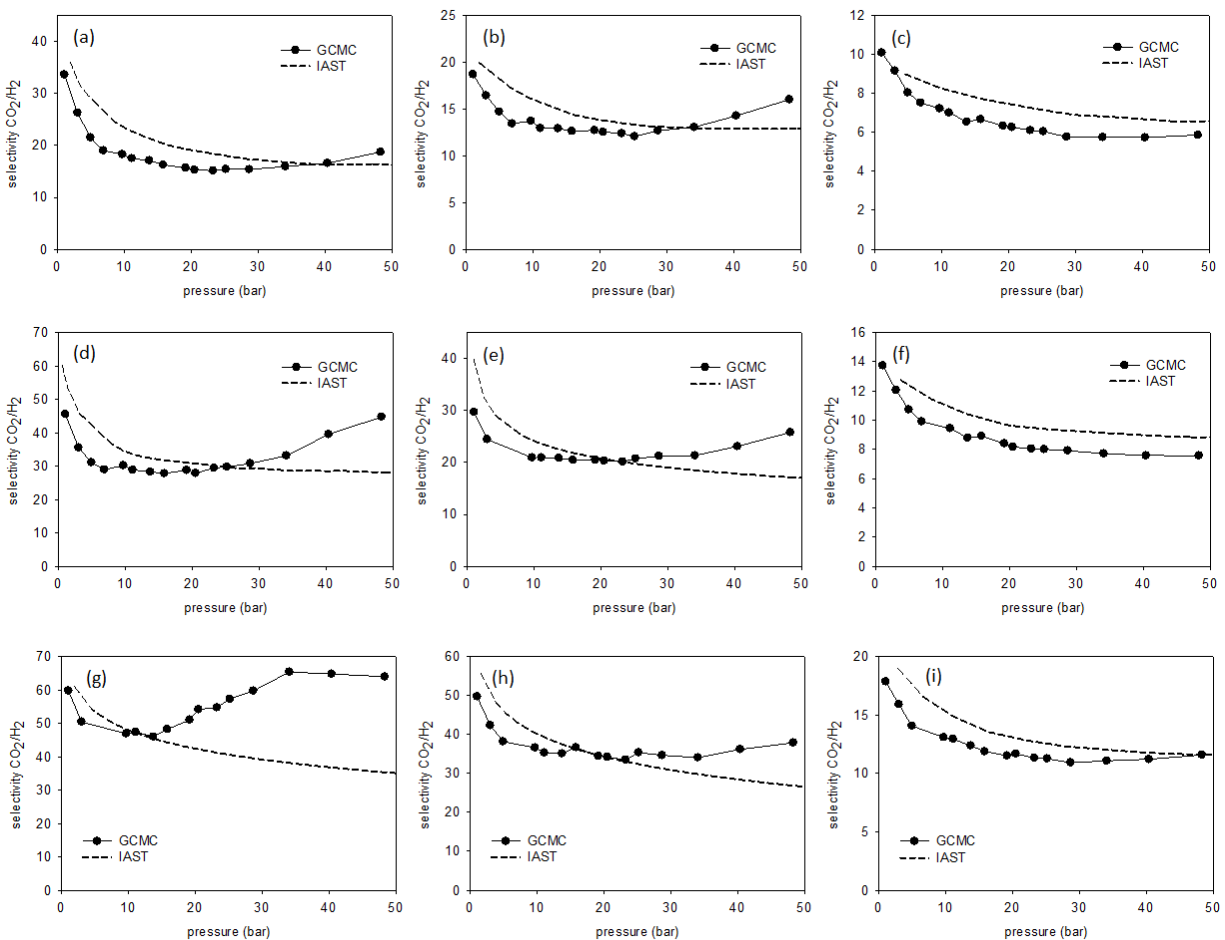


Figure 5.S2. Selectivity comparison between GCMC and IAST for equimolar binary mixture of CO_2/H_2 (a) low density 0 % - OTiCl_3 structure. (b) low density 50 % - OTiCl_3 structure. (c) low density 100 % - OTiCl_3 structure (d) middle density 0 % - OTiCl_3 structure. (e) middle density 50 % - OTiCl_3 structure. (f) middle density 100 % - OTiCl_3 structure. (g) high density 0 % - OTiCl_3 structure. (h) high density 50 % - OTiCl_3 structure. (i) high density 100 % - OTiCl_3 structure.

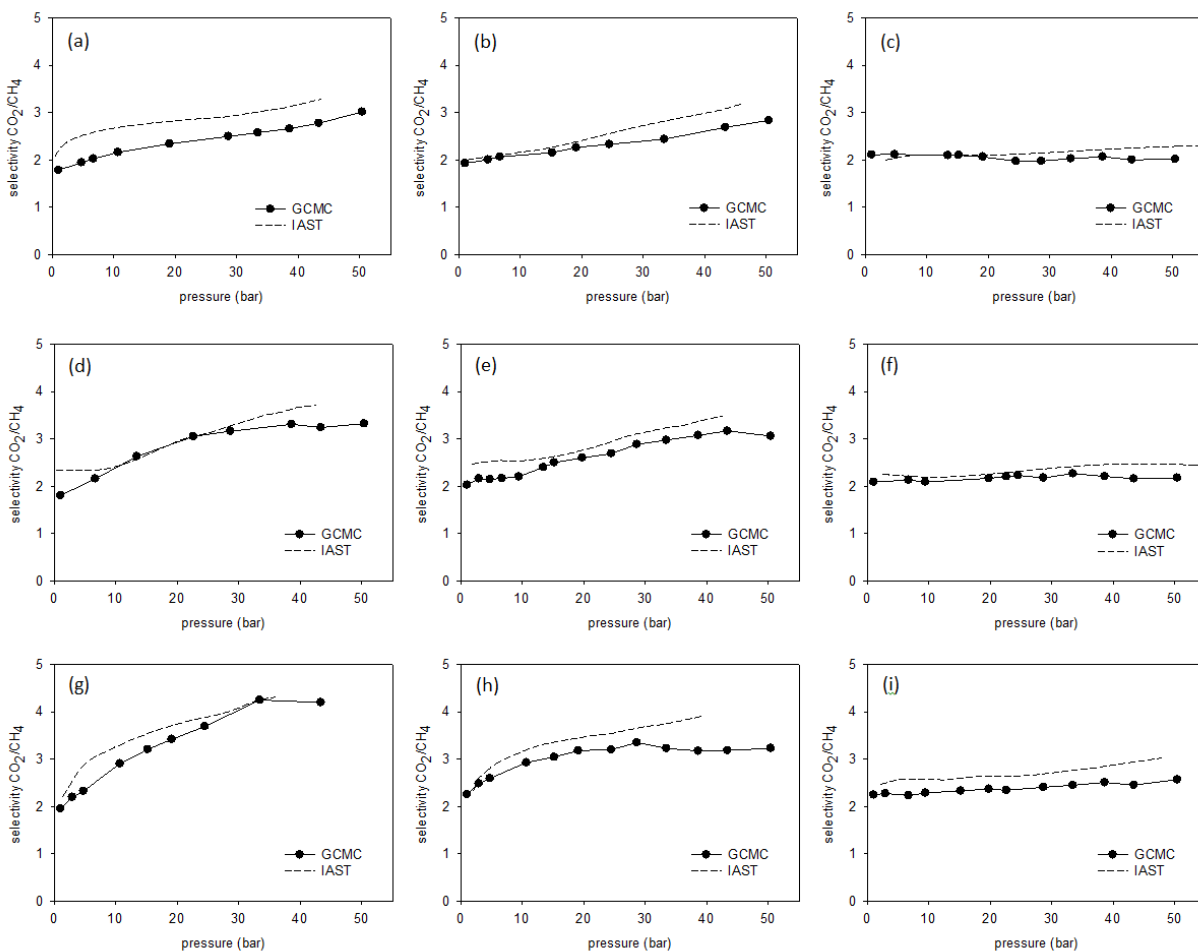


Figure 5.S3. Selectivity comparison between GCMC and IAST for equimolar binary mixture of CO_2/CH_4 (a) low density 0 % - OTiCl_3 structure. (b) low density 50 % - OTiCl_3 structure. (c) low density 100 % - OTiCl_3 structure (d) middle density 0 % - OTiCl_3 structure. (e) middle density 50 % - OTiCl_3 structure. (f) middle density 100 % - OTiCl_3 structure. (g) high density 0 % - OTiCl_3 structure. (h) high density 0 % - OTiCl_3 structure. (i) high density 0 % - OTiCl_3 structure.

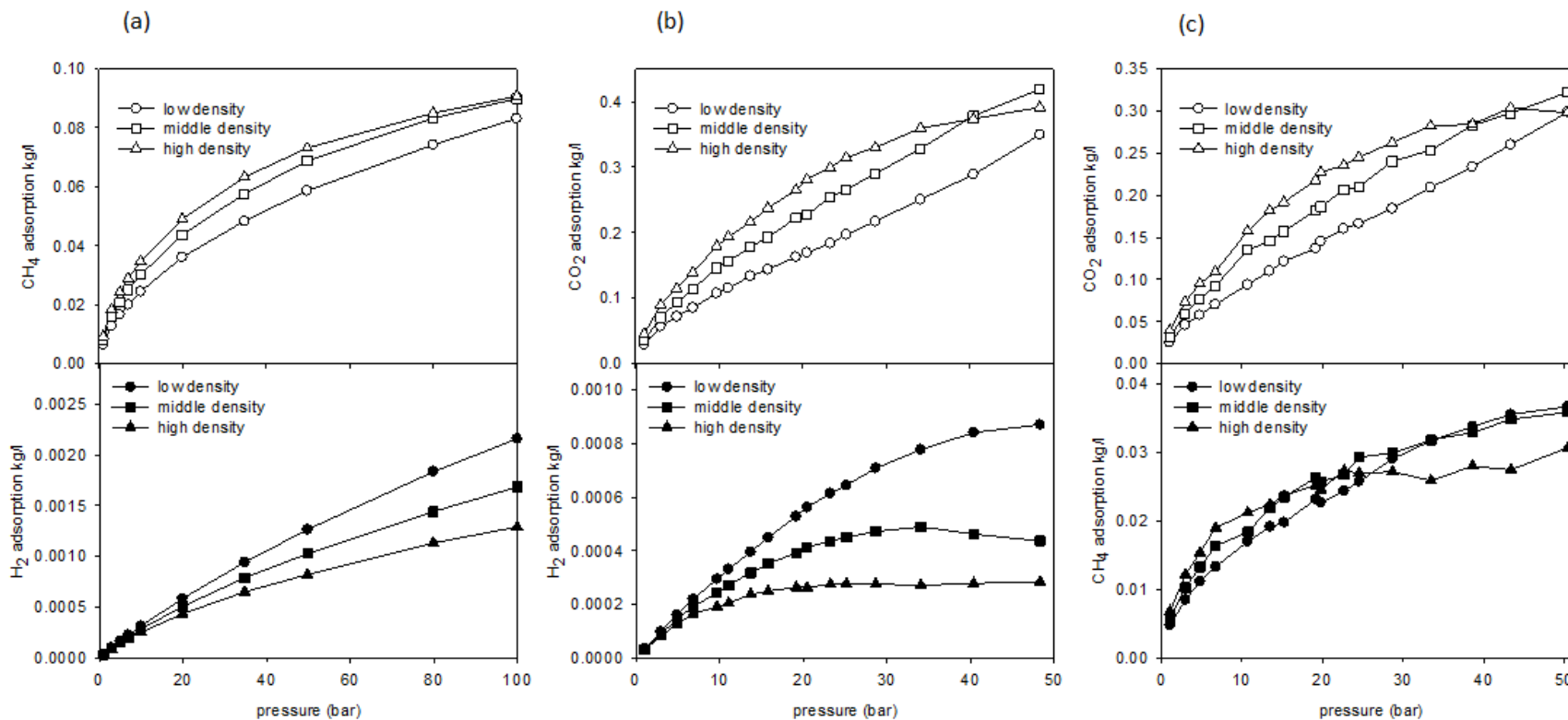


Figure S4. Volumetric isotherms comparison based on effect of density for 0% Ti structure (a) CH₄/H₂, (b) CO₂/H₂, (c) CO₂/CH₄

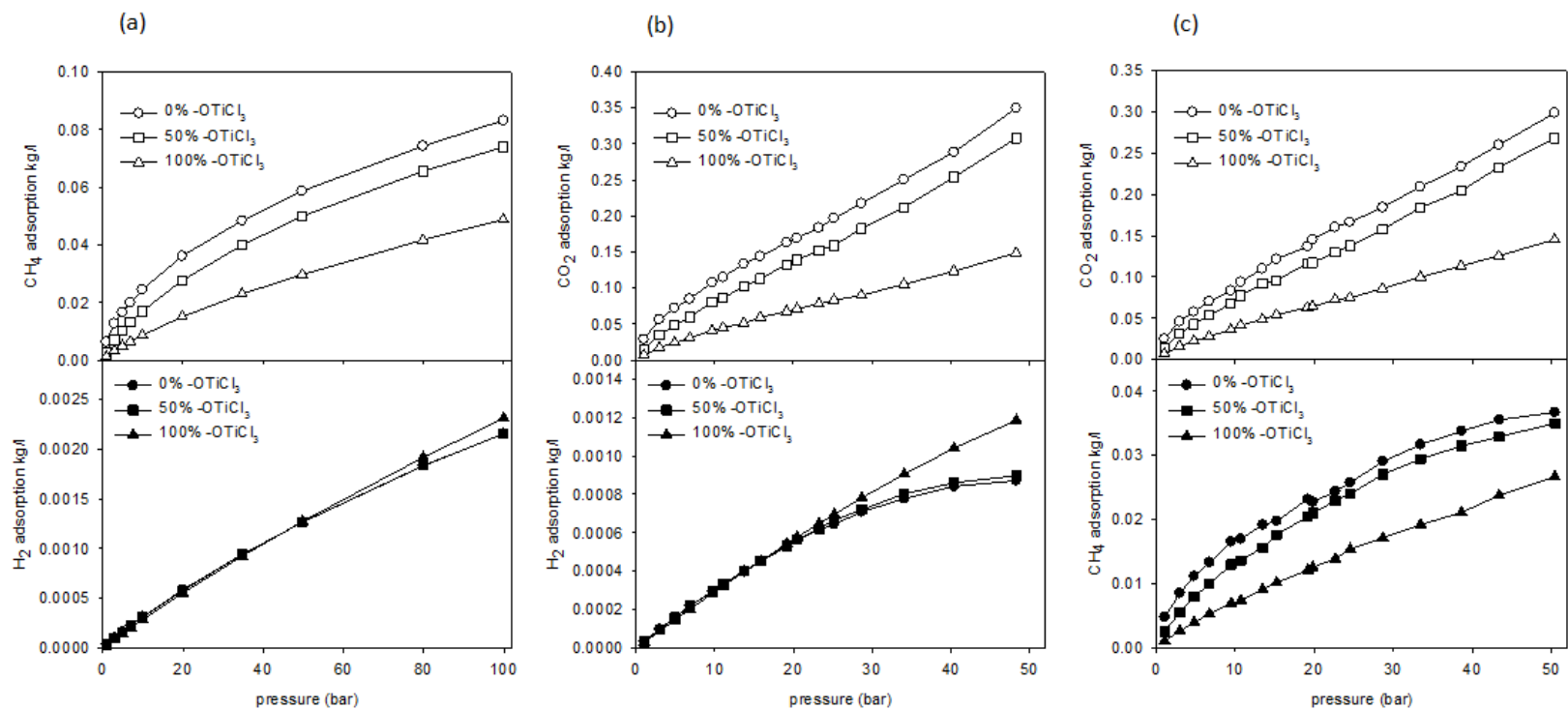


Figure S5. Volumetric isotherms comparison based on effect of Ti content for low density structure (a) CH₄/H₂, (b) CO₂/H₂, (c) CO₂/CH₄

CHAPTER 6

Conclusions

The Conclusion chapter consists of three sections. First, the conclusions from each research chapter are summarized. Second, the overall significance of this study related to current issues in gas storage and separation is stated. Third, a list of potential future research directions, based on the work described in this dissertation, is presented.

6.1 Chapter summary

Chapter 2 presents a study of adsorptive and diffusive behavior of molecular hydrogen in ten different iso-reticular metal-organic frameworks (IRMOFs) using molecular-level simulation. Adsorption isotherms and heats of adsorption at 77 K and 300 K, up to 10 bar, were generated for adsorption by physisorption using Path Integral Grand Canonical Monte Carlo simulations. Self-diffusivities & activation energies for diffusion were generated using Molecular Dynamics simulations. Based on statistical correlations for adsorption properties as a function of surface area (SA), accessible volume (AV), and binding energy important adsorption regimes were identified. At 300 K, the adsorption process is governed by entropic considerations for the entire pressure range. At 77 K, there is more than one adsorption regime. At low pressures, the adsorption process is governed by energetic considerations and at the high end of the pressure range the adsorption becomes a process dominated by entropic considerations. Using density distributions, adsorption sites were identified and are located at the vertices of the cages of the crystalline structure. The self-diffusivity of hydrogen at infinite dilution is highly correlated energy of adsorption and AV.

In Chapter 3, a computational investigation is presented, describing the adsorptive and diffusive behavior of hydrogen in a set of amorphous, nanoporous adsorbents composed of spherosilicate building blocks and incorporating isolated metal sites. The adsorbent were modeled to correspond to experimentally synthesized materials and they contain cubic silicate building blocks (spherosilicate units: Si_8O_{20}), which are cross-linked by SiCl_2O_2 bridges and decorated with either $-\text{OTiCl}_3$ or $-\text{OSiMe}_3$ groups off of the other cube corners. Adsorption isotherms and energies at 77 K and 300 K for pressures up to 100 bar were generated via molecular simulation describing physisorption. The presence of $-\text{OTiCl}_3$ did not enhance physisorption and a low density (high accessible volume) material with no $-\text{OTiCl}_3$ groups

proved to be the best performing adsorbent. Pair correlation functions were used to identify the favorable adsorption sites for hydrogen. They were located in front of the faces of the spherosilicate cubes. The self-diffusivity of hydrogen is highly correlated with accessible volume (AV).

Chapter 4 examines the adsorptive and diffusive behavior of methane and carbon dioxide in the same amorphous silicate adsorbents composed of spherosilicate building blocks and isolated metal sites. Using GCMC, adsorption isotherms and energies via physisorption were generated at 300 K for pressures up to 100 bar for methane and for pressures up to 50 bar for carbon dioxide. The strongest adsorbent for both methane and carbon dioxide is a low density material with 0% Ti content, again proving the presence of oxidized Ti as $-\text{OTiCl}_3$ does not contribute in enhancing physisorption of gases. The gravimetric penalty associated with the $-\text{OTiCl}_3$ groups is high, resulting a lower gravimetric based adsorption in the structures with high Ti content. Also, since the non-bonding well-depth of Ti in the Lennard-Jones potential is weak, they have lower adsorption even on a volumetric basis. At 300 K, at low pressures, the adsorption process is governed by energetic considerations and at the high pressure the adsorption is governed by entropic considerations. Similar adsorption sites for adsorbents were identified that are located in front of the faces of the spherosilicate cubes.

Chapter 5 analyzes the adsorption of equimolar binary mixtures of CH_4/H_2 , CO_2/H_2 and CO_2/CH_4 in adsorbents containing cubic silicate building blocks (spherosilicate units: Si_8O_{20}), which are cross-linked by SiCl_2O_2 bridges and decorated with either $-\text{OTiCl}_3$ or $-\text{OSiMe}_3$ groups. Adsorption of gases via physisorption is considered. GCMC simulations were used to generate adsorption properties for the three different gas mixtures at 300 K and pressure up to 100 bar for the CH_4/H_2 mixture and pressure up to 50 bar for the CO_2/H_2 and CO_2/CH_4 mixtures. Selectivity, which gives a better view of the ability for separation of gas mixtures in the porous materials, were calculated using GCMC results. CO_2 is selectively adsorbed over the other two gases and CH_4 is selectively adsorbed over H_2 . The best separator of gases studied herein is a high density material with 0% Ti content which has smaller pores that generates more energetically favorable sites to adsorb gases. Selectivity was also calculated using Ideal Adsorbed Solution Theory (IAST), based on the pure component adsorption data. It predicted the selectivity calculated by GCMC to a good extent for the mixtures of CH_4/H_2 , CO_2/CH_4 . However, for CO_2/H_2 mixtures,

IAST poorly predicted the trend at higher pressures. The presence of Ti as $-OTiCl_3$ does not enhance physisorption capacity or selectivity for the gas mixtures.

6.2 Significance

Gas storage and separation using porous materials is a popular area of study as it is relevant to the global challenges presented by the finite resources of fossil fuels as well as the climate change due to fossil fuel consumption. For example, these materials are candidates for hydrogen or methane storage in either stationary or vehicular applications, because they are able to store the gas at a relatively high density at relatively low pressures. Nanoporous materials are also being investigated for their CO_2 capacity in the area of carbon sequestration. In both applications, either the generation of pure H_2 or CH_4 fuels, or the storage of CO_2 , purification steps are required. Again, these materials have potential as the active agent in separation processes.

In this research we first investigated IRMOFs and derived some important structure-property relationships that can be used to model new materials with enhanced gas storage capacities. Then a novel porous material composed of spherosilicate building blocks and isolated Ti metal sites was studied for its adsorption and separation capabilities. This material is in its first stages of development, both experimentally and computationally. Even at this earlier stage it shows the competitive behavior with other adsorbents.

The heat of adsorption of hydrogen is higher for spherosilicate structures compared with the other popular adsorbents (by physisorption) such as IRMOFs [1, 2]. This is a good indication that even higher binding energies could be achieved with further modifications in the structure and in the simulations such as seeking the effect of chemisorption with inclusion of reduced Ti.

In comparison to the DOE targets of 180 v(STP)/v (under 35 bar and near ambient temperature), the maximum CH_4 adsorption calculated for the spherosilicate structures is 110.6 v(STP)/v at 34.75 bar, while some other novel adsorbents [3, 4] are capable of adsorbing even beyond the DOE target. Future studies could investigate improving the adsorption capacity to meet the DOE targets.

Comparison with Babarao *et. al.* [5] shows at low pressure (1 bar) spherosilicate structures adsorb more CO₂ than IRMOF-1 and less CO₂ than single-walled carbon nanotubes (SWNT). But at high pressure (up to 50 bar) spherosilicate structures adsorb less CO₂ than IRMOF-1 and considerably more CO₂ than SWNT.

Selectivity of CH₄/H₂ for the best gas separating spherosilicate structures is between 10 and 35, proving to be a good CH₄/H₂ separator compared to other materials. Selectivity of CO₂/H₂ is between 45 and 65 acting as a middle range separator compared to other materials. Selectivity of CO₂/CH₄ is between 2 to 4, a relatively poor result compared to other materials. Overall, the spherosilicate structures perform as a promising adsorbent with positive hopes for the future to improve more with further modifications to the structure.

6.3 Future work

The success of the current modeling and simulation work has enabled us to foresee the following future work. The current modeled structures have only 2-connecting bridges (SiCl₂O₂). We can model structures with 3- connecting (SiClO₃) and 4-connecting (SiO₄) bridges. This increases the connectivity of the structure and the surface area providing more energetically favorable adsorption sites for gases. Our experimental collaborators can generate structures combining these multiple connecting bridges in various ratios. Therefore modeling these complex structures would open the door to compare with experiments more closely.

In our simulations we observed that the structures with high Ti content adsorb less gas, since the non-bonding well-depth of Ti in the Lennard-Jones potential (based on the force field we used-UFF) is weak relative to other atoms (e.g.: Si). In the future we would figure out a better choice of force field for our simulations to predict the experimental results with a higher level of agreement.

The overall goal of the project is achieving higher adsorption capacity using the increased binding energies of the Ti metal centers that are between those associated with physisorption and chemisorption. Therefore a major future step for the modeling work is to include adsorption by chemisorption in our simulations. (Currently the simulations include adsorption by physisorption only). For this task, an analogous material should be developed, in which the Ti is reduced and can act as a chemisorption site for gases. In a reduced state, the Ti metal centers provide catalytic

sites, which mimics the favorable adsorption energy associated with physisorption and chemisorption

Finally the experimentalists are planning to investigate the effect of using different metals to replace Ti to see which brings more gas storage capacity. The simulation team would also work in line with them to make predictions in order to identify better metals.

References

- [1] N.S. Suraweera, R.C. Xiong, J.P. Luna, D.M. Nicholson and D.J. Keffer, *On the relationship between the structure of metal-organic frameworks and the adsorption and diffusion of hydrogen*, Mol Simulat. 37 (2011), pp. 621-639.
- [2] N.S. Suraweera, A.A. Albert, J.R. Humble, C.E. Barnes and D.J. Keffer, *Hydrogen Adsorption and Diffusion in Amorphous, Metal-Decorated Nanoporous Silica*, Int. J. Hydrogen Energy. under review (2013).
- [3] S.Q. Ma and H.C. Zhou, *Gas storage in porous metal-organic frameworks for clean energy applications*, Chemical Communications. 46 (2010), pp. 44-53.
- [4] L. Huang, Z.H. Xiang and D.P. Cao, *A porous diamond carbon framework: a new carbon allotrope with extremely high gas adsorption and mechanical properties*, Journal of Materials Chemistry A. 1 (2013), pp. 3851-3855.
- [5] R. Babarao and J.W. Jiang, *Molecular screening of metal-organic frameworks for CO₂ storage*, Langmuir. 24 (2008), pp. 6270-6278.

Vita

Nethika Suraweera was born in Colombo, Sri Lanka on December 13th, 1982. She grew up in Kadawatha, Sri Lanka and did her schooling in Vihara Maha Devi girls' school. In 2002, she attended to University of Moratuwa, Sri Lanka where she received a Bachelor of Science Degree in Chemical Engineering in 2006. In August 2008, she was admitted into the Ph.D. program in the Department of Chemical and Biomolecular Engineering at the University of Tennessee, Knoxville, TN (USA) and accepted assistantship at the Computational Materials Research Group.

Nethika Suraweera completed her doctorate in Chemical Engineering at the University of Tennessee, Knoxville, TN, in December, 2013.